THE UNIVERSITY *of* EDINBURGH

Magnetic Gear Design for Wave Energy Converters

Ben McGilton

Doctor of Philosophy
University of Edinburgh
2019

Abstract

With renewable energy an increasingly essential element in providing clean, abundant energy and combating climate change, wave energy presents an enormous untapped resource. Key to the challenges facing the industry are the high operation and maintenance costs associated with operating in offshore environments. A recent technological development that could address this issue is the magnetic gear. The magnetic gear allows for smaller and more efficient electrical machines while providing inherent protection to the drivetrain and requiring substantially reduced maintenance due to the contactless nature of operation.

With magnetic gears now reaching a high technology readiness level there is a need to develop accurate and efficient design methods. This work looks at developing these methods, along with design tools, with a focus on application to wave energy devices.

This work introduces the concept and operating principles of magnetic gears and gives a state of the art in the variations available. Following a discussion of design considerations and methodology, the tools developed in this work are applied in the design and development of two prototypes which are tested for a range of operating conditions followed by a critical analysis of the results.

Declaration

I declare that this thesis was composed by myself, that the work contained herein is my own except where explicitly stated otherwise in the text, and that this work has not been submitted for any other degree or professional qualification except as specified.

Date:

Signed:

List of Publications

"A Review of Magnetic Gear Technologies and their Application to Marine Energy",
B. McGilton, R. Crozier, A. McDonald, M. Mueller, IET Renewable Power Generation, 2017.

"Optimization Procedure for Designing a Magnetic Gear",
B. McGilton, R. Crozier, M. Mueller, IET Journal of Engineering, 2017.

"An Investigation into Linear Generators with Integrated Magnetic Gear for Wave Energy Power Take-Off",
B. McGilton, A. A. Almoraya, M.A.H. Raihan, R. Crozier, N.J. Baker, M. Mueller accepted for publication, IET Journal of Engineering 2019.

"Dynamic Model Testing of a Combined C-Gen Magnetic Gear System for an Oscillating Wave Surge Converter",
B. McGilton, R. Crozier, M. Mueller, presented at the Asian Wave and Tidal Energy Conference, 2018.

"Magnetic Gear Design for an Oscillating Wave Surge Converter",
B. McGilton, R. Crozier, M. Mueller, presented at the European Wave and Tidal, Energy Conference, 2017.

For my parents: Ón monarcha, an táirge

Acknowledgements

First and foremost I would like to thank my supervisors Professor Markus Mueller, Dr. Richard Crozier and Dr. Alasdair McDonald without whose expertise, guidance and support this work would not be what it is. I would also like to thank the staff at the University of Edinburgh who aided in so many ways to the completion of this work. In particular I would like to acknowledge Anup Nambiar for his enormous help during the testing phase and Douglas Carmichael for his expertise in all things practical.

I would like to thank the lecturing and support staff at the Wind and Marine Energy Systems, Center for Doctoral Training for giving me the best start possible in the renewables sector.

My sincere thanks also go to Mike Galbraith of Fountain Design Ltd for developing the prototypes and for his patience during the design stages. To all my friends in IES and Strathclyde, thank you for all the support and good times.

I gratefully acknowledge the financial support provided by the Engineering and Physical Science Research Council, carried out by the Wind and Marine Energy Center for Doctoral Training.

Finally I would like to thank the Mother, the Pops, Sib and Savs, for everything else.

Contents

List of Figures

List of Tables

Chapter 1

Introduction

1.1 Climate Change - A Global Challenge

Climate change presents one of the greatest threats to modern society. The rise in temperatures has resulted in extreme weather conditions, increased flooding and droughts. Rising sea levels are an immediate concern for coastal communities both in terms of land loss and as a threat to sources of freshwater.

The international scientific community has attributed this global warming to the higher levels of green house gases in the atmosphere. In particular, the massive increase in Carbon Dioxide ($C0_2$) from the use of fossil fuels for energy supply, transportation and industry is a leading contributor. Emissions have grown by 80% since the 1970s and in the years between 1995 - 2004 there was a higher rate of growth than in the previous 25 years. In 2018 the Intergovernmental Panel on Climate Change (ipcc) released a report detailing the most recent assessment of the effects of climate change in the near future [31]. Beyond outlining the catastrophic effects a > 2 °C increase in global temperatures would have on virtually every aspect of life, it urges the adoption of renewable energy to curtail $C0_2$ emissions.

The response from the international community has grown rapidly in the last decade. Efforts like the Paris Agreement have put the global community on a path of low emission societies. As of year end 2017 more than 150 countries have renewable energy targets with 85 countries, states or provinces having targets of more than 50% [32].

In order to meet these targets it is essential that the renewable energy industry continues its development and expands beyond its current levels.

Wave Energy

With an estimated worldwide potential of between 2 PWh/yr and 5.5 PWh/yr, ocean wave energy has enormous potential as an abundant and reliable low carbon energy resource.

To put this in context, even assuming a recoverable resource of 44% of the gross potential, wave energy could provide 2/3s of global energy consumption [1]. Furthermore, wave energy has some advantages when compared to other renewables. In 2014, Fadaeenejad et. al found that wave energy has the highest energy density of all renewables, is predictable and continuous, and has a low level of environmental impact [33]. Wave energy has particular potential in remote areas and islands, especially in developing regions. The lack of grid connection means that these communities are largely dependent on imported fossil fuels. Many of these communities, particularly in South East Asia [34], have reasonable wave energy density and the development of local micro grids could have enormous benefits [33]. Additionally, there is a growing research area into multipurpose wave energy devices such as combined WEC and breakwater structures [35] and projects which use wave energy to produce clean drinking water [36]. The global distribution of wave energy, as shown in Figure 1.1 in kW per meter of wave front, suggests that it could increase energy security for many countries and has a global market.

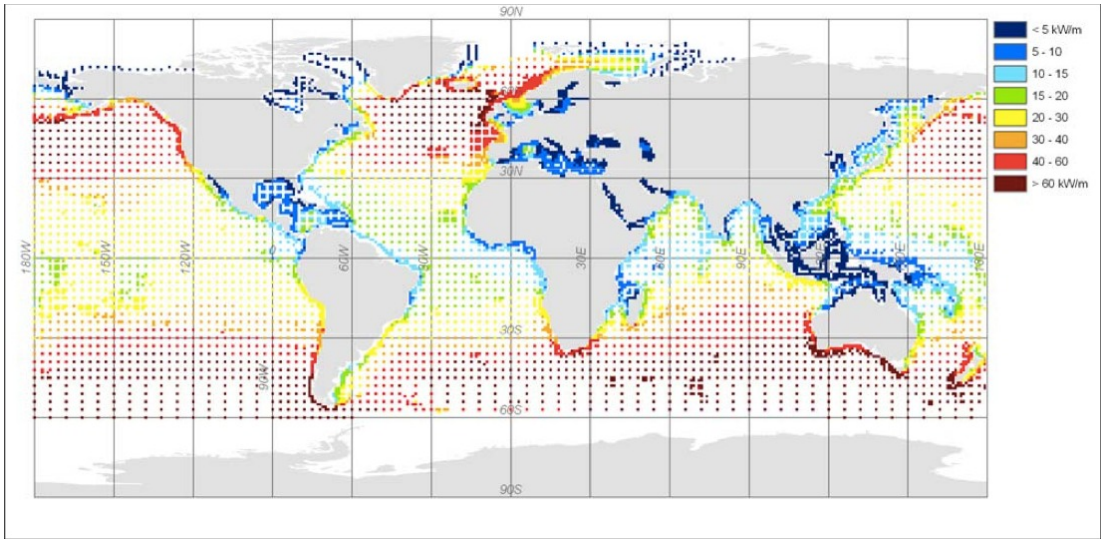

Figure 1.1: Annual global gross theoretical wave power [1]

The UK in particular has a large untapped resource with a study in 2012 by the Carbon Trust concluding that there is between 32 and 42 TWh that could practically

and economically be harvested, equating to 10-13 GW of installed capacity [37].

As well as the environmental and social potential in carbon emission reduction and remote energy access, wave energy presents an enormous economic opportunity. According to a RenewableUK report, by 2035 the combined wave and tidal energy industry is predicted to create around 20000 jobs in the UK with a projected value of £6.1 billion [38].

This opportunity has resulted in highly innovative developments, and a myriad of solutions with the European Marine Energy Centre (EMEC) listing over 220 wave energy developers currently working on devices.

However, despite the undeniable potential, and decades of research and development, wave energy converter (WEC) technology has still not achieved commercial readiness. When compared to onshore renewable technologies, wind in particular, a key obstacle is the significantly higher operation and maintenance (O&M) costs associated with any offshore installation including specialised equipment, heightened health and safety requirements, and the need for weather windows to perform necessary maintenance and repair procedures [24, 39]. This is exacerbated by operating in the harsh environments usually associated with marine energy i.e highly saline, high wave height and strong tidal flows. Additionally, the forces these devices can encounter during normal operation can vary greatly with storms and irregular sea conditions requiring most devices to have a high degree of survivability. These associated costs have resulted in a focus on low failure, robust systems. A further issue is that, unlike wind energy, the technology has not experienced significant design convergence such as the three bladed horizontal axis wind turbine most commonly found. While this is possibly as a result of the high variation in wave energy sites, it has made characterizing and comparing devices a non-trivial matter.

A suggested method has been to organise the devices into how they interact with the wave energy. This results in 8 types:

A) Attenuator devices are characterized as a floating device operating parallel to the incoming waves. Energy is captured from the relative motion between device components through either a hydraulic PTO or direct connection to a generator.

B) Point Absorbers absorb energy from all directions, most commonly generating energy from the heave element of waves.

C) Oscillating Wave Surge Converters are fixed or floating devices which absorb energy

predominantly from the surge element of waves.

D) Oscillating Water Columns convert energy as waves cause compression and decompression in a hollow structure with the use of an air turbine.

E) Over-topping Devices create a height differential in a water reservoir from waves over-topping a fixed structure. Energy is usually then generated with the use of a low head turbine.

F) Submerged Pressure Differential devices are generally bottom mounted devices that capture energy from the pressure difference in the water as waves pass over the device.

G) Bulge Wave Devices are most commonly a water filled tube which experiences pressure variations along the tubes length with each passing wave. These variations cause a bulge effect in the tube and the energy can then be extracted with a low head turbine.

H) Rotating Mass Devices capture energy through heave and swaying motion where the movement causes an eccentric weight to rotate. The weight is attached to a generator inside the device. These primary 8 types are shown in Figure 1.2 with animations available on the EMEC website [2]. There is an additional 9th type which is used to categorize those devices which fall beyond the mentioned categories. Given the variety of devices, advancements in one device may not benefit the industry as a whole. With common issues affecting a wide range of devices, there is a requirement for solutions that are adaptable for a variety of devices such that the industry as a whole may benefit.

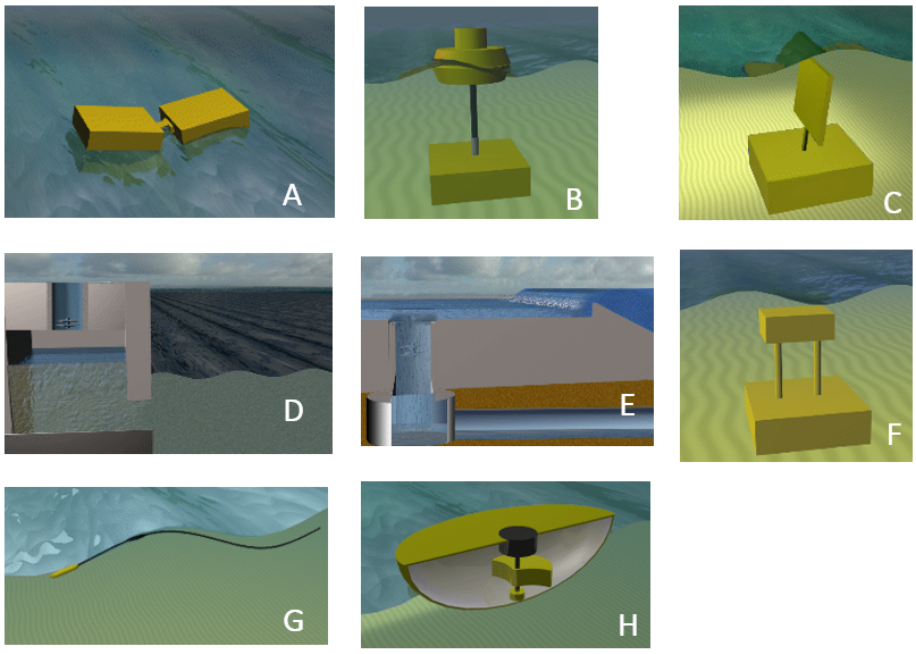

Figure 1.2: Primary types of WEC [2]

1.1.1 The Power Take-Off and Wave Energy

Key to addressing the economic challenge of wave energy is the power take-off (PTO). In a WEC the PTO is the mechanism by which the energy in the wave is converted to useful energy. Though other methods, such as dielastomers [40], are being investigated the use of an electrical generator is by far the most commonly employed method for converting the potential and kinetic energy into electrical energy. However, the use of traditional generators leads to some challenges when employed in a wave energy application. Though wave sites can have very high energy density and generation potential, the low frequency element of the resource is not conducive to efficient electrical energy generation at grid frequency [41]. The physical size of machines is a particular concern for offshore installations as larger devices make transport difficult and when installing require specialised equipment like ship mounted cranes which can be very expensive to rent with a daily rate for multicats being upwards of £30k.

The overall size of an electrical machine is governed by a few well established equations. The power ratings of the machine is directly related as follows:

$$P = T\omega \tag{1.1}$$

where ω is the rotational speed in radian/s and T is the torque in Nm which can be calculated as:

$$T = Fr = \sigma Ar = \sigma 2\pi r^2 l \tag{1.2}$$

where F is the equivalent force (in Newtons), σ is the shear stress in N/m^2 in the machine's airgap, A is the area (m^2) of the airgap, r and l are the machine's airgap radius and stack length respectively. Thus, for a fixed rated power the volume of the machine is inversely proportional to the rotational speed as follows:

$$V = \frac{P}{\omega 2\sigma} \tag{1.3}$$

Therefore in order to have a small, compact machine a high rotational speed is required.

With the low frequencies associated with wave energy a speed enhancement system, usually a mechanical gearbox, is necessary with the alternative being a large direct drive machine. While both these systems allow for more conventional machines to be used both have related issues which are exacerbated by the marine application.

Direct Drive Versus Geared Machines

Though substantial published information on O&M costs is currently unavailable for marine energy devices, wind energy, in particular offshore wind, has similar requirements in terms of machine conditions and frequencies. A critical analysis of both geared and direct drive systems highlights the shortcomings for application in wave energy devices.
This section of the thesis is part of a paper published in the IET RPG 2016 Special Issue Journal [42].

Mechanical gearboxes are regarded as having a critical effect on reliability as the associated down time per failure is high compared to other turbine components [43, 44]. Furthermore, despite advancements, traditional gearboxes have yet to achieve design life goals (20+ years), often requiring substantial repairs or overhauls [45]. This can be largely attributed to wear resulting from the physical interaction between mechanical elements under force. This is potentially exacerbated in a highly saline environment with irregular loadings.

In [46] Henk Pollinder et al. examined and compared 5 different generator concepts (namely: doubly fed induction generator with 3 stage gearbox [DFIG3G], direct-drive synchronous generator with electrical excitation [DDSG], direct drive permanent magnet generator [DDPMG] , permanent-magnet generator with single stage gearbox (PMG1G) and DFIG with single stage gearbox [DFIG1G]) with the comparison focused on cost and annual energy yield for a given wind climate. The results of the comparison found that while the industry standard DFIG3G was the lightest and lowest cost it suffered from low energy yield with high losses, 70% of which are associated with the mechanical gearbox. Furthermore, it was noted that since the machine consists mostly of components consisting of copper and iron, major improvements and cost reductions cannot be expected. The DDPMG, though more expensive due to its size and power converter requirements, was shown to have the highest energy yield. Additionally, a key point was that, unlike the DFIG3G, further improvements can be reasonably expected due to the improvement in power electronics, the expected reduction of PM material cost and further optimisation and integration of the generator system. Therefore it would suggest that using direct drive systems and eliminating the gearbox associated

O&M costs would result in a superior more cost effective machine.

However, along with requiring a physically larger system there are further issues. In [47] David McMillan et al. established a techno-economic comparison of operational aspects between direct drive (DD) and the standard three-stage gearbox-driven (GD) wind turbines by providing analytical calculations regarding the availability of traditional wind turbine devices. From this a clearer understanding of the technical and economic merits of DD and GD systems can be gained. The paper supposes that the assumption that DD systems have reduced maintenance issues due to the elimination of those associated with a gearbox only holds if all other factors remain unchanged and highlights findings that indicate much higher failure rates of electrical components and generators of DD turbines when compared to GD equivalents. Though the paper excluded consideration of PM machines due to the lack of deployment, it provides some interesting results with regards to DD vs GD machines. The results state that while DD is marginally better in terms of availability, looking at revenue generated suggests GD machines have a much larger economic benefit and that from an economic analysis, GD machines are still preferable unless manufacturing costs of direct drive technology can be significantly reduced. Nonetheless, it was surmised that the operational availability of DD can be significantly higher than GD as long as the majority of generator failures are minor electrical failures as opposed to severe mechanical failures (e.g bearing problems).

Tavner et al. [48] found that DD systems were less reliable due to increased generator, inverter and electrical system failures. However the authors recognized that overall availability would also be affected by component repair times i.e mean time to repair for a gearbox is much more than electronics. This issue becomes much more relevant in offshore installations as extensive work can be greatly delayed due to accessibility, weather windows and equipment or vessel availability.

In [49] Echavarria et al. analysed a similar data set and found that DD systems have twice the generator failures as GD equivalent systems and that the power electronics had an approximately 50% higher failure rate in DD synchronous machines compared to an induction machine equivalent. It should be noted that power electronics have greater opportunity for design redundancy due to component size and cost and there is ongoing research and development in related fields, such as HVDC systems [50], which

could be of benefit.

From these studies it can be surmised that there is no clear solution in addressing the downtime associated with drivetrain failures in wind energy which is an established industry with substantial financial support. The operational issues are anticipated to be greater in a marine application with even lower operating speeds ($\approx$ 1 rpm) and under increased mechanical strain from the considerably denser fluid. Furthermore, the potential for some devices to be completely submerged will increase maintenance procedure complexity, increasing repair times and reducing converter availability.

Alternatives

A number of researchers, designers and developers have proposed intermediate energy conversion and conditioning steps in order to step down force/torque and step up speed with hydraulics being the mostly widely employed.

Hydraulic PTO's benefit from the technology's maturity with the required accumulators and valves being relatively cheap and available. Additionally, hydraulics allow short term energy storage [51], a certain level of control [3] and are readily adaptable to the low frequency, high force conditions of wave energy. Hydraulic PTO's, however, suffer from two major issues: efficiency and reliability. The efficiency is affected by the inherent losses associated with a hydraulic system, namely shear losses, leakage losses, compressibility losses and flow losses and, while more advanced systems have been proposed suggesting 80% [52], a more common value cited is around 60% [24, 53]. While not a certainty, it is generally considered that the more complex a system is, the lower its overall reliability. Hydraulic PTO's involve multiple, interdependent cycling parts (example: Figure 1.3) which will all have associated failure rates and can negatively affect a device's availability and O&M costs. There is further concern with the use of hydraulics in marine energy converters as, depending on the hydraulic fluid used, a leakage may contaminate the area affecting the local wildlife.

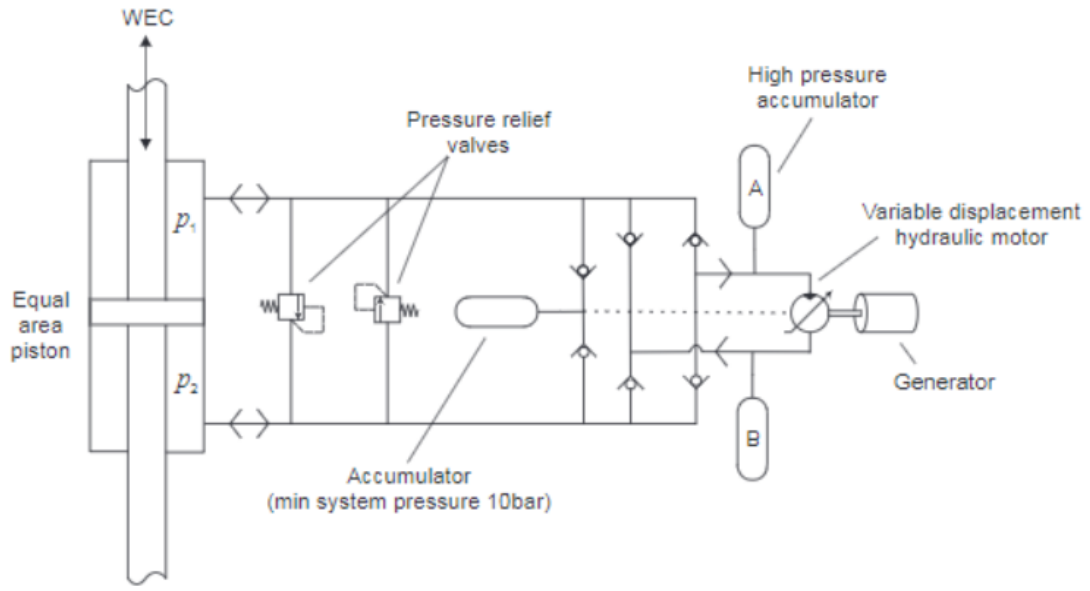

Figure 1.3: Example hydraulic PTO [3]

With existing commercially available solutions falling short, there is room for revolutionary new systems. Among these is the magnetic gear which is a rapidly growing technology applicable across a number of industries [54]. Now reaching a high technology readiness level the magnetic gear has the potential to address many of the discussed issues.

1.2 The Magnetic Gear

Magnetic gears (MGs) have been of interest since the early 20th century with the earliest designs being very similar to conventional mechanical gears with the gear teeth replaced by magnetic counterparts [55,56]. However these designs received little attention, most likely due to the low torque densities achieved as a result of the permanent magnet (PM) materials available at the time (namely SmCo5).

A renewed interest came in the 1980s with the development of neodymium iron boron (NdFeB) magnetic material though the designs still relied on direct mechanical substitution, thus resulting in poor PM utilisation and never achieved torque densities high enough to compete with traditional mechanical alternatives [57,58]. More detailed reviews of the early development of the technology over the past 100+ years are given in [59, 60].

The term "magnetic gear" can be applied today to any system that establishes a torque speed step change through magnetic transfer of forces between actuators. As

topologies can differ greatly, a standard value for comparison of MG types is the torque density or the maximum torque which can be applied to the gear for a volumetric meter. The leading MG types are generally considered those with competitive torque densities to traditional mechanical gears (50-150 kNm/m^3 for a helical gear and 100-200 kNm/m^3 for a spur type gear). The unit of torque per volume is a useful comparator as it will directly affect important power train design characteristics such as physical size and weight [4].

A comprehensive review was done by Li and Bird in 2018 of the leading modern rotary magnetic gears with particular emphasis on the torque density and achieved ratio [4]. The work clearly showed the wide array of MG types and the rapid development in the last two decades.

The following section introduces the leading gear types, namely: the magnetic spur gear, the magnetic planetary gear, the cycloidal magnetic gear and the flux modulated magnetic gear (FMMG) and discusses some of the most relevant developments in the field.

Magnetic Spur Gear

The Magnetic Spur Gear (MSG) is the simplest realisation of a magnetic gear. As shown in Figure 1.4 in both the external and internal types, the topology of the MSG is the same as that of a traditional mechanical gear but with the rotor teeth being replaced with magnetic poles [61].

While benefiting from simplicity of design and operation it is clear that only a small amount of the magnetic material is employed for torque transfer at any point. This results in a low torque density, as reported in [61] with 17.6 kNm/m^3.

The gear ratio G_r for an external spur gear (a) is determined by:

$$\omega_2 = -\omega_1(\frac{p_1}{p_2}) \tag{1.4}$$

where ω_1 and ω_2 are the rotational speeds of the rotors and internal (b):

$$\omega_2 = \omega_1(\frac{p_1}{p_2}) \tag{1.5}$$

The G_r then is:

$$G_r = \frac{p1}{p_2} \tag{1.6}$$

where p_1 and p_2 are the magnetic pole pair numbers on the respective rotors.

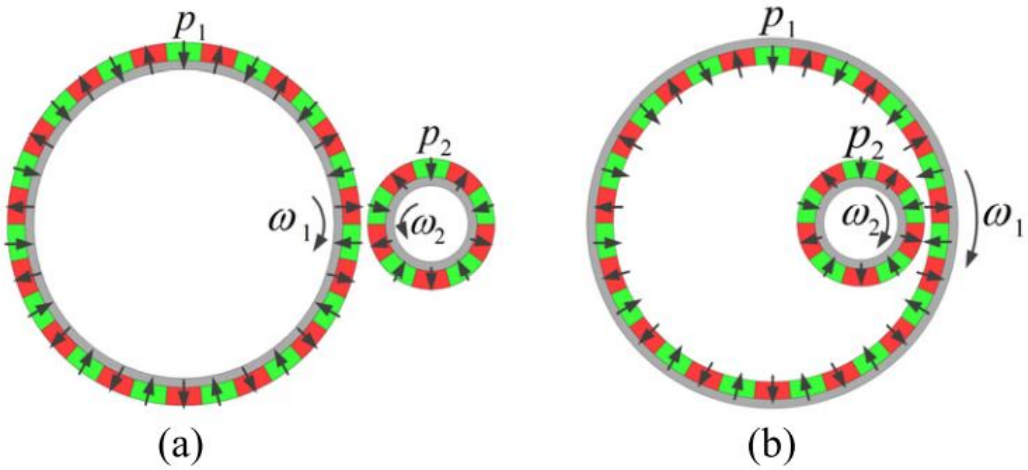

Figure 1.4: Spur type MG [4]

Magnetic Planetary Gear

The Magnetic Planetary Gear (MPG) proposed by Huang et al. [5] is another adaptation from traditional mechanical gears and operates through the same principles as a traditional mechanical planetary gear (Figure 1.5). While the calculated torque density was over 100 kNm/m^3 the experimental results proved considerably lower (16 kNm/m^3). The reason for this substantial drop in expected torque density was not explained. As with the mechanical planetary gear the MPG is capable of 3 transmission modes depending on which ring is fixed.

The gearing ratio is determined by:

$$G_r = \frac{p_r}{(p_s + p_r)} \tag{1.7}$$

where p_r and p_s are the pole-pairs on the magnetic ring gear and sun gear respectively with the pole-pair relationship on the planetary gear determined by:

$$p_p = \frac{(p_r - p_s)}{2} \tag{1.8}$$

Like the spur gear, the MPG has a similar issue in that not all of the permanent magnet material is utilised during torque transfer. Additionally, the multiple moving elements make the model a complicated structure.

A new MPG topology was proposed in 2015 by Davey et al. [6]. This model proposed increasing the planet rotors as shown in Figure 1.6. This resulted in an extremely high

torque density 300 kNm/m^3 though fabricating and constructing this model would be very challenging at an industrial scale.

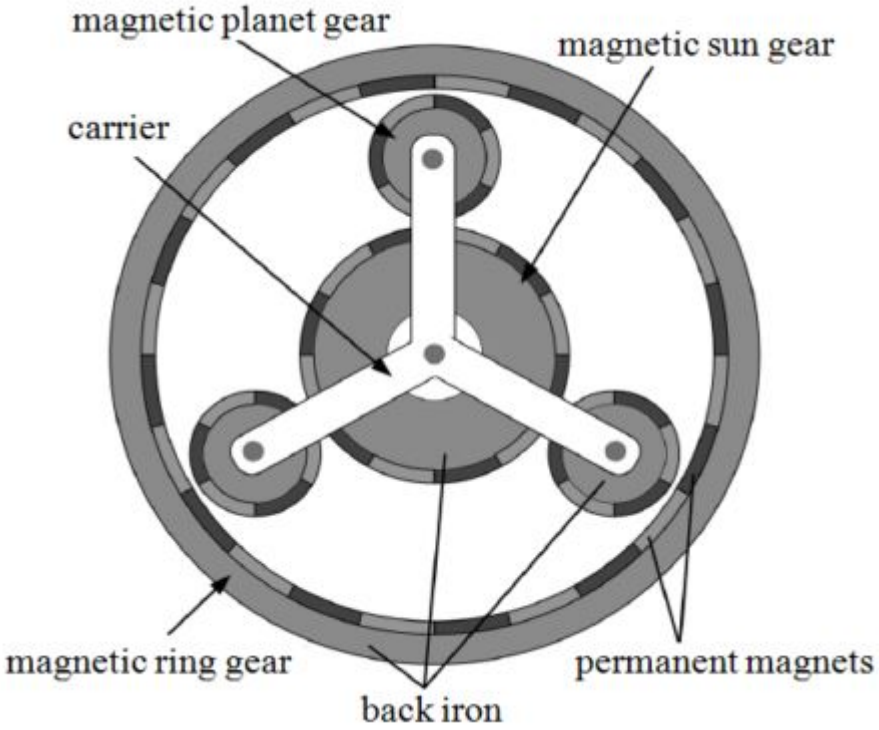

Figure 1.5: Magnetic panetary gear topology [5]

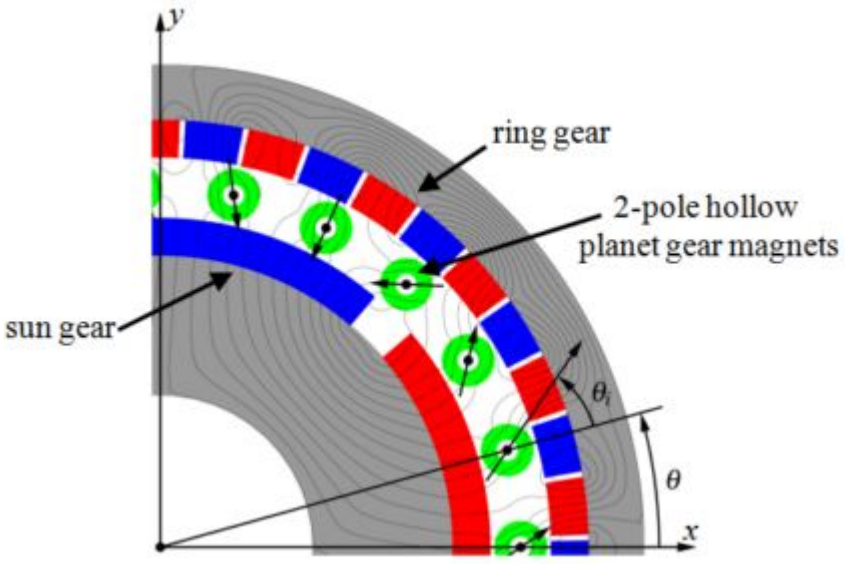

Figure 1.6: Magnetic planetary gear with multiple planetary rotors [6]

Magnetic Cycloidal Gear & Magnetic Harmonic Gear

The Magnetic Cycloidal Gear (MCG) and the Magnetic Harmonic Gear (MHG) operate through constant change of the magnetic field in the airgap between rotors established from the eccentric movement of one of the rotors.

The MCG, as shown in Figure 1.7, is an adaptation of the spur gear and was first presented in 2008 by Jorgensen et al. [7]. With this gear the inner rotor will rotate with an eccentric orbit creating a non-uniform radial force. This action makes a high ratio possible (20:1) and reported a torque density of 141.9 kNm/m^3. The requirement for constant rotor eccentricity can cause considerable wear on the bearings however and there may be issues maintaining the airgap.

The MHG operates in a similar method to the cycloidal gear, except employs a flexible rotor to produce a time-varying sinusoidal variation of the magnetic field in the airgap between the rotors [8]. An example is shown in Figure 1.8 and, though attractive for its torque density (140 - 180 kNm/m^3), high gear ratios and smooth torque transmission, the flexible rotor is complicated to construct and, like the cycloidal gear, may encounter issues maintaining the airgap. The ratio is determined as follows:

$$G_r = \frac{(-1)^{(k+1)} p_w}{p_l} \tag{1.9}$$

with p_l and p_w representing the number of poles on the low speed rotor and the number of sinusoidal cycles between low speed rotor and stator respectively and k representing the various asynchronous space harmonics which are associated with each harmonic of the magnetic field produced by the permanent magnets.

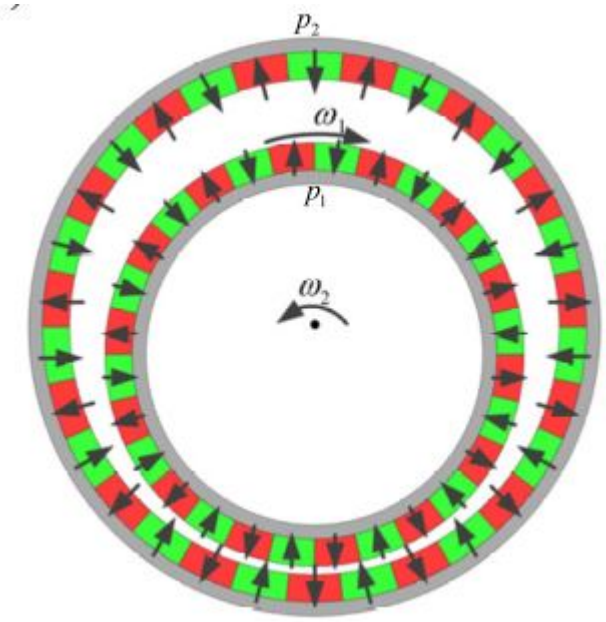

Figure 1.7: Cycloid magnetic gear topology [7]

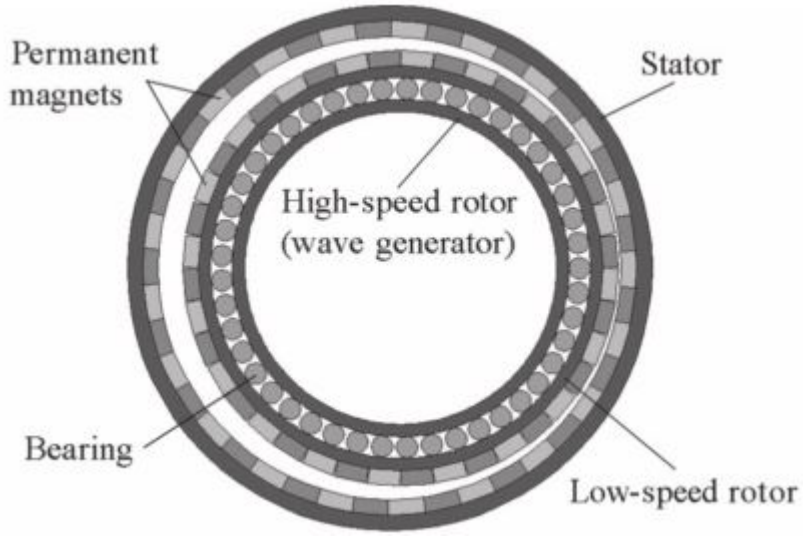

Figure 1.8: Harmonic magnetic gear topology [8]

1.2.1 Flux Modulated Magnetic Gear

The FMMG is generally considered the leading design. Though a similar design can be seen in T. B. Martin's 1968 patent, "Magnetic transmission" [62], it was in Atallah & Howe's paper in 2001, under the name Concentric Magnetic Gear (CMG), that the design's high torque density capabilities (>100 kN/m^3) were demonstrated [63].

The CMG was the first of the category of FMMG in that it employs ferromagnetic Flux Modulating Pole (FMP) segments in order to modulate the magnetic flux active

between rotors. This design allowed for full utilisation of all PM material and resulted in high torque density in the range of 70-150 kNm/m^3 with a relatively simple design. To explain the operation of the FMMG the standard coaxial CMG will be used as an example as this design is used in the majority of the MG concepts. The CMG consists of three main elements: an outer and inner rotor with PM poles and a FMP rotor in the space between them as shown in Figure 1.9.

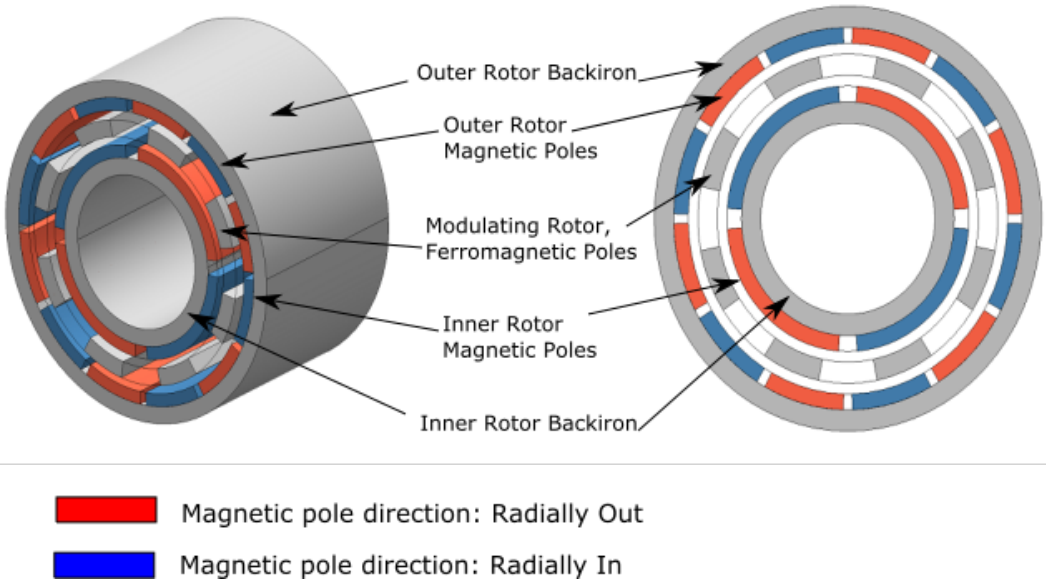

Figure 1.9: Basic elements of a concentric magnetic gear

The FMP's modulating effect is demonstrated in Figures 1.10 & 1.11. The figures show a gear with the inner rotor magnetic poles removed and 19 magnetic pole pairs on the outer rotor.

Comparing the model with no FMPs, Figure 1.10, with Figure 1.11, where the FMPs have been included, there is clear modulation and 6 distinct magnetic flux fields with which 3 pole pairs could align. By plotting the flux acting on the inner rotor in a circle graph, this effect is further highlighted as shown in Figures 1.12 & 1.13.

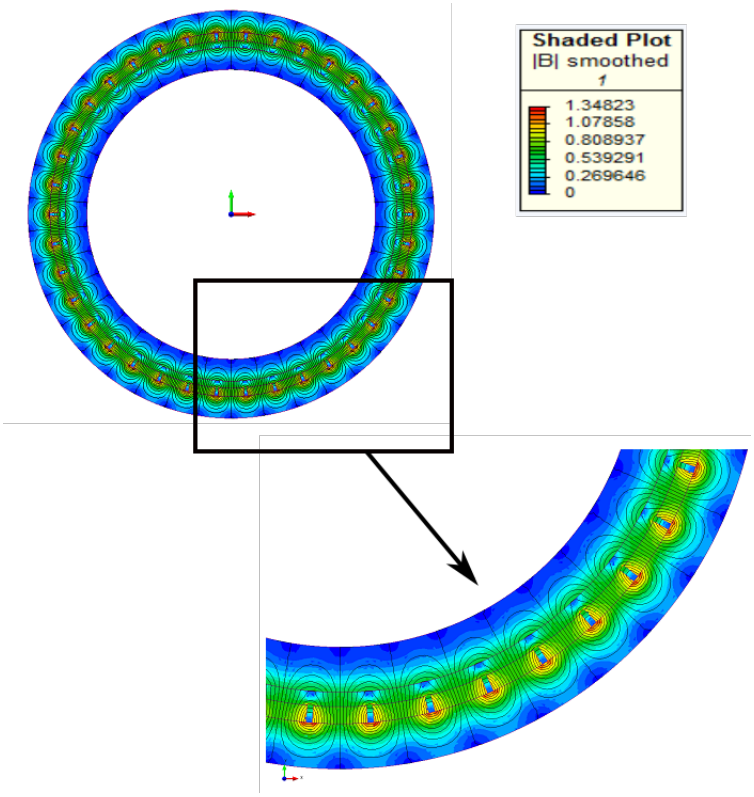

Figure 1.10: Magnetic field without FMPs

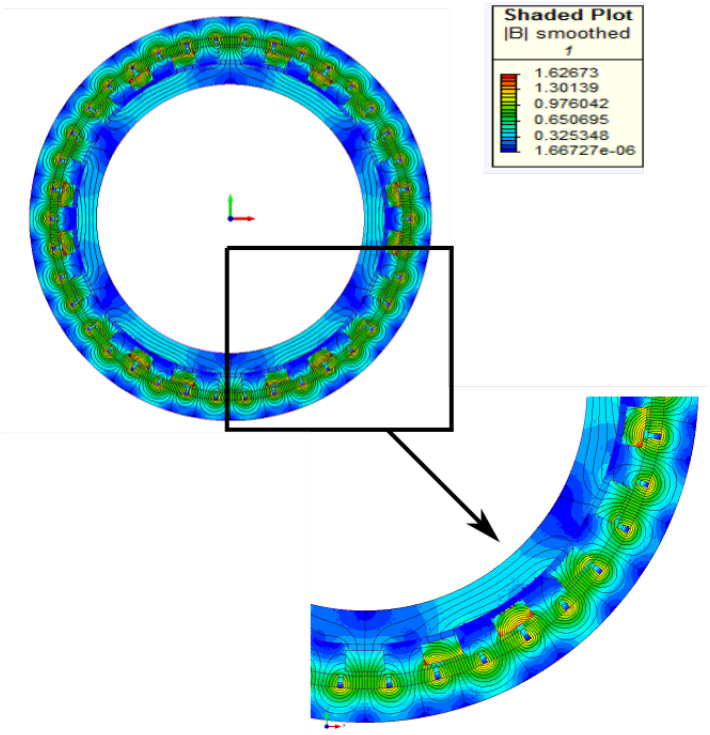

Figure 1.11: Magnetic field with FMPs

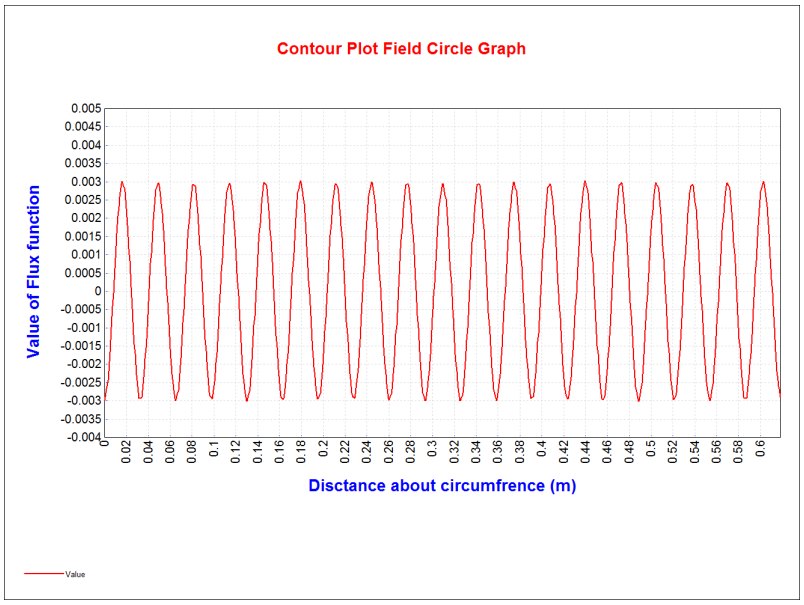

Figure 1.12: Magnetic field plot without FMPs

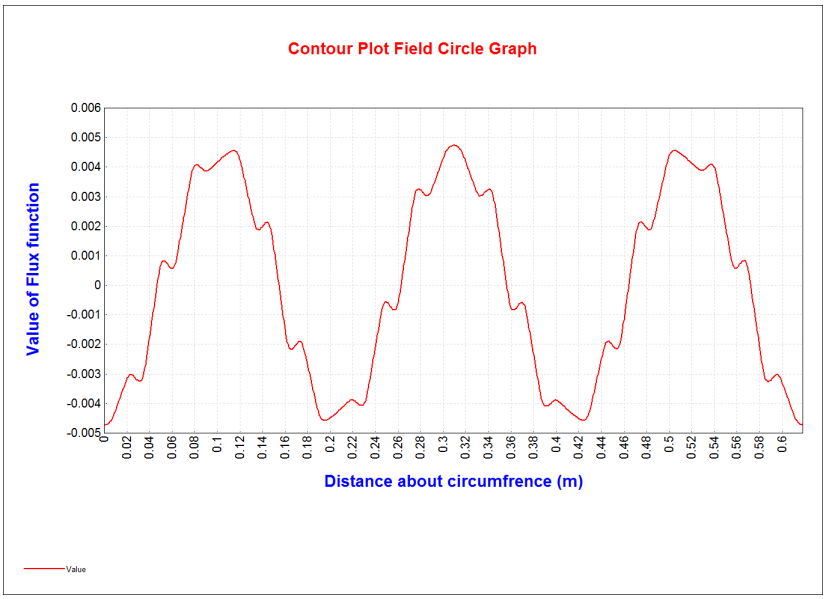

Figure 1.13: Magnetic field plot with FMPs.

When the outer rotor is then rotated the gearing effect can be observed. Figure 1.14 shows the initial magnetic field and when the outer rotor has been rotated 5 degrees. The magnetic field at the inner rotor has rotated 31.65 degrees in accordance with the gear ratio. Placing inner rotor poles with the correct number then fully establishes the gear system where torque is transferred from one rotor to the other through magnetic action only.

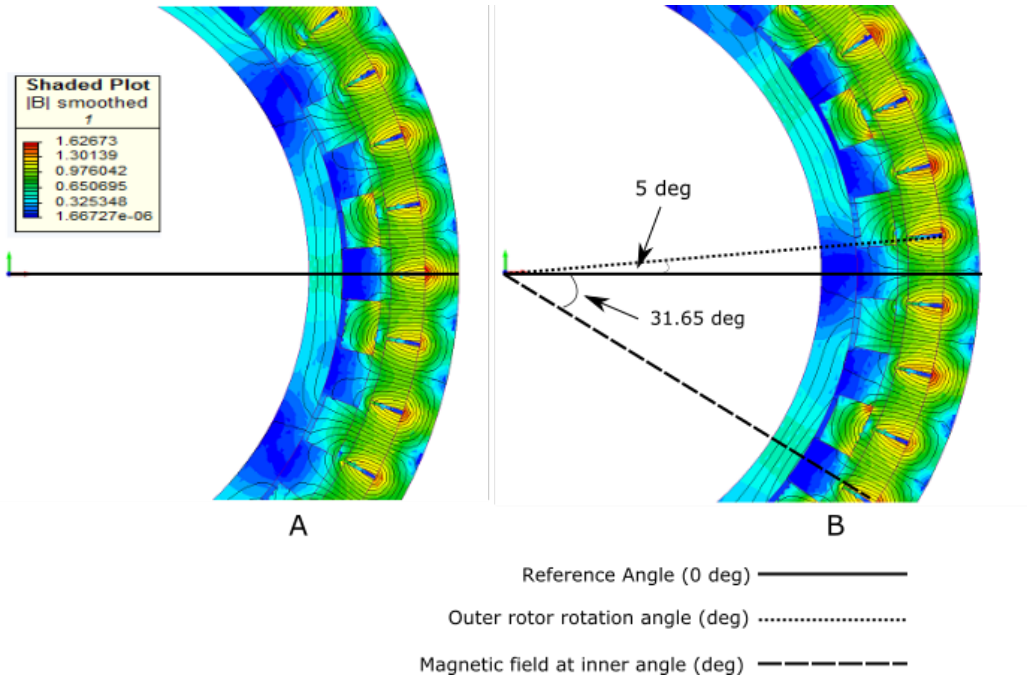

Figure 1.14: Magnetic field rotation with ratio. A) Initial reference position, B) 5° rotation of outer rotor.

A FMMG has two operating modes depending on which of the three rotors is held stationary. The rotor with the low number of magnetic pole pairs will be the high speed, low torque rotor. The low speed, high torque rotor will then be either the FMP ring or the high magnetic pole number ring. The gear ratio can be calculated as follows:

$$G_r = \frac{p_l}{p_h} = \frac{(n_s - p_h)}{p_h} = \frac{-\omega_h}{\omega_l} \tag{1.10}$$

where ω_h and ω_l are the rotational speeds of the high and low speed rotors respectively. The minus sign here indicates that the rotors will rotate in opposite directions. Alternatively, with the ferromagnetic elements allowed to rotate and the outer high pole number rotor held stationary the gear ratio will be:

$$G_r = \frac{n_s}{p_h} = \frac{\omega_h}{\omega_s} \tag{1.11}$$

Therefore for the same configuration a higher gear ratio can be achieved.

The number of FMP pieces for optimal field modulation and torque transfer was determined in [63] and is calculated as:

$$n_s = p_l + p_h \tag{1.12}$$

where n_s, p_l and p_h are the ferromagnetic pole pairs, the magnetic pole pairs on the low speed side and the magnetic pole pairs on the high speed side respectively.

Given the advantages of the FMMG and its readiness for industrial application this type of MG was selected as the focus for this work.

1.2.2 Alternative Versions

Within the category of FMMGs there is considerable variation in topologies, magnetic pole array, materials and forms of operation. The following discusses some of the most relevant developments to establish the state of the art of the technology.

Magnetic Material

Though it is the high torque capabilities resulting from the use of NdFeB magnets that has brought the recent rapid growth in the field it is still useful to consider the magnetic alternatives such as ferrite magnets. In 2017 Johnson et al. did a comparison of NdFeB and ferrite magnets for CMGs. The study found that for most historical prices, NdFeB gear designs generally result in lower active material costs and always have much higher torque densities [64]. However it was noted that the analyzed ferrite gears are capable of higher efficiencies, particularly at higher speeds and generally emit less leakage flux. The higher efficiency can be attributed to the lack of iron in the ceramic based ferrite magnets as opposed to the iron heavy NdFeB, rare earth, magnets. The iron element will result in eddy currents within the magnetic poles which can be significant at higher speeds [65]. This is discussed further in Chapter 2. The lower leakage flux is a result of the materials low reflectance allowing it to easily conduct the magnetic flux [64]. There is also a concern about price fluctuations and availability of NdFeB magnets as China dominates the supply chain with 80% of the worlds NdFeB magnets being produced in the country [66].

Halbach Array

Recent developments have shown that significant improvements can be made in MGs if alternative magnetic pole alignments are used as opposed to the standard arrangement. In [9] Jian et al. compared a CMG with Halbach array with a conventional CMG of the same size (Figure 1.15).

Though using a Halbach array can be mechanically difficult to assemble, the result-

ing design was found to have a higher torque density, 110.7 kNm/m^3 vs 91.1 kNm/m^3. A further potential advantage is that the backiron is not necessary and can be replaced with a non-ferrous material which may be lighter or cheaper. This may be particularly advantageous in marine applications as the use of a non-ferrous material for the structure would greatly reduce maintenance issues associated with rust and potentially biofouling.

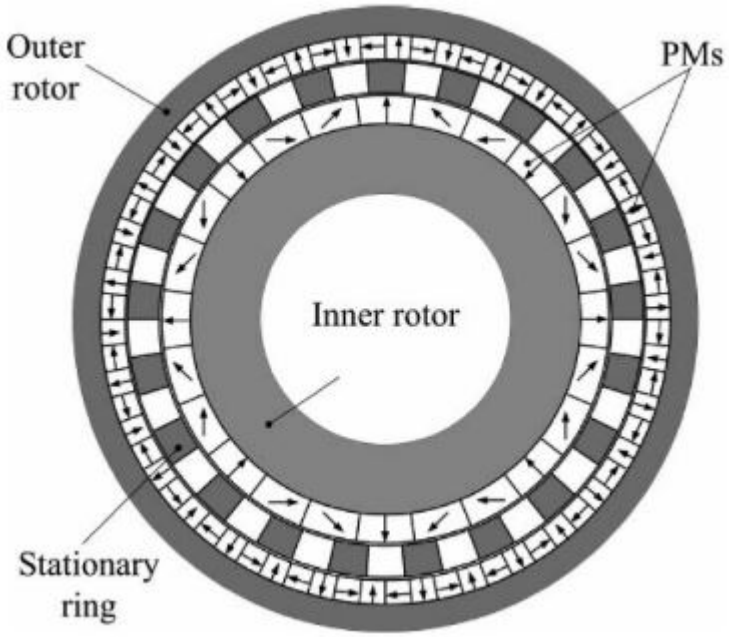

Figure 1.15: Halbach array MG [9]

Flux Focusing & Flux Concentrating

Designs have been proposed to improve on the flux density for a given gear volume or to reduce the amount of PM material required. A flux focusing MG was first proposed in 2005 by Rasmussen [10]. As shown in Figure 1.16, the design had a Finite Element Analysis (FEA) predicted torque density of 92 kNm/m^3 though the lower value of 54.5 kNm/m^3 was measured when a scaled prototype was built and tested. The cause of this drop was suggested to be the end effects that had not been accounted for in the FEA and that, with the prototype having a relatively short axial length, these end effects were substantial.

In 2012 the concept was further developed by Uppalapati et al. who looked at flux focusing MGs with both ferrite and NdFeB magnetic poles. The design, shown in Figure 1.17, resulted in a measured torque density of 239 kNm/m^3 [11].

The concept of flux concentrating MGs was investigated by Fu et al. in 2016 [12]. The design, shown in Figure 1.18, is extremely complicated but resulted in a 2D FEA high torque density of 382.7 kNm/m^3.

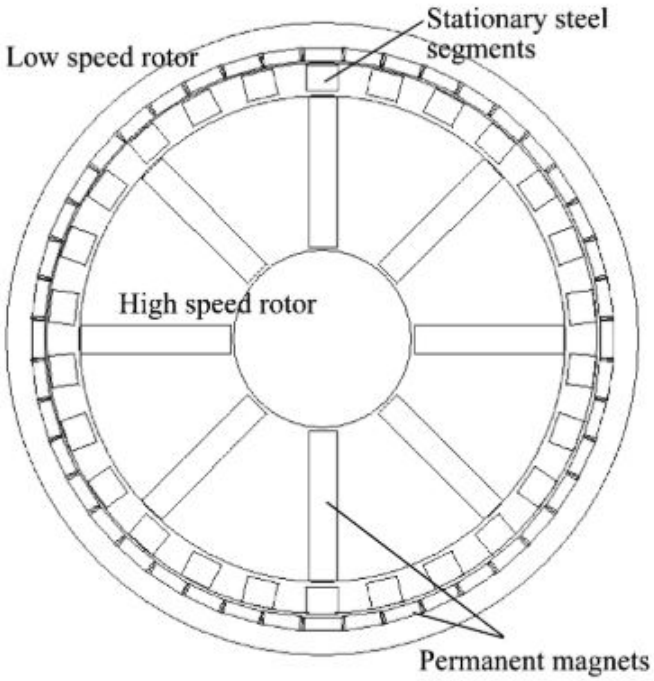

Figure 1.16: Flux focusing MG with NdFeB magentic poles [10]

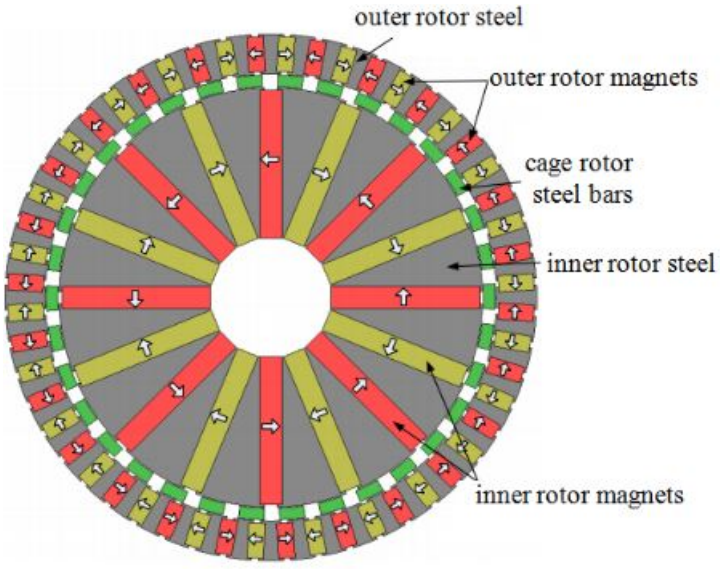

Figure 1.17: Flux focusing MG with ferrite magnetic poles [11]

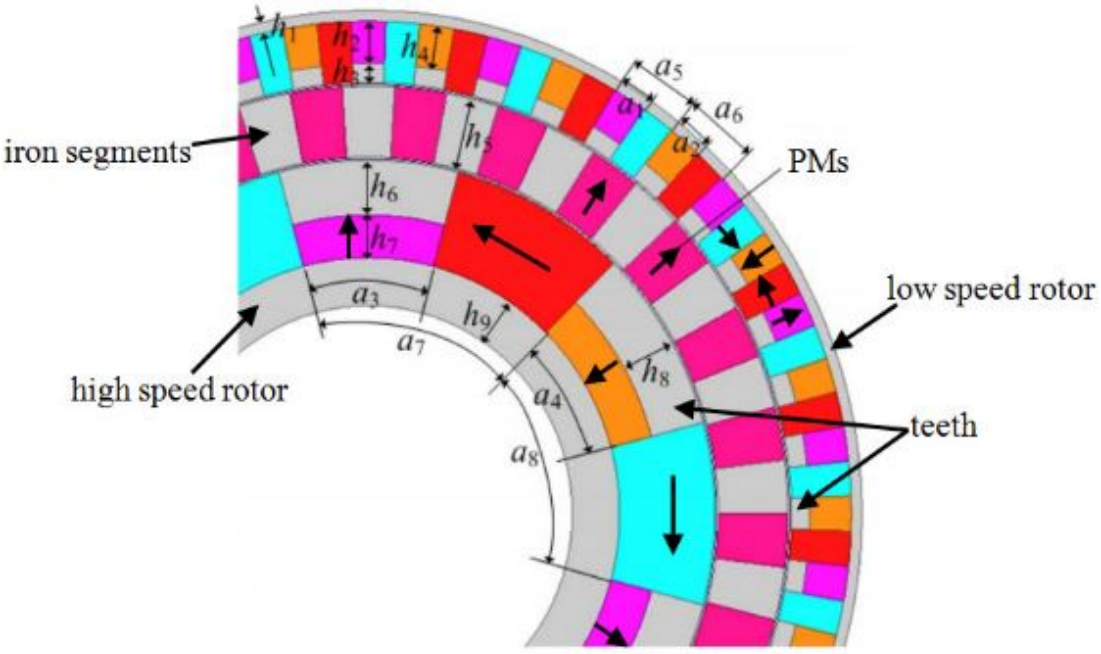

Figure 1.18: Flux concentrating magnetic gear [12]

1.2.3 Topology Variation: Axial, Linear, Transverse Flux and Trans-Rotary MGs

Given the wide array of wave device types, adaptability is a highly attractive attribute for a PTO system if it is to be adopted by the industry. Following Atallah's work, the FMMG design has been investigated for axial, linear and transverse flux topologies.

Axial

Following on from Atallah's work, Mezani et al. developed the axial field FMMG. Operating by the same principles as the CMG, the axial version had a calculated torque density of 70 kNm/m^3 (Figure 1.19).

Two recent works further developed the design. Using a flux focusing array (Figure 1.20), Acharya et al. achieved a torque density of 289.8 kNm/m^3 [13]. Then in 2015 Johnson et al. employed Halbach arrays on both rotors and produced a gear with predicted torque density of 183.9 kNm/m^3 [67].

The axially arranged MG has great potential in applications where complete hermetic separation is required between rotors. In marine energy applications this would be particularly useful when considering sealing options.

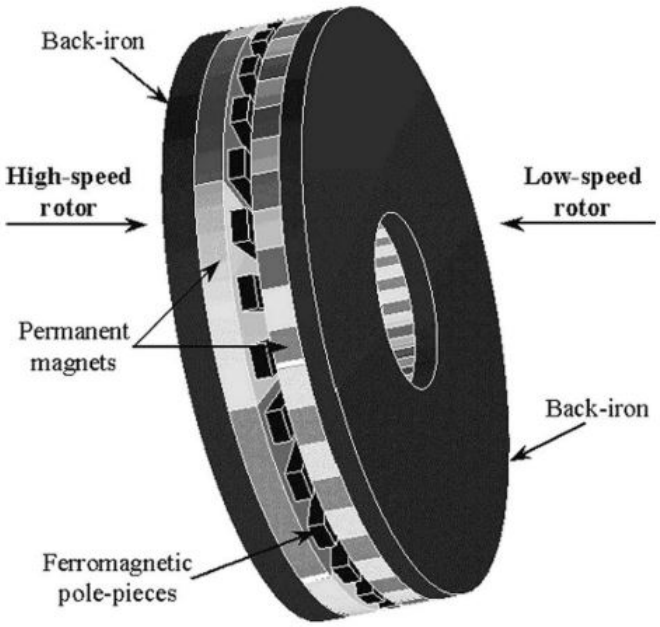

Figure 1.19: Axial Flux MG

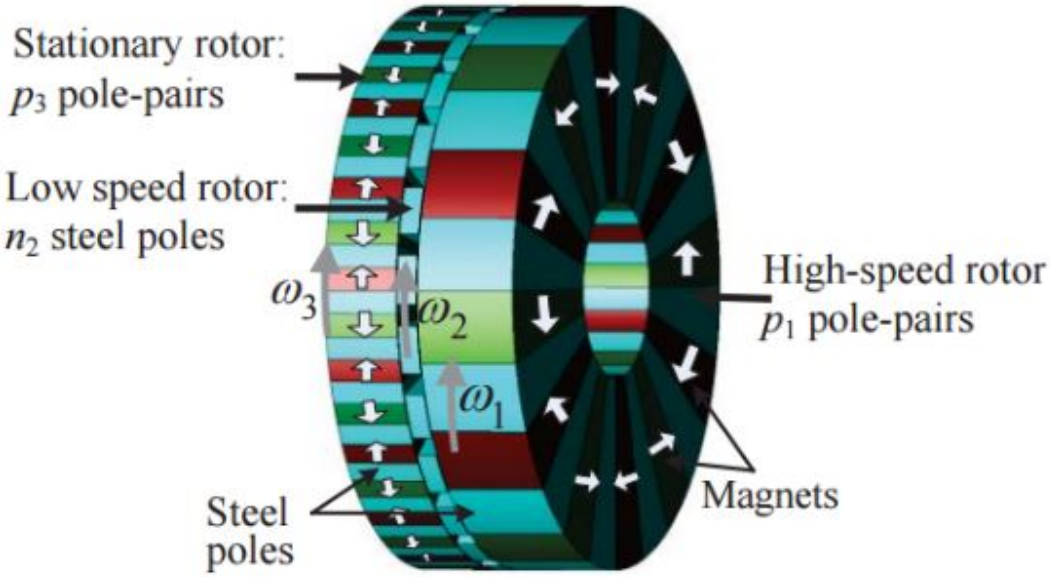

Figure 1.20: Axial MG with flux focusing arrangement [13]

Transverse Flux

A transverse flux FMMG was first proposed in 2008 by Tong et al. [68]. While this design resulted in a very low torque density of 2.4 kNm/m^3 the concept was revised in 2014 with Bomela et al. and resulted in a predicted torque density of 80.6 kNm/m^3 [14]. The topology of this gear is shown in Figure 1.21.

In 2016 an axial version of the transverse flux gear was developed by Zhu et al. as shown in Figure 1.22. With this arrangement the calculated torque density was 77 kNm/m^3 [15].

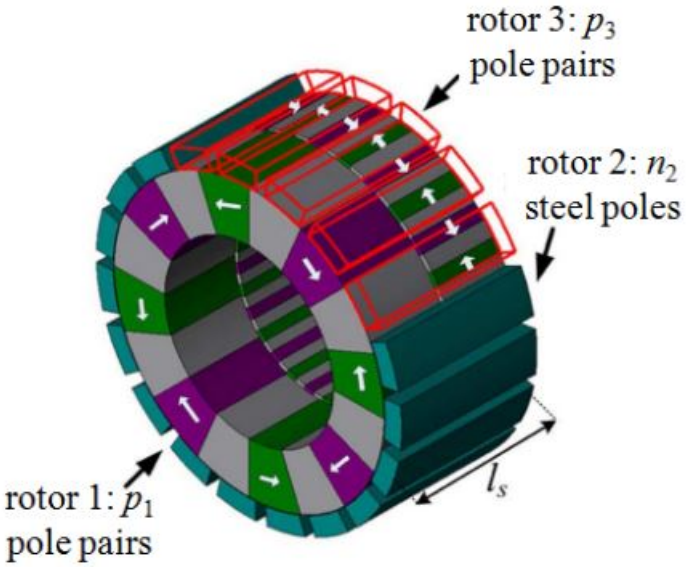

Figure 1.21: Transverse flux MG [14]

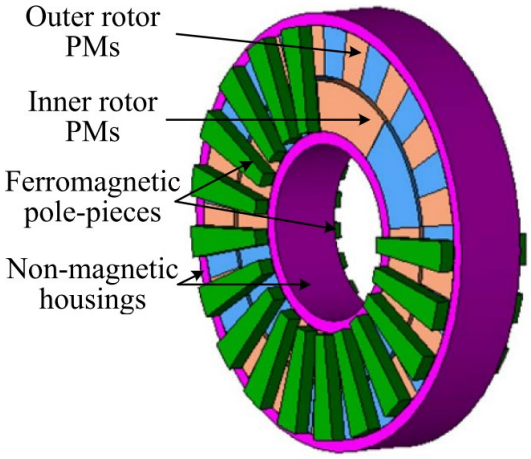

Figure 1.22: Axially orientated transverse flux MG [15]

Linear

The linear version of the FFMG was first proposed in 2006 by Atallah et. al [69]. The structure as shown in Figure 1.23 operates through the same principles as a rotary FMMG and has a reported force density in excess of 2 MN/m^3. The design was further investigated in [17] and a prototype with structure as shown in Figure 1.24 was tested. The prototype had a measured peak force of 8 kN.

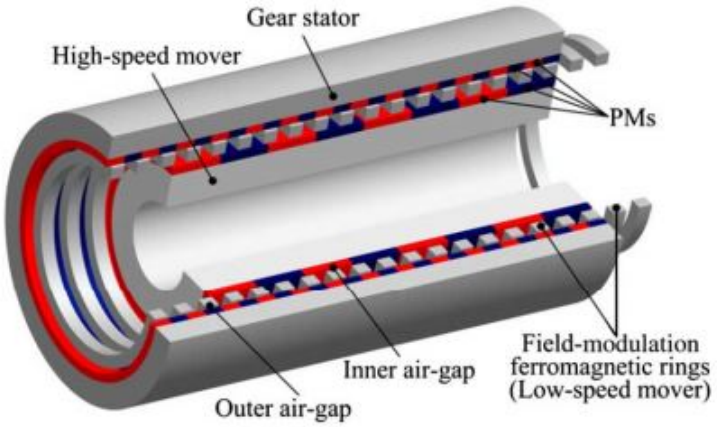

Figure 1.23: Linear magnetic gear topology [16]

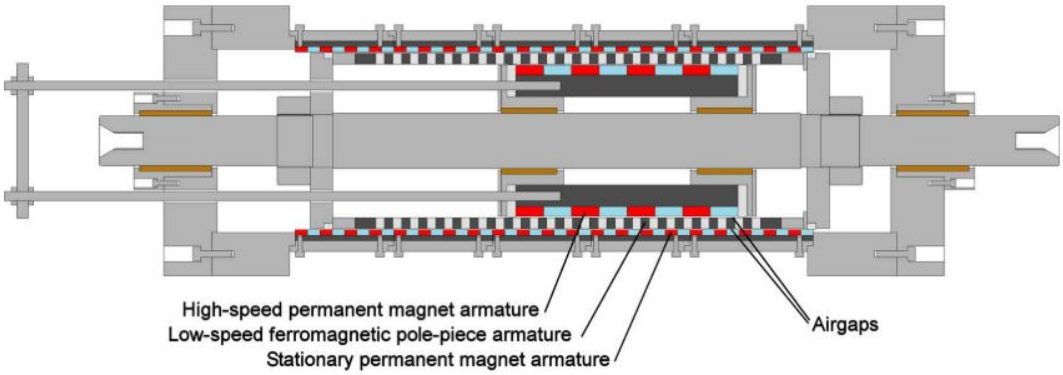

Figure 1.24: Linear magnetic gear prototype structure [17]

Trans-rotary Magnetic Gears

Trans-rotary MGs operate similarly to that of a mechanical lead screw in converting linear motion to rotary with the thread being replaced with magnetic material (Figure 1.25). This form of MG is potentially highly applicable to wave energy as the typically low speed linear motion of, say, a heaving buoy type WEC will not only have a speed increase but could also allow a more conventional rotary electrical machine to be applied.

Though the trans-rotary MG concept can probably be traced back to a 1945 patent [56] and a patent for a magnetic screw device was recorded in 1997 [70], it was with J. Wang et. al in 2011 [71] that the high force density capabilities of a magnetic lead screw (MLS) were analysed in detail. From this analysis it was determined that a thrust force density in excess of 10 MN/m^3 was possible in models with airgaps varying from 0.4

mm to 0.8 mm with a lead (λ) greater than 7 mm.

S. Pakdelian et al [72] further developed the concept by establishing the speed-torque relationship and the design and scaling of such a device, now dubbed the Trans-Rotary Magnetic Gear, or TROMAG. Here the gear ratio is established as the ratio of the rotor angular speed to the translator linear speed ω (rads^{-1}) and V (ms^{-1}) respectively (eqn (1.13)).

$$G_r = \omega/V = 2n\pi/V = 2\pi/PW \tag{1.13}$$

where P is the number of poles, W is the magnet width and n is the rotor speed in rpm.

By employing a low number of poles and narrow magnets it is then theoretically possible to convert a speed of 1 ms^{-1} on the linear translator to 1500 rpm on the rotor. With both the high torque and large gearing effects established, the technology's application to wave energy was further developed in [24] and [73].

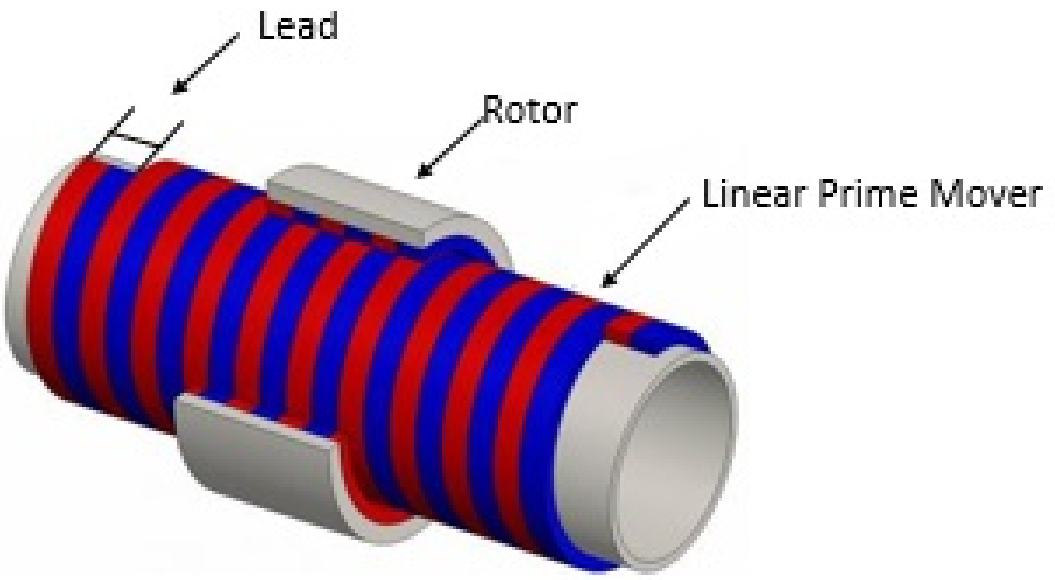

Figure 1.25: Magnetic lead screw

While the TROMAG has great potential in WECs, the requirement for a large amount of magnetic material on the linear translator makes the device expensive. In 2016 Bird et al. developed a new magnetically geared lead screw (MGLS) that combines the operating principles of a linear magnetic gear and a TROMAG [18] . The design consists of three main sections: an inner rotor of helically skewed, radially magnitised

pole pairs (p_i), an outer cylinder structure consisting of magnetic elements arranged with flux focusing steel segments and the translator made of ferromagnetic annular skewed pole pieces (n_i) (Figure 1.26). With the outer section held stationary a velocity relationship can be established such that:

$$\omega_i = v_t(n_i/(p_i k_i)) \tag{1.14}$$

where ω_i is the angular velocity of the inner rotor, v_t is the linear translator velocity and k_i is given by:

$$k_i = \lambda_i/(2\pi) \tag{1.15}$$

where λ_i is the inner rotor lead.

The proposed design was modeled and the analysis of this presented a force density capability of 18.7 kN/m^3. While the MGLS has a lower force density than either the LMG or the TROMAG, the force per magnet for the MGLS will not change as the stroke length increases and the increase in cost will be much less due to the use of ferromagnetic or iron material, as opposed to permanent magnetic material, for the prime mover.

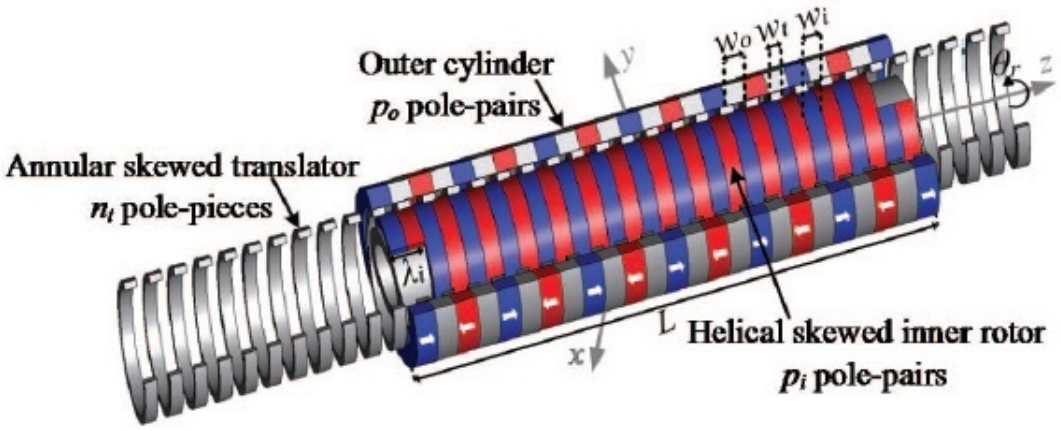

Figure 1.26: Magnetic gear lead screw [18]

1.2.4 Variable Transmission

Building on the core concepts, further work has been undertaken to increase the functionality and operating range of MGs with a key achievement being the development

of variable transmission designs. This is potentially an important development in applying the technology to marine energy as sea states can often vary wildly and being able to change the transmission ratios gives designers more scope regarding control such as maintaining a generator's optimum speed from a varying input torque. There are three leading methods of establishing variable transmission operation in MGs: controlled rotor, magnetic field control and variable pole number. Both the controlled rotor and magnetic field controlled designs are considered split power drives due to the requirement of power to be introduced to or extracted from the systems to vary the transmission speed with the torque ratios on each rotor conserved. The variable pole number design is a fully variable magnetic gear in terms of both torque and speed being affected.

Control Rotor

The first instance of a variable magnetic transmission was with Jian & Chau's 2010 publication [19]. Adapted from the mechanically geared Toyota Prius E-CVT system, in this design the FMP rotor is connected to an external drive and can be rotated at a controlled speed. With this control rotor it is possible to vary the ratio established by the modulated flux between the high and low torque rotors. Proposed for use in hybrid electric vehicles the full system layout is shown in Figures 1.27 & 1.28 with M/G indicating a Motor/Generator electrical machine.

Through the control rotor, the gear ratio is determined by:

$$\omega_1 + G_r\omega_2 = (1 + G_r)\omega_3 \tag{1.16}$$

with ω_1, ω_2 and ω_3 being the rotational speeds on the outer rotor, the inner rotor and the FMP rotor respectively. The gear ratio is calculated as with a standard CMG with fixed FMP rotor. This system was further explored in [74] where it was proposed for use in a wind turbine and a similar design is employed in Magnomatics' MAGSPLIT drive for hybrid vehicles [75].

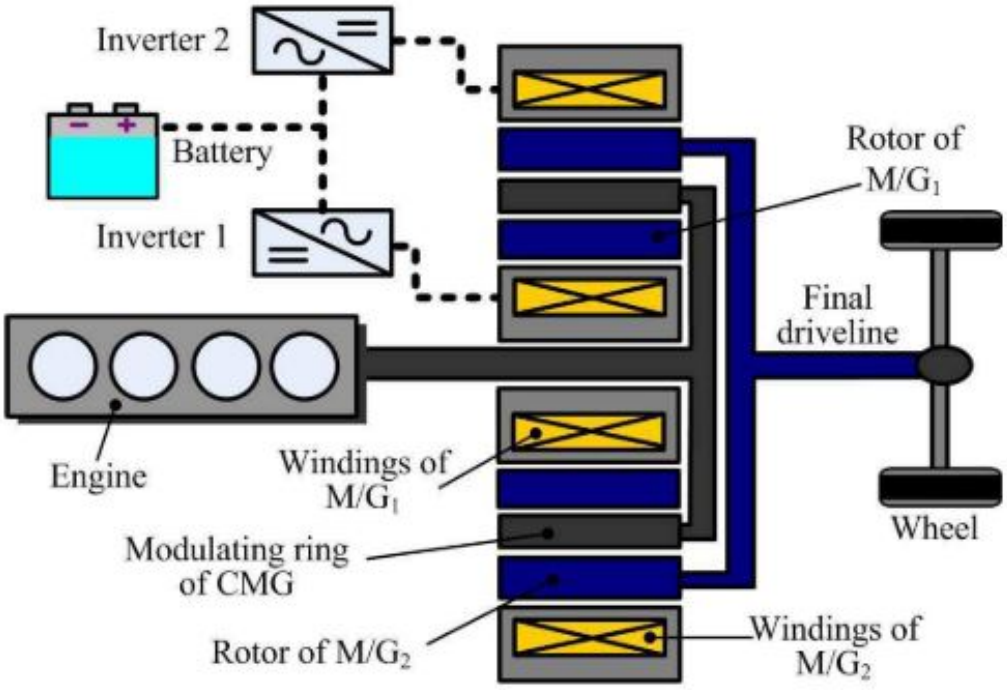

Figure 1.27: Layout of proposed variable MG with control rotor for hybrid vehicle [19]

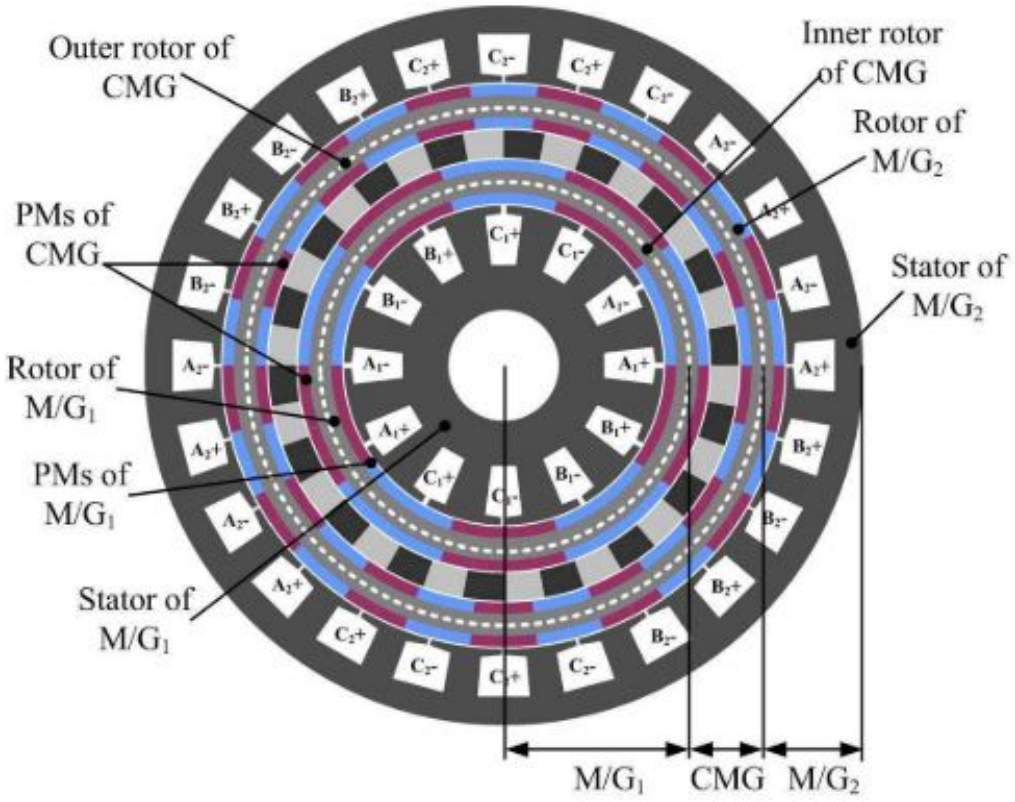

Figure 1.28: Combined MG and generator system with control rotor [19]

Magnetic Field Control

While the controlled rotor is effective it requires multiple rotating structures and a high amount of high cost permanent magnet material. Alternatively, Fu & Wang proposed removing the inner, high speed, magnetic pole rotor leaving just the stator [20] [76]. As shown in Figure 1.29 the topology is similar to that of a Vernier Hybrid Machine [77].

While Fu concluded that due to greatly reduced torque this design could not be recommended for low speed applications, the design was revised in 2013 by Padmanathan et al. for use in a wind turbine DFIG like application [21]. With a new high number slot winding stator and a flux focusing MG rotor, as shown in Figure 1.30, the design's potential was demonstrated, though it does suffer from high torque ripple caused by harmonics resulting from the fractional slot stator.

With this model the operation of the rotor speeds is established as follows:

$$w_h = \frac{n_1}{p_h}\omega_l - \frac{1}{p_h}\omega_s \tag{1.17}$$

where ω_s , ω_h, and ω_l is the stator electrical frequency, the angular velocity of the high speed rotor and the low speed rotor respectively. As in a standard MG n_l is the FMP number and p_h is the magnetic pole pair number on the high speed rotor.

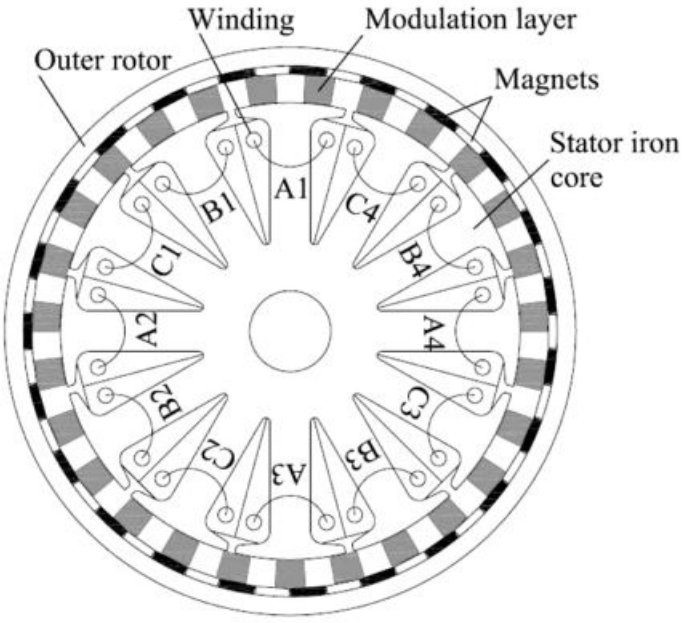

Figure 1.29: Magnetic field controlled variable MG schematic [20]

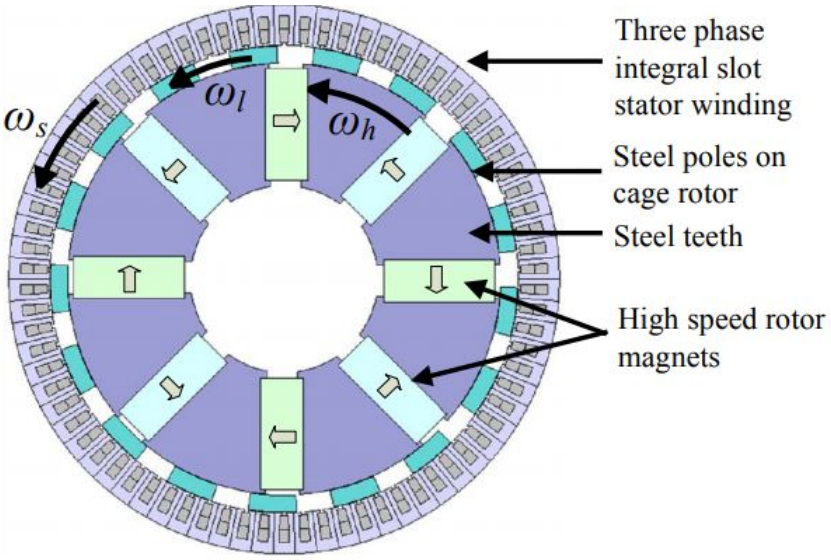

Figure 1.30: Revised magentic field controlled variable MG [21]

Variable Pole Number

The third type of variable MG establishes a variable ratio by utilising high-remanence low-coercivity permanent magnets, namely aluminum-nickel-cobalt (Alnico), shown in Figure 1.31 [22].

Due to the low coercivity, the poles can be magnetised or demagnitised by the windings as in memory machines [78] effectively changing the pole numbers. The resulting gear was analysed across 6 different gear ratios from 2.67 to 0.38. Despite this small range and the expected poor torque density due to the magnetic material, the design does have an additional advantage in using the lower cost Alnico magnetic material.

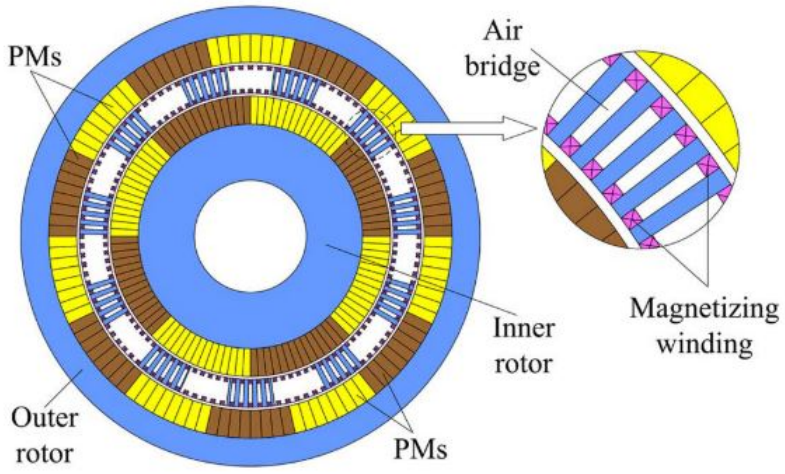

Figure 1.31: Variable pole number type variable MG [22]

1.2.5 Magnetic Gear Applications in Wave Energy Devices

Survivability is a key concern for WECs which are often subjected to extreme conditions. The inherent overload protection of MGs has great potential in marine energy where forces can vary dramatically depending on environmental conditions. In the event of excessive force being applied the rotors will slip without damage occurring to the gear components and will naturally realign when the force is lowered. This contrasts with mechanical gears which, in a similar event, could result in significant damage. Additionally, the lack of interlocking parts greatly reduces the system's requirements for lubrication. Lacking meshing parts, MGs cause reduced acoustics meaning the environmental impacts are lower than a mechanical alternative. Finally, as torque is transfered contactlessly, additional options are available with regards to system sealing with sections being hermetically separated. This can be of great benefit when considering machine marinisation [10].

With the evident advantages of MGs in marine applications there has been some work in investigating their use in WEC PTO's and some of the leading concepts are presented in the following section.

Heaving Buoy Wave Energy Converter (with linear generator)

While point absorber, heaving buoy WECs work by a simple concept of using a buoyant structure that oscillates with incoming waves, the PTO of these devices can be quite complicated due to the linear nature of the device's primary motion. There have been some proposed models that use a linear generator [79] but due to the low frequency a large number of poles are required and there is poor utilistation of magnetic material.

One of the earliest works to look at a combined MG-WEC was to address this low frequency challenge. In 2010 Du et al. proposed an integrated system as shown in Figure 1.32 [23].

This concept was further developed in 2011 by Li et al. [16]. This design saw the use of a LMG cascaded with a linear PM generator, most likely to reduce the structural complexity of the proposed design in the previous study [23]. This allowed the high speed mover of the gear and the translator of the generator to share the same shaft. With the proposed design the low speed mover of the LMG is coupled with the heaving buoy structure as shown Figure 1.33. As the buoy rises and falls

with wave propagation the high speed mover connected to the linear generator's speed is amplified by a factor of the gear ratio. A similar rated machine without the MG system was calculated to have a volume 4 times that of the proposed system and with greater volumes of PMs, iron cores and copper windings (167% 214% and 271% respectively) would have a considerably higher cost. Additionally, the gearless machine was calculated to have higher copper losses. Therefore, while reportedly reducing cost and volume, the proposed machine has a greater efficiency and power density. The study does not clearly indicate whether the reduced material volumes are solely for the linear machine or the combined system but it is highly likely it is omitting the extra material required for the linear gear. Furthermore it should be noted that linear systems have additional issues when compared to rotary systems. Key among these are that not all material is active during power generation and a much larger machine is required for a similarly rated rotary system, increasing both weight, volume and cost. Maintaining an airgap over the full length of a linear system, particularly in high power applications where stroke lengths can be in excess of 3 m, is structurally challenging requiring substantial support material. Unlike rotary machines end-stops will be required such that the prime mover in a linear system does not exceed the operational length and potentially damaging the structure. These endstops will have to be designed to withstand a considerable amount of force and if incorrectly positioned could result in reduced operational ranges and system damage from repeated impacts. Further issues are discussed in Chapter 6.

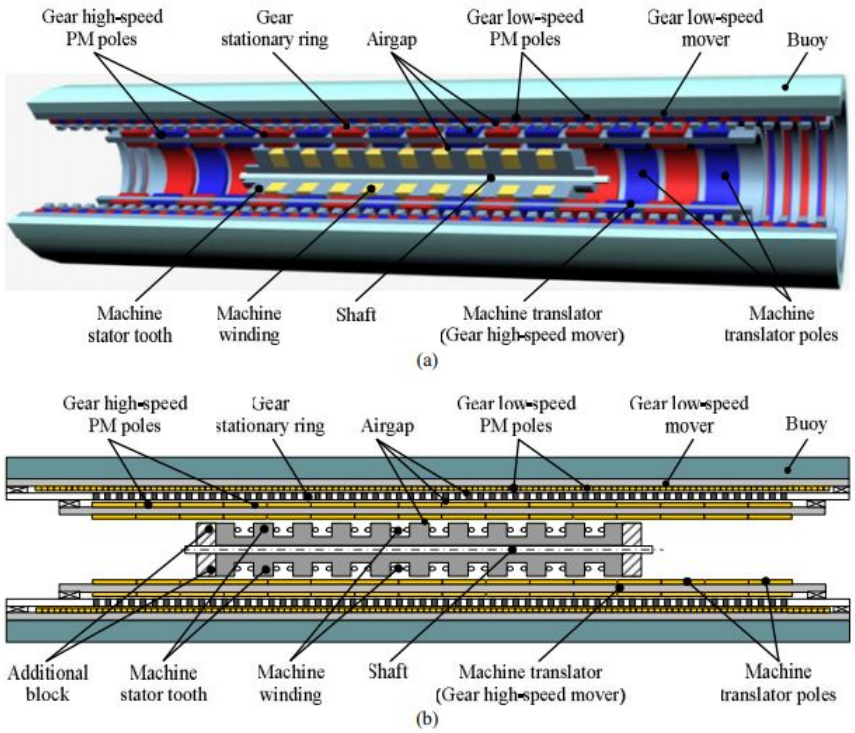

Figure 1.32: Proposed linear magnetic-geared PM machine configuration. a) 3-D model, b) Schematic [23]

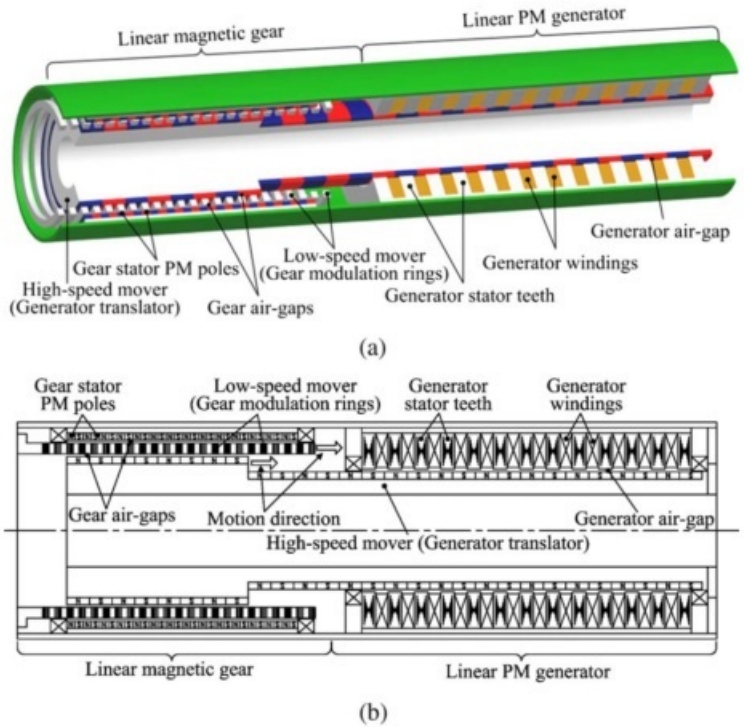

Figure 1.33: Proposed heaving buoy MG system option (a) Solid model. (b) Schematic [16]

Heaving Buoy Wave Energy Converter with Magnetic Lead Screw

Interestingly, in 2005 Polinder et al. noted that in wave energy a major challenge was building a robust, maintenance-free gear for converting the linear to rotary motion for electrical generation, and there has been a preferred focus on the development of direct drive linear machines [80]. Transrotary MGs now have the potential of addressing this issue and have been investigated to some extent as they would allow for more industry standard equipment to be used along with potentially more compact PTOs.

Pakdelian et al. proposed such a system with the electrical machine with integrated trans-rotary magnetic gear (MITROMAG) for use in WECs in 2012 [81]. This concept was further developed for specific wave energy conversion applications in [82] and was investigated for use with a specific WEC, namely the Wavestar 500kW, reported by Holm et al.'s work in 2013 [24].

The Wavestar concept operated as a point absorber with multiple floats being attached to a stationary platform [83]. The aim of the work was to design a PTO incorporating the MLS technology which would have a requirement of 500 kN force with a 2m stroke that could replace the hydraulic PTO [84]. The proposed system can be shown in Figure 1.34. After calculating the required dynamics a scale model was built for 17 kNm which resulted in an efficiency in the range of 80% with this value expected to increase given that the test rig was only capable of 25% of the anticipated maximum speed.

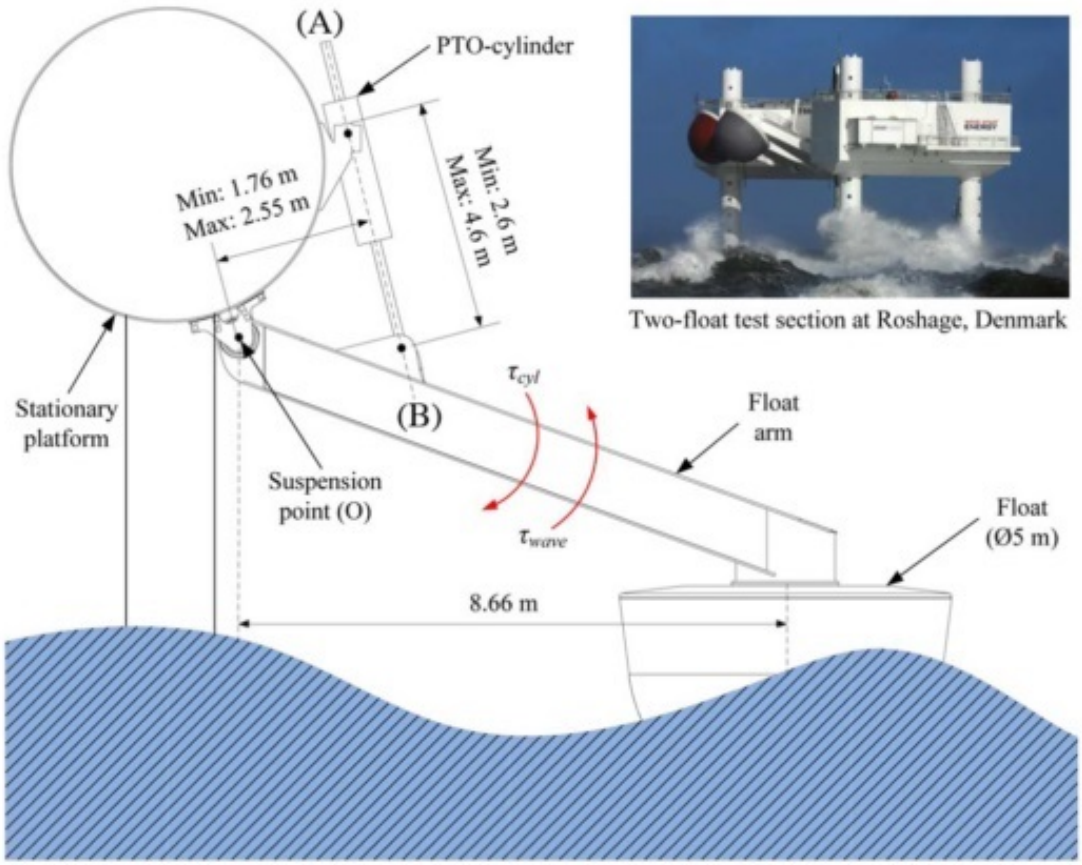

Figure 1.34: Wavestar 500 schematic [24]

Oscillating Wave Surge Converter

The use of a MG with ferrite PMs in an OWSC was first proposed in 2012 by Uppalapati et al. [85] as an alternative to the mechanically geared system previously proposed [86].

A similar concept was fully realised in 2017 by Johnson et al. with very positive results [87]. A full technical report presents the results of the full study which was partnered with ABB and Resolute Marine and funded by the US Department of Energy [25]. The work produced one of the largest combined MG - Generator systems ever developed with a peak torque of 3870 Nm. While not implemented within a WEC the proposed application is shown in Figure 1.35 with the combined MG system topology shown in Figure 1.36.

An axial version of the combined model was also developed (Figure 1.37) and resulted in the highest theoretical power and torque density though it was noted that implementing the design saw increased manufacturing difficulty and expense due to the size increase. For this reason the radial design was used for the full scale (3870 Nm) system.

The report concluded that there was the potential of a 3x reduction in weight and 6x reduction in mass when compared to the closest commercial, off the shelf direct drive permanent magnet machine. Though difficult to verify without extensive testing a 50% reduction in downtime was also expected. Even assuming similar downtimes, there was an expected 18% reduction in LCOE when compared to a hydraulic PTO alternative resulting from increased efficiency. It was further reported that this could be increased to 35% if the thermal limits of the inherently over-loadable electrical generator and system are used to increase the peak power output compared to an equivalent cost hydraulic system.

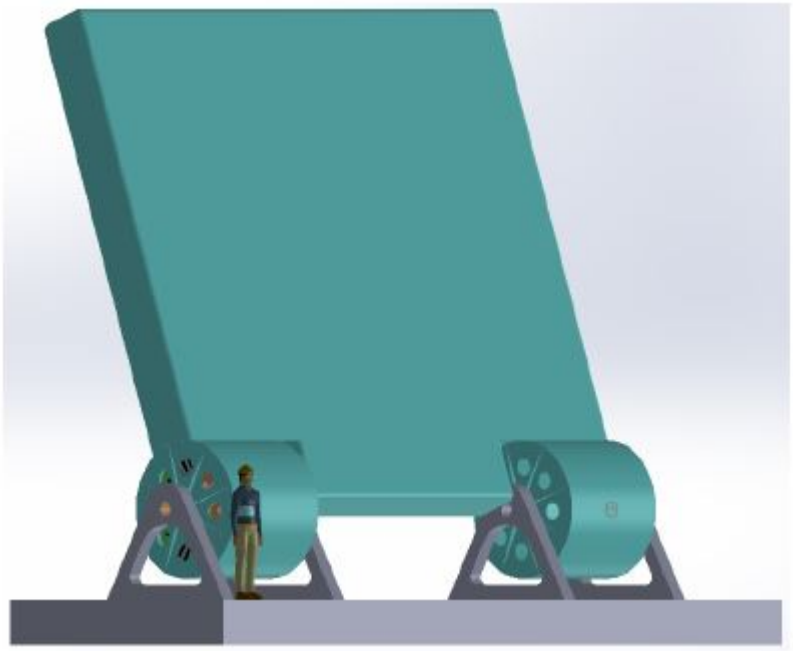

Figure 1.35: Proposed OWSC with MG PTO conceptual design [25]

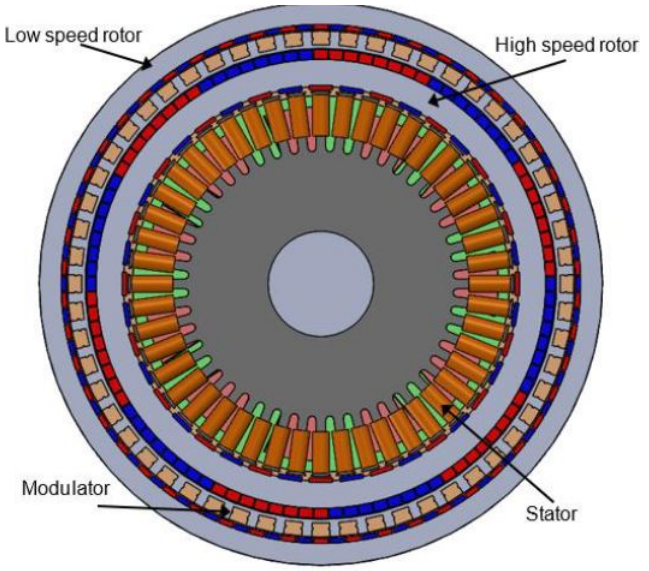

Figure 1.36: ABB designed combined radial MG-Generator system [25]

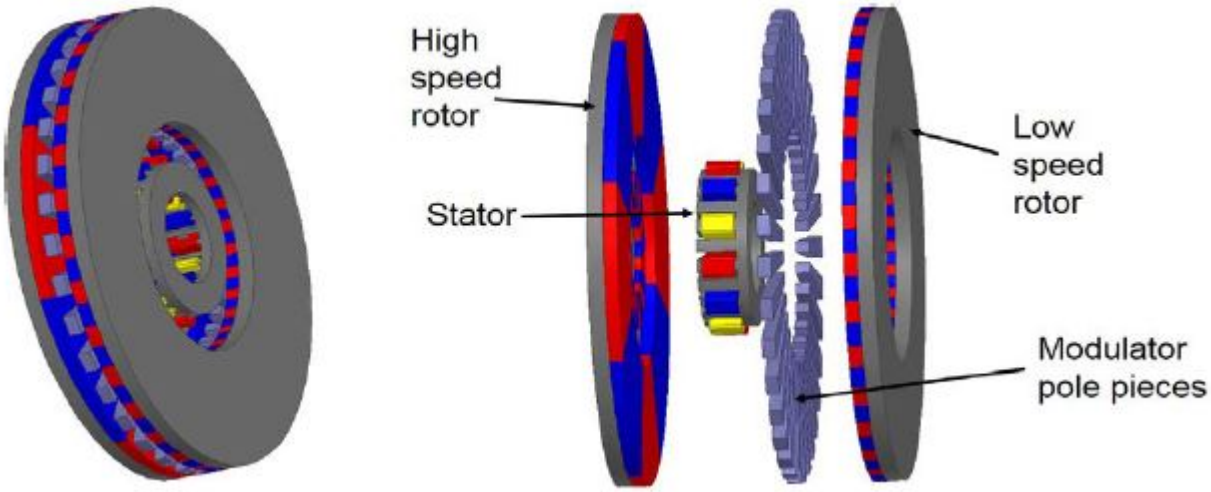

Figure 1.37: ABB designed combined axial MG-Generator system [25]

1.3 Summary and Thesis Outline

With the increasing importance of renewables and the enormous potential of magnetically geared systems, an in-depth study of design procedures and specific applications, in this case wave energy, can both advance the technology and address key challenges in the developing marine energy industry. This work was undertaken with these objectives and is outlined in the following section.

1.3.1 Thesis Outline

The work in each chapter of this thesis is as follows:

Chapter 2 - Magnetic Gear Design: This chapter discusses some of the key considerations in designing a magnetic gear.

Chapter 3 - Dynamic Analysis of a Magnetic Gear in an OWSC: Chapter 3 presents the findings of a dynamic model analysis of a magnetic gear in an OWSC PTO.

Chapter 4 - Prototype Development and Testing: Chapter 4 discusses the production of a prototype MG system and the test setup procedure. The results of the prototype testing are presented and discussed.

Chapter 5 - Genetic Algorithm Design Method: Following the design considerations outlined in Chapter 2, a method for optimal MG design is proposed and discussed.

Chapter 6 - Design and Analysis of a Linear Magnetic Gear for Wave Energy Conversion: As discussed, a magnetically geared linear generator system has been proposed for use with a heaving type WEC. Chapter 6 further explores the practicality of this system and discusses it's benefits and challenges.

Chapter 7 - Summary & Conclusion: Chapter 7 summarises the major findings from the work in the context of contribution to the existing body of knowledge and discusses planned further work and suggested improvements.

Chapter 2

Magnetic Gear Design

With MGs now reaching a high technology readiness level it is important to develop design techniques and tools for efficient gear design that will encourage industry adoption and the technology's proliferation. Beyond the relatively simple structure and basic operation theory, the design of a MG is a non-trivial process with multiple interconnected parameters. While some of these parameters have been examined individually [10, 88, 89], it was with D. Evans & Z. Q. Zhu's [90] paper that the coupling effects between parameters were established. A primary objective of this work was to further investigate these design elements and establish some standard considerations that should be taken into account when designing MGs, particularity for high torque, low speed applications.

This chapter discuses these considerations as a critical analysis of best practices in MG system design.

Two design tools were developed through this work for MG design, analysis and optimisation. The tools, built on the MATLAB, FEMM and MagNet software packages are discussed in the following in relation to their applications and limitations.

xfemm

xfemm is a software package developed by Dr. Richard Crozier for electrical machine modeling and design. The package provides cross-platform streamlined MATLAB API for accessing the core finite element codes of the open-source FEMM software [91]. Due to the high level functionality and matrix management within MATLAB, a large number of models can be created, solved and analysed rapidly with automatic optimisation procedures. xfemm is limited to 2D analysis and therefore cannot account for

3D effects which can strongly affect the resulting gear system. Due to its speed of use, it was primarily used for the initial design and optimisation process before being passed for 3D modelling and analysis.

Being limited to 2D solutions, inherently 3D topologies such as axially and trans-rotary orientated systems are at this point beyond the scope of this software. However using a sweep function it is possible to model linear type FMMGs.

While the software is limited to static analysis, the xfemm toolbox is capable of rapid analysis of key MG characteristics such as obtaining the torque and magnetic field values.

When modelled, the design can be opened in FEMM for visualization with examples shown in Figures 2.1 and 2.2.

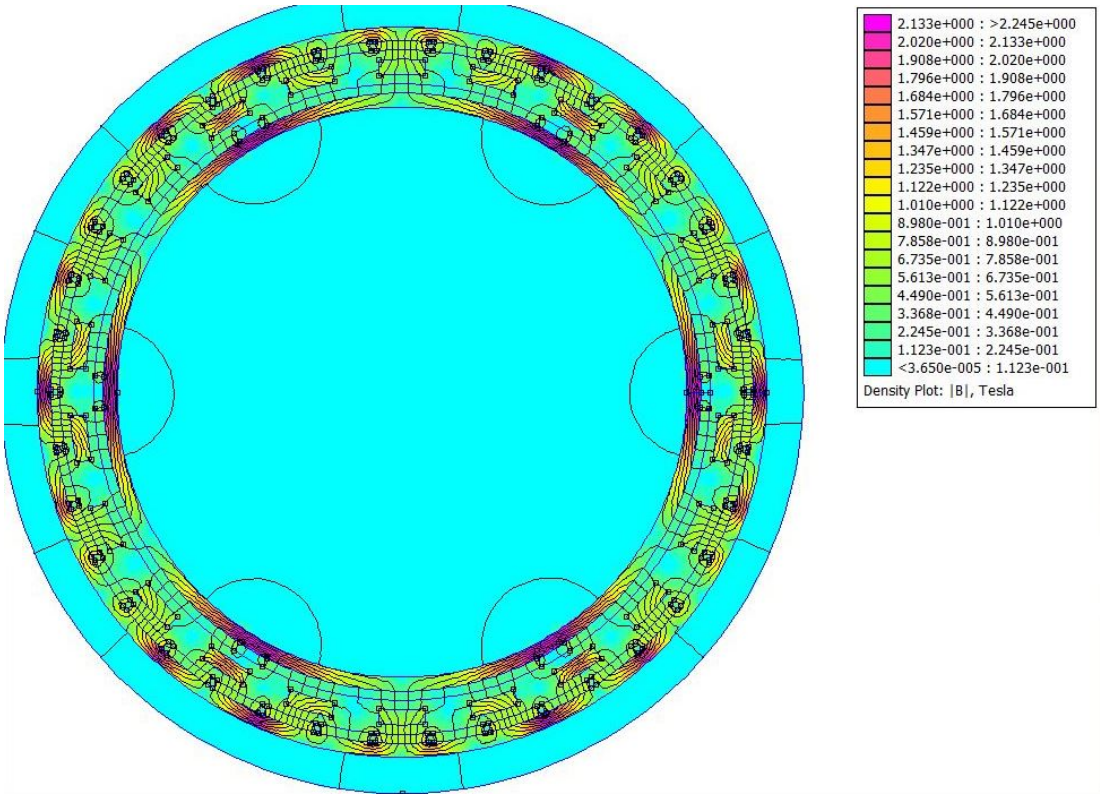

Figure 2.1: xfemm rotary CMG example

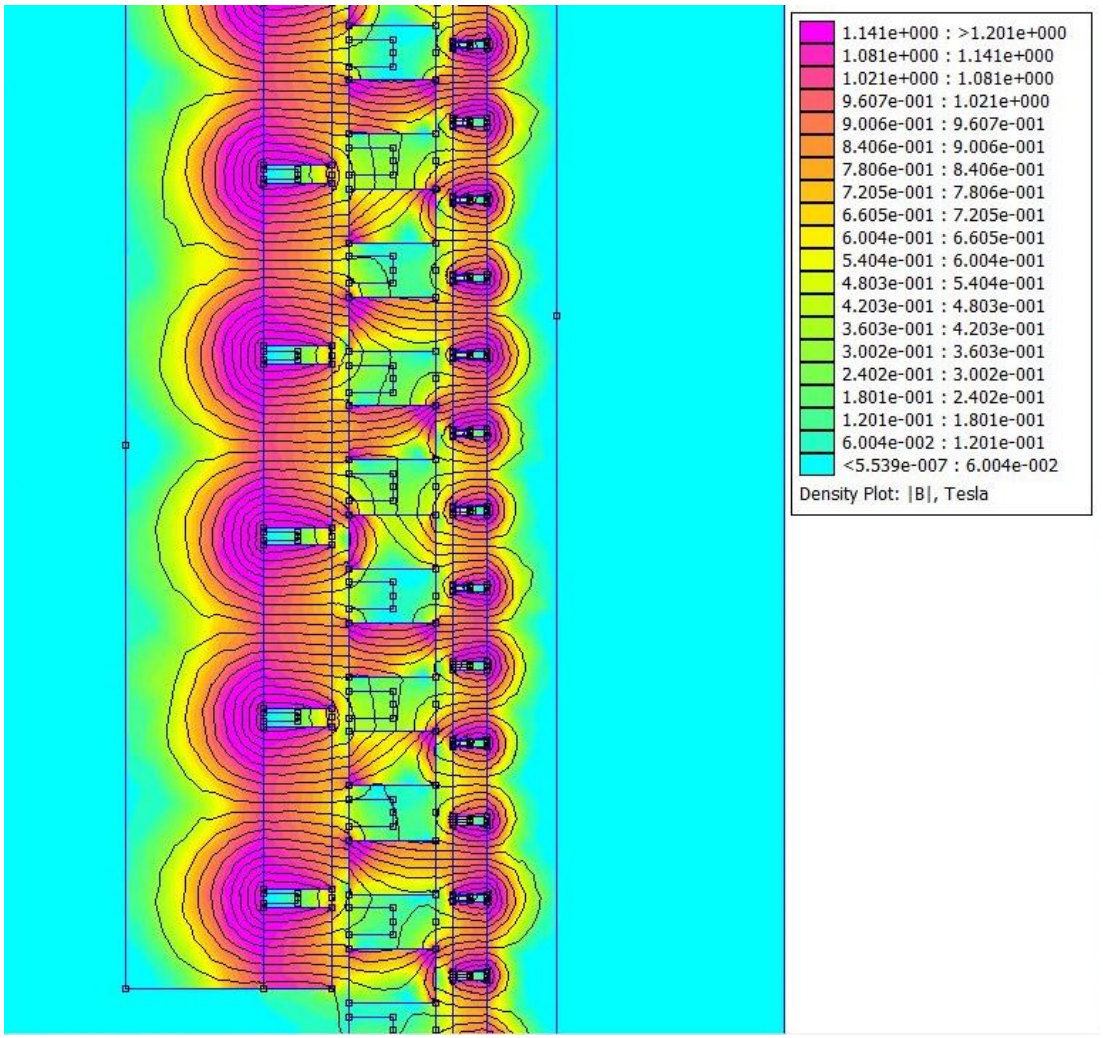

Figure 2.2: xfemm linear MG example

MagNet

The 3D magnetics modeling software MagNet from developers Infolytica [92], now owned by Siemens, is a powerful tool that allows for full 3D finite element analysis of magnetics problems with static, time harmonic and transient solutions. MagNet models can be scripted in the visual basic language which allows for quick model design alterations. The MagNet tool was generally used for full 3D modeling following initial design in xfemm or for purely 3D systems such as axial orientated topologies. Solve times are largely related to model size for a given mesh number. This can become extensive with 3D models given that the maximum element mesh size must remain small in the airgap between rotors for reliable accuracy. With this tool concentric, linear and axial models can be designed and solved with a high degree of accuracy. The tool was expanded for pole arrangement analysis to allow for non standard pole

arrangement such as flux focusing and Halbach arrays. The developed user interface also allows images of the gear to be graphically shown. An example of the interface with a modeled axial MG with Halbach array is shown in Figure 2.3 showing the magnetic flux distribution.

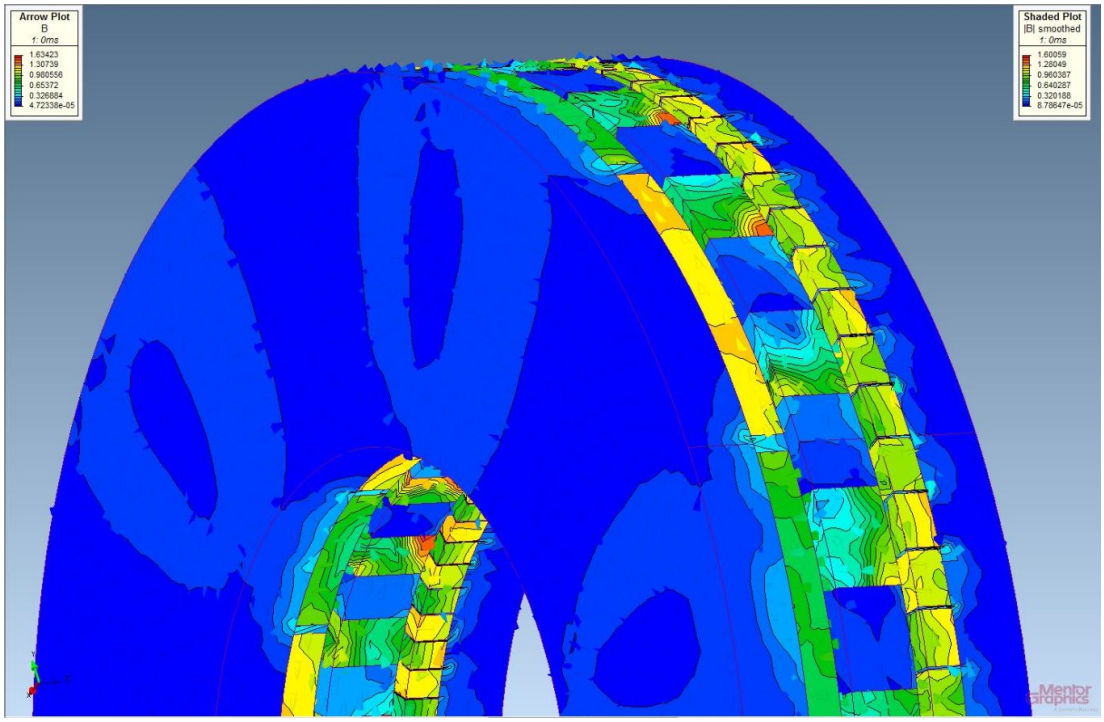

Figure 2.3: Modelled axial MG with Halbach Array - MagNet

2.1 Design Considerations

The key design objectives of a MG are the peak torque, gear ratio and efficiency. The following sections discuss these gear characteristics and some considerations for designing a gear for a specific application.

2.1.1 Peak Torque

As discussed, MGs have the ability to slip when excessive torque is applied between rotors. While this has the potential to be used as an inherent overload protection mechanism, the gear must also be suitably rated to cope with the operating torque. As discussed in [93], the torque, T, is directly proportional to the magnetic flux B between rotors as determined by:

$$T(r) = \frac{l_a r^2}{\mu_0} \int_0^{2\pi} B_{rad}(r,\theta) B_\theta(r,\theta) d\theta \tag{2.1}$$

where l_a is the gear's axial length and r is the gear's airgap radius.

The maximum torque of a gear is then proportional to its physical dimensions while the shear stress σ remains constant for a constant B:

$$\sigma = \frac{T(r)}{\pi r^2 l_a} \tag{2.2}$$

Therefore the magnetic strength and volume of the magnetic material are the primary determinants of peak torque. For fixed sized magnetic poles the airgap radius and axial length of the gear will be the scaling parameters.

In a standard radial CMG the gear will be at rest, or balanced, when the spaces between rotors are aligned. The angle of rotation from this zero torque point to the peak torque position (θ_{0-p}) occurs when there is maximum relative displacement between poles and is dependent on the pole pair number, pp, of the rotor being rotated. The zero and peak torque positions are shown in Figure 2.4.

$$\theta_{0-p} = 90/pp \tag{2.3}$$

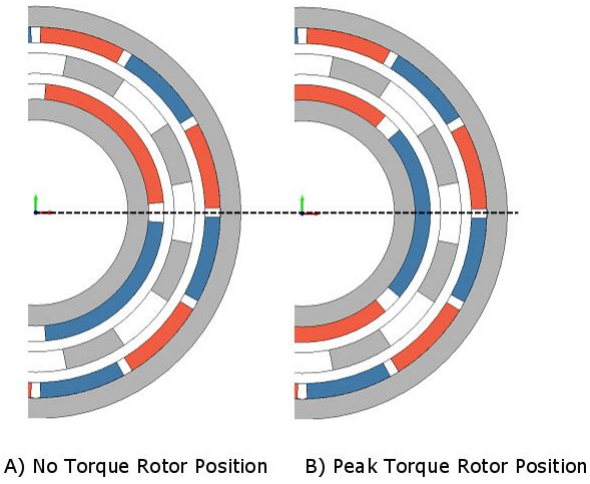

Figure 2.4: No Torque and Max Torque positions

After assessing the peak torque it is then useful to obtain the torque curve. This is achieved by fixing two of the rotors and rotating the final rotor through a full pole cycle. The torque curves for a MG with inner to outer pole pair ratio of 3:19 are shown in Figures 2.5 and 2.6 where the outer and FMP rotors have been held stationary and the inner rotor is rotated through a full torque cycle (120 degrees) in 120 steps with a transient 2D motion solution being obtained at each point.

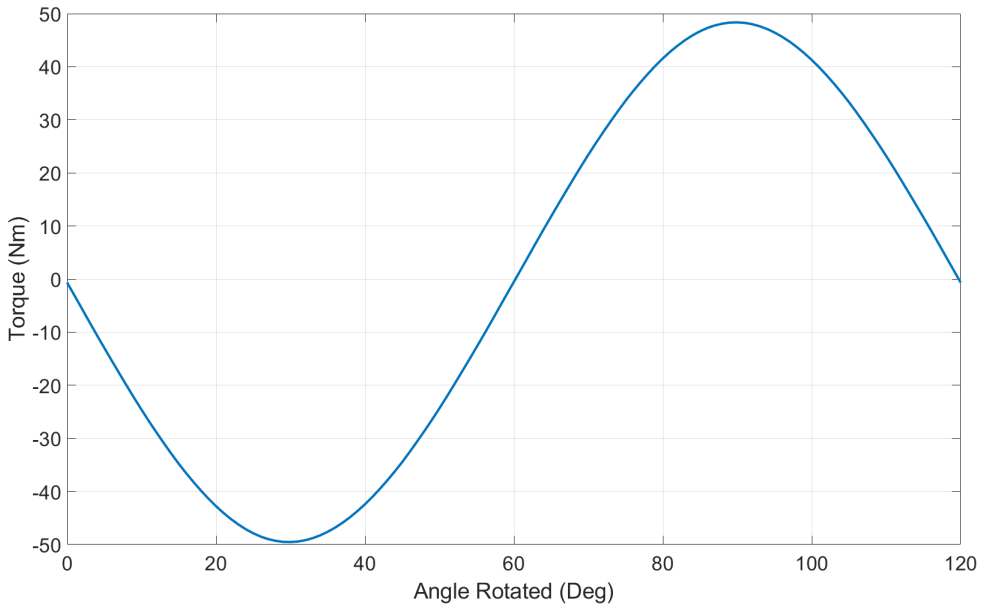

Figure 2.5: Torque curve on outer rotor (2D Solver)

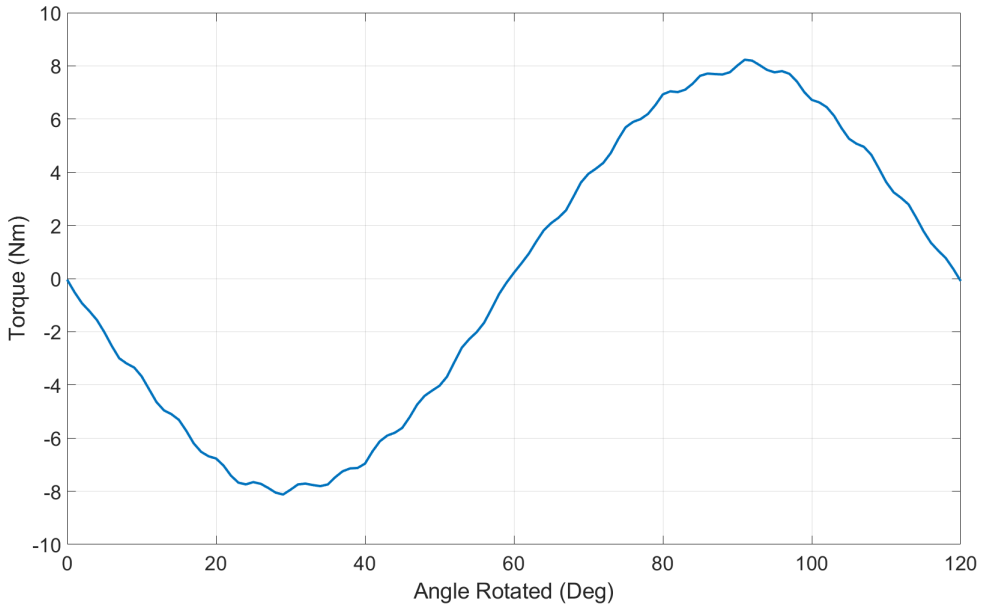

Figure 2.6: Torque curve on inner rotor (2D Solver)

With each step (in this case 1 degree) the torque acting on each rotor will increase. The sign (+/-) indicates in which direction the torque will act about the z axis. In practice the same process will occur in a gear with the outer rotor allowed to rotate. There will be an amount of relative motion until there is sufficient torque to overcome the inertia and friction forces whereby the outer rotor will then proceed to rotate until

the balanced position is once again reached.

These torque curves also clearly demonstrate the torque gearing effect. With a pole pair set up of 3:19 the established ratio will be ≈ 6.3:1. From the analysis the peak torques on the outer and innerer rotor are 49.5 Nm and 8.2 Nm respectively.

2D vs 3D analysis

As mentioned, end effects, such as leakage flux between magnetic poles on each rotor, can have substantial effects on a gear's performance. Therefore for accurate torque capability assessment a full 3D analysis is recommended. To demonstrate this, the previous example is analysed with the same parameters and test points but with MagNet's 3D solver. The resulting torque curves are shown in Figures 2.7 and 2.8. From these results the peak torques on the inner rotor and outer rotors are 5.3 Nm and 32.3 Nm respectively resulting in differences of approximately 35%. It must also be taken into consideration that the sum of these torques will be experienced by the FMP rotor as shown in Figure 2.9. This is an important design consideration as the iron poles lack the backiron structure of the inner and outer rotor and are therefore more delicate. The torque ripple element has also reduced slightly. The cogging torque resulting from alignment of the magnetic pole edges will be less of a component in the transmitted torque when the full 3D end effects are accounted for. The end effects create additional flux paths which will affect how the magnet poles interact when in motion.

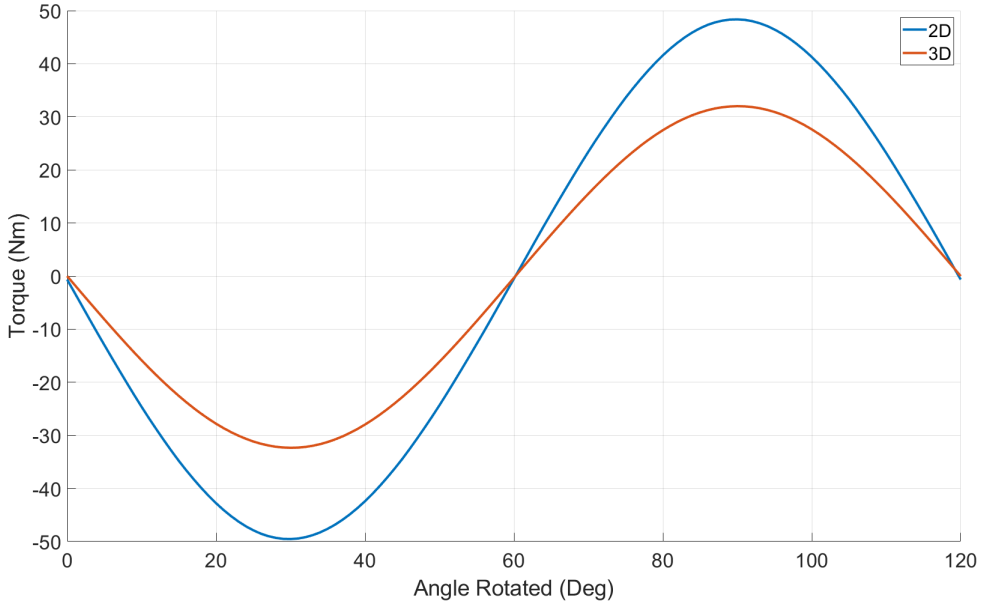

Figure 2.7: Torque curve on inner rotor (3D Solver)

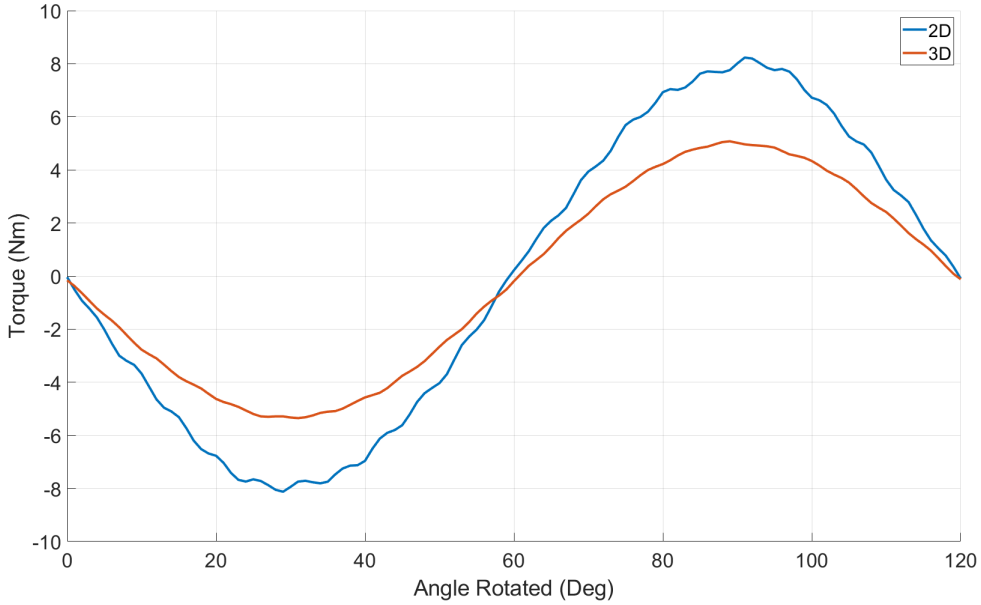

Figure 2.8: Torque curve on outer rotor (3D Solver)

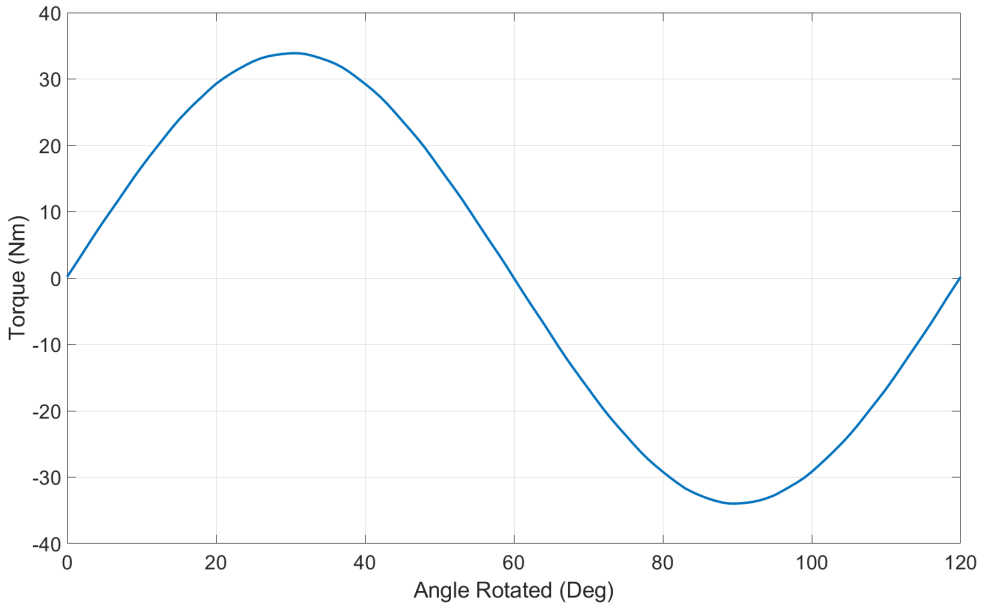

Figure 2.9: Torque curve on FMP rotor (3D Solver)

2.1.2 Gear Ratio & Pole Number

Previous studies into the relationship between gear ratio and gear performance have noted that higher ratios strongly affect the transmittable torque between rotors [89].

To further demonstrate this relationship a series of tests were run in xfemm for gears with the same parameters but with increasing pole pair ratios of 7:3, 10:3, 19:3,

31:3, 41:3, and 52:3 (corresponding to ratios 2.33:1, 3.33:1, 6.33:1 10.33:1 13.67:1 and 17.33:1).The increasing ratio is plotted in Figure 2.10 and the results are shown in Figures 2.11 & 2.12. From this it can be ascertained that while high gear ratios are possible, there reaches a point of diminishing practical returns. This effect is further clarified by plotting the peak torques against increasing outer rotor pole pair number as shown in Figures 2.13 & 2.14.

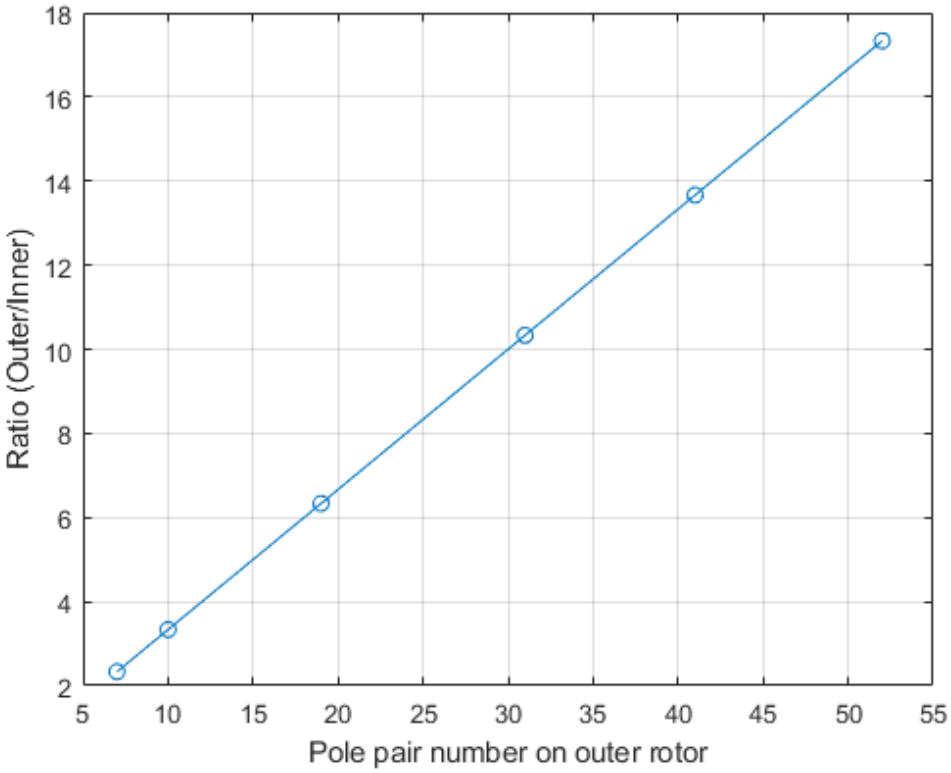

Figure 2.10: Torque ratio with increasing outer rotor pole pair number

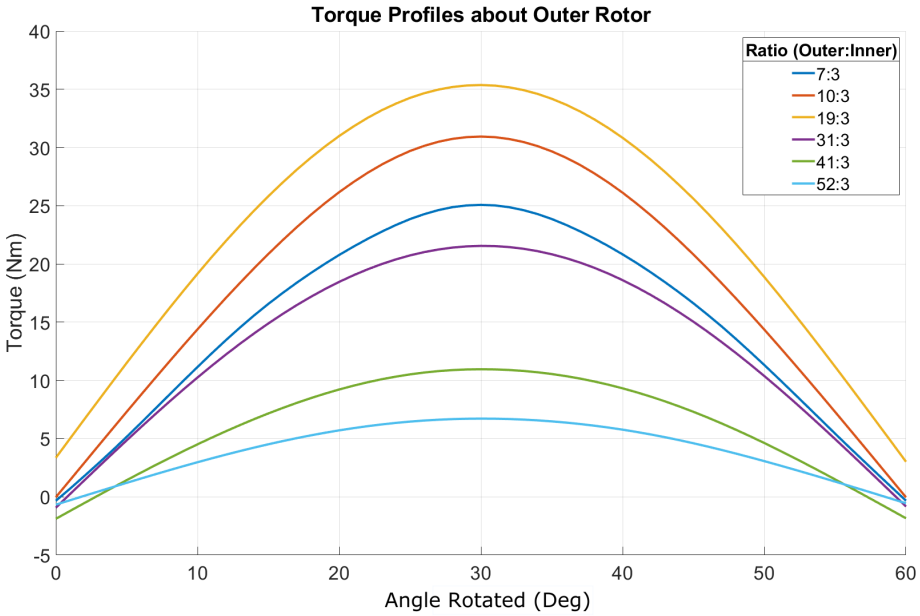

Figure 2.11: Torque on outer rotor with increasing ratios

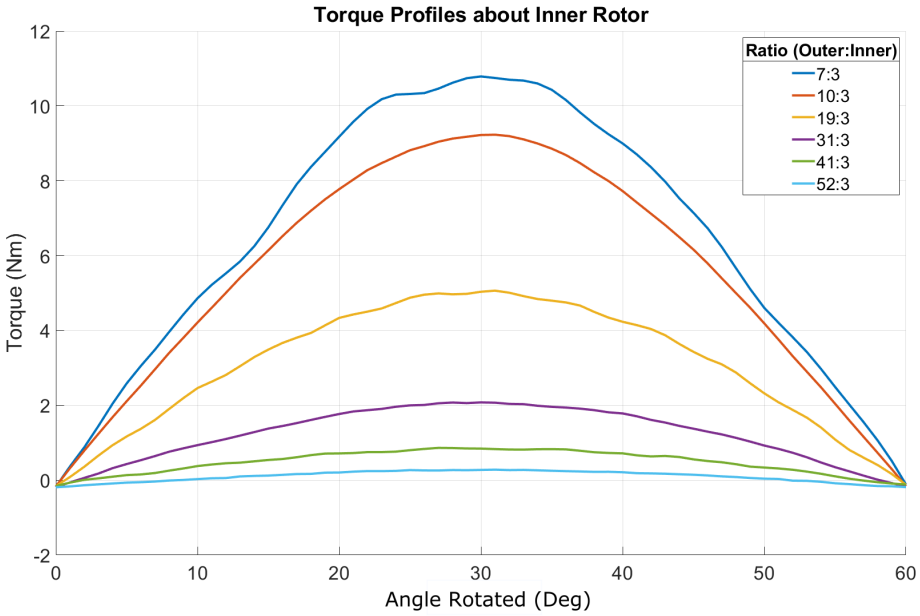

Figure 2.12: Torque on inner rotor with increasing ratios

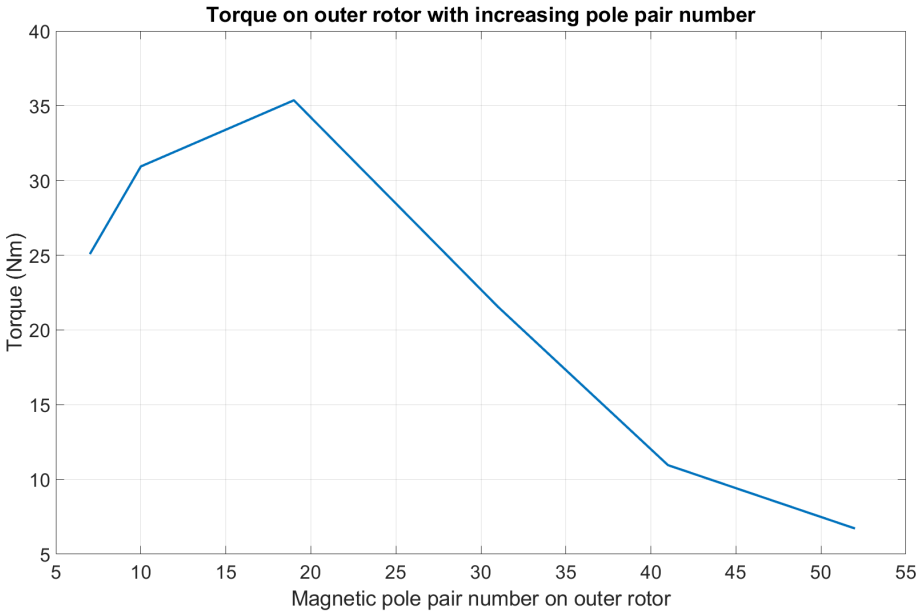

Figure 2.13: Peak torque on outer rotor with increasing outer rotor pole pair number

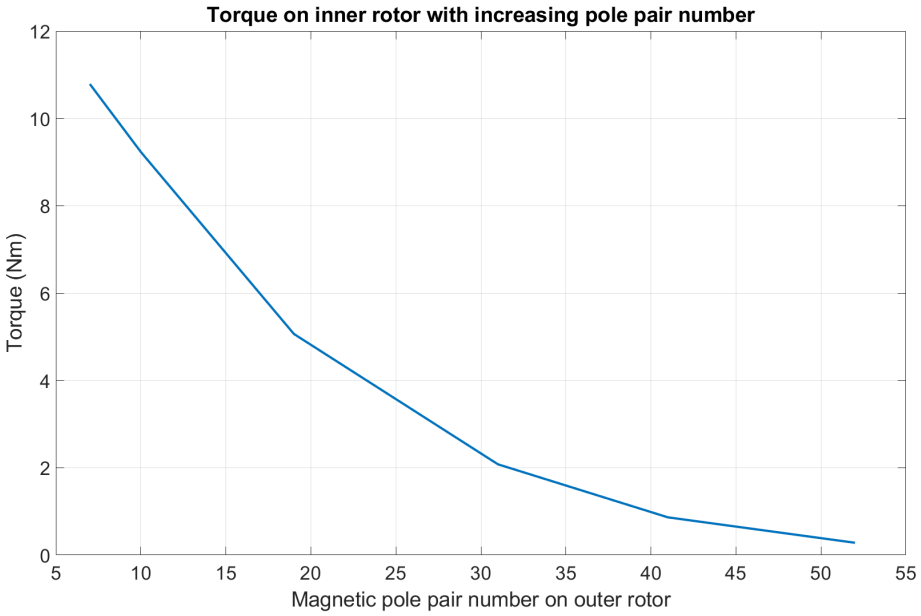

Figure 2.14: Peak torque on inner rotor with increasing outer rotor pole pair number

Torque Ripple

An important factor when selecting pole numbers is torque ripple or cogging torque. Torque ripple, as investigated in [94], results from the magnetic flux harmonics that arise from the modulation occurring between magnetic pole rotors and is highly dependent on the pole numbers selected.

Adapted from permanent magnet machine analysis [95], the cogging factor is generally used as an indication of torque ripple severity. The cogging factor, f_c, is calculated as follows:

$$f_c = \frac{2pn_s}{LCM(2p, n_s)} \tag{2.4}$$

where p is the pole number of either inner or outer rotors, n_s is the modulating pole number and LCM, the least common multiple. In general, a higher f_c will be associated with a higher torque ripple and, for low torque ripple, pole pair arrangements with higher least common multiples should be chosen.

To demonstrate this the following tests were done with ratios 1:6, 2:13, 3:19, 4:25 and corresponding LCMs: 6, 26, 57 and 100. The tests begin by rotating the inner rotor from the zero torque point to the peak torque with the outer rotor then rotated at the rotation determined by the ratio. The results of these tests are shown in Figures 2.15 - 2.22. The graphs clearly show that the high speed rotor experiences significantly higher torque ripple and that while the ratio in each test is similar there is substantial difference in torque ripple magnitude, in particular when considering a whole number ratio. Such a torque ripple would make the gear practically inoperable. With the increase in LCM, this torque ripple is reduced to between 5-10%. This corresponds with previous studies which noted that whole and half number pole pairs can have substantial torque ripple with whole ratio numbers in the <100% range [89].

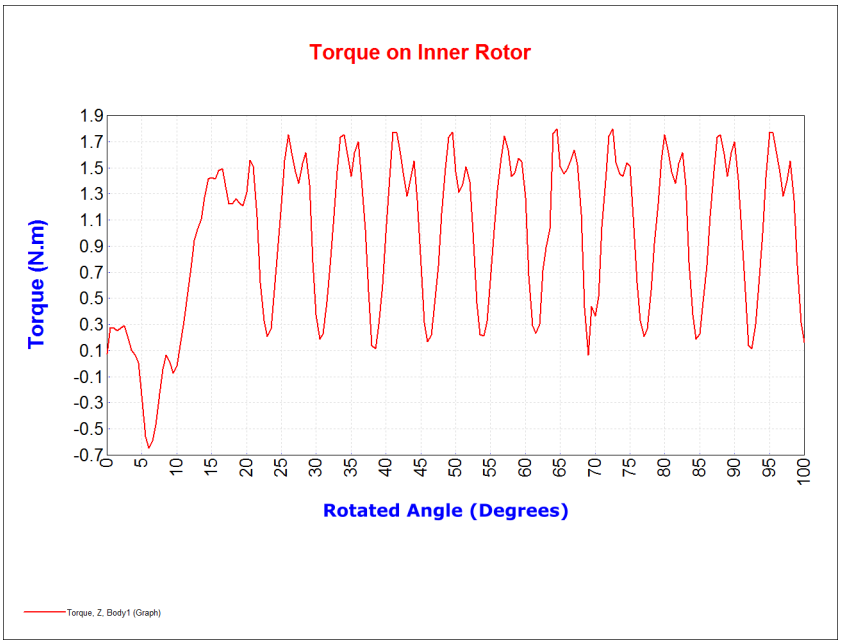

Figure 2.15: Torque on Inner Rotor for PP ratio 1:6

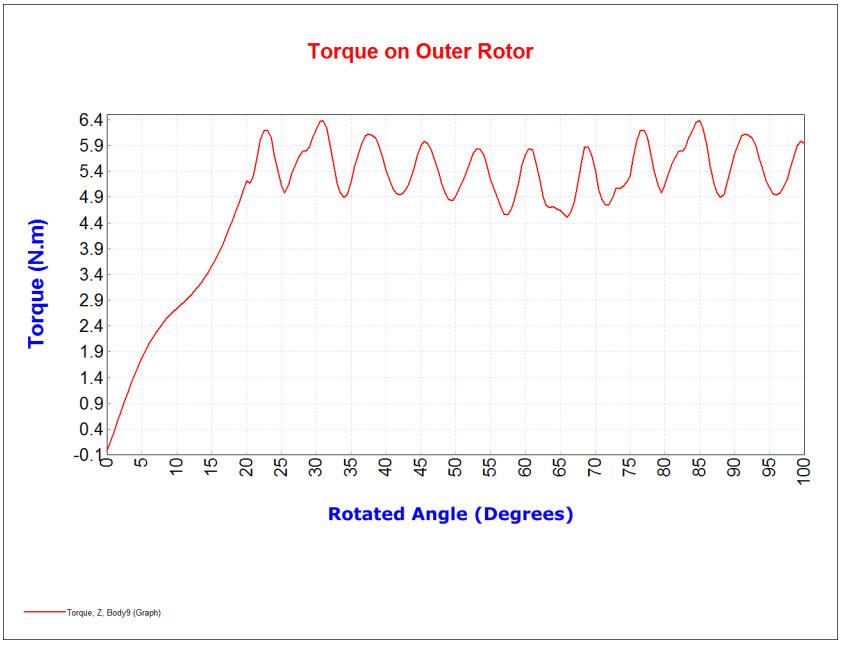

Figure 2.16: Torque on Outer Rotor for PP ratio 1:6

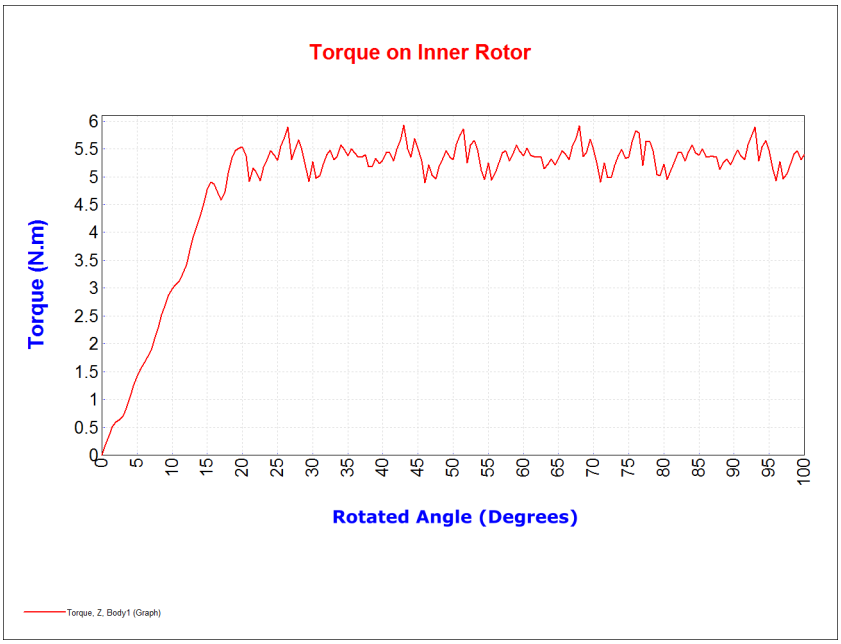

Figure 2.17: Torque on Inner Rotor for PP ratio 2:13

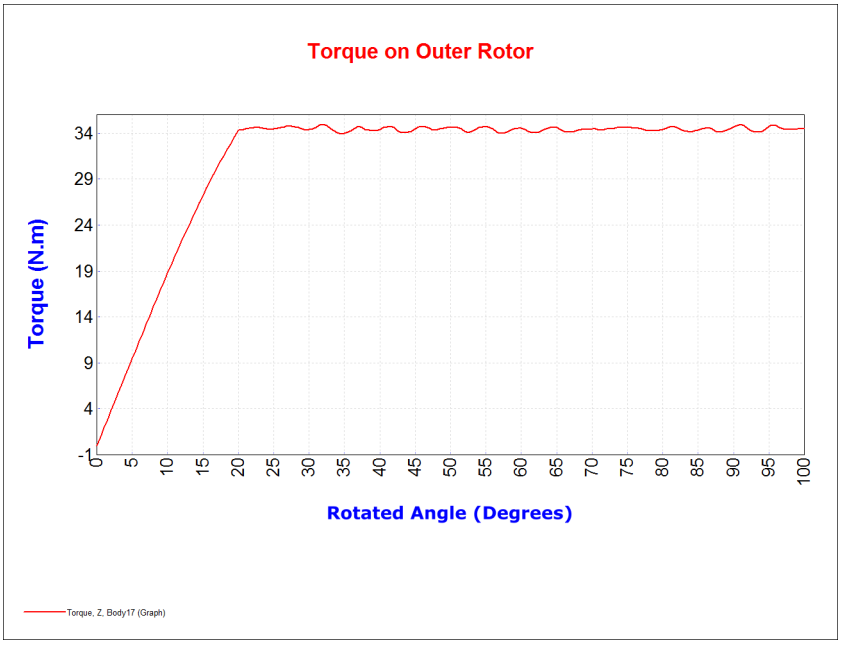

Figure 2.18: Torque on Outer Rotor for PP ratio 2:13

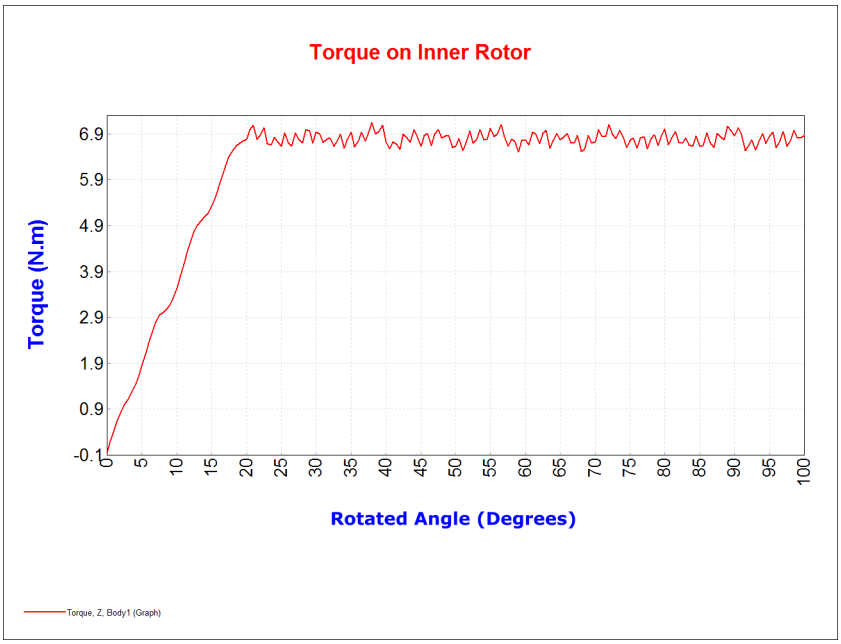

Figure 2.19: Torque on Inner Rotor for PP ratio 3:19

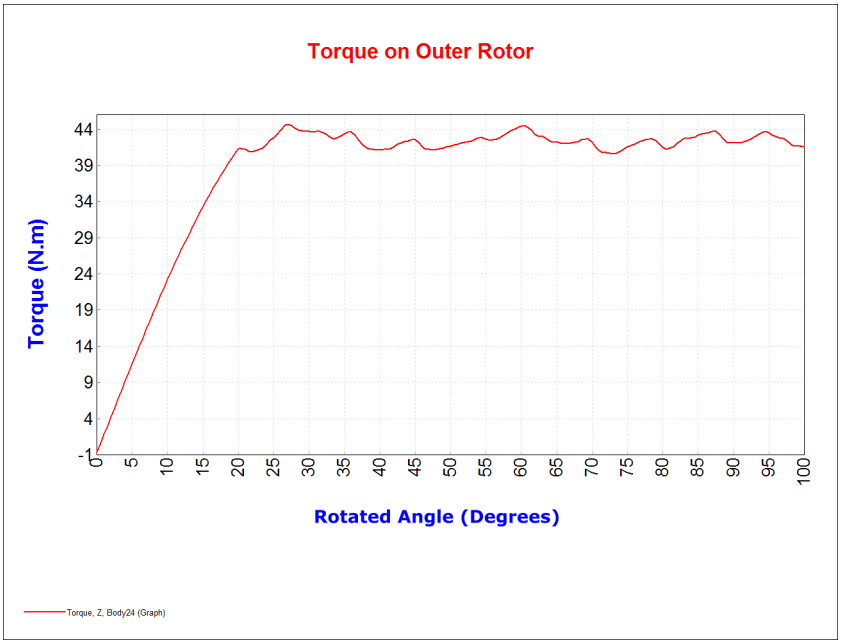

Figure 2.20: Torque on Outer Rotor for PP ratio 3:19

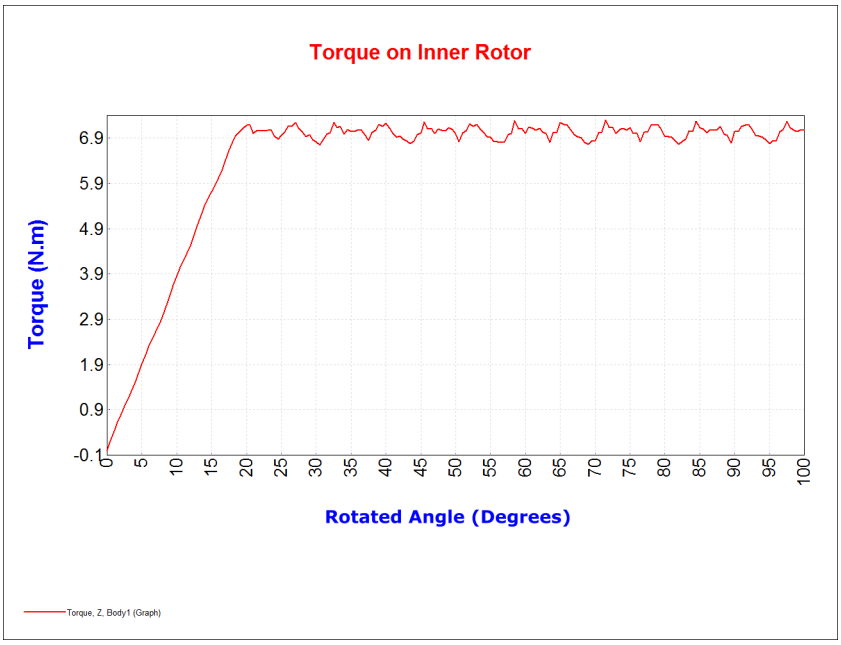

Figure 2.21: Torque on Inner Rotor for PP ratio 4:25

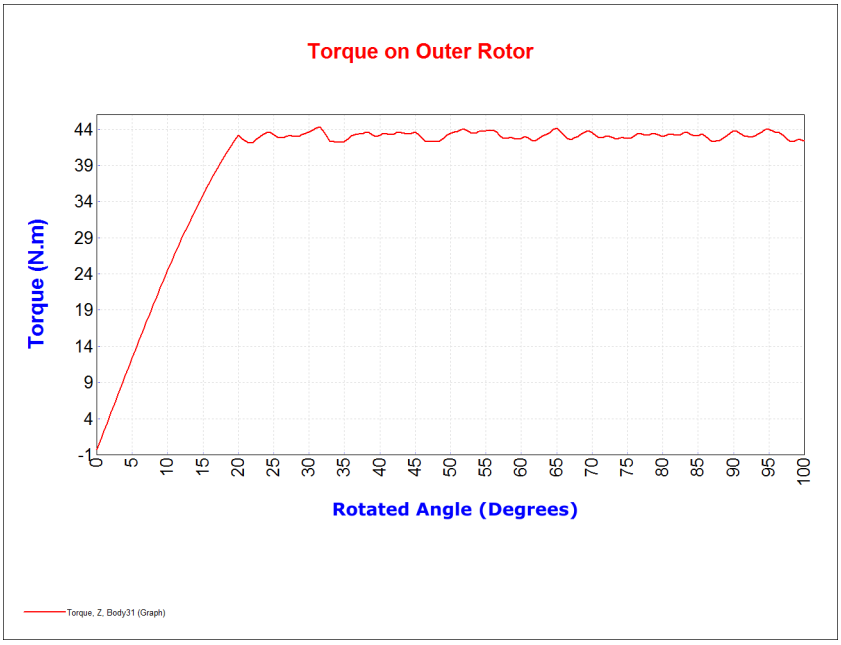

Figure 2.22: Torque on Outer Rotor for PP ratio 4:25

2.1.3 Rotor Airgap and Eccentricity

As in permanent magnet machines, small rotor airgaps reduce the magnetic reluctance and result in greater transmitted torque. However there are practical limitations with this and considering the high amount of magnetic material the attractive forces between rotors must be considered. In a perfectly centered MG, the magnetic field is

balanced and there should be negligible attractive forces between rotors. However if any eccentricity occurs during operation this can result in substantial attractive forces.

To investigate this a series of tests were performed to examine the resulting effect of a slight misalignment of the rotors. The type of eccentricity can be classified as static as the point of eccentricity will not change during motion. A small gear was modeled with a peak torque of approximately 34 Nm on the high torque FMP rotor. The inner and outer airgaps were 3.5 mm and 3.2 mm respectively. To test the effect of eccentricity the inner rotor and FMP rotors were shifted such that the outer airgap was decreased at the bottom of the gear while the outer airgap on top increased. An analysis for shifts of 0.25 mm, 0.5 mm, 1 mm and 2 mm was completed with the inner rotor rotated from the zero torque point to the peak torque. The shifted elements are shown in Figure 2.23 with the misalignment clearly shown. A full 3D transient solution was obtained and the vector forces acting in the x and y directions were obtained along with the vector sum, or magnitude, of these forces.

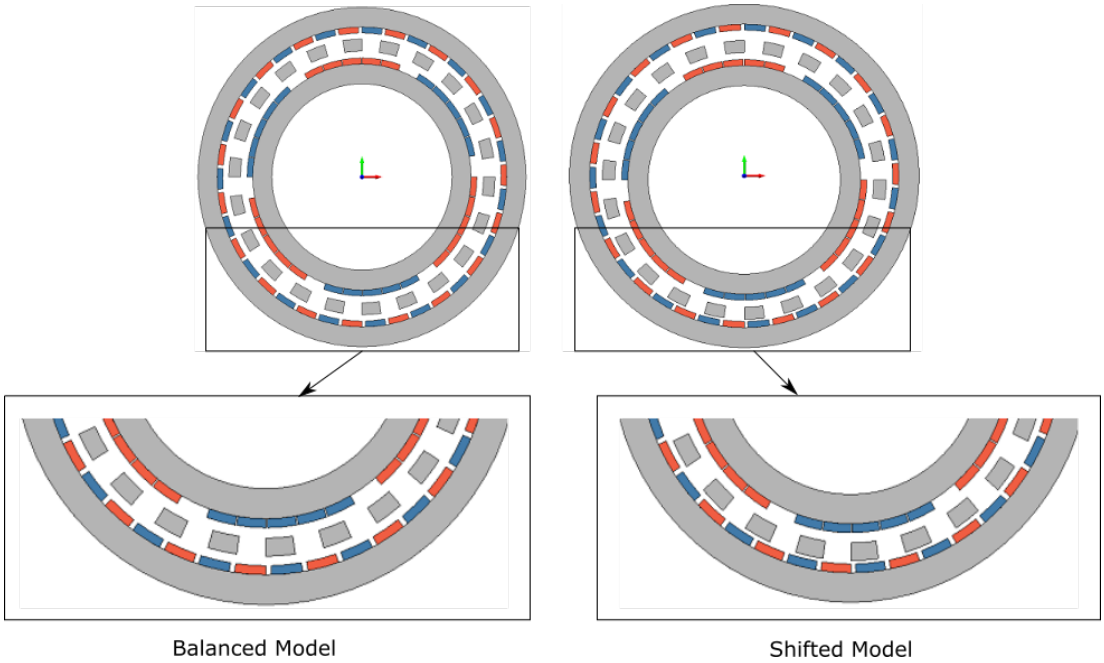

Figure 2.23: Rotor eccentricity test

A MG with an even FMP pole number that is perfectly aligned will be balanced in terms of magnetic forces. When a misalignment is introduced it is shown in Figures 2.24 - 2.29 that the rotors now develop significant X and Y vector elements. From the results it is clear that even a slight misalignment in a small gear will cause substantial vector forces. These forces will be orders of magnitude higher for larger gears. If a

constant torque is applied then this may be acceptable as long as the bearings have been rated for these forces. However, in an oscillating motion like wave energy, where the torque will be cyclical, the bearings will experience constant varying forces that may add wear on the bearings. It should be noted that MGs with an odd number of FMPs will have an unbalanced force even if the rotors are perfectly aligned. Furthermore, practical limitations in construction methods will inevitably introduce some amount of structural inconsistencies which will subsequently result in some unbalanced forces. This is an important consideration as the reduced O&M issues of MGs is often cited as a main advantage. The addition of these forces may also introduce further harmonics into the gear system which must be accounted for during the design process.

Despite these forces, the torque profile remains the same as shown in Figures 2.30 & 2.31.

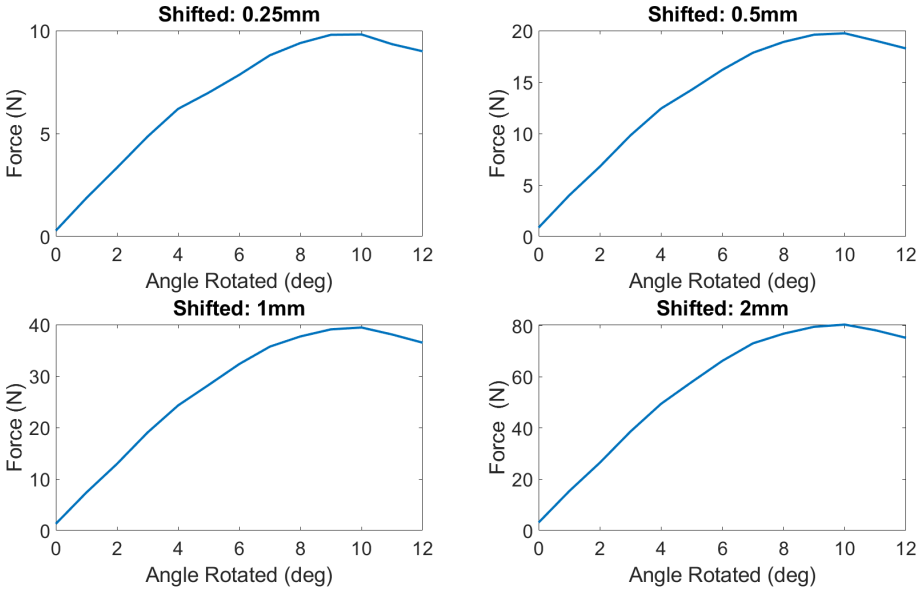

Figure 2.24: Inner rotor X forces with rotor shift

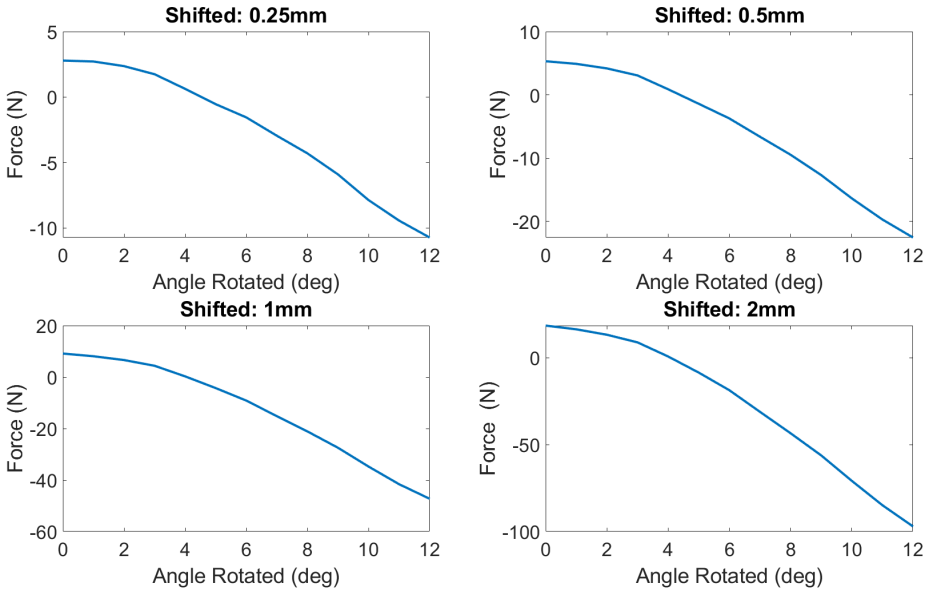

Figure 2.25: Inner rotor Y forces with rotor shift

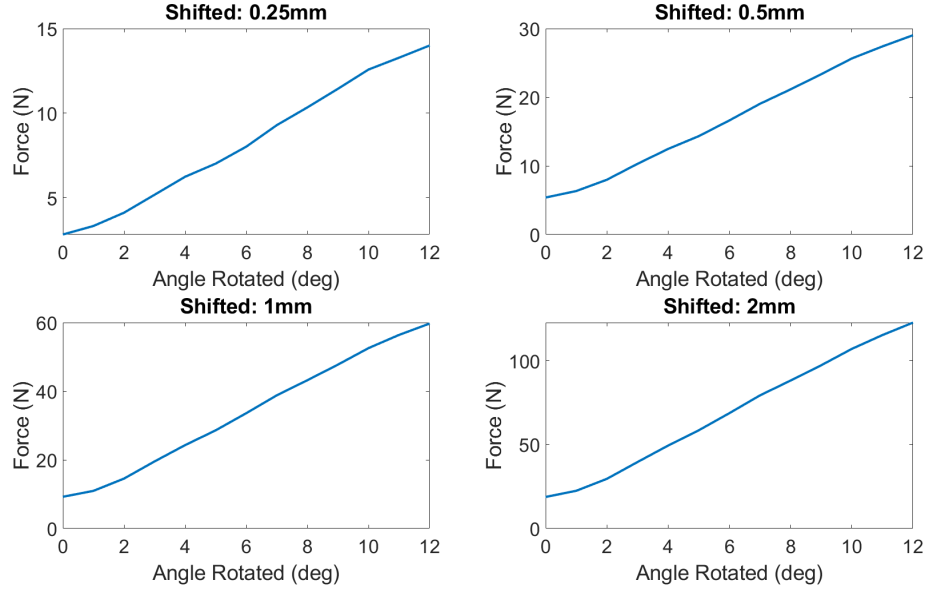

Figure 2.26: Inner rotor magnitude forces with rotor shift

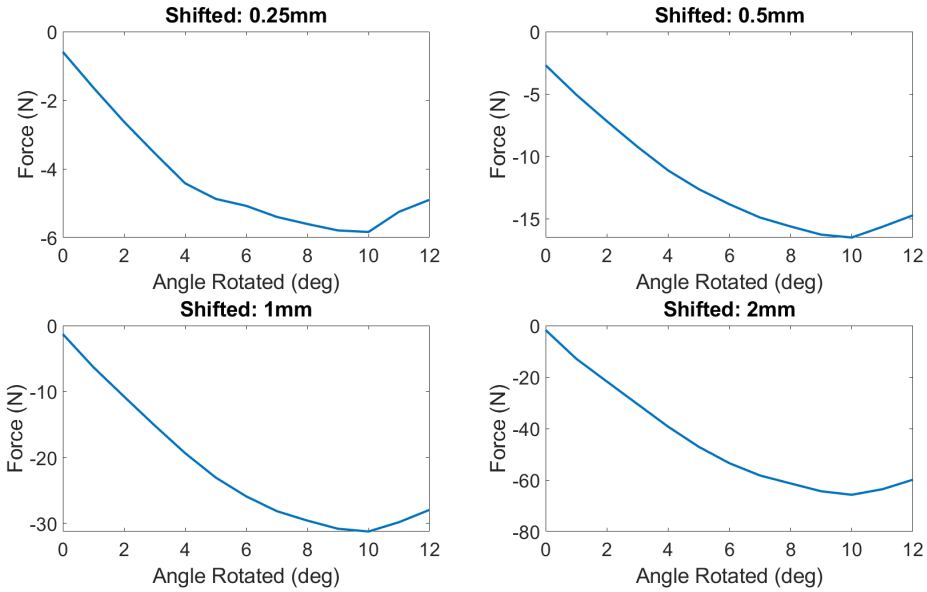

Figure 2.27: FMP rotor X forces with rotor shift

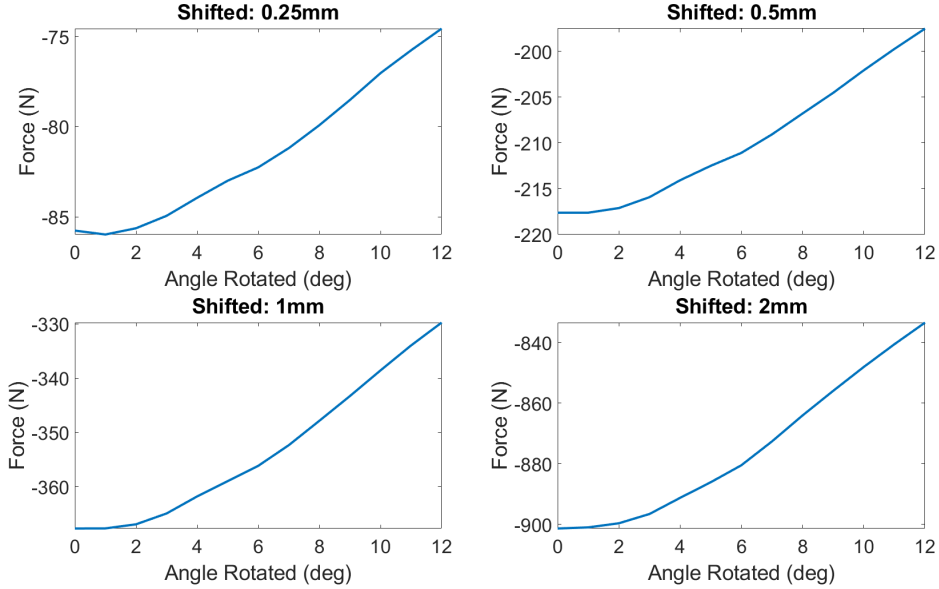

Figure 2.28: FMP rotor Y forces with rotor shift

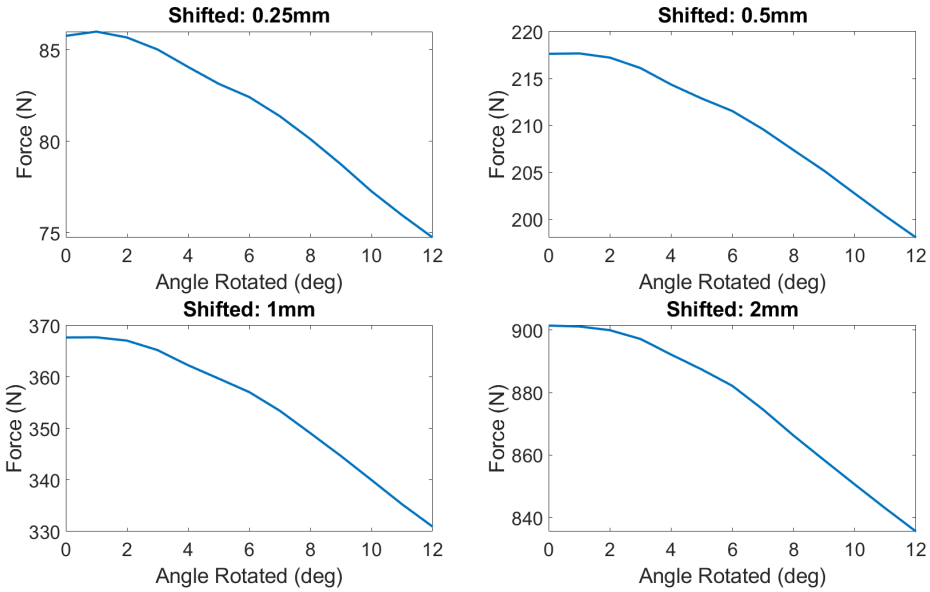

Figure 2.29: FMP rotor magnitude forces with rotor shift

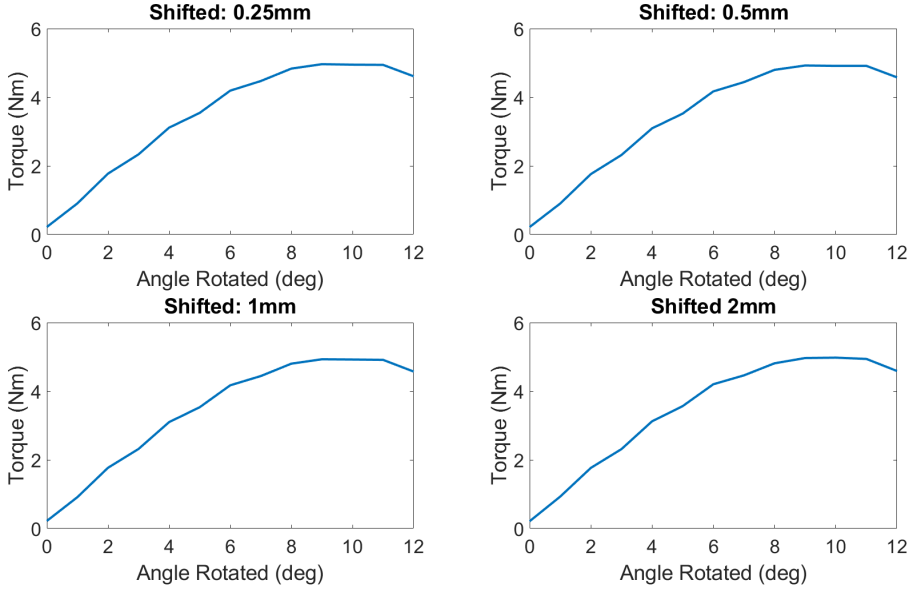

Figure 2.30: Inner rotor torque curves with rotor shift

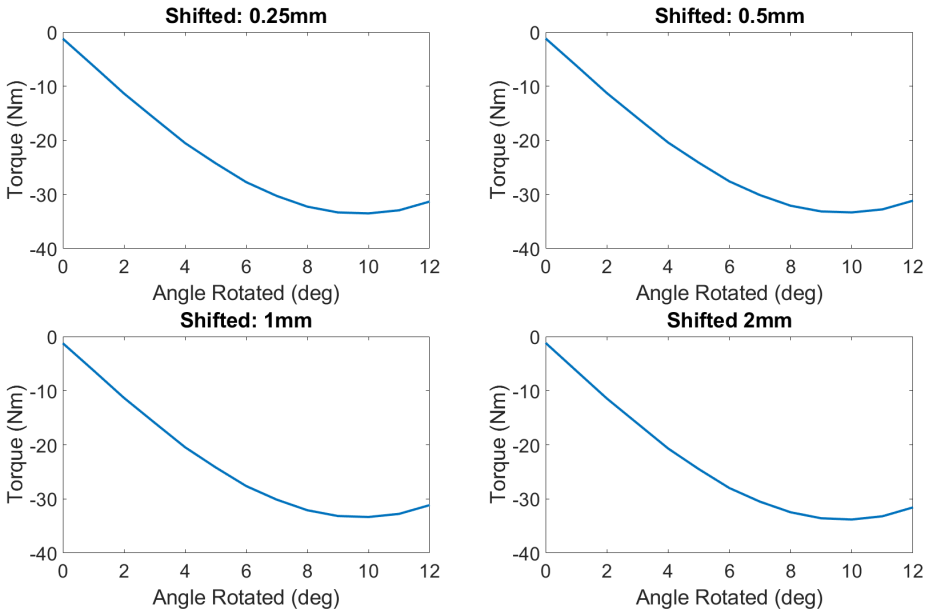

Figure 2.31: FMP rotor torque curves with rotor shift

2.1.4 FMP Radial Width

With the FMPs lacking the support of a backiron structure like the other two rotors and experiencing the combined magnetic forces of both magnetic pole rotors the FMPs can be susceptible to bending during motion, potentially compromising the airgap. Having thicker FMP elements is an option to increase structural strength. In the analytical models that have been proposed for MGs, a general assumption is that the iron has infinite permeability [96–99] allowing the FMPs to be radially thicker increasing rigidity and therefore structural stability. In reality the permeability is not infinite and there exists an optimal radial width for a given gear. To demonstrate this, a series of models were analysed for increasing FMP radial width. As the radial width increases the magnetic material on the outer rotor increases and therefore the torque should increase proportionally. The results, as shown in Figure 2.32, show that an optimal width exists before there are diminishing returns. Also shown is that while increasing the magnetic material from 3 mm to 6 mm increases the advantage range, the point of diminishing returns remains.

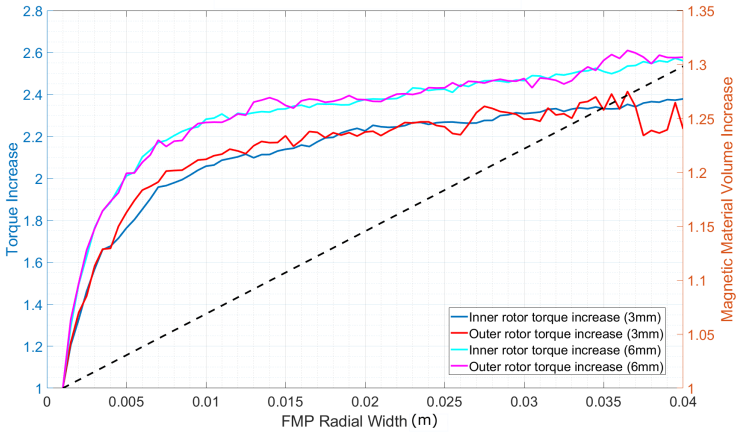

Figure 2.32: Increase in torque with increasing FMP radial width

2.1.5 Losses & Efficiency

As mentioned, MGs have been reported to have very high efficiencies as the mechanical losses are effectively solely limited to bearing friction. Aside from mechanical losses there will be the further losses resulting from a time varying magnetic field. These iron losses comprise hysteresis & eddy current losses and will be a function of both magnetic flux density (B) and the angular frequency (ω_s). The iron loss density p_{iron} can be calculated from eqn (2.5) [100].

$$p_{iron} = p_{hyst} + p_e = k_h B^{\beta} \omega_s + k_e B^2 \omega_s^2 \tag{2.5}$$

where p_{hyst} & p_e are the hysteresis and eddy current loss densities and k_h, k_e and β are the hysteresis constant, the eddy current constant and the Steinmetz constant which will be dependent on the material properties.

To achieve these high efficiencies it is important to consider all elements of the gear's structure. Some key considerations are discussed here.

FMP Material

The FMPs are subjected to time varying magnetic fields and so can experience high iron losses if not accounted for [26]. Reducing hysteresis losses generally requires the use of materials which can be magnitised and demagnetised easily such as silicon steel and steel alloys. The trade off with such materials will be higher costs and lower rigidity depending on the material used.

From electrical transformer design and machine design, a reduction in eddy current losses is achieved through the use of laminated materials. The sections between laminations will have a high electromagnetic resistance, restricting the flux path and reducing the perpendicular currents which results in a resistive torque against the direction of rotation. Though eddy currents will still exist within the laminations it is substantially less than in solid elements. While very effective at reducing eddy current losses, particularly in high frequency applications, there will be an increase in cost and construction complexity and a reduction in structural integrity.

FMP Support Structure and End Rings

The correct choice of the support material for the FMP rotor structure is essential as the ferromagnetic material will, like iron, create additional flux paths causing flux leakage and lower the transmitted torque. It is additionally essential to avoid the use of conductive materials such as copper or aluminum. While these materials will not affect the peak torque, during rotation a voltage will be induced creating a current which will create an opposing magnetic field in the same manner as a squirrel cage in induction motors. In MGs this will effectively establish a magnetic breaking element and greatly affect the transmitted torque and efficiency. Ideally the use of rigid polymers, ceramics or other electrically insulated material should be used.

Backiron

While not as severe as the FMP elements, the backiron used to support the PMs will also experience iron losses and so an assessment of both the material selection and the use of laminations is necessary during system design [101]. As with the FMPs the use of laminations will reduce eddy current losses but increase cost and manufacturing complexity.

Losses in the PM material

The composition of Neodymium Iron Boron makes the material highly conductive and therefore susceptible to large eddy current losses induced within the magnets [65]. A method for reducing these losses would be the use of segmented magnets that would form a whole magnetic pole. While this will have an effect on costs and construction complexity it is an important factor to be considered, particularly in high torque

applications with large magnetic pole areas.

Windage

Windage losses, resulting from the fluid resistance opposing the motion of the rotors, is an important factor for MGs in marine application. While windage has been found to have a greater effect on high speed applications [102], if the gear is flooded the resistance caused by motion through water will be substantially higher than in a sealed or non-marine application [103].

Previous Studies in MG Efficiency

In 2004 Atallah et al. reported a MG efficiency exceeding 97% when the load torque was >75% of the pullout torque [26]. The results of these tests are shown in Figure 2.33.

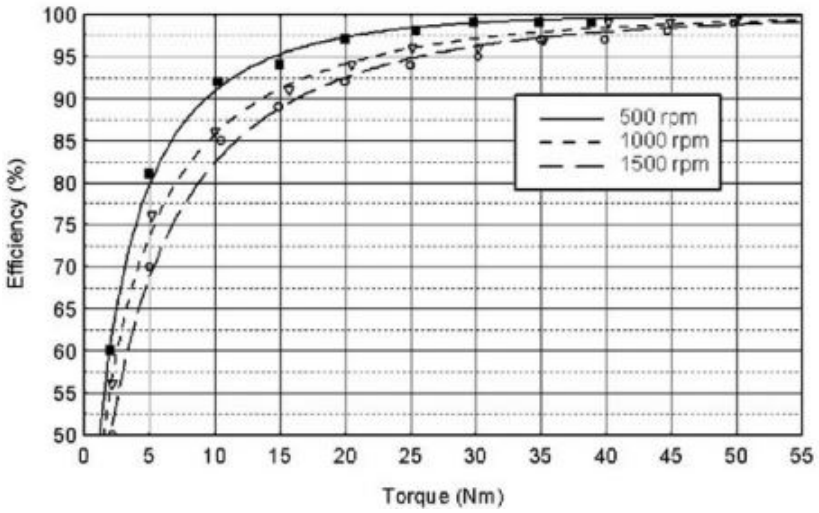

Figure 2.33: Efficiency of magnetic gear with increasing torque load [26]

In a wave application with oscillating motion and torque, this may then require adaptive load control on the generator side. A further study in 2013 looked at the effect of rotational speeds and the effect on efficiency [27]. The work found that the efficiency of MGs increases as the speed is lowered. The peak efficiency, reported as 99%, occurred at the lowest tested speed of 300 rpm (Figure 2.34). Further studies confirmed the results with efficiencies in the 96-99% range [10, 27].

A prominent study in MG efficiency was part of the ABB-Texas A&M project that specifically looked at MG efficiencies under the low speed and high torque wave energy conditions [25]. As shown in Figure 2.35 the gear has extremely high efficiencies at

lower speeds when tested with 2D FEA. A scaled 10 kW prototype was tested and a full system (MG and generator) efficiency of 92% was reported with the MG's efficiency being calculated at 97%.

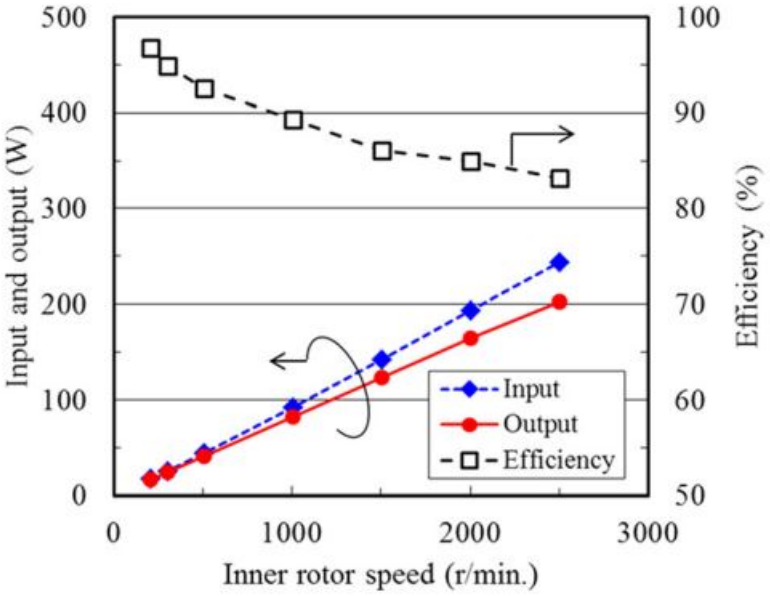

Figure 2.34: Efficiency of magnetic gear with increasing speed [27]

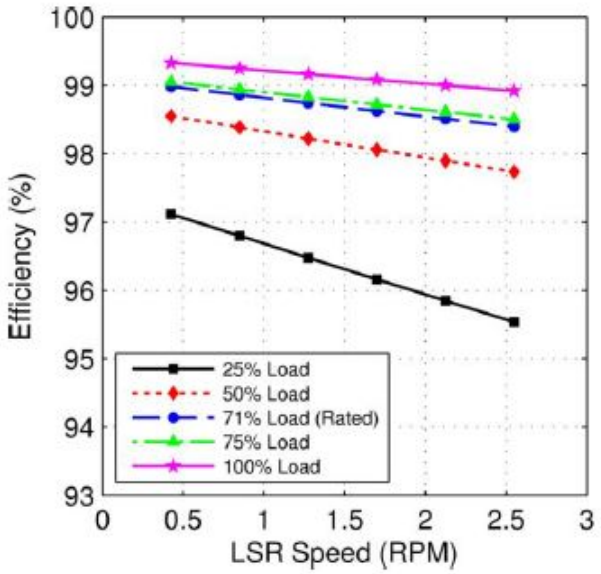

Figure 2.35: Efficiency of magnetic gear w.r.t speed and load [25]

2.2 Conclusion

The points discussed in this chapter cover some of the major considerations in the MG design process. With the technology's maturation these considerations will form the basis of industry standards which will increase design confidence and streamline the design process. With multiple interdependent parameters, the design of a MG can be time consuming if a purely iterative process is used and an optimal solution may be missed. Chapter 5 proposes a solution to this with the use of a genetic algorithm.

Chapter 3

Dynamic Analysis of a Magnetic Gear in an OWSC

3.1 Dynamic Analysis Introduction

MG systems are fundamentally dynamic in nature as, unlike mechanical gears, there will be relative motion between rotors. For example, as torque is applied to the low speed rotor the rotor will move as the torque increases on the low torque rotor. When the torque is sufficient to overcome the low speed rotor's inertia only then will there be reciprocating motion. A spring effect then occurs whereby the rotor will attempt to catch up with the other rotor while a gearing effect is also observed. As inertia is built on the high speed rotor in the event of a sudden halt in motion there will be some overshoot as the gear attempts to realign to the 0 torque point [104].

A dynamic analysis then provides a more accurate analysis of a MG's operation in a system. Furthermore it allows for an analysis of the "slipping" capabilities of a MG under extreme forces where the peak force is exceeded. In a unidirectional setting this would mean separation of the rotors requiring breaking systems but given the oscillating nature of a WEC this dynamic may lend to auto correction.

This chapter is part of work presented at the Asian Wave and Tidal Energy Conference, 2018 [105].

3.2 The Dynamic Model

The dynamic model of the MG was developed in MBDyn [106], a free multibody dynamics and multiphysics simulation tool with a focus on scientific accuracy, developed for nearly 20 years and first released as an open source tool in 2001. MBDyn uses the concept of "structural nodes" which refer to entities with kinematic degrees of freedom. These nodes can then be constrained with joint elements, have forces or couples applied to them, and masses attached to them. MBDyn provides a very wide range of elements with which to create the multibody system simulation.

In MBDyn, three nodes and five joints are required to model the gear. The first node represents the low speed rotor, while the third node is the low speed rotor. The second node is an intermediate node used to connect the system in the appropriate manner. The first and second nodes are connected by "Revolute Hinge" joints which constrain the position and orientation of the nodes such than only rotation about a common axis is possible. The second and third nodes are constrained in the same way. In addition to this, the first and second node are connected by a "Gear Joint" which imposes a relative angular velocity between the two nodes such that the angular velocity of the first node is some multiple of that of the second node. The gear joint element is not available at the time of writing in the official release of MBDyn (which is version 1.7.3). It is a part of the loadable module "module-fabricate" which will be available in a forthcoming release. A preview version of this element was helpfully provided by the developers. To achieve a similar effect to the gear joint, it is also possible to use the "Axial Rotation" joint which imposes an angular velocity on a node about a chosen axis. This angular velocity can be set to be a multiple of the angular velocity of another node. However, the Gear Joint is more reliable and efficient being custom made for this use case.

As shown previously, the torque between the rotors is sinusoidally varying and directionally dependent with relative displacement of the two rotors. The high speed rotor sees a torque, τ_{HS} which varies as in (3.1), where θ_{HS} is the angular displacement of the high speed rotor, θ_{LS} is the angular displacement of the low speed rotor, τ_{HSmax} is the maximum cogging torque of the gear.

$$\tau_{HS} = \tau_{HSmax} \sin(p_h(\theta_{HS} - G_r\theta_{LS})) \tag{3.1}$$

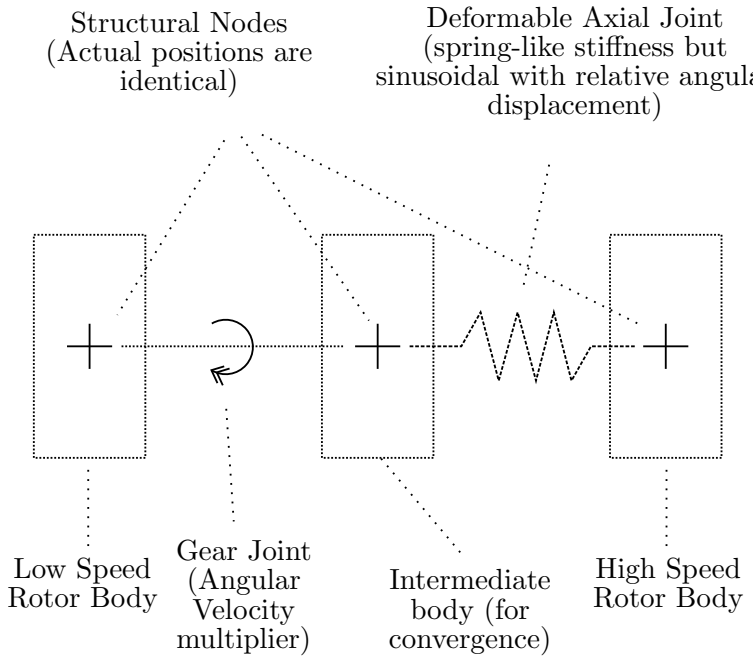

Figure 3.1: MBdyn dynamic model of a MG system

To implement this in MBDyn the "Deformable Axial Joint" was used. The deformable axial joint allows a configuration dependent moment to be applied between two nodes based on their relative rotation about a specified axis. This moment can be defined as a function, which must be differentiable. MBDyn does not yet implement a differentiable sine function and so was modified to add this feature. Three bodies were then attached to the structural nodes. Bodies in MBDyn connect mass and inertia to structural nodes. The low speed rotor body was attached to the first node, and the high speed node to the third node. A very small mass was attached to the intermediate node purely to improve convergence of the solution. A diagram of the multibody system for the gear is shown in Figure 5.1 where it should be noted that the locations of all structural nodes (and bodies) are coincident, and not displaced as shown in the diagram. The full system modeled elements are shown in Figure 3.6.

3.3 Case Study

In 2009 Dr. Keysan et. al. produced a study on the application of a C-Gen type electrical machine for the Aquamarine Oyster device PTO (Figure 3.4) in place of the hydraulic system then used [28, 107]. The key findings of the report were that due to

the low rotational speed (<1rpm) the system would require a single stage gearbox to be feasible. With a gear ratio of between 10-15:1 the efficiency of the generator was around 90% and the total mass was substantially reduced in comparison to a similar direct drive system. The proposed PTO was to place a gearbox-generator system on either side of the device's hinge as shown in Figure 3.4. The report further established the torque-speed characteristics of the device finding that having a system capable of 6.2 MNm torque (or two 3.1 MNm, one on each side) would suffice for the device 99.95% of the time and account for 99% of the energy output. However, including even a single stage gearbox reduces the advantages of a proposed direct drive system due to the increase in O&M costs associated with mechanical gears. As MGs are theoretically not subject to these high O&M requirements could allow for a highly efficient system without the additional cost. The MG system developed in this work was for a similar system with two gears developed for 3.1 MNm peak torque and a gear ratio of at least 10:1. The proposed topology is shown in Figure 3.5. The parameters for this model are shown in Table 3.1 with the parameters shown in Figure 3.7. The rotor torque curves shown in Figures 3.2 & 3.3 are used as a reference for the torque acting on the system for a given angular displacement.

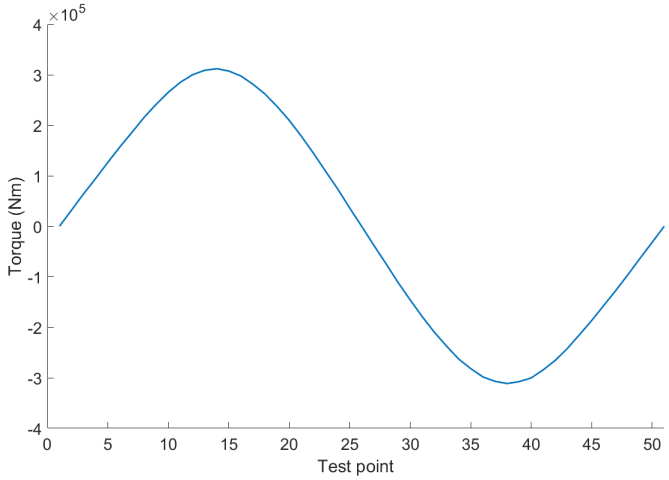

Figure 3.2: Torque profile of the high speed, low torque rotor

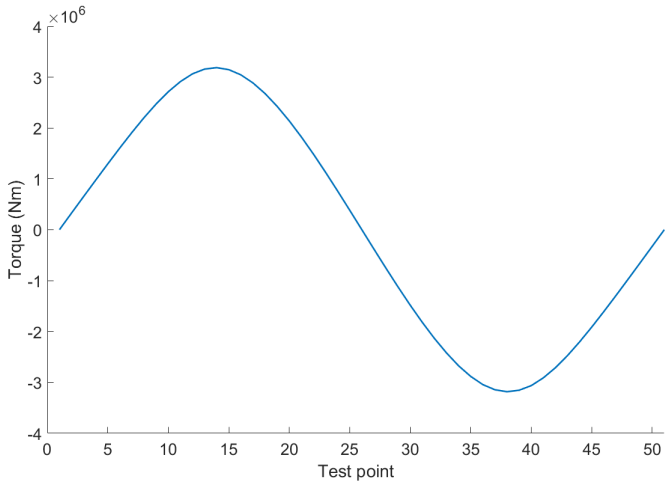

Figure 3.3: Torque profile of the low speed, high torque rotor

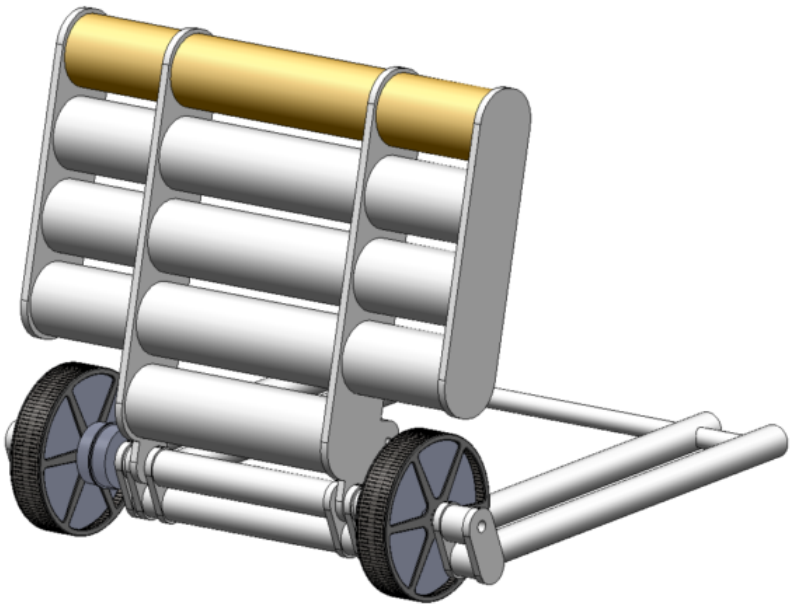

Figure 3.4: Aquamarine Oyster Wave Energy Convereter [28]

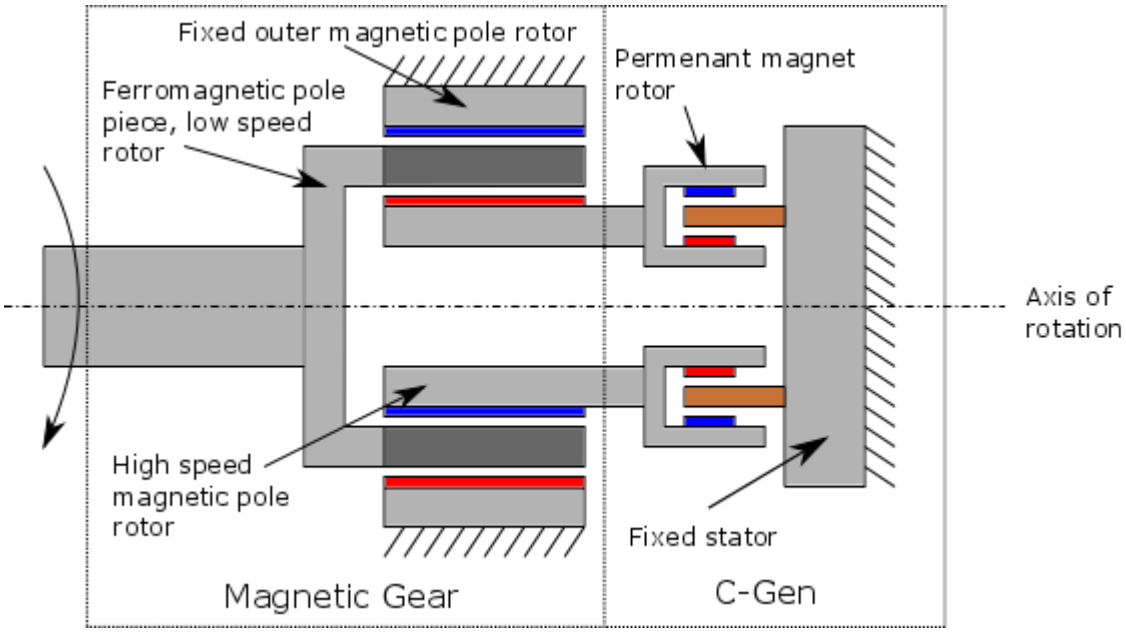

Figure 3.5: Proposed MG - Generator topology

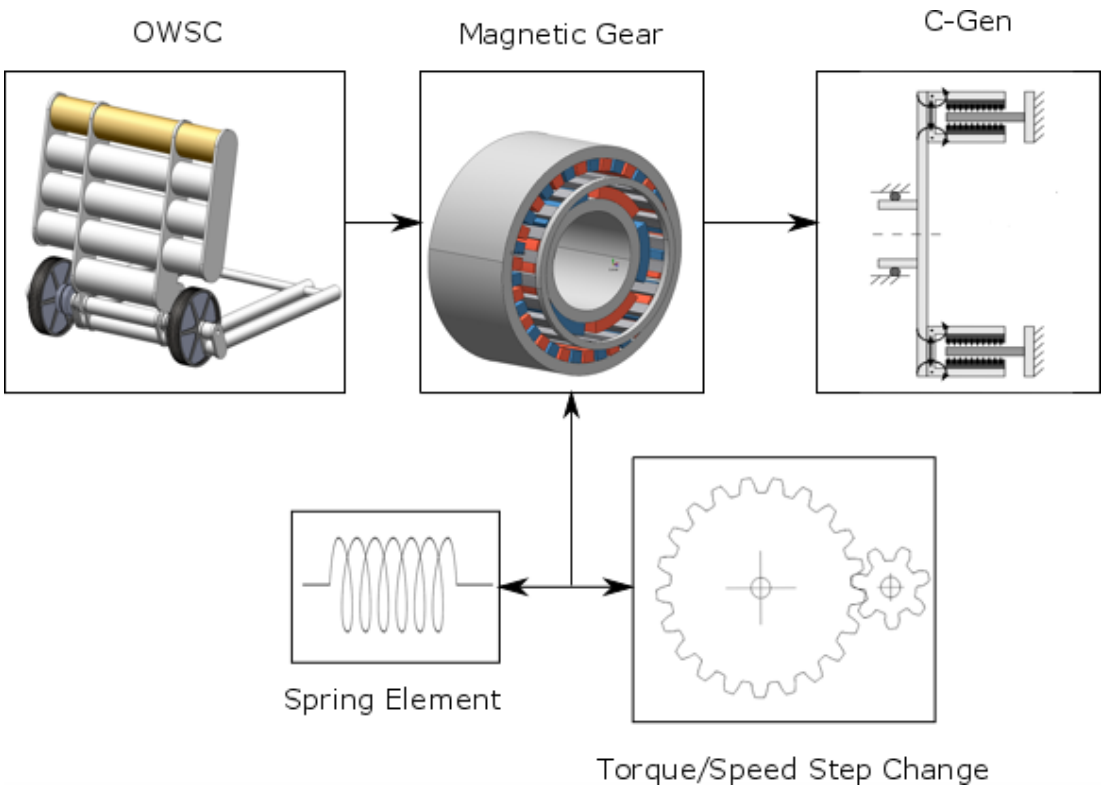

Figure 3.6: Full PTO layoput

Table 3.1: MG parameter values

Parameter	Value	Unit
Inner rotor magnetic pole height	0.015	m
Outer rotor magnetic pole height	0.010	m
FMP radial thickness	0.020	m
Airgap radius	1.4	m
Gear axial length	3	m
Inner rotor airgap width	0.001	m
Outer rotor airgap width	0.001	m
Outer rotor backiron thickness	0.020	m
Inner rotor backiron thickness	0.020	m
Outer (fixed) rotor pole pair number	157	
Inner (high speed, low torque) rotor pole pair number	17	
FM (low speed, high torque) rotor pole number	174	
Ratio	10.24:1	
Target high torque	3.1	MNm
Peak (high) torque	3.187	MNm
Peak (low) torque	-0.31198	MNm
Magnetic mass (total)	4224	kg
Active iron mass (total)	10424	kg
Mass of high speed rotor (active)	6576	kg
Mass of low speed rotor (active)	1043.9	kg
Total gear mass (active)	14649	kg

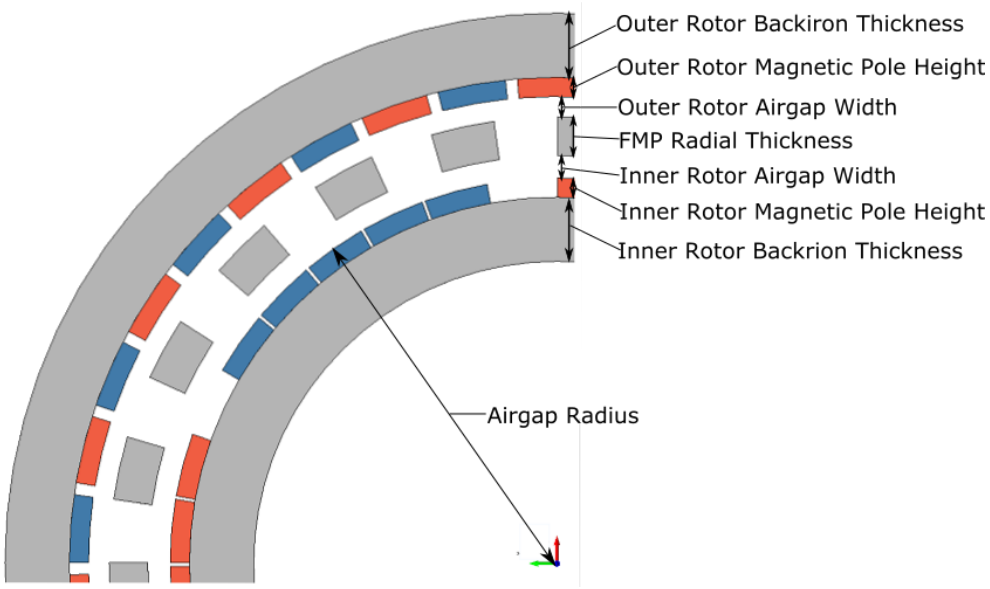

Figure 3.7: Magnetic gear parameters.

3.4 Simulations

3.4.1 Simply Driven Gear and Load Model

A fully integrated WEC and PTO model has internal feedback, i.e. the torque applied by the PTO affects the motion of the WEC. For this reason, to demonstrate some properties of the gear dynamic performance in a clear way, some results of a simulation of the gear only, using a very stiff drive are now presented. A simulation was performed with the low speed side of the gear driven in a prescribed sinusoidal motion with an angular velocity amplitude of 0.189 rads^{-1} and period of 8 s. At the same time a damping torque was applied, i.e. where the load torque was given by the formula $\tau_L = -c\omega_{HS}$ with a coefficient, c, of 169 kNs, and where ω_{HS} is the angular velocity of the high speed side of the gear. This damping coefficient was chosen such that the maximum gear transmission torque would be just exceeded as the peak of the sine wave was approached. Although this may seem simplistic, simple linear damping is a common control strategy used in WECs which have been demonstrated at sea [108]. In some cases, active damping, where the coefficient is modified to suit the wave conditions is also used. More advanced control strategies are available, but usually require bi-directional power flow and therefore require significantly more complex systems to implement.

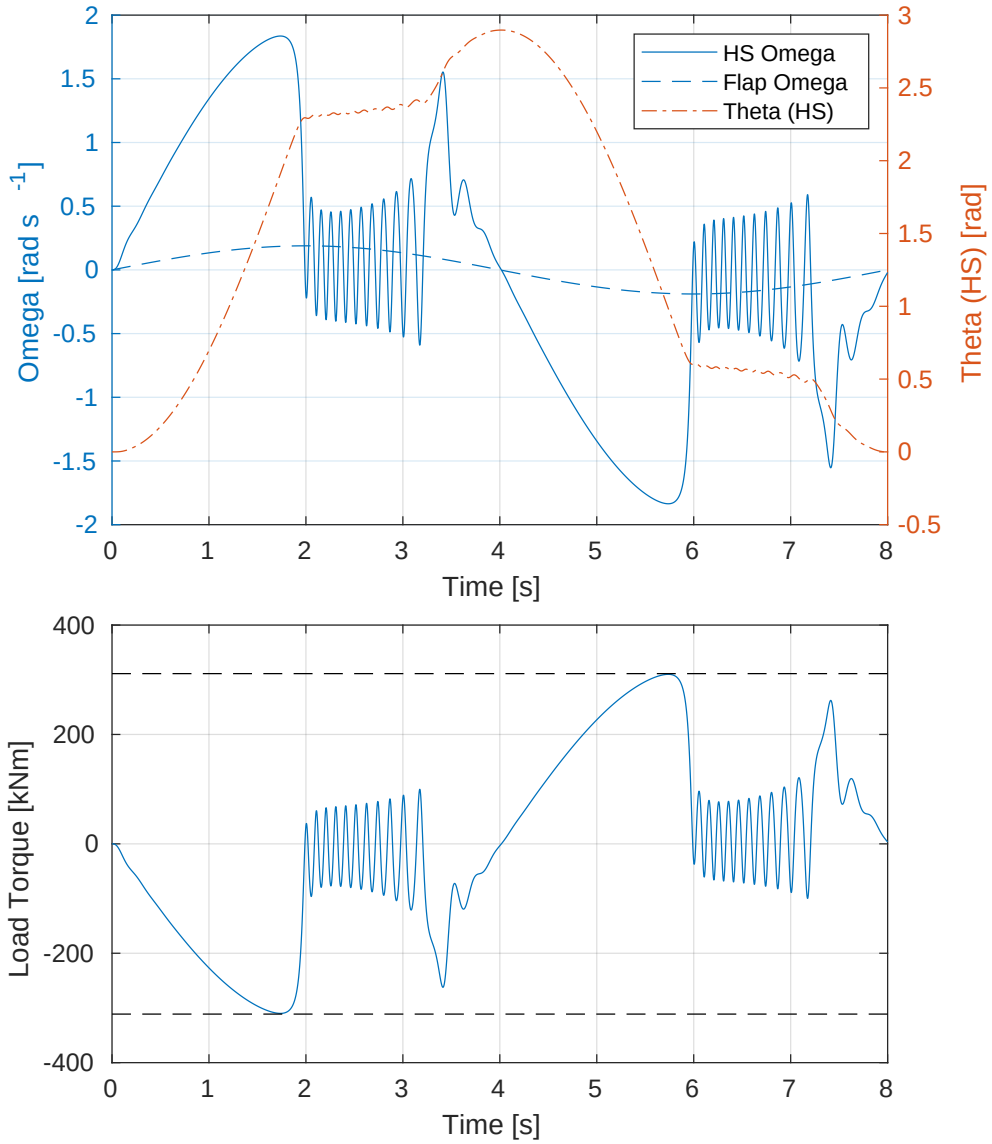

Figure 3.8: (top plot) Angular velocities of the Low speed (flap) side of the gear and high speed side, and the angular displacement of the high speed side. (bottom plot) Load torque during simulation (solid line) and max/min gear torques (dashed lines).

The results of this simulation are presented in Figure 3.8. It can be seen that the gear initially tracks the motion of the input drive until the damping torque exceeds the maximum gear torque. At this point, the torque transmission is essentially lost as the gear high speed rotor begins making small (but rapid) oscillations with a low average angular velocity. In this period the net angular displacement does continue to rise slightly, probably due to the gear inertia and neglection of friction. The high frequency oscillations occur as the high speed rotor attempts to reconnect with the still moving low speed rotor. Due to the low stiffness element and spring effect the rotor experiences rapidly varying torque which will have a corresponding effect on the angular velocity.

However, as the input drive speed falls from the peak, the gear parts reconnect and the gear begins to again transmit torque and track the input drive motion. This shows that the gear can be used to ride through high torque incidents, and reconnect passively without an advanced control system.

3.4.2 Results Comparison with Simulink Model

In order to validate the new model, a dynamic model of the stand alone gear was developed in Simulink. The model, as shown in Appendix A, is similar to that described in [109] but adapted for comparison with the Simply Driven Gear and Load Model test. The same values for the high torque side angular velocity and torque dynamics as described in equation 3.1 were used. The results of the Simulink model are consistent with the new model as shown in Figures 3.9 and 3.10.

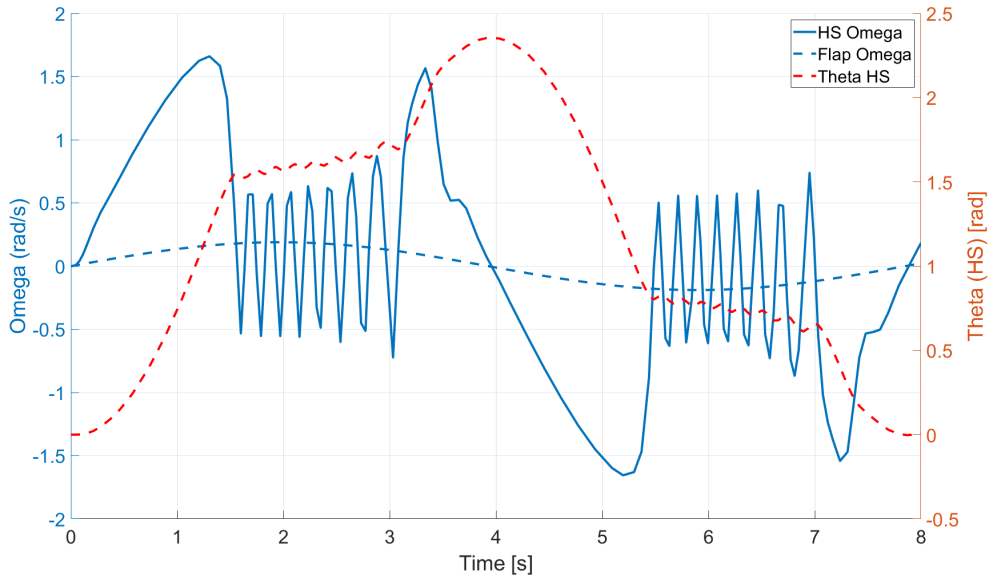

Figure 3.9: Angular velocities of the Low speed (flap) side of the gear and high speed side, and the angular displacement of the high speed side, Simulink model

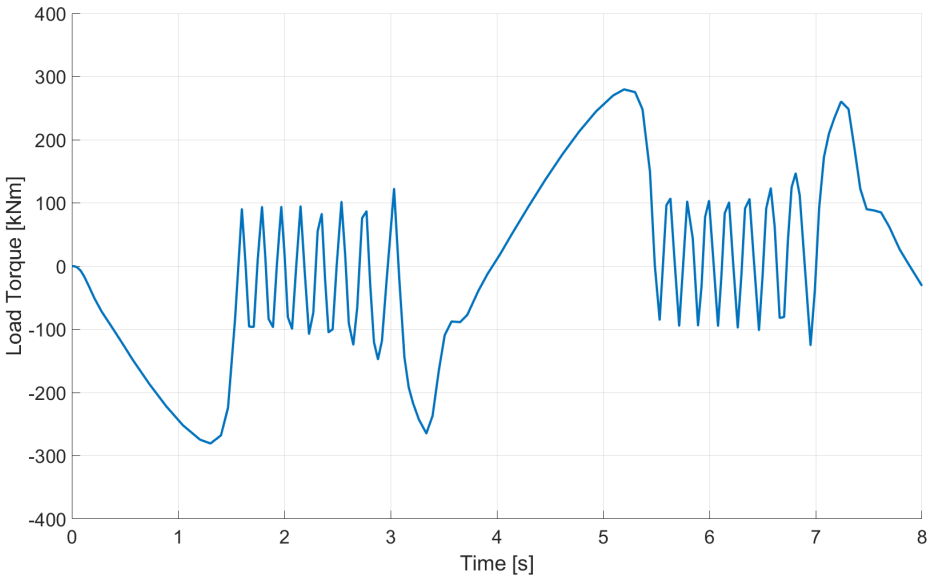

Figure 3.10: Load torque during simulation (solid line) and max/min gear torques, Simulink model

3.4.3 Gear, Flap and Load Model

To demonstrate that the same basic operation is seen in the full system, a simulation has been performed with the gear operating as part of the drive train of a full OWSC system. The OWSC which will be evaluated is Reference Model 5 (RM5) from the NREL Marine Hydrokinetic Reference Model Project [110]. This model was chosen due to its similarity to the Oyster device and the ready availability of the detailed data required for its simulation which has already been validated by experimental tests. Figure 3.11 shows a plot of the device, and detailed information on its design may be found in [110].

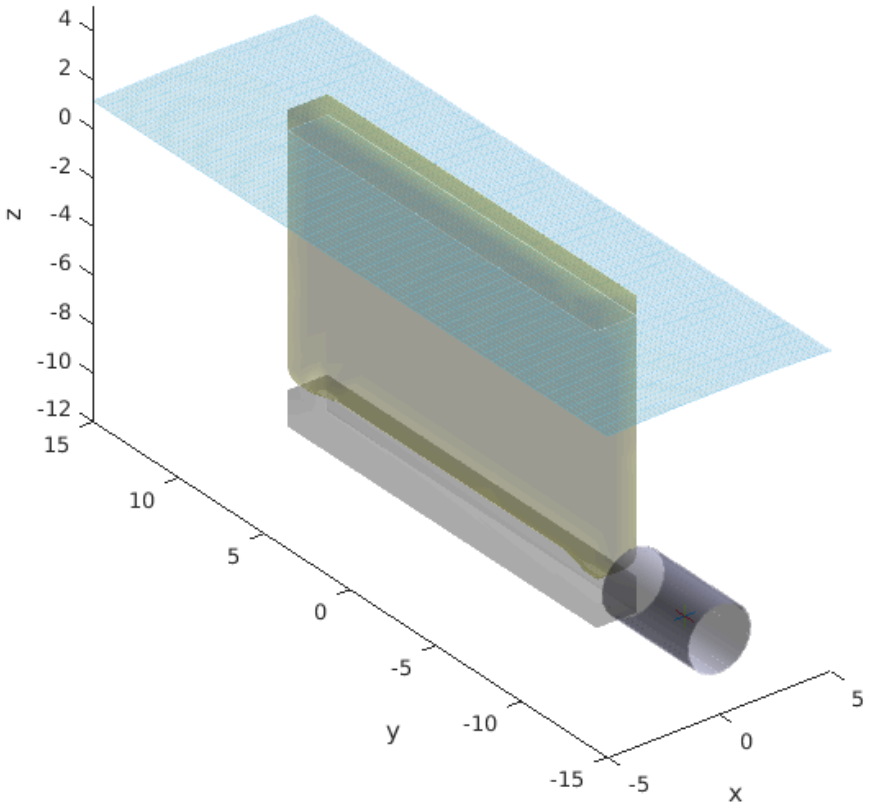

Figure 3.11: Diagram of OWSC simulation configuration. Flap is shown in yellow above a fixed base plate, the gear is represented as two annular sections, and the water level is indicated with the blue meshed surface.

To simulate the hydrodynamics, a simulation system derived from WEC-Sim [111] was used, the details of which may be found in [112]. This model replaces the use of the Simulink Simscape Multibody with MBDyn for the multibody dynamics calculations, supports multi-rate simulation for different model components and has advanced pre and post-processing capabilities. The development sources of this open-source tool are available online [113]. This model consists of two structural nodes and two bodies and was coupled to the previously described MG model by constraining the rotation of the gear low speed node to be the same as that of the flap node. In the real system two gears would be used and two generators. For the purposes of this simulation, the double gears were modelled by doubling the length of the gear, as the torque in this model scales linearly with length. The mass and inertia matrices were also scaled appropriately, which led to a reduction in simulation time by reducing the number of degrees of freedom.

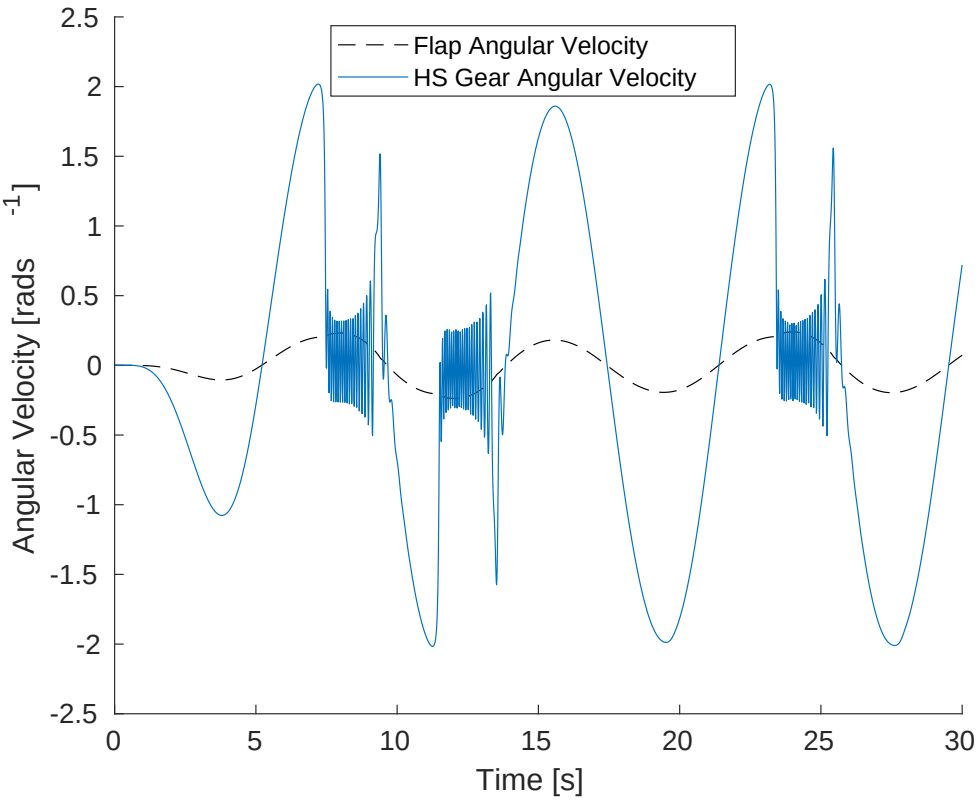

Figure 3.12: Angular velocities of the Low speed (flap side) of the MG and high speed side during the OWSC simulation.

The OWSC was simulated with an incoming regular wave, but with an amplitude being increased with a ramp from zero to a peak significant wave height of 2.5 m. The waves have a period of 8 s, and the ramp up in wave height occurs over a 5 second duration. As in the previous simulation, a damping torque which scales linearly with angular velocity was applied, in this case with a damping coefficient of 307.4 kNs (or 153.7 kNs per gear). This value was mainly chosen through trial and error to result in the gear peak torque being just exceeded close to the peak angular velocity of the WEC motion. The resulting angular velocities of the flap and high speed side of the MG are shown in Figure 3.12. The applied PTO torque over the same period is shown in Figure 3.13.

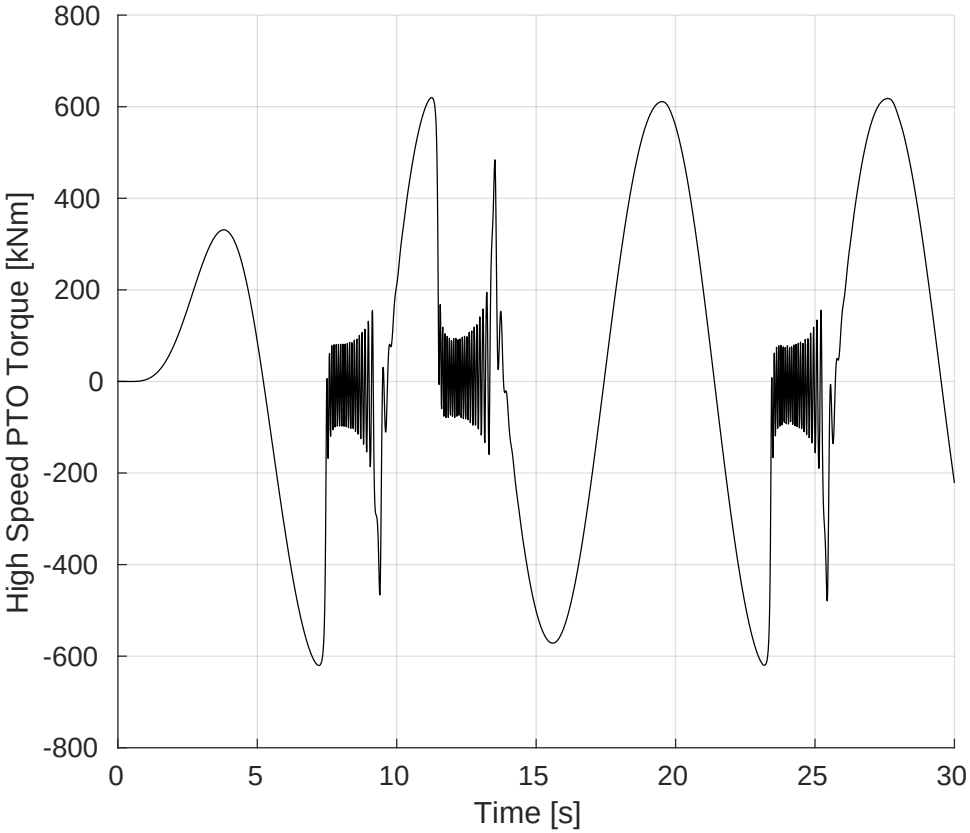

Figure 3.13: High speed load torque during the OWSC simulation.

These results show that the results from the simple simulation also hold for the full system simulation, at least in this specific case. The gear connection slips at the peak velocity, but passively reconnects as the wave event progresses. Interestingly, in some cases this seems to impact the system performance in the following wave such that the maximum angular velocity which is achieved is reduced and no slipping occurs.

3.5 Discussion

A much more extensive study in a greater range of wave conditions, especially random waves from a wave spectrum, would be necessary to fully understand the dynamic behaviour of the gear. These preliminary results indicate that the gear can offer some additional protection for extreme wave events (or control or PTO failures) where it can act as a kind of filter for extreme torque spikes on either side of the gear. The statistical distribution of waves mean extreme events are to be expected, and must be designed for in any system. A magnetic gear interface could facilitate the design of the PTO by providing a limit on the possible peak loading from the prime mover. As the

peak loads are one of the main drivers of the design, this could ease significantly the required specifications of the PTO.

The control system used for the PTO here was very basic, a simple damper. It is possible that with a slightly more advanced system, the duration of the slip event could be significantly reduced, and the gear brought back into operation much faster, e.g. by tracking the motion of the flap during the slip event. Similarly one could simply limit the maximum PTO torque on the high speed side to a value less than the maximum MG transmission torque. The gear would still provide protection for failures in the PTO, e.g. a short-circuit fault in the generator, or a control system failure, preventing them from impacting the rest of the system significantly.

There are also possible negative consequences of slip. One is a total loss of control of the device during the slipping period as there is no torque transmission. For some devices, such as a OWSC this is probably not a significant issue, as an undamped OWSC is limited in the deviations it will experience, even in extreme storm conditions. In fact the MG may allow continued power production during such conditions, where previously this was impossible. However, for other types of WEC, this could be a serious issue if the PTO is used to prevent excessive motion.

Another negative aspect of slip, which has not been modelled in this work is that it will likely lead to losses in the MG which do not occur during normal operation. Under slip conditions there is much more relative motion of the various conductive components and the magnetic fields from the magnets. This will result in iron losses and heating in the gear components. Furthermore, the magnetic poles are forced into opposing one another periodically which, together with the heating, will increase the risk of demagnetisation of the magnets. A detailed study of these aspects would be necessary before implementing a system designed to slip under extreme conditions. However, if the design is such that slip events are rare and short lived, it is likely that any heating should be limited, and the demagnetisation risk can be designed out appropriately.

Although a MG is likely to be significantly more costly than a conventional gear, it may be the case that the reduced intervention rates required for maintenance, coupled with the inherent overload protection could make it cost-competitive with conventional systems when a holistic view is taken of the system.

3.6 Conclusion

The simulation of the dynamic performance of a MG system during extreme torque events shows that in a simple isolated MG simulation with an oscillating drive, the MG can slip and exit the slip condition without any active control intervention. It further shows that through a system simulation of an OWSC in regular waves this behaviour can still be observed.

Chapter 4

Prototype Development and Testing

4.1 Introduction

In order to test the accuracy of the design tools two prototype gears were designed, built and tested. The designed gear parameters and test rig setup are described in the following Chapter.

As discussed in Chapter 1, MGs have potential in an OWSC with Chapter 3 suggesting the dynamic effects of a MG may improve the energy capture by smoothing out some of the extreme events. Part of the long term goals of the e-Drive project [114] is to develop a magnetically geared PTO that can be incorporated into an OWSC and tested at the FloWave facility. The planned test rig is discussed further in Chapter 7. Though this is beyond the scope of this PhD the prototype gears were designed for this application. Following the discussion of the prototype design and test layout the results of the tests are presented and discussed.

4.1.1 Prototype Design

A key objective of the FloWave tests was to observe the gear's effects on a WEC drive train under extreme load - slip conditions. Using Froude scaling for the test rig, the expected peak torque acting on the flap was calculated to be 80 Nm (approximately 1/16th scale Oyster device). To account for this two gears with target peak torques of 35 Nm were chosen which would allow for a similar PTO layout as described in [115]. This peak torque would allow for a wide range of operating conditions while

also being low enough such that the peak torque could be exceeded and the slipping effect observed. The prototypes were designed through an iterative process which took into consideration available off-the-shelf elements, such as iron tubing diameters for the backiron and PM sizes, which allowed for simpler manufacturing and lower costs. The initial design was for a ratio of >10:1 but following an analysis this was lowered to 7.33:1 which allowed for the target peak torque value at reduced material costs. This ratio was established with 3 and 19 pole pairs on the inner high speed rotor and fixed outer ring. The FMP ring then, which is the low speed - high torque rotor has 22 poles. The prototype's parameters are detailed in table 4.1 and the design with dimensions is shown in Figure 4.1. Following the 3D analysis of this design the peak torque was found to be 34.4 Nm. The magnetic poles are NdFeB 38s and the back iron and FMPs are simple mild steel. The FMPs are supported with non-magnetic aluminum discs. The rotating elements structure is shown in Figure 4.2 and the fixed outer housing with magnetic poles shown in Figure 4.3. The gears were designed using a similar process as in [115] and built by Fountain Design Ltd [116]. The two finished gears are shown in Figure 4.4.

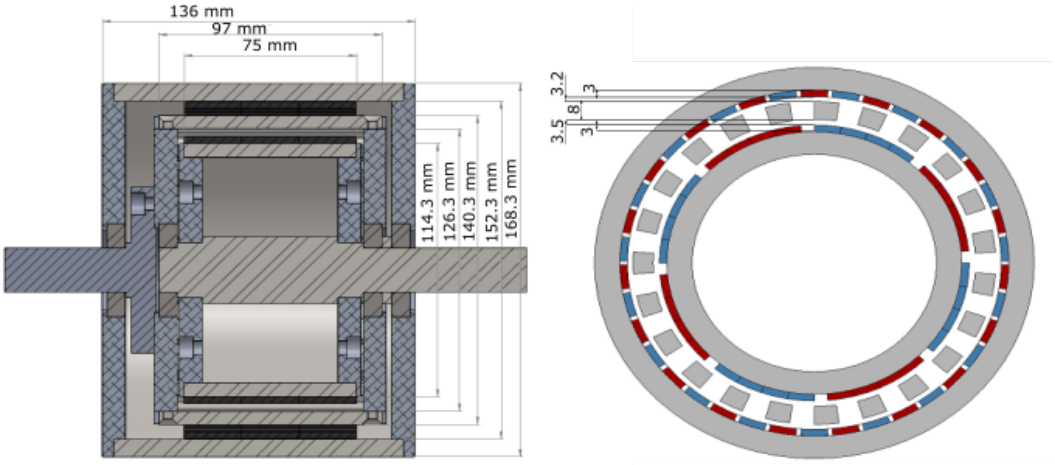

Figure 4.1: Prototype CAD with dimensions

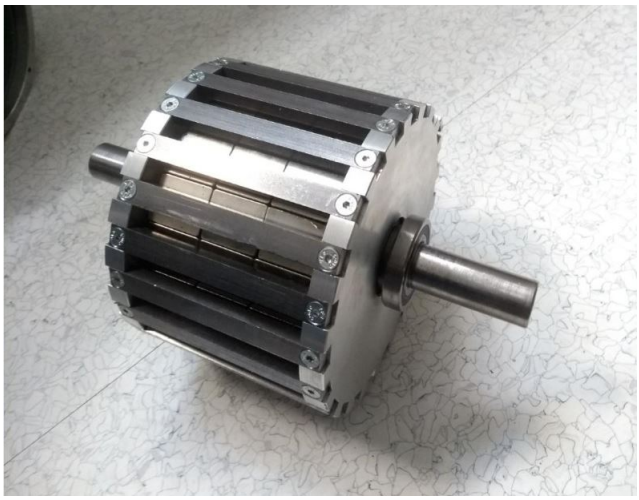

Figure 4.2: Rotor mechanism

Figure 4.3: Gear outer magnetic ring

Table 4.1: MG prototype parameter values

Parameter	Value	Unit
Inner magnetic pole thickness	0.003	m
Outer magnetic pole thickness	0.003	m
Ferro-magnetic pole thickness	0.006	m
Airgap radius	0.06015	m
Gear active axial length	0.075	m
Inner airgap	0.0035	m
Outer airgap	0.0032	m
Outer backiron thickness	0.010	m
Inner backiron thickness	0.010	m
Outer (fixed) rotor pole pair number	19	
Inner (high speed, low torque) rotor pole pair number	3	
FM (low speed, high torque) rotor pole pair number	22	
Designed ratio	7.33:1	
Target high torque	35	Nm
Peak (high) torque 2D	53	Nm
Peak (high) torque 3D	34.4	Nm

Figure 4.4: Completed Gears

4.2 Gear Test Rig

A test rig was designed with the goal of being easily adaptable if alterations were required. The test rig was first designed in Solidworks (Figure 4.5) and can be set up with or without the gear (Figures 4.6 & 4.7). The gearless setup was used to test the motor's operation and characteristics to then be compared with a geared system.

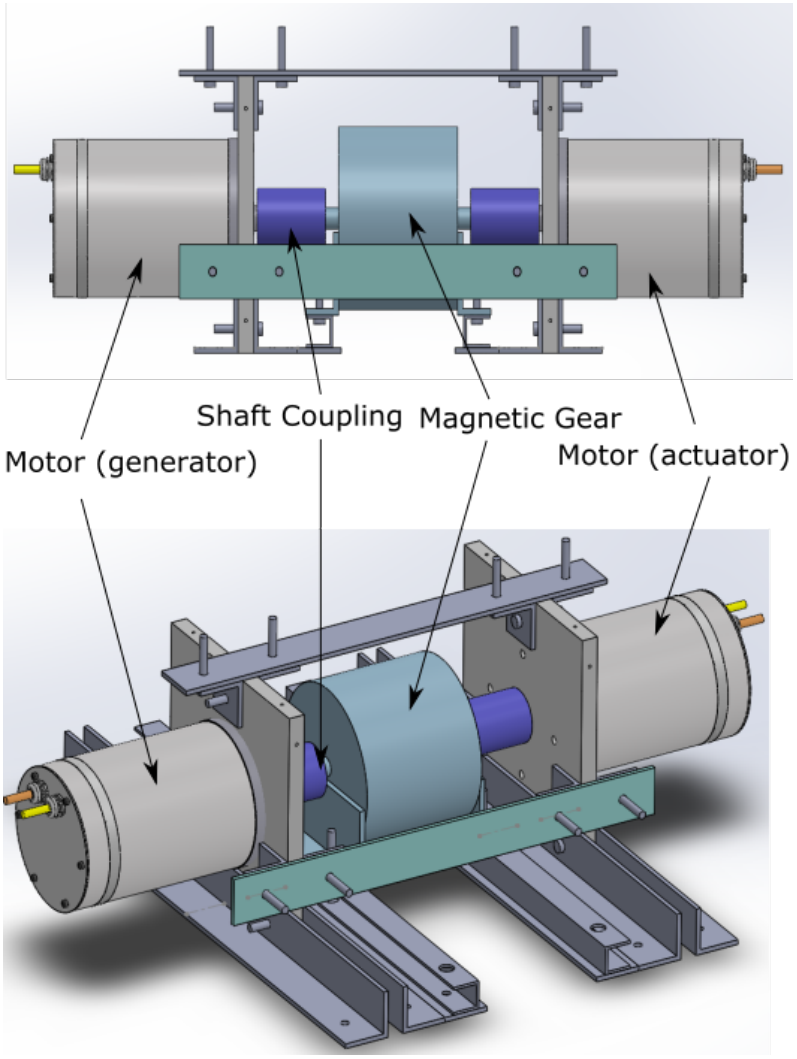

Figure 4.5: Test rig CAD design

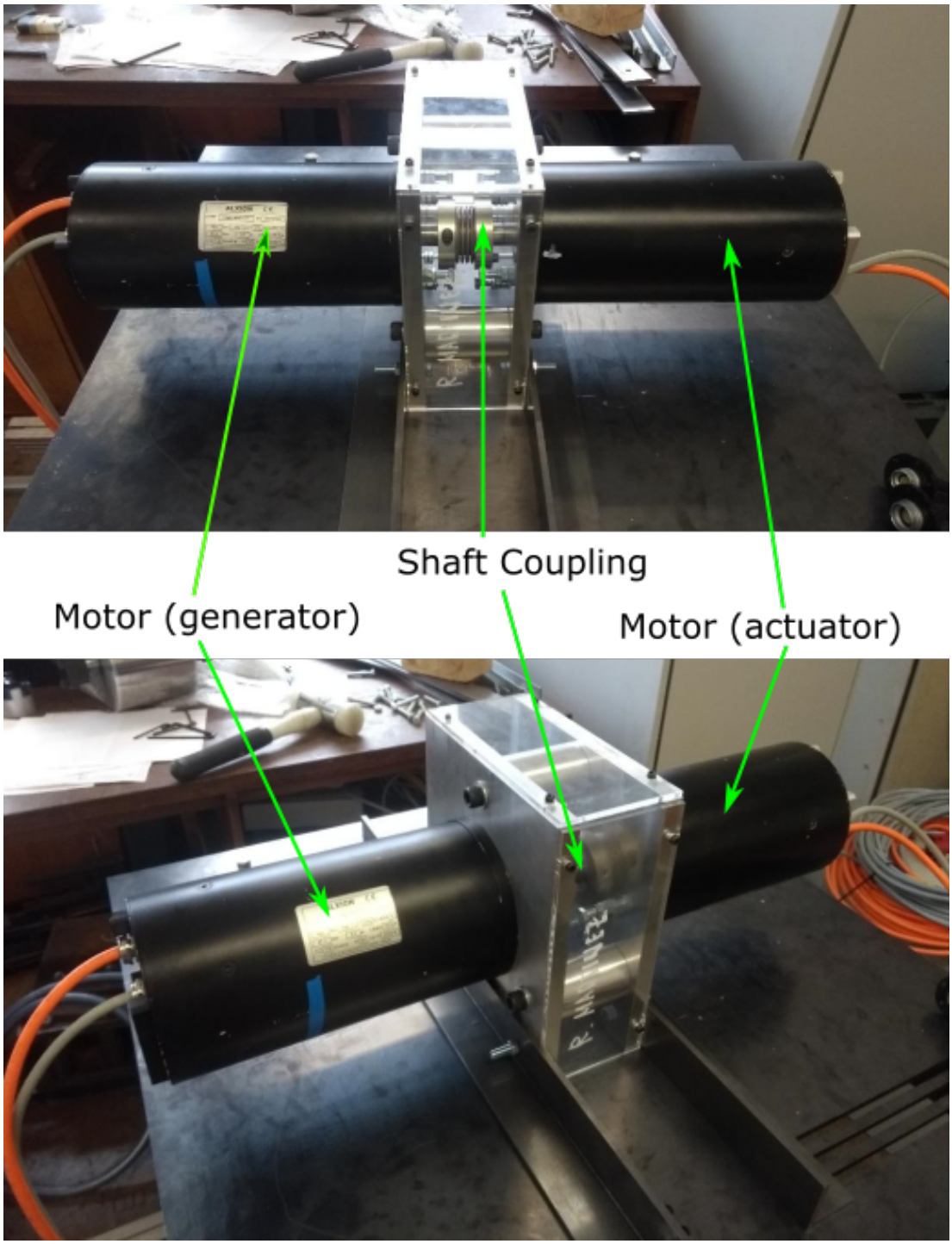

Figure 4.6: Test rig realised, no gear

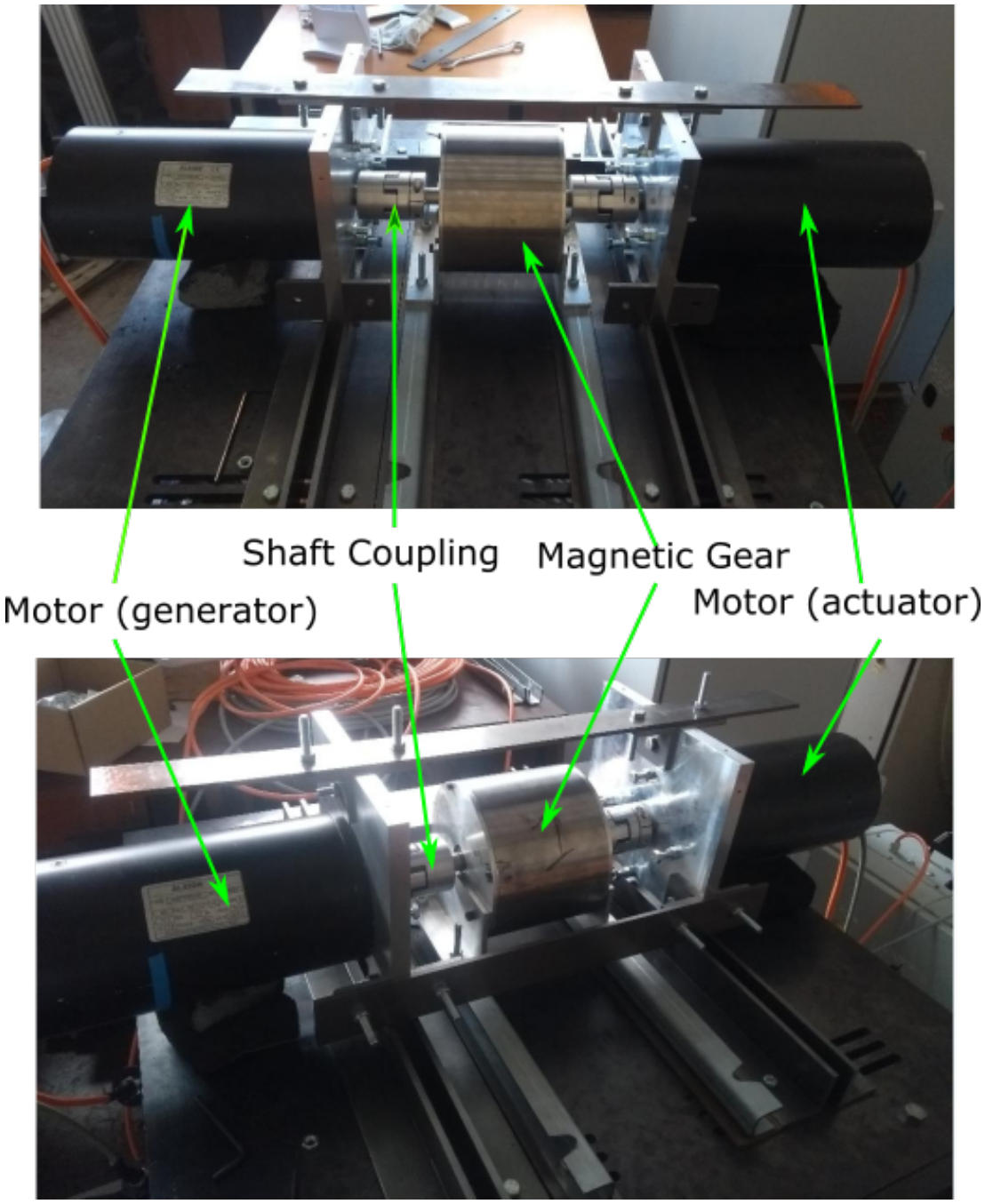

Figure 4.7: Test rig realised, with gear

4.2.1 Motors

Two motors were used to act as the actuation control and as a generator. The motors, which were loaned from the FloWTurb project [117], were 12 pole brushless AC custom Alxion 145ST machines with a nominal torque of 12 Nm per amp and a peak current of 5.5 A. The motors have inbuilt encoders for velocity measurements and are extremely efficient at higher torques in the range of 98%. For the tests the peak velocity was set

to 220 RPM, after which the motors are automatically disabled to prevent overspeed.

4.2.2 Shaft Couplings

The couplings selected for connecting the motors to the gears were ABSSAC Satrflex ALS (B) Types with clamp type tightening [29]. The advantage of these couplings was that while capable of high torque transference, they also allow for slight misalignment correction. The main elements are shown in Figure 4.8.

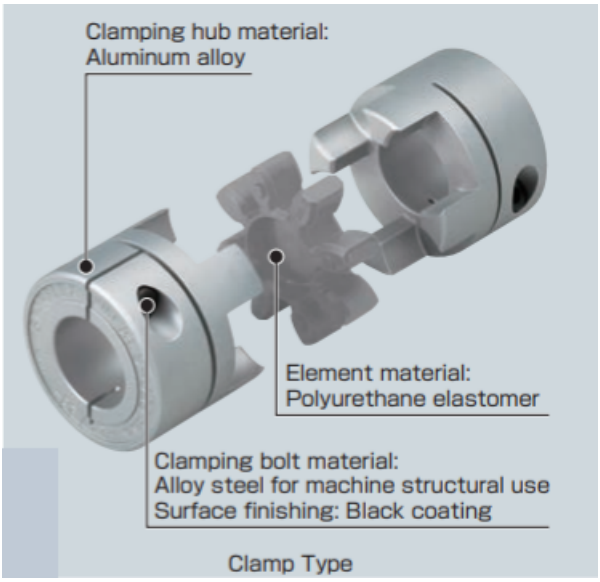

Figure 4.8: ABSSAC Starflex coupling elements [29]

4.3 Full Test Rig Setup

The control and measurement recording of the motors required additional elements and the full test system's layout is shown in Figure 4.9. The drives and control software, as with the motors, were loaned from the FloWTurb project.

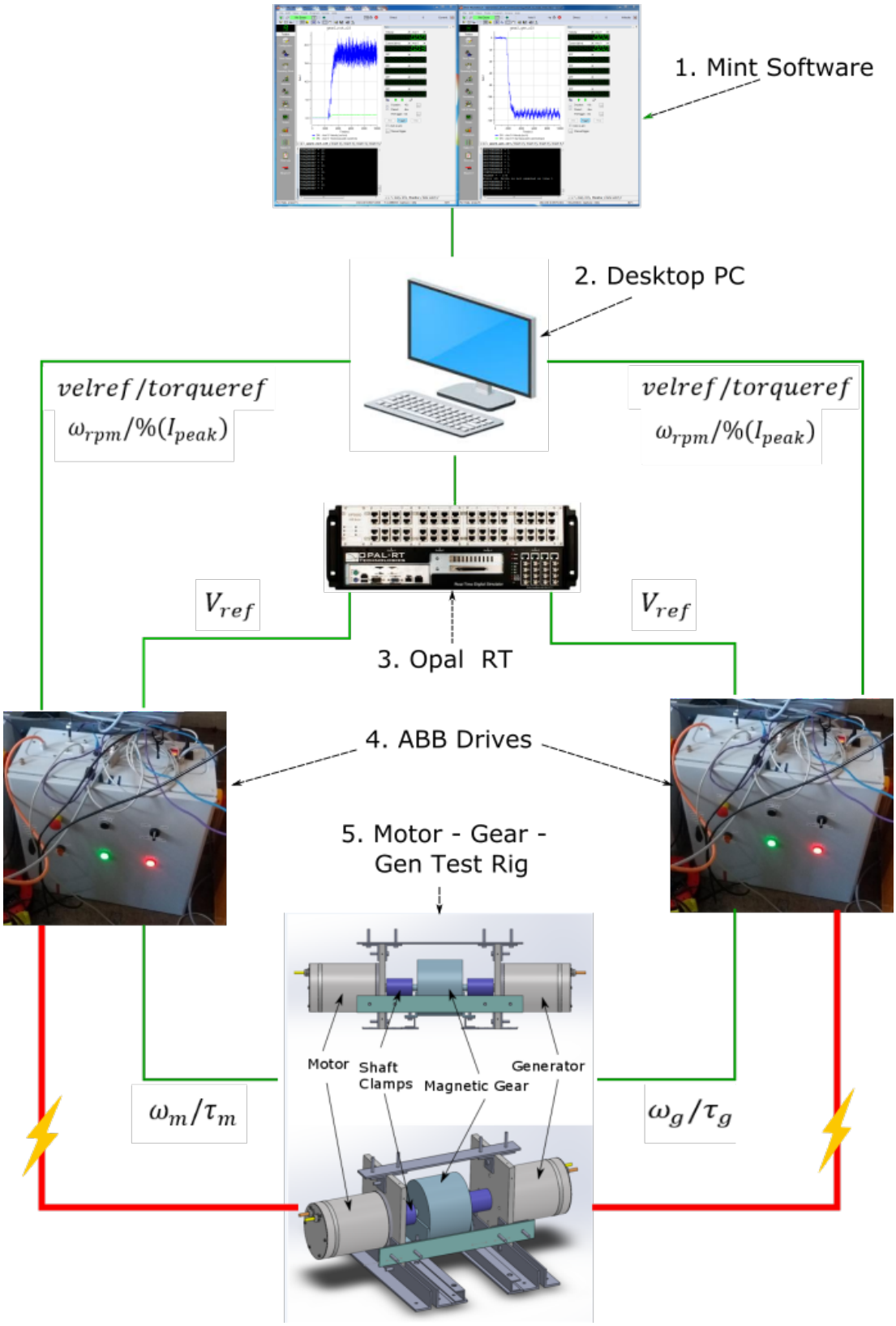

Figure 4.9: Full test rig system layout

4.3.1 Mint Workbench

The Mint Workbench is a Windows based tool compatible with ABB drives. Direct control of the motors was executed from the Mint Environment including enabling the drives, setting the speed and torque references and where the results are recorded following a test run. There is a fixed amount of memory when recording results meaning that the longer the run and the more recorded values (i.e. current, velocity, voltage demand etc) increases the time step between sample points. The control source was set through Mint, either direct control (user input) or from the OPAL RT, as well as the control mode i.e. velocity or torque reference. When under direct control, the speed reference can be given directly whereas the torque is given as a percentage of the peak current (5.5 A) with each amp equating to 12 Nm.

4.3.2 OPAL RT

The OPAL RT OP5600 is a versatile real-time digital simulator that allows for real time signals to be generated. The OPAL RT software allows for signals to be developed in a Simulink model, loaded to the OPAL RT platform and executed. This was very useful during the testing as it allowed sinusoidal and ramp functions to be executed. The output is a digital signal with values ranging from 0-10 Volts which is interpreted by the motors' drives as a percentage of peak torque or peak speed.

4.3.3 ABB Drives

The motor drives were custom ABB Motiflex e180s and provide the nominal 400V supply for the motors and convert the velocity and torque reference signals from the Mint Workbench or the OPAL RT to the corresponding speed or torque enacted by the motors. Both the Mint Workbench and the OPAL RT were directly connected to the drives with the sources being selected through the Mint software. Both drives were connected to an emergency stop button which allows for the power to be immediately shut off if required.

4.4 Practical Testing Considerations

4.4.1 Generator Setup

In order to use one of the motors as a generator a load must be applied. A load bank could not be attached to the motors without substantial alteration and therefore for the motor to act in pseudo generation mode an opposing torque was applied as a load. The current required to produce this torque is then considered the generated current during testing.

4.4.2 Control

The motors can act upon a reference torque or reference speed but not both. Therefore a purely power rating could not be applied making the testing less realistic. Under real conditions the load applied to the generator side would have a corresponding effect on the actuation resulting in reduced torque or speed. However in this setup there is effectively infinite power as the motor will draw more power from the mains to achieve the required torque or speed. This limits the range of realistic control strategy response.

4.4.3 Measurements

All the operational measurements were recorded as current reference signals from the motor's drives and related to the corresponding speed and torque values. There will be an amount of noise in such systems which will have some effect on results accuracy. To account for this, the mean values over a run time was taken for most key operation results.

4.5 Initial back to back tests

In order to set the base operating characteristics of the motors, that can then be compared when a MG is introduced, a series of tests were done with the motors in back to back setup as shown in Figure 4.6.

The key operational measurements are the speed ripple obtained by taking measurements of 6 operating speeds (4 rpm, 8 rpm, 16 rpm, 32 rpm, 54 rpm, 128 rpm) across a range of load torques applied to the generator side ranging from 0, or no load, to 40 Nm and the required starting torque under no load.

4.5.1 Velocity Ripple

In order to account for deviations from the speed demand that may result from encoder measurement inaccuracies or fluctuations due to the drive's feedback control, the speed ripple ω_r was obtained using a equation (4.1) with ω_{peak}, ω_{min} & ω_{mean} being the peak measured speed, the minimum measured speed and the average measured speed. The results are shown in Figure 4.10.

$$\omega_r = \frac{\omega_{peak} - \omega_{min}}{\omega_{mean}} \tag{4.1}$$

The results show that there is substantial speed ripple at the lower speeds which decreases rapidly with increasing rotational speed. The speed ripple is largely unaffected by increasing the generator load.

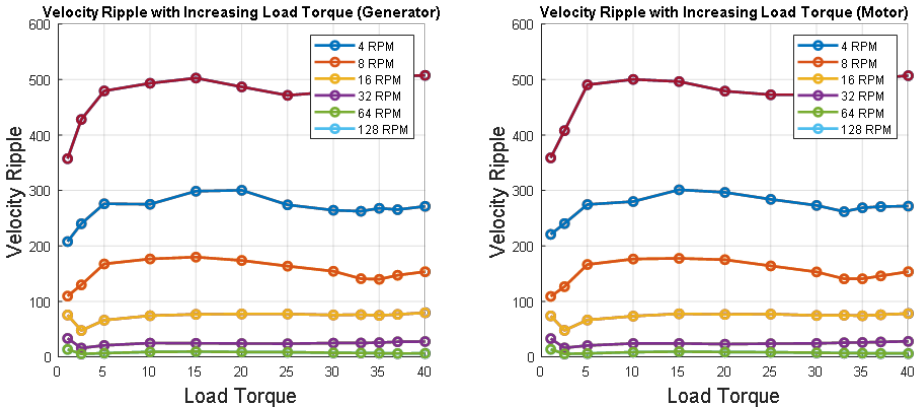

Figure 4.10: Velocity ripple on the motor and generator for back to back tests

4.5.2 Starting Torque and Torque-Speed Relation

In order to determine the starting torque of the machines the torque was measured with both the generator disabled and a torque demand of 0 for a ramping speed. The results show that there is no substantial effect on the torque as the speed is increased (Figure 4.11). The averaged motor torque was 0.5578 Nm and 0.4339 Nm for the generator disabled and for the 0 torque respectively. This difference is largely due to the substantial torque ripple and is clarified when measuring the no load torque for the previous tests which were found to be: 0.4956 Nm, 0.4699, 0.4504 Nm, 0.4593 Nm, 0.3630 Nm and 0.5234 Nm for 4 rpm, 8 rpm , 16 rpm, 32 rpm , 64 rpm and 128 rpm respectively. For purposes of comparison with the gear tests, the average of these values, 0.47 Nm, is considered the machine's starting torque.

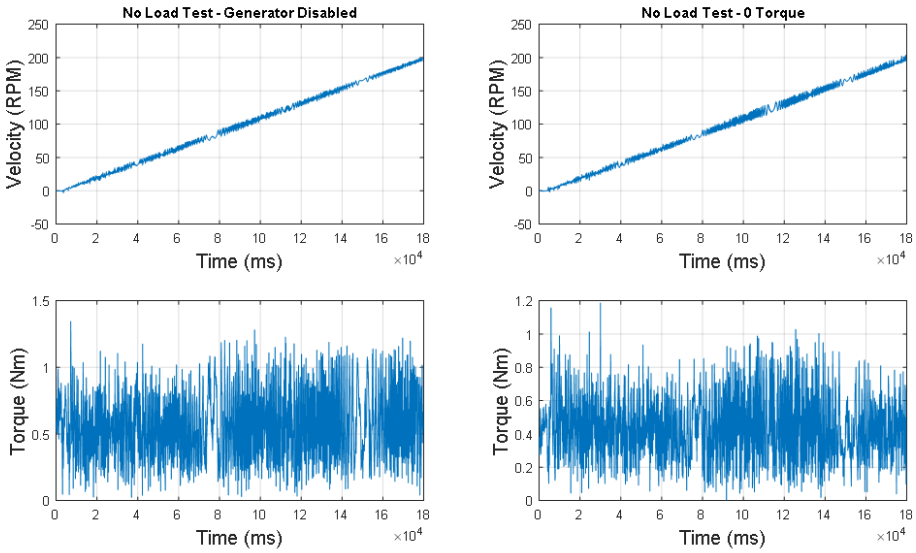

Figure 4.11: Toque and speed with ramp speed function

4.6 Geared System Tests

With the fundamental operation of the system without gears established, the fully geared system was then constructed as shown in Figure 4.7. The setup, control inputs and measured outputs are clarified in the block diagram below (Figure 4.12). The key test objectives were to investigate the effects on starting torque, the gearing effect, peak torques, torque ripple and efficiency.

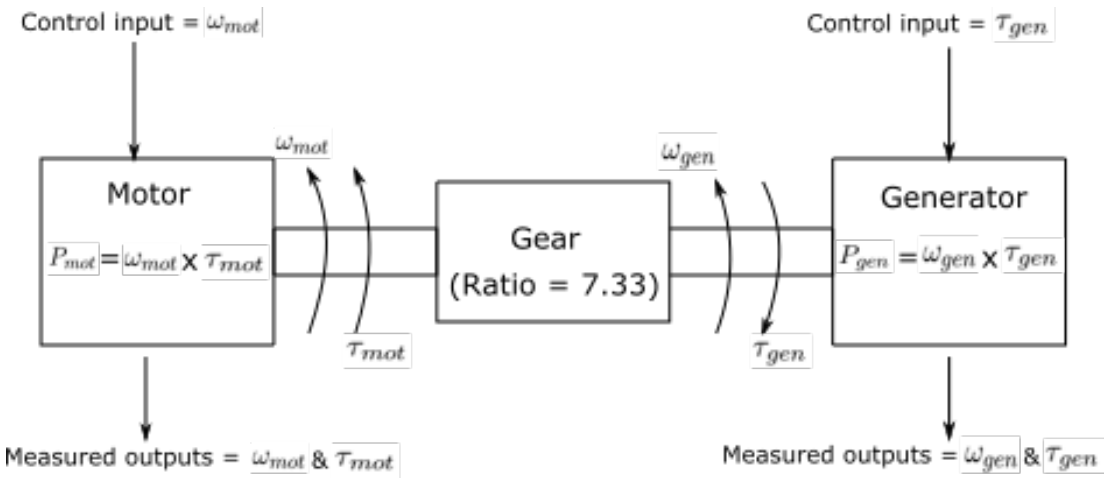

Figure 4.12: Block diagram of test setup.

Table 4.2: Geared test rig: no load speed results

Demand Speed	Gear Number	Average Motor Speed (rpm)	Average Generator Speed (rpm)	Ratio
4 rpm	1	3.656	26.725	7.31
8 rpm	1	7.646	56.104	7.33
16 rpm	1	15.655	114.818	7.33
4 rpm	2	3.69	26.693	7.233
8 rpm	2	7.662	56.113	7.322
16 rpm	2	15.675	114.8148	7.324

4.6.1 No Load Tests

No load tests were used to establish the basic operating characteristics of the now geared system. Both gears were tested with no load on the generator for three speeds, 4 rpm, 8 rpm and 16 rpm. The speed results are plotted in Figure 4.13 and shown in Table 4.2 along with the established ratio.

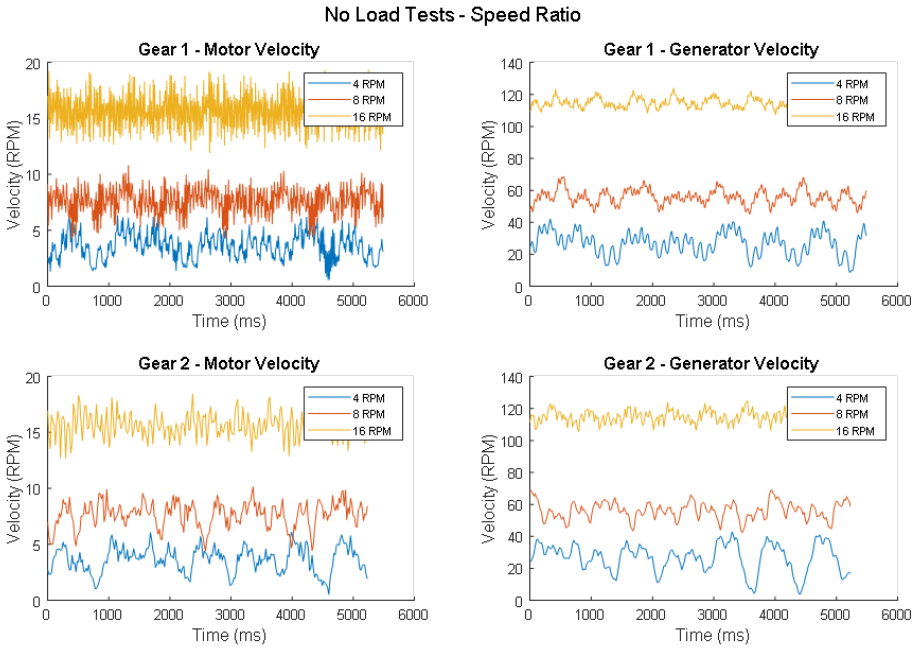

Figure 4.13: Motor and generator speed results, no load tests

With the the inclusion of a gear, an increase in torque is required for an increase in speed when the load torque remains constant. This is explained by extrapolating

from a basic power equation and is fully explained in Appendix B. The motor torques for the no load tests are shown in Figure 4.14. The average torques for each test were 4.77 Nm, 6.09 Nm and 10.049 Nm for Gear 1 and 5.33 Nm, 6.43 Nm and 10.65 Nm for Gear 2. As 4 rpm was found to be the slowest speed possible with consistent rotation the combined starting torque of the gear and generator is assumed to be 4.77 Nm and 5.33 Nm. Taking the generator's starting torque as 0.47, or 3.45 Nm when translated to the high torque side, the starting torques of the gears are then at least 1.32 Nm and 1.88 Nm for Gear 1 and Gear 2 respectively.

From a ramp speed test as shown in Figure 4.15 there is a clear proportional relationship between speed demand and required torque. This relationship is reciprocal and inputing a torque demand will result in a corresponding rotational speed. The plots show there is a very high degree of similarity in the operation of both gears.

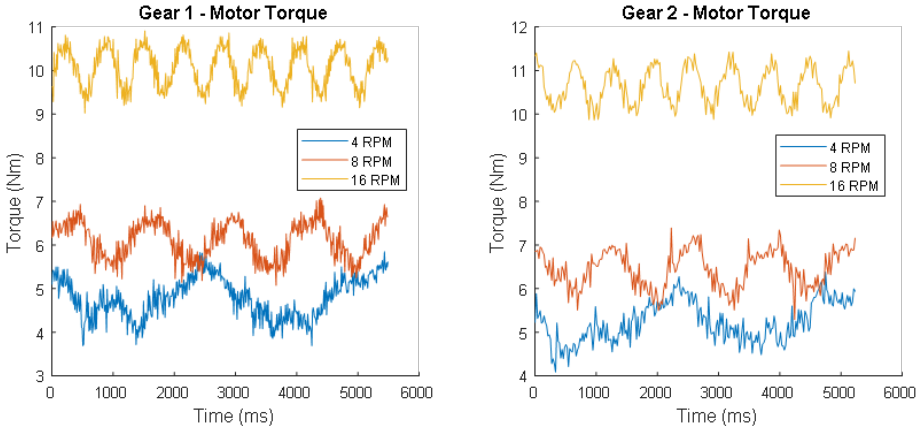

Figure 4.14: Motor and generator torque results of no load tests

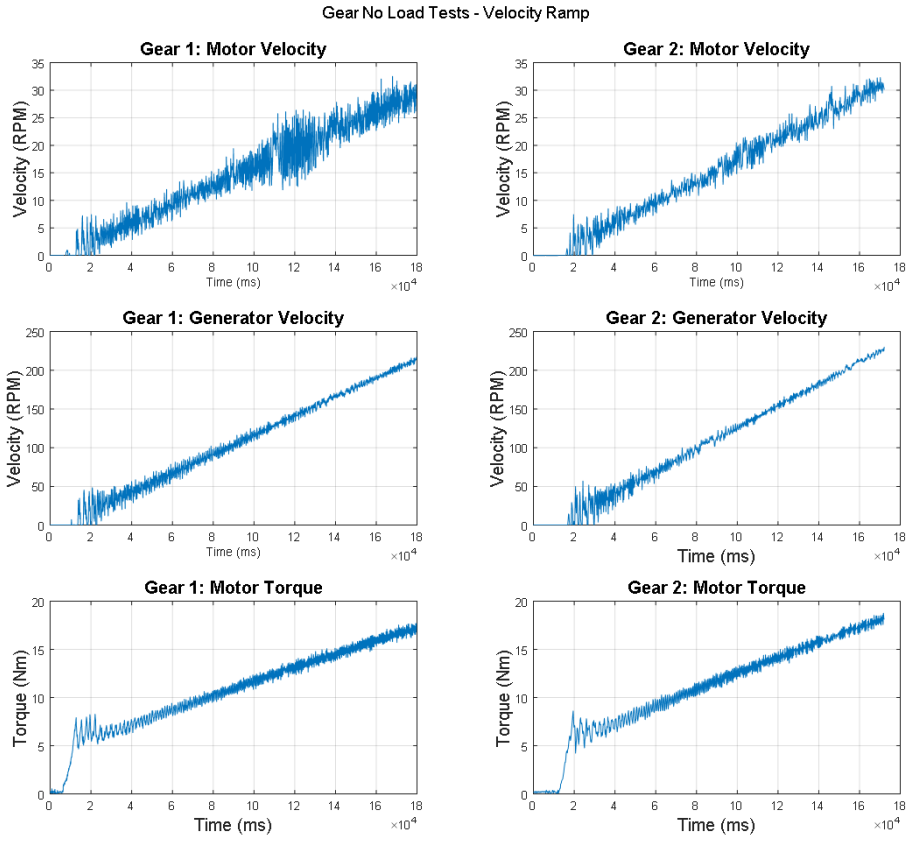

Figure 4.15: Motor and generator response to speed ramp function

4.6.2 Gear Load Tests

With the no load operation established a series of tests were completed to test the response of the geared system under increasing load torques. Gear 2 was used for these tests. The tests examined the system response for seven speeds (6 rpm, 8 rpm, 10 rpm, 12 rpm, 14 rpm, 16 rpm, 18 rpm) across a load torque ranging from 0.2 Nm to 3.4 Nm in increases of 0.2 Nm. The measured test results can be found in full in Appendix C.

4.6.2.1 Speed Ratio

From the no load tests the gear system established the correct ratio with a high degree of accuracy. This was further examined in the increasing load torque tests. The results calculated as in equation (4.2) are shown in Figure 4.16.

$$\omega_{ratio} = \frac{\omega_{gen}}{\omega_{mot}} \tag{4.2}$$

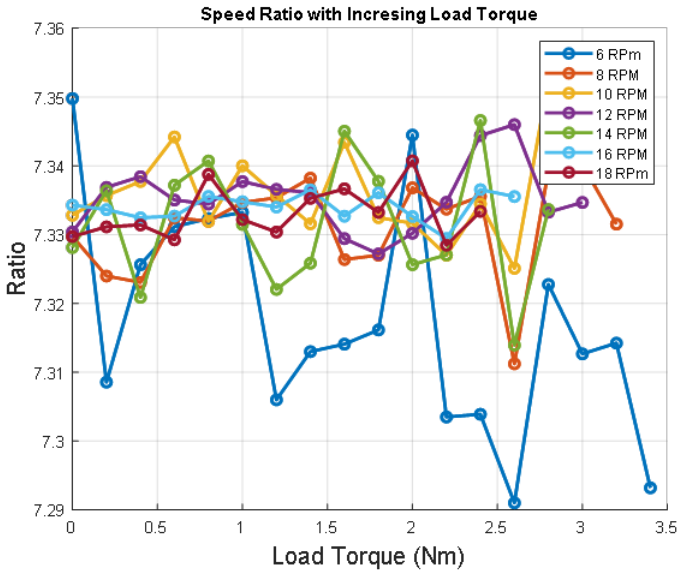

Figure 4.16: Speed ratio for increasing load torque

The ratios across all the tested speeds averages and with increasing load torque are very close to the designed ratio of 7.33. This was further clarified by taking the calculated speed ratio as percentage of the designed ratio ($\omega_{ratio_{dif(\%)}}$ from equation (4.3)) shown in Figure 4.17. The small variation in the ratio is most likely as a result of errors in the encoder and some speed variation resulting from the torque ripple meaning the speed is constantly adjusting.

$$\omega_{ratio_{dif(\%)}} = 100 \times \frac{(7.33 - \omega_{ratio})}{7.33} \tag{4.3}$$

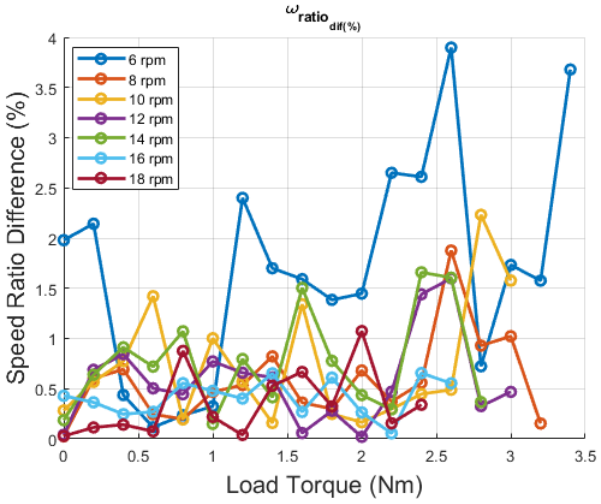

Figure 4.17: Speed ratio difference for increasing load torque (%)

4.6.2.2 Torque Ratio

Obtaining the torque ratio requires a more detailed analysis as increasing the speed results in an increased torque with a constant load torque. Using solely the measured average motor and generator torques (τ_{mot}, τ_{gen}) the torque ratio, τ_{ratio}, is calculated as in equation (4.4) with the results shown in Figure 4.18.

$$\tau_{ratio} = \frac{\tau_{mot}}{\tau_{gen}} \tag{4.4}$$

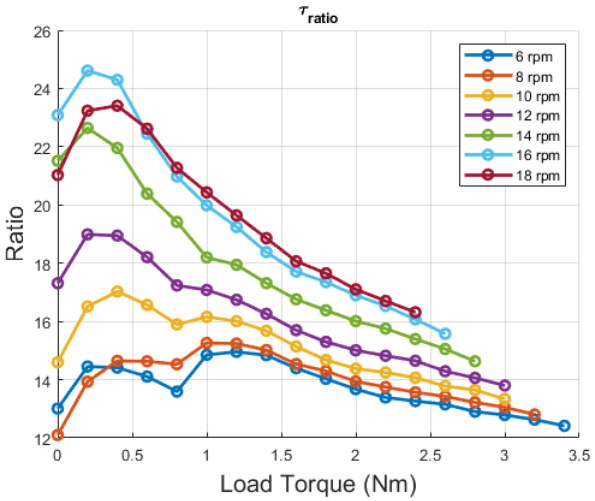

Figure 4.18: Ratio of measured motor and generator torque with increasing load

Calculating these torque ratio values as a percentage of the designed ratio, $\tau_{ratio_{dif(\%)}}$ (equation (4.5)), further clarifies the gear's operation. These values are shown in Figure 4.19.

$$\tau_{ratio_{dif(\%)}} = 100 \times \frac{\tau_{ratio} - 7.33}{7.33} \tag{4.5}$$

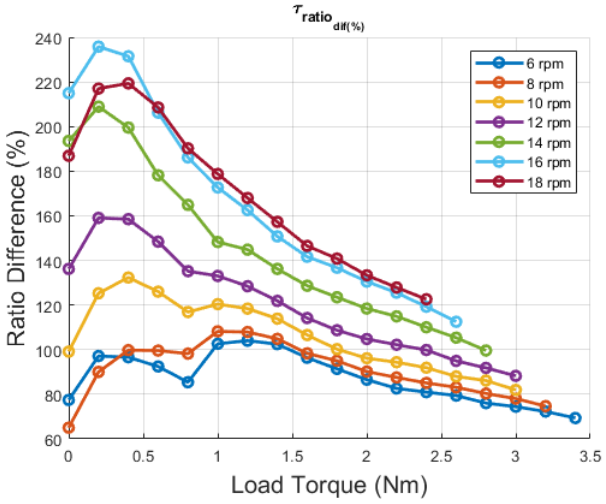

Figure 4.19: Difference between measured ratio and gear ratio (%)

It is additionally useful to compare the ratios of the increase in torque measured by the motor and generator as the load torque is increased. The increases in torque between each test, as calculated in equation (4.6), is shown in Figure 4.20. From this, it is shown that a load of at least 1 Nm is required before the system displays a clear trend. The dashed line in both the generator and motor plots shows the expected increase with the torque demand which shows that there is a substantial drop from the expected torque increase and the average measured torque. This is most likely as a result of the high torque ripple meaning the averaged torque for the test period is lower than the demand.

$$\Delta\tau = \tau_{i+1} - \tau_i \tag{4.6}$$

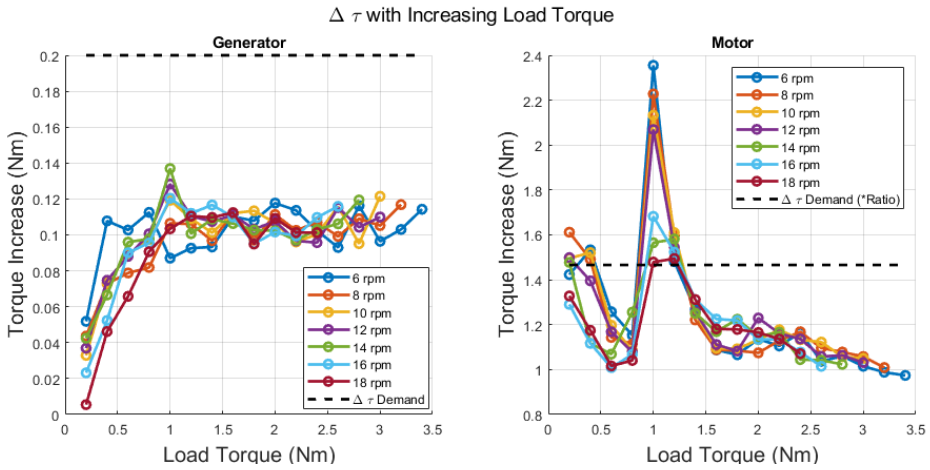

Figure 4.20: Torque increase with increasing load torque

Plotting the ratios of the torque increases ($\Delta\tau_{ratio}$ from equation (4.7)) then gives a more accurate account of the torque gearing effect. As shown in Figure 4.21 the ratio is now approaching the designed ratio with the closest ratio, 8.5, occurring at the peak torque for the 6 rpm series. In a similar fashion to $\omega_{ratio_{dif(\%)}}$ and $\Delta\tau$ the difference in gear ratio for torque increases was calculated from equation (4.8) with the results shown in Figure 4.22.

$$\Delta\tau_{ratio} = \frac{\Delta\tau_{mot}}{\Delta\tau_{gen}} \tag{4.7}$$

$$\Delta\tau_{ratio_{dif(\%)}} = 100 \times \frac{\Delta\tau_{ratio} - 7.33}{7.33} \tag{4.8}$$

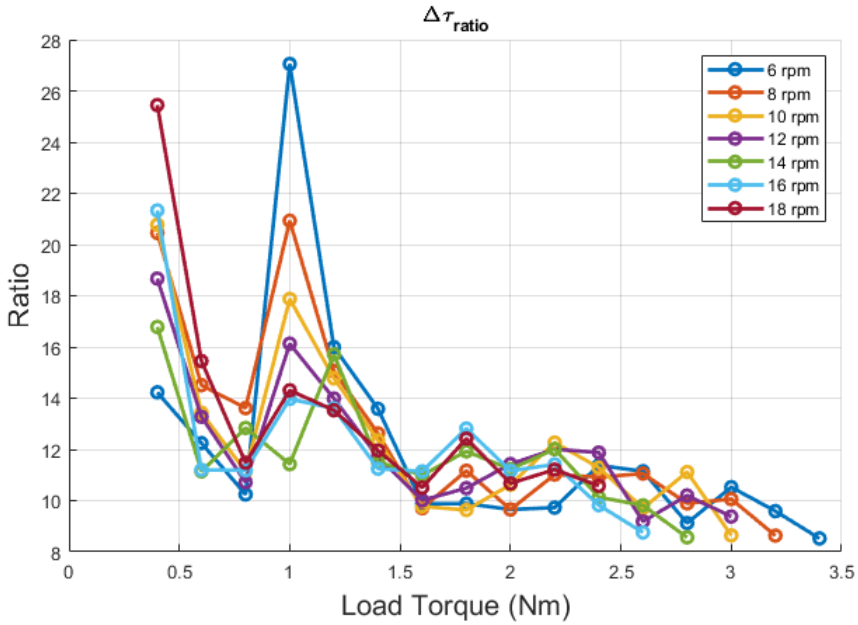

Figure 4.21: Ratio of torque increases

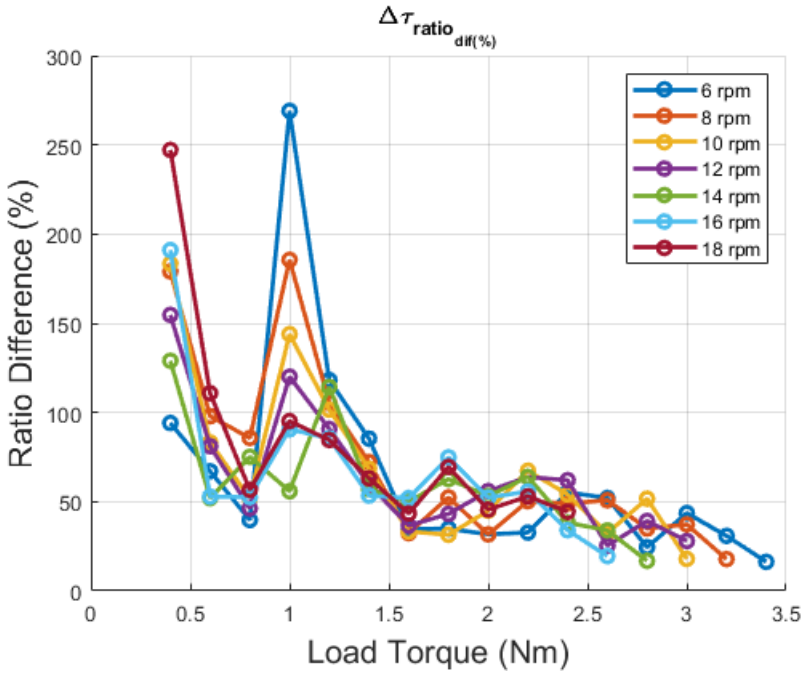

Figure 4.22: Difference in ratio of torque increases

4.6.3 Efficiency

The efficiency for the averaged power values is calculated as in equation (4.9) with the results shown in Figure 4.23. The highest efficiency was for the 6 rpm speed. From the back to back tests the system efficiency without the gear was found to be approximately 90% for this load torque. Taking this into consideration the gear's efficiency is taken as 69%.

$$\eta = 100 * \frac{P_{gen}}{P_{mot}} = \frac{\omega_{gen}\tau_{gen}}{\omega_{mot}\tau_{mot}} \tag{4.9}$$

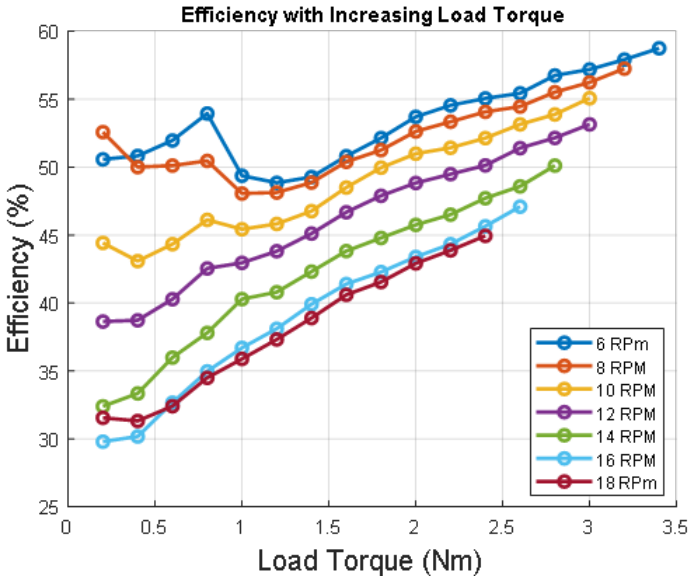

Figure 4.23: Full system efficiency of average motor power and average generator power

As it has been established that the gear is operating correctly in terms of speed ratio, the drop in efficiency is a result of the drop in torque across the gear. This can be calculated from the difference between the measured motor torque and the measured generator torque multiplied by the gear ratio. This is calculated as in equation (4.10) with the results shown in Figure 4.24.

$$\tau_{dif} = \tau_{mot} - (\tau_{gen} \times 7.33) \tag{4.10}$$

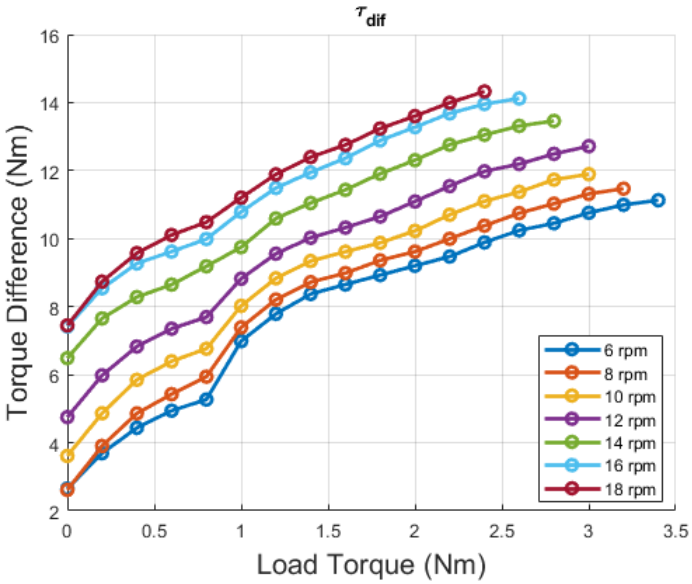

Figure 4.24: Diffrence between measure motor torque and ratioed generator torque

Calculating the difference as a percentage of the motor torque ($\tau_{dif(\%)}$, equation (4.11)) shows clearly that the torque lost in transmission is the main determinate in the reduced efficiency (Figure 4.25).

$$\tau_{dif(\%)} = 100 \times \frac{\tau_{dif}}{\tau_{mot}} \tag{4.11}$$

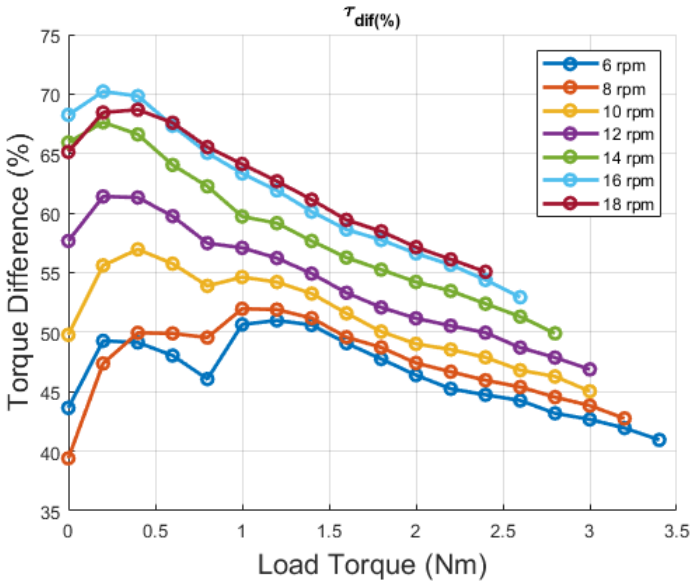

Figure 4.25: Difference between measure motor torque and ratioed generator torque

As the starting torque values dominate, it was useful to analyse the system's torque response as the load torque was increased (i.e the required increase in motor torque for an increase in generator load torque). This value was calculated as in equation (4.12) with results shown in Figure 4.26.

$$\Delta\tau_{dif} = \Delta\tau_{mot} - (\Delta\tau_{gen} \times 7.33) \tag{4.12}$$

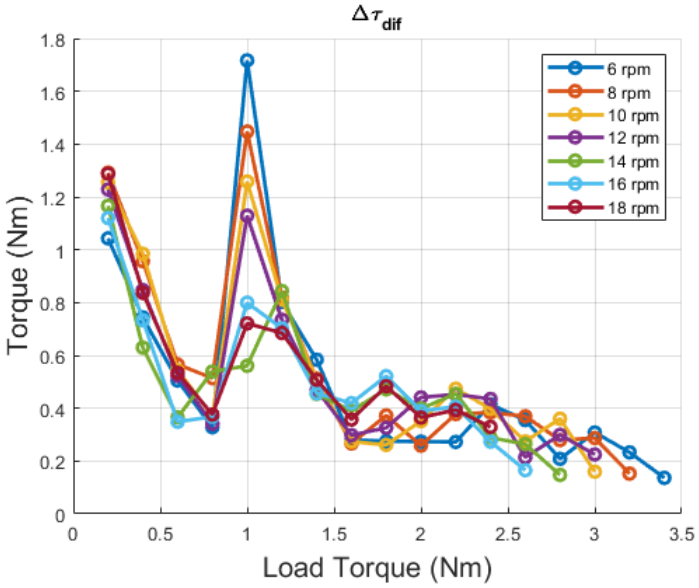

Figure 4.26: Difference between measured torque and the ratioed generator torque

Taking $\Delta\tau_{dif}$ as a percentage of the motor torque further clarifies this value as an indicator of the gear's operation. This was calculated as in equation (4.13) with results shown in Figure 4.27.

$$\Delta\tau_{dif(\%)} = \frac{\Delta\tau_{dif}}{\Delta\tau_{mot}} \tag{4.13}$$

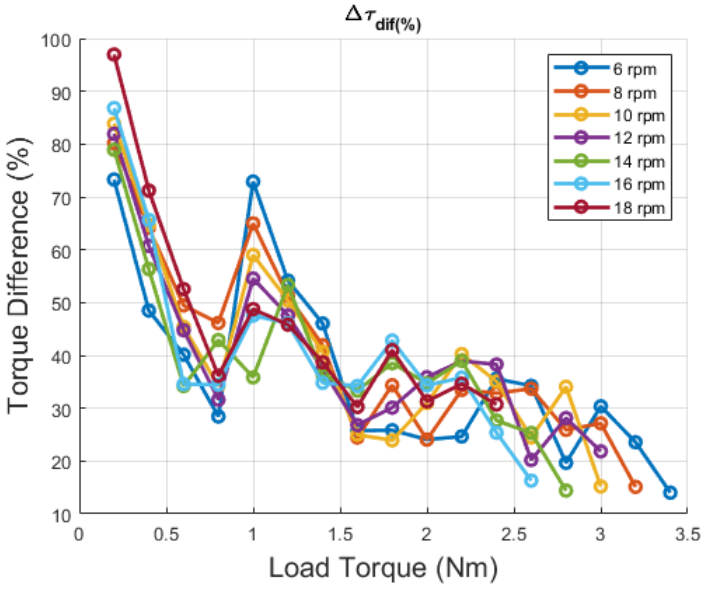

Figure 4.27: Percentage difference between motor torque and ratioed generator torque

From $\Delta\tau_{dif}$ it can be seen that the torque transference is reasonably high when approaching peak torque and calculating the power difference then shows the power

drop across the gear as the load is increased. This value, $\Delta P_{dif(\%)}$, was calculated from equations (4.14) and (4.15). The results are shown in Figure 4.28.

$$\Delta P = P_{i+1} - P_i \tag{4.14}$$

$$\Delta P_{dif(\%)} = 100 \times (1 - \frac{\Delta P_{gen}}{\Delta P_{mot}}) \tag{4.15}$$

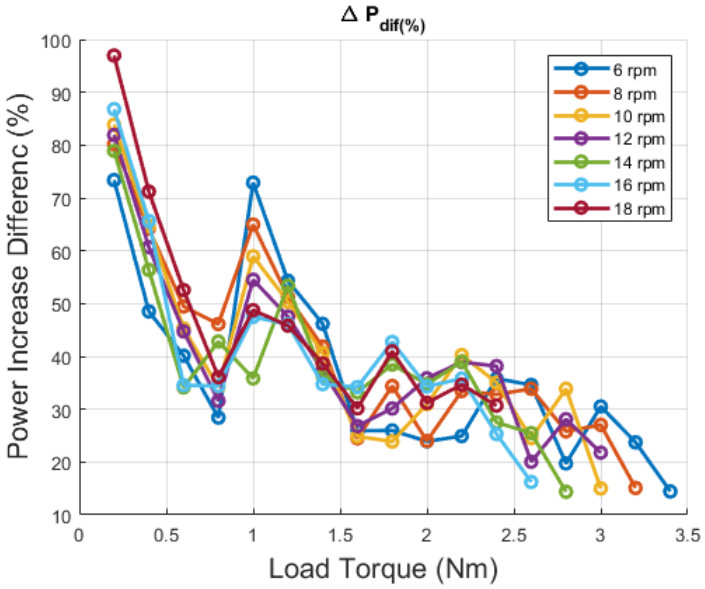

Figure 4.28: Power increase difference with increasing load torque

When looking at $\Delta P_{dif(\%)}$ when approaching the peak torque, up to 85% of the power increase is transmitted. Given that the efficiency of the system without a gear is approximately 90% when below 5 Nm, the power transfer could be up to 95%. Reducing the starting torque would then have a substantial effect on the total system efficiency. The results additionally correlate with previous studies in that higher efficiencies are observed at lower speeds and when operating close to the peak torque as discussed in Chapter 2.

4.6.4 Torque Ripple

Measuring the torque ripple for the series allows for further assessment of the impact on the system with the addition of the gear (equation (4.16)). This also establishes a context for results analysis, particularly how it affects the efficiency and peak torque. The results are shown in Figure 4.29.

$$\tau_r = 100 \times \frac{\tau_{peak} - \tau_{min}}{\tau_{mean}} \tag{4.16}$$

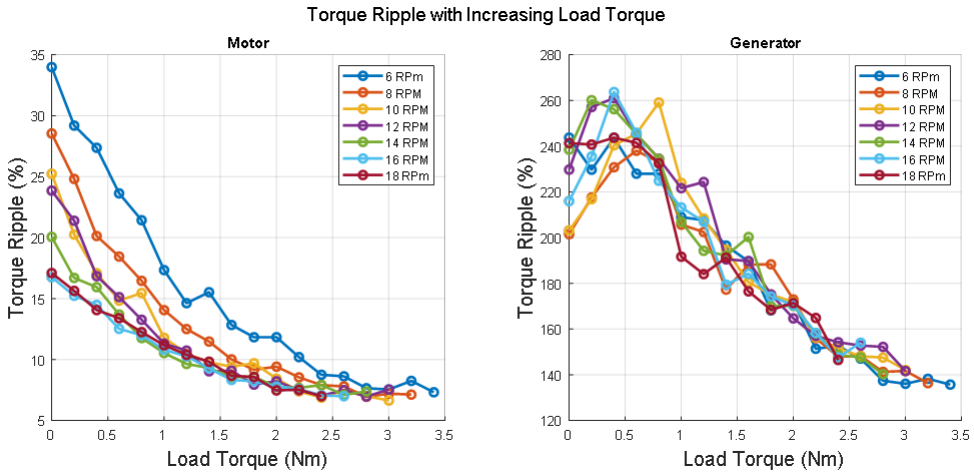

Figure 4.29: Torque ripple with increasing load

From the results the torque ripple is highly similar to the gearless setup at higher loads but has increased at lower torques on the generator side, increasing from 180% to 200-220% at 1 Nm load.

4.6.5 Peak Torques

A key design characteristic and an important validation step for the design tools was the peak torques on the low speed rotors that the gears could achieve before slipping.

Both gears were tested where, for a constant speed, the generator load is gradually raised until the gears slipped. At the slipping point the motors undergo rapid acceleration and exceed the peak allowed speed causing the drive to disable the motor. The results are shown in Figure 4.30.

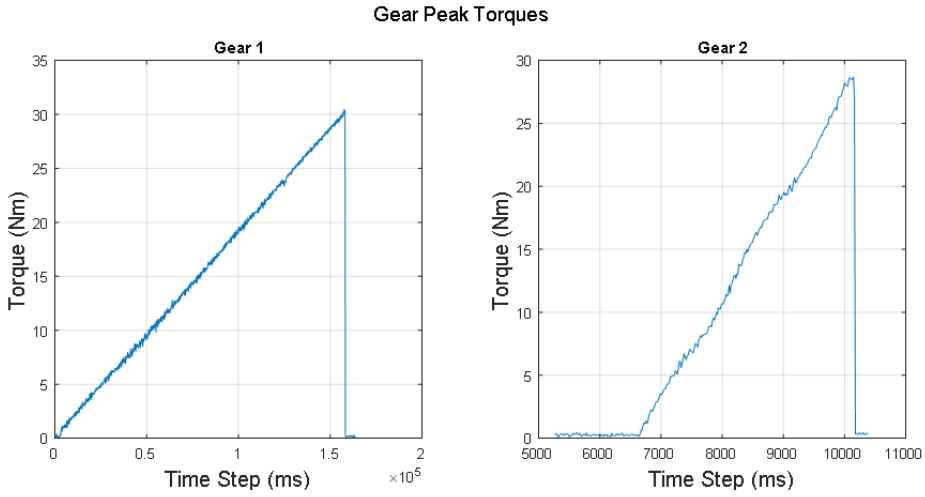

Figure 4.30: Peak torques on low speed rotors

The peak torques were found to be 30 Nm and 28.5 Nm for Gear 1 and Gear 2 respectively. When compared with the peak torques as modeled in 3D FEM , 34.4Nm, this resulted in a difference of 13% and 17%.

Static Peak Torque Test

In order to validate the measured peak torque results a static test was performed on Gear 1 where one side of the gear was locked and a force was applied to a lever on the opposing side until a slip occurred. The torque could then be calculated. A mechanical spring balance with a 0.02 kg gradient and a digital scale with 0.01 kg were used to assess the applied force in kg. When compared to a known weight the mechanical spring balance had an offset of -0.400kg. There was some variation as the force was increased so the test was repeated a number of times with the average value taken. The peak torque on the low speed side was found to be 32.67 Nm (from a force of 13.6 kg @ 0.245 m) and 4.8 (from a force of 2 kg @ 0.245 m) on the high speed side. When compared to the modeled peak torque this equates to a difference of just over 5%.

4.7 Slipping effect

The slipping effect is a key point of interest when determining the viability of MGs in wave energy devices as passive power limiting devices.

The process involved a steady build up of the torque on the motor side with a constant velocity held on the generator side. Once exceeded the gear slips and without

a fixed velocity referenced the motor over-speeds and is disabled while the generator continues rotating. The torque is then reduced to operable levels and the motor re-enabled. Two tests were completed with Gear 2 showing two slip events. The torques acting on both the motor and generator are shown in Figure 4.31 with the measured speed during each event shown in Figure 4.32 and the same results over smaller time step in Figure 4.33.

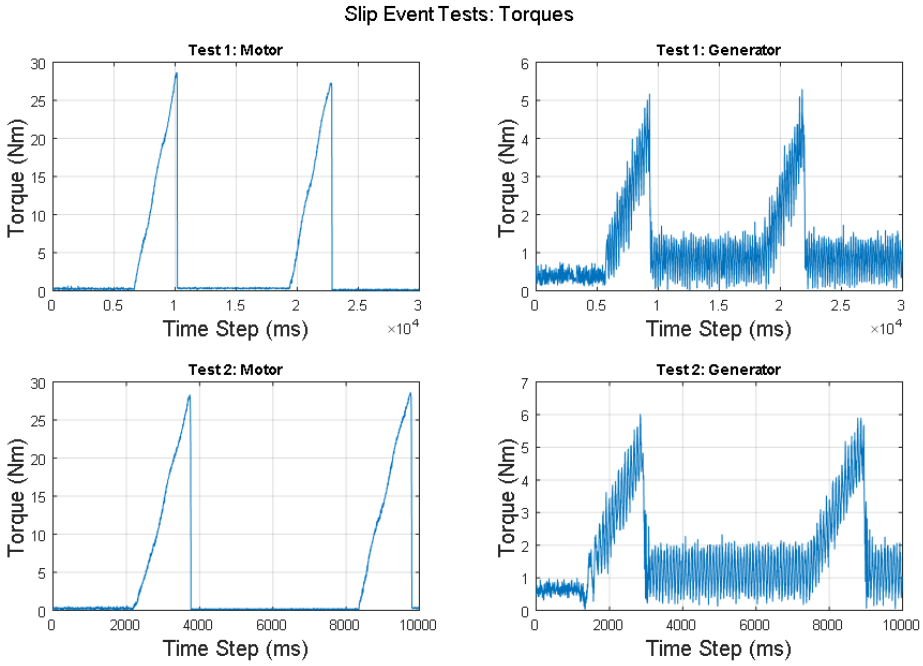

Figure 4.31: Torque response during slip event

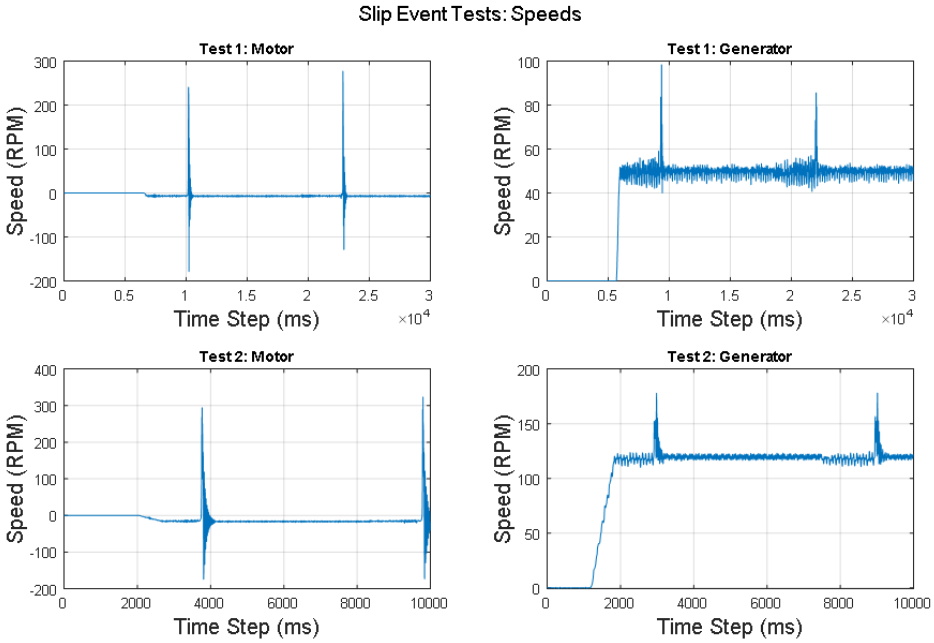

Figure 4.32: Measured speed during slip event

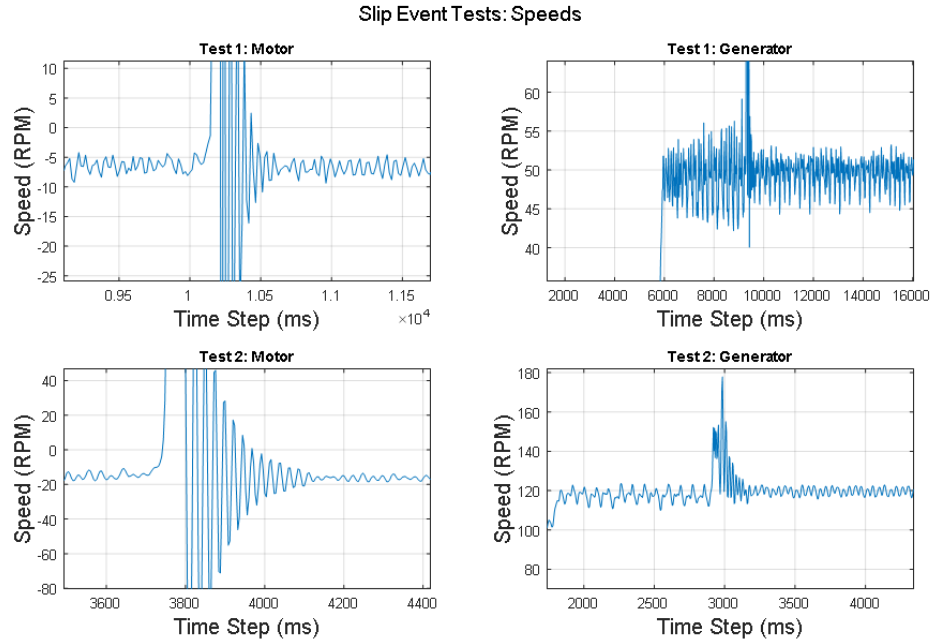

Figure 4.33: Measured speed during slip event, smaller time step

The results clearly show the slipping ability when the peak torque is exceeded with the gear then reengaging without any noticeable effect on performance. Looking at Figure 4.33 the immediate response of the system in a slip event is observable. Following the momentary high speed of the slip the system oscillates until stable. The

results show rapid oscillations before settling of a similar nature to that observed from the dynamic model. While a comparison with the dynamic model would be useful, it was not possible to implement at this stage due to the unknown motor controller values and the automatic over-speed disable function.

When the torques acting on both rotors are observed the high torque ripple could be a cause of the lower than expected low speed peak torque. In the second test a torque of 6 Nm is measured before the slip event. This would equate to a torque of 44 Nm on the high torque side and exceed the peak torque. It is likely that the high torque ripple causes the gear to slip before the absolute peak torque is achieved on the high torque side. This is an important factor that should be taken into account during the design stage.

4.7.1 Oscillating Waveform Tests

In order to test the gear under conditions more in line with WEC operation a sinusoidal torque demand was applied to the motor. The torque was defined by peak amplitude and frequency, with the motor oscillating.

First the system was tested without any control to determine the system's response. Two amplitudes were tested (15 Nm and 20 Nm) at a frequency of 0.1 rads^{-1}. The results are shown in Figure 4.34. From the results it clearly demonstrates that the system will only start moving when the inertia is overcome at approximately 5 Nm. The system will then increase in speed according to the applied torque.

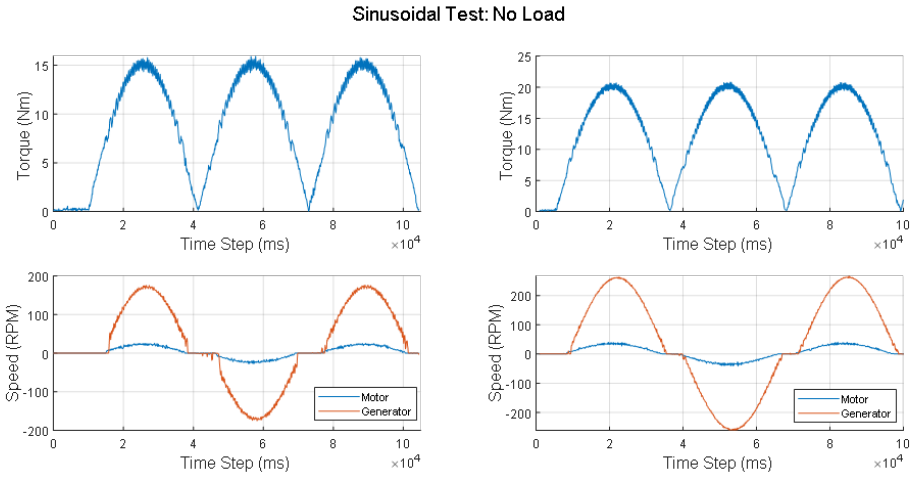

Figure 4.34: Sinusoidal torque test, no control

With the fundamental operation established a control strategy can then be selected.

The practicality of this is limited as there is no real time communication between the motors that could have established an adaptive control. Since actuation is predetermined, an idealised control method can be implemented as an example. In this case it is a latching and pseudo-reactive speed control strategy that sees the generator held until the torque exceeds 5 Nm. The generator's speed is then set to match the frequency of the actuation torque. The results of this is shown in Figure 4.35.

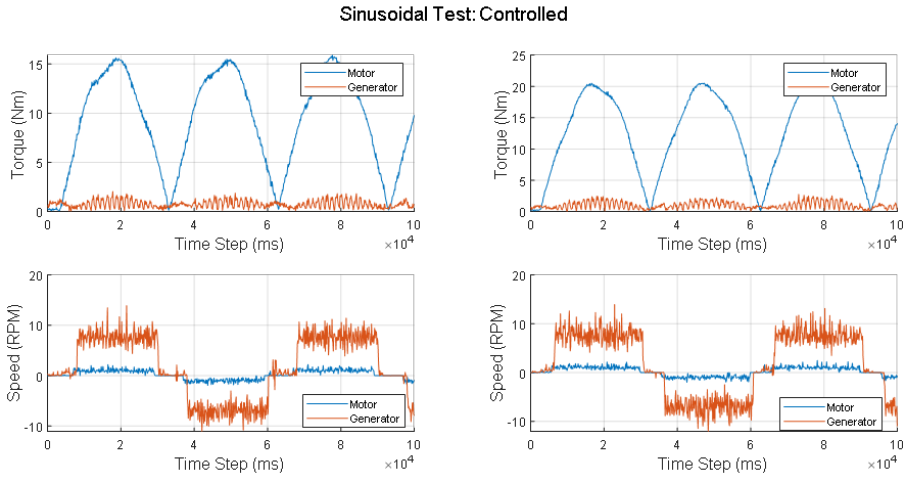

Figure 4.35: Sinusoidal torque test, reactive control

The results highlight a key advantage of a geared system. The reactive torque required to maintain speed is substantially lower meaning in practice a much smaller machine could be employed. It also highlights the challenges involved in practical system control. Even under these idealised conditions the system response is highly variable when subjected to constantly varying values and realistic sensing limitations (encoder accuracy, measurement signal noise & torque ripple).

4.8 Results Discussion

The results confirm the successful design process of a MG and the resulting speed ratio conforms closely with the design ratio. While the high torque ripple makes the accuracy of peak torque and efficiency difficult to accurately assess the values are somewhat in line with the FEM results. Following a static torque test the difference was found to be approximately 5%. Unfortunately the motor setup means that full control analysis and efficiency operating over a range of typical wave states was not possible though an idealised setup demonstrated the potential operation. The slipping effect and the

inherent overload protection is observed and the gears function under oscillating actuation demonstrated. There was a substantial drop in the power across the gear resulting in a measured whole system peak efficiency of 59%. Taking the motor efficiency at this torque to be 90% then the gear's efficiency can be taken as $\approx$ 70% for the lowest test speed at peak torque. From the power transfer analysis it was shown that there is decent power transfer when the gear is in motion and the efficiency was largely affected by the high starting torque. As mentioned in Chapter 2 the use of aluminum support rings for the FMPs was a poor design choice and, while preventing flux leakage reducing the peak torque, effectively established a squirrel cage which induced a current and a resistive torque during motion. While the gear test speeds were low, the use of solid iron elements for the prototype's FMPS and backiron will result in non-trivial hysteresis and eddy current losses further reducing the efficiency. Methods of addressing this are discussed in Chapter 7.

Chapter 5

Genetic Algorithm Design Method

Previous methods used in designing MGs have been to establish a look up table for the peak torque through an iterative process with the two scaling parameters, the inner airgap radius and the axial length of the gear [115]. The remaining design parameters such as magnetic pole height, FMP rotor axial width and pole number are fixed. While effective, this method may miss optimal designs due to the interdependent nature of the parameters. A process by which the initial design procedure can be automated while accounting for these different parameters would then be a useful tool. A method of design proposed and investigated in this work is the use of the genetic algorithm method.

A Genetic Algorithm (GA) is a global search method based on natural biological evolution that is now commonly applied to engineering problems. It works by choosing a fixed set of parameters which define a design. These parameters are then operated on to choose the best values according to some scoring mechanism which takes a set of these values as input. Improvement is achieved by having a population of these parameter sets, where each "individual" is one parameter set. GAs operate on this population of potential solutions by applying the principle of survival of the fittest to produce increasingly better approximations to a solution. At each generation, a new set of designs is created by the process of selecting individuals according to their level of fitness (i.e. their assigned score) and breeding them together using operators mimicking natural processes. Other processes such as mutation are also typically used in a similar way in

which they would occur in nature. This process leads to the evolution of populations of individuals that are better suited to their environment than the individuals that they were created from, just as in natural adaptation. It is an effective method of optimising systems with complex interdependent parameters.

A GA was implemented with the Genetic Algorithm Toolbox developed by the University of Sheffield [118], and applied to a specific case study. The GA was implemented in MATLAB which made it compatible with the xfemm design tool developed for MG analysis.

This work was presented at the 2017 IET Renewable Power Generation Conference in Wuhan and subsequently published in the IET Journal of Engineering [119].

5.1 Problem Introduction

The GA method used in this case attempts to find an optimal design that has the least amount of high cost PM material while achieving the desired torque rating on the low speed - high torque rotor to a chosen tolerance. It is also expected that using multiple parameter optimisination may also help to develop an understanding of design trends for future applications. The case study in this work looks at using the GA Toolbox to design a gear for a high torque application. The initial design objectives were for a solution similar to that discussed in Chapter 3 with a peak high torque rating of 3.1 MNm. However, since each solution must be solved in FEA each solution time was substantial and would require a reduction in either the number of generations or a reduction of individuals within each generation. It was decided to reduce the target peak torque to 250 kNm which allowed for a reduction in the solution time while remaining a large system of approximately 1:3 scale with a lower gear ratio of between 7:1 and 8:1. The flexibility in the gear ratio allows for different pole number configurations which further test the capabilities of the optimising model. For this design study, the parameters and the allowed ranges are shown in Table 5.1 with the pole configurations shown in Table 5.2.

The limits on the primary system volume parameters, the airgap width and axial length are for practical reasons as when designing a MG system for application to a specific power take off system there will be limitations on the space available for the gear. The backiron thickness on the inner and outer rotor was set to 0.06m.

Parameter	Lower limit	Upper Limit	Unit
Inner rotor magnetic pole height	0.005	0.04	m
Outer rotor magnetic pole height	0.005	0.04	m
FMP rotor radial width	0.01	0.08	m
Gear Axial Length	1.5	3	m
Inner Airgap Radius	0.2	0.4	m

Table 5.1: GA design parameters and ranges

Case No.	Inner Rotor Pole No.	Outer Rotor Pole No.	Ratio
Case 1	16	124	7.75
Case 2	8	60	7.5
Case 3	16	116	7.25

Table 5.2: Magnetic pole configurations and resulting ratios

Fitness Scoring

In order to assign each potential design with a fitness score the resulting MG design from each of the individual parameter group is solved using xfemm. Parameter specific designs are passed directly from the GA Toolbox for evaluation and the values then returned for post processing. The individual designs were then tested for the maximum torque that occurs on the outer and inner rotors. To achieve the desired torque, a penalty is added to the score for a design. This gives the GA the information required to achieve the target torque range. In the event that the torque is outside the target torque range a heavy penalty is applied to the fitness score of that individual and thus makes the design extremely unlikely to be continued into further generations. A graphical representation of the design process is shown in Figure 5.1 with the penalty calculation formula explained in equation (5.1).

$$pen = \begin{cases} 10S_b(\frac{\tau_{cal}}{\tau_{tar}}) + S_b(10\frac{\tau_{cal}}{\tau_{tar}})^2, & \text{if } \tau_{cal} > 262.5kNm \\ 10S_b(\frac{\tau_{cal}}{\tau_{tar}}) + S_b(10\frac{\tau_{cal}}{\tau_{tar}})^2, & \text{if } \tau_{cal} < 237.5kNm \\ 0, & \text{otherwise} \end{cases} \tag{5.1}$$

pen is the penalty value to be added to the fitness score thus reducing the design's fitness, S_b is the base fitness score calculated before the penalty is applied, τ_{cal} is the torque calculated from the design currently being tested and τ_{tar} is the target torque. The equation establishes a highly exponential penalty function the further the resulting torque is from the target torque range.

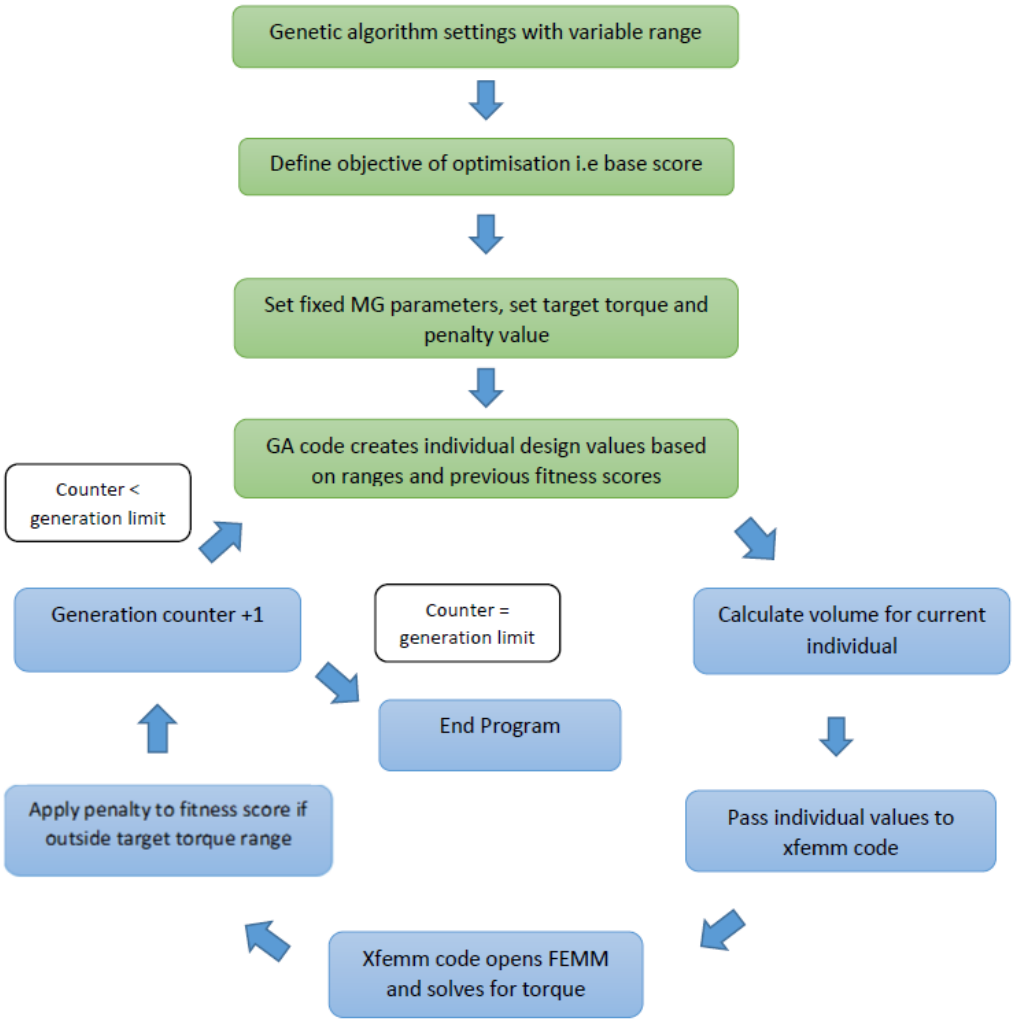

Figure 5.1: GA flow order

5.2 Results

Figures 5.2-5.7 show key results (total magnetic material volume, total iron volume, total system volume, torque on outer rotor, torque on inner rotor and ratio between inner and outer rotor) of running the optimising program for 50 generations. In each case the figures show the calculated quantity for the best individual in each generation. The final optimised design had the parameter values shown in Table 5.3.

Parameter	Value	Unit
Inner rotor magnetic pole height	16.2	mm
Outer rotor magnetic pole height	7.2	mm
FMP rotor radial width	27.56	mm
Gear Axial Length	2811	mm
Center Radius	387.4	mm

Table 5.3: GA design results

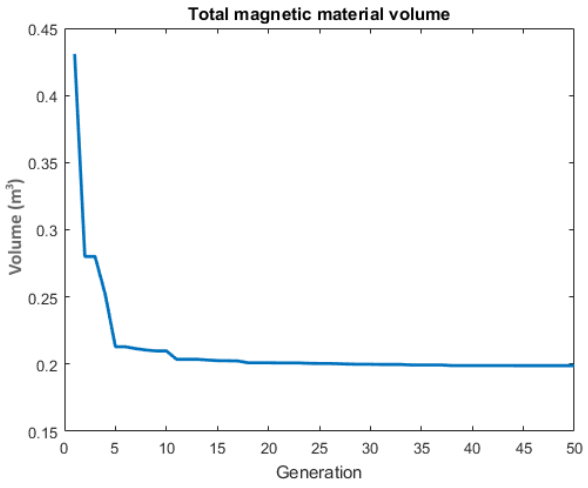

Figure 5.2: Total permanent magnet material volume

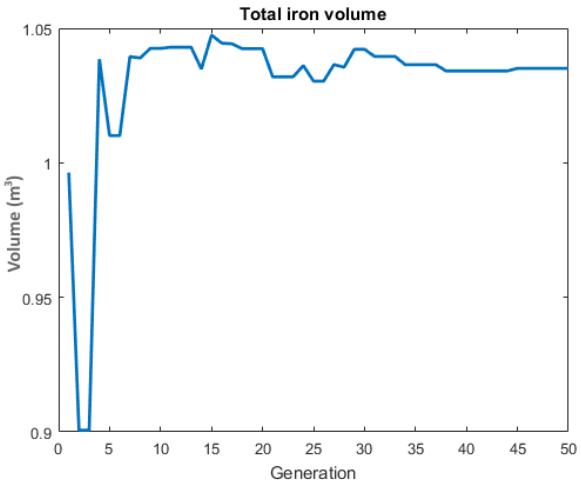

Figure 5.3: Total iron material volume

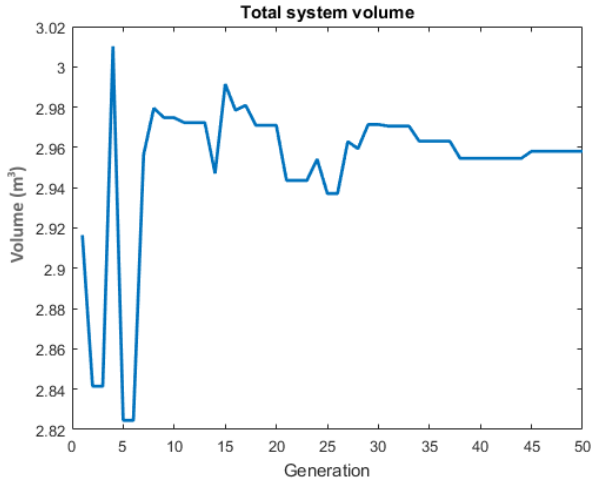

Figure 5.4: Total system volume

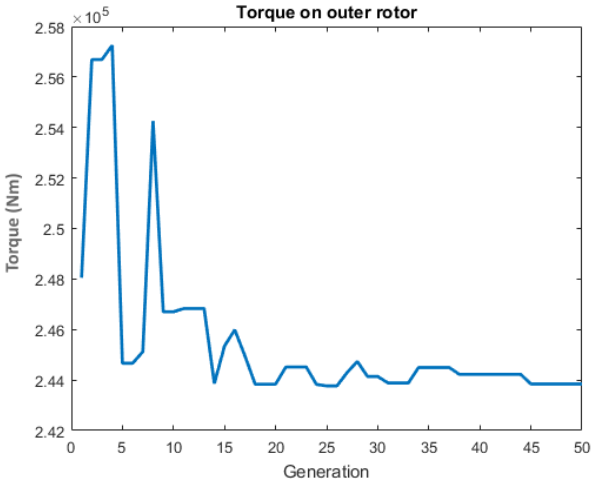

Figure 5.5: Torque on outer rotor

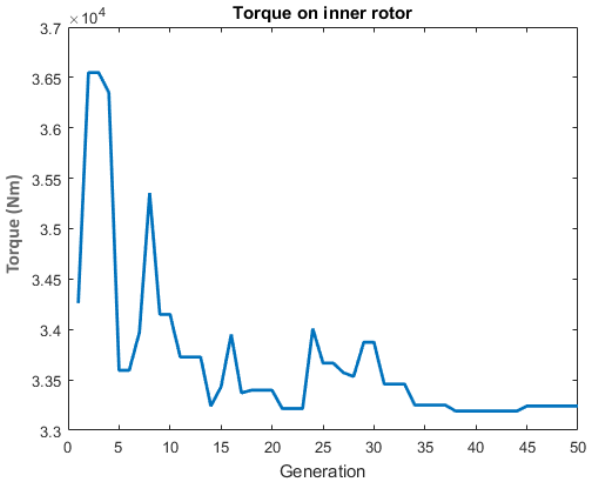

Figure 5.6: Torque on inner rotor

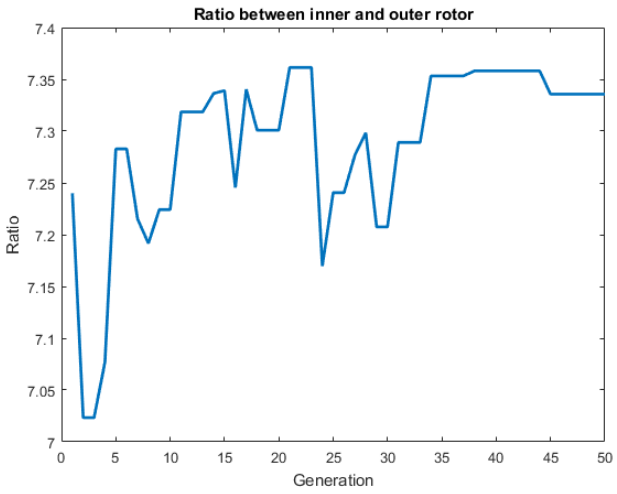

Figure 5.7: Ratio between inner & outer rotor

5.3 Results Discussion

Figure 5.2 shows that the program successfully optimised for the primary target of reducing the high cost permanent magnetic material. From the first proposed solution to the 50th generation the magnetic material volume is reduced from 0.4309 m^3 to 0.1989 m^3, a reduction of over 53%. Additionally there is no change from the 45th generation to the 50th so it is assumed that for this generation limit the optimal solution has been achieved. It is proposed for future work to extend the generation limit in order to verify this assumption. The primary design constraint of achieving a torque value of 250 +/-5% kNm is also successful. The final design had a torque value on the lower end of the allowed tolerance range, 243.8 kNm, which is to be expected as the lower torque would inherently require less magnetic material. Despite the large reduction in magnetic material there is not a significant change in either the required iron volume and the complete system's space volume. Therefore there will be an overall reduction in the cost of the system from the best individual in the first generation and the best individual in the last generation. From Figure 5.6 the torque on the inner rotor follows a suitable trend as the torque on the outer rotor. The ratio established undergoes some variation (Figure 5.7) this is most likely due to fact that the torque calculated is only at the max torque point for both rotors and small variation in the rotor's max value can have a significant effect on the calculated ratio. The final calculated ratio is 7.34:1 resulting from the 116:16 pole number setup. This achieves the final design objective of a ratio between 7.25:1 and 7.75:1.

5.4 Conclusion

The genetic algorithm method is a powerful tool in designing a multi-parameter, inter-dependent system. The case study in this chapter successfully achieved the required torque and ratio values while reducing the magnetic material. Proposed further work is to apply the optimisation procedure to a wider array of parameters and multiple objectives. This would allow for an examination of possible trends that would aid in the development of future MG design processes. While effective, an issue with using the genetic algorithm method is that increasing the parameters to be considered can greatly increase the solving time, as will increasing the number of generations required for an optimal design.

Chapter 6

Design and Analysis of a Linear Magnetic Gear for a Wave Energy Converter

6.1 Introduction

Linear systems, as discussed in Chapter 1, have particular potential in a heave type WEC allowing for direct energy conversion, potentially reducing complexity and increasing reliability.

Previous work in linear machines has shown that amplitude amplification can be advantageous for power take-off in wave energy, where the increased translator mass required to accommodate the increased oscillation amplitude can be offset by reducing the axial length of the machine due to the reduced force requirement [120].

Introducing amplitude amplification in the form of a linear gear is therefore a method of reducing the burden on the electrical machine albeit at the expense of a longer stroke length. This concept can only be considered advantageous if the combined mass and cost of the gearbox and smaller electrical machine is significantly below that of a comparable direct drive machine.

This chapter looks at a case study where a direct drive linear generator is scaled to deliver rated power for a WEC PTO. A LMG is then designed for integration with the generator. This requires the linear machine to deliver a lower force at increased frequency, hence requiring a smaller active area (smaller stator) but over a larger displacement (longer translator). Mass and efficiency savings, calculated from 3D model

FEA, are presented to assess the merit of using LMGs in a WEC application.

This work was done in collaboration with Newcastle University as partners in the e-Drive project [114]. The work was presented at the IET Renewable Power Generation 2018 conference and has been accepted for publication in the IET Journal of Engineering.

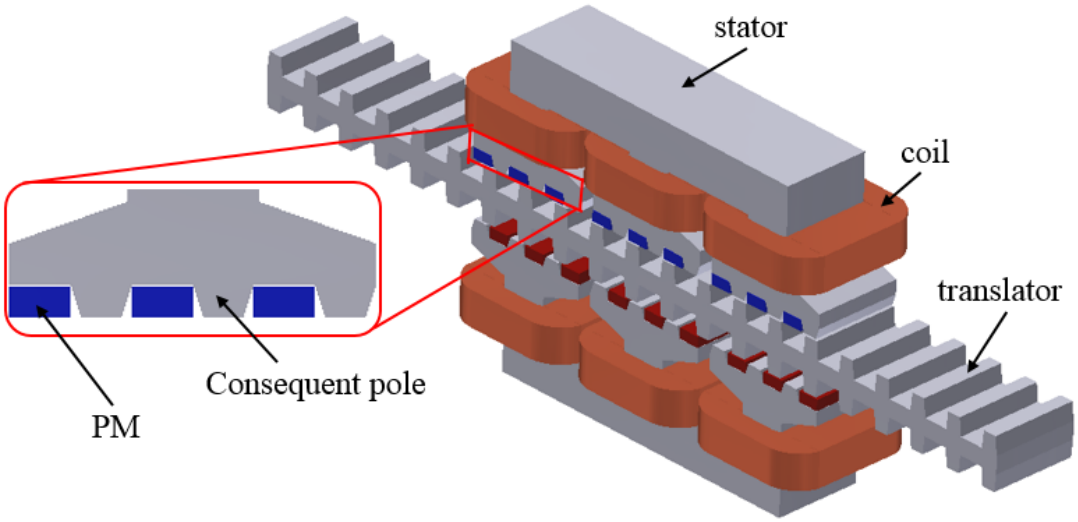

Figure 6.1: Configuration of CPLVHPM machine [30]

6.2 Consequent Pole Linear Vernier Hybrid Permanent Magnet Machines

The Consequent Pole Linear Vernier Hybrid Permanent Magnet (CPLVHPM) machine [30] is a developed version of the Vernier hybrid machine (VHM) with an improved magnet consumption [121]. This machine is comprised of double-sided stators with two identical E-cores facing each other in which both permanent magnets and windings are located in the same part of the machine, the E-shaped stator. A long iron laminated translator with salient teeth is sandwiched between the stator sides as shown in Figure 6.1. The translator possesses a simple, rigid pure iron structure which is inherently low cost.

This class of machine has the same basic structure as a baseline VHM where PM poles have been substituted with consequent tapered ferromagnetic poles. All remaining magnets have the same polarity, while the ferromagnetic poles take over the role of the missing poles. Hence, the number of effective pole pairs of the PM for a baseline VHM and the consequent pole machine are equal. Figure 6.2 shows the flux of both machines

and that there is smaller pole to pole flux leakage produced by the consequent pole machine when compared to its VHM counterpart. In other words, the flux linkage of the consequent pole machine is higher than that of the baseline machine. A detailed analysis of the effect of employing tapered consequent poles on the back EMF and cogging force characteristics has been investigated in [30]. The salient feature of using this configuration is the saving of 50% of the PM materials, especially in longer stroke applications.

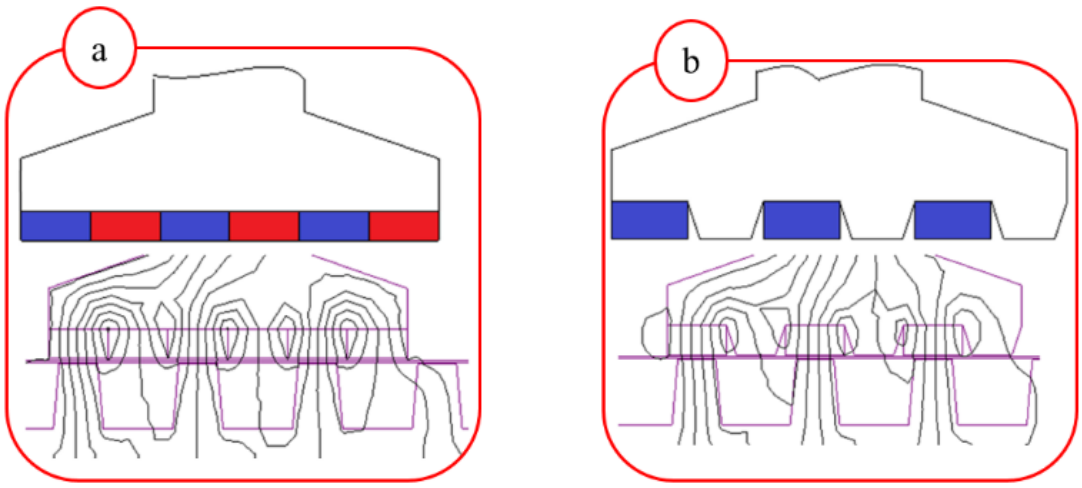

Figure 6.2: The effect of consequent poles on leakage flux [30]

The operating principle of the CPLVHPM is based on the magnetic gearing effect where the translator teeth are utilised to modulate the stationary magnetic field produced by the PMs to the high speed traveling magnetic field in the airgap. When the translator is at its initial position and its salient teeth are fully aligned the flux linkage in the coils reaches its maximum negative value, while the back EMF is zero. As the translator moves 90 electrical degrees the flux linkage drops steadily to zero, at which point the back EMF achieves its maximum positive value. The polarity is then reversed in the next alignment position, corresponding to a 1/2 translator pitch of movement. Therefore, a small translator displacement can produce a high rate of change in the flux linkage, and enhance the thrust density making the machine suitable for low speed direct drive applications.

6.3 Case study

A case study was proposed combining a CPLVHPM machine with a LMG which would operate as a PTO for a heaving buoy type wave energy converter. A block diagram for the proposed system is shown in Figure 6.3. In order to investigate the advantages of a combined system the linear machine was first designed as a scaled direct drive PTO. The key design parameters were a max thrust force of 740 N and a speed of 1.2 ms^{-1} resulting in a peak power rating of 888 W. A LMG with a ratio of 3.3:1 was then designed with an objective peak force of 740 N. LMGs must be designed for a given stroke amplitude as this will greatly affect the size and cost of the device. As the high speed translator will move increased distances determined by the gear ratio, having a large ratio might result in a prohibitively large system. In this case study a stroke amplitude of 5 cm was chosen for the low speed translator. The high-speed translator will then move 16.5 cm at maximum amplitude and the fixed outer rotor magnetic poles will have to be at least this height in order to ensure continual magnetic field connection between translators.

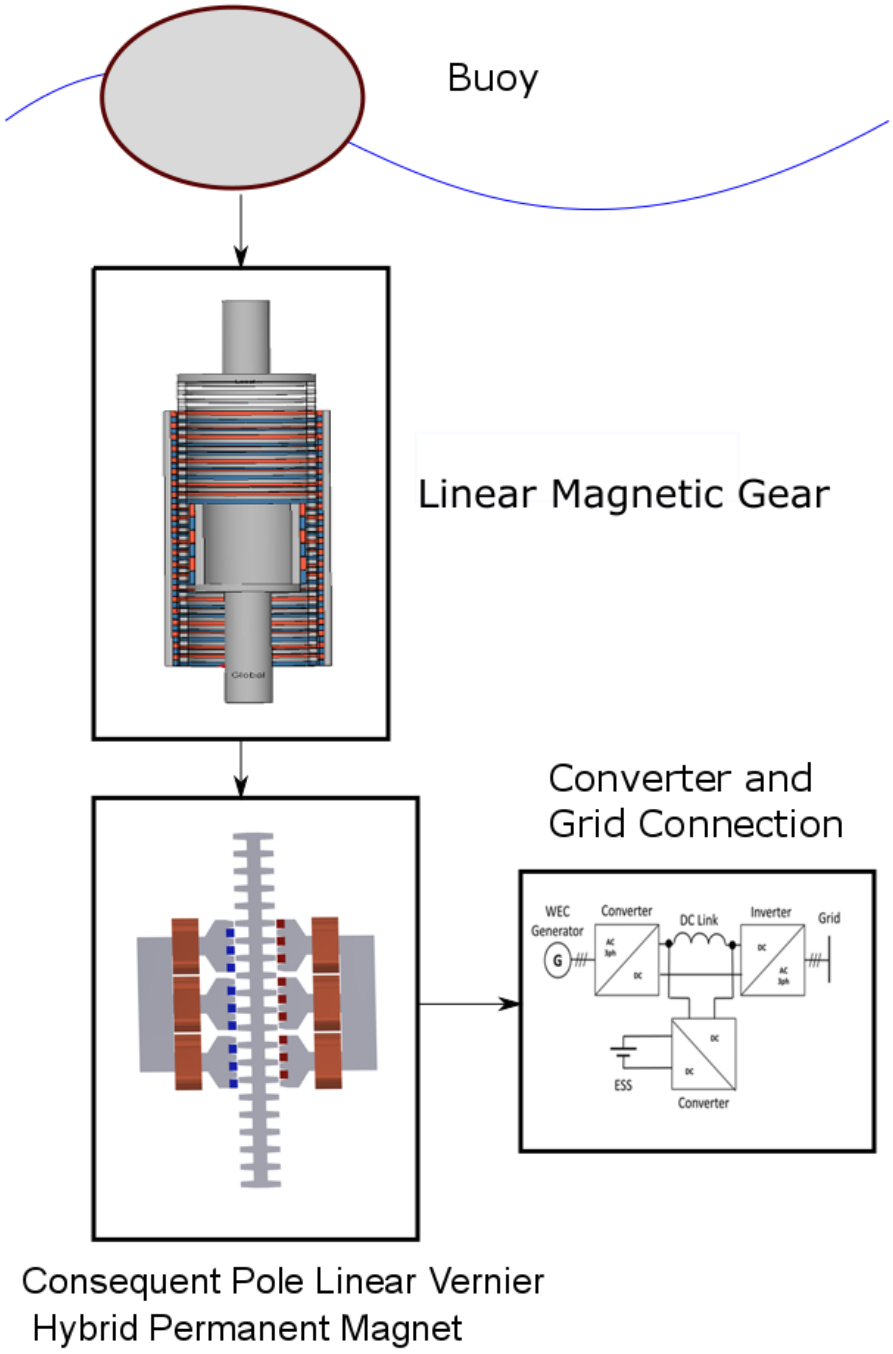

Figure 6.3: Combined system layout

Table 6.1: LMG parameter values

Parameter	2D Model (from FEMM)	3D Model (from 2D design)	3D Model (from MagNet)
Inner magnetic pole thickness (m)	0.004	0.004	0.004
Outer magnetic pole thickness (m)	0.002	0.002	0.002
Ferro-magnetic pole thickness (m)	0.005	0.005	0.005
Airgap radius (m)	0.025	0.025	0.025
Inner translator height (m)	0.063	0.063	0.069
Inner airgap (m)	0.001	0.001	0.001
Outer airgap (m)	0.001	0.001	0.001
Outer backiron thickness (m)	0.008	0.008	0.008
Inner backiron thickness (m)	0.008	0.008	0.008
Magnetic mass (kg)	0.422	0.422	0.623
Active iron mass (kg)	3.116	3.116	4.158
Total active gear mass (kg)	3.538	3.538	4.781
Peak (high) force (N)	772	684	784

6.3.1 Linear Magnetic Gear Design

The LMG was designed through a similar process to that detailed in [115] with initial design and optimisation in xfemm and then a full 3D analysis in MagNet to verify the results. When the 3D analysis was performed with the same parameters as the 2D model, there was a reduction of approximately 11% in the peak forces. To address this difference, the 3D model was revised such that the correct target force was achieved in order to assess the extra material required for a completed design. The key values and results are shown in Table 6.1 with the force curves of the initial 2D model, 3D model of the same design and the 3D model of the adapted design shown in Figures 6.5 & 6.6. The models were statically solved across 25 points in order to determine the full force range of each model. The primary force affecting parameters are the magnetic pole thickness, airgap radius and the height of the inner high speed translator. The airgap radius is defined as the distance from the center axis to the start of the inner airgap while the inner translator's height determines the active magnetic area. These parameters are shown in Figure 6.4.

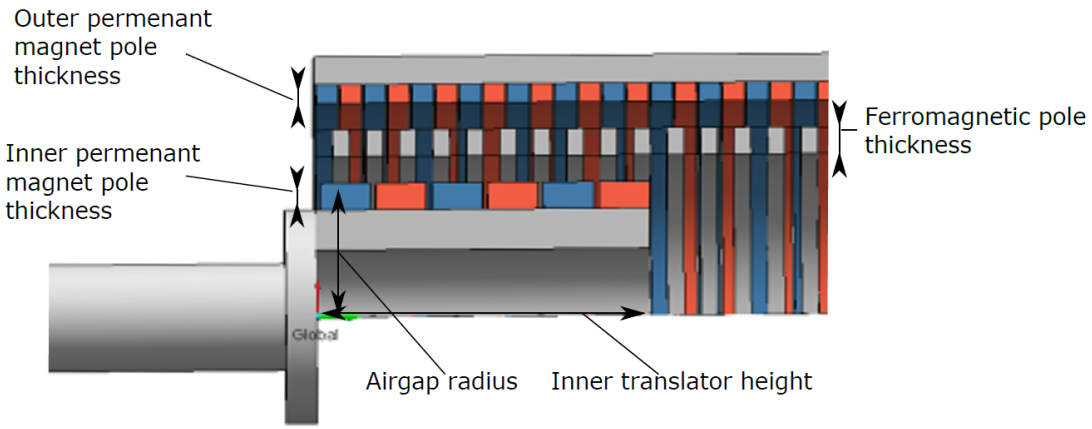

Figure 6.4: Main magnetic gear parameters

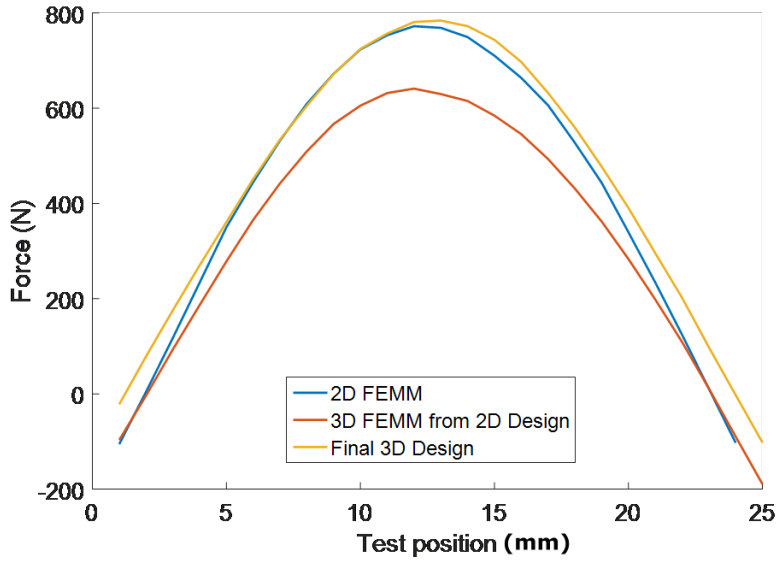

Figure 6.5: Forces on low speed, ferromagnetic pole translator

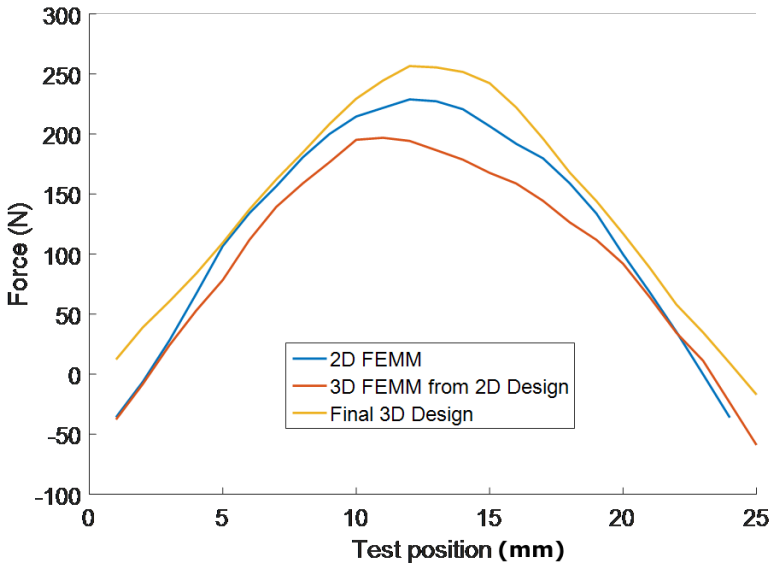

Figure 6.6: Forces on high speed, PM pole translator

6.4 Combined System Results

The key results of the combined system for the CPLVHPM machine are shown in Table 6.2 where the machine's mass values are shown before and after the combination with the LMG. With the addition of the LMG the linear machine's total mass is reduced by almost 63% with the key high cost permanent magnet (PM) material reduced by 66%. Though there is an increase in iron and eddy current losses in the PMs, due to the increase in frequency, the dominant copper losses are reduced by approximately 1/3. The resulting machine is then more efficient while being lighter, materially cheaper and more compact. The full 3D FEM which accounts for 3D effects was used for the comparison for accuracy and the final design resulted in a total mass reduction of 30%. The key results of the direct drive and combined system using the 3D results are presented in Figures 6.7, 6.8 & 6.9. These values are for active material only however and auxiliary elements will be required to connect and support the system. Additionally, including the LMG will increase the complexity of the drive train and increases the total high cost PM material (47%) as the PM material volume, V_{pm}, also increases rapidly with regards to both stroke amplitude S_{amp} and higher gear ratio GR.

$$V_{pm} \propto \pi S_{amp} GR \tag{6.1}$$

As the CPLVHPM machine has been purposefully designed in order to decrease the

high volume of PM material, a combined MG system with greater PM requirements will be, in most cases, unfeasible. Furthermore, as a main advantage of direct drives is the relative simplicity of the PTO, the addition of a gearing element without substantial advantages in efficiency or initial capital costs would result in no net benefit. Despite these issues the proposed system could have applications where the conditions are charaterised by low amplitude, low frequency regular waves. This could potentially increase the viability of certain sites for wave energy development.

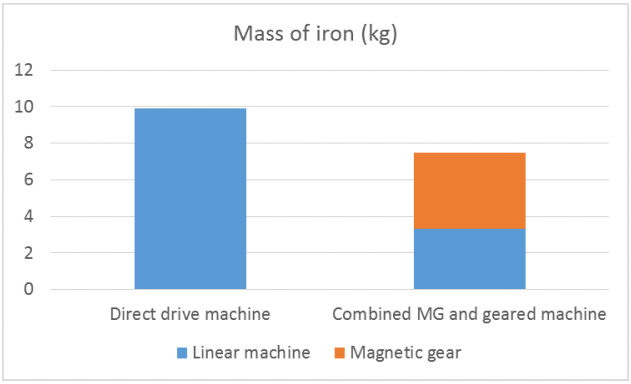

Figure 6.7: Mass of iron of designs

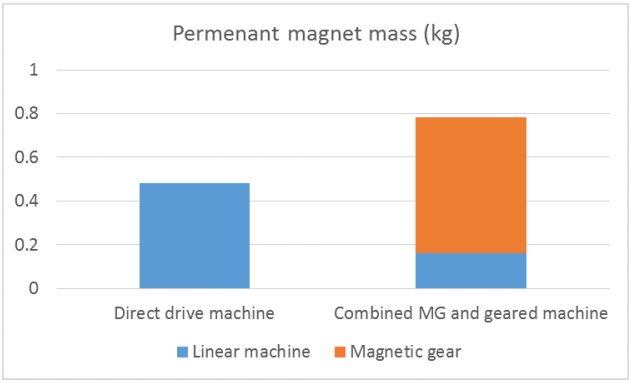

Figure 6.8: Permanent magnet mass of designs

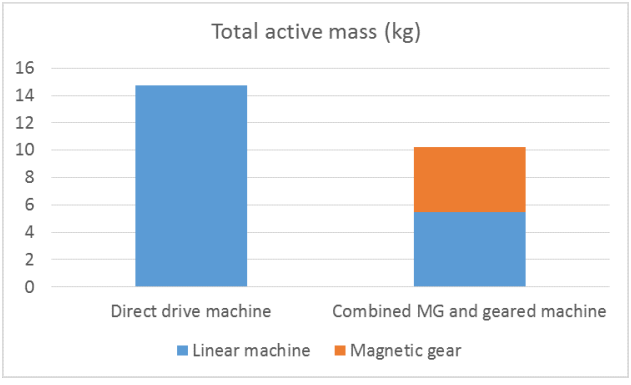

Figure 6.9: Total active mass of designs

Table 6.2: CPLVHPM values before and after MG

Description	Direct Drive System	Geared System	Unit
Velocity	1.2	3.96	m/s
Force	740	225	N
Axial length of the machine	50	15.15	mm
PM mass	0.48	0.16	kg
Copper mass	4.35	2	kg
Mass of laminations	9.9	3.3	kg
Total Machine mass	14.73	5.46	kg
Iron loss	18.3	23.7	W
Copper loss	42.4	27	W
Eddy current loss in PM	1.09	4.2	W
Total losses	61.8	54.9	W
Efficiency	93.5	94.2	%

6.5 Conclusion

The magnetically geared linear generator presented in this chapter has some potential in a WEC PTO. The resulting model, fully realised in 3D FEM, was lighter than the non-geared alternative while resulting in a more efficient generator. Despite these advantages such a system will have limited application as the addition of the gear will increase the complexity of the PTO and the larger amount of required PM material reduces the advantage of using a CPLVHPM machine. While this conclusion is specific to this particular case study it is likely to be reflected in most applications requiring a significant stroke length. Further work is planned to investigate whether it is possible to design a more integrated system rather than the basic series setup described in this work. This could potentially increase the viability of a combined system.

Chapter 7

Summary and Conclusion

The main outcomes of the thesis and proposed future work are here summarised and discussed. Several recommendations for improvements are also identified.

7.1 Contribution to Knowledge

7.1.1 New Modeling Tools

The design tools developed in this work in xfemm and MagNet allow for 2D & 3D model analysis and rapid design of MG systems. These tools will allow for further advanced designs to be developed and novel systems devised and tested. With the MagNet program now being executable from MATLAB, it is planned to transfer the Visual Basic tool to MATLAB scripts. When this is implemented the entire design process can be completed through the MATLAB environment with optimisation and result validation between 2D FEMM, 2D MagNet and full 3D MagNet.

7.1.2 Design Methods

An automated design method was investigated to deal with the multi-parameter result varying MG systems. A genetic algorithm method was implemented and successfully optimised a MG for reduced mass.

While effective, the GA method can time-consuming on a standard desktop computer and more case studies are required for further validation.

7.1.3 Prototype Development and Testing

Using the tools developed in this work two MG prototypes were designed, built and tested. The results showed close operating characteristics to those designed, validating the design process. When tested the prototypes clearly demonstrated the gear's use as a clutching mechanism that could be hugely beneficial in high torque applications. Through the prototype construction a solid knowledge of the difficulties of MG construction was gained that will be useful in future designs and in the development of advanced construction, assembly and maintenance techniques.

7.1.4 Magnetic Gears for Marine Energy Devices

This worked focused on the specific application of MGs to marine energy. An essential factor that must be addressed if the technology is to proliferate is proving substantial advantages over existing solutions. Through this work the advantages in high torque applications is demonstrated while noting the inherent challenges. This work has further contributed to the growing field of research that shows the advantages of all electric systems in marine energy converters.

7.2 Recommendations & Future Work

The development of magnetically geared systems for marine energy converters is an ongoing endeavor which has great potential in the emerging industry. The work covered in this thesis provides the basis for further developments and this section presents planned work and recommendations arising from the work to date.

7.2.1 Prototype Improvements

The efficiency of the prototype was lower than comparable systems and, from the power transfer analysis, it was found that the high starting torque is the leading cause. The following are proposed improvements that could reduce the power lost during operation.

FMP Rotor Structure Replacement

As previously noted the use of a conducting material like aluminum was a poor choice as it allowed for a current to be induced and established a resistive torque. Replacing

the aluminum with non conducting material like ceramics will eliminate this effect and have a substantial effect on the efficiency.

FMP Replacement

The rotor airgaps in the prototypes were very large, particularly for a gear of this size. With the design tools verified, a new model was analysed where the FMP's radial widths were increased from 6 mm to 10 mm, reducing the airgaps from 3.5 mm and 3.2 mm to 1.5 mm and 1.2 mm respectively. The new model saw an increase in the peak torque from 34.4 Nm to 54.6 Nm. While this will also increase the cogging torque the starting torque will be proportionally less than the peak torque. As the power transfer excluding starting toque was found to be high when approaching the peak torque, increasing the peak torque is expected to have a positive effect on the overall efficiency. For higher efficiencies using laminated material will also be considered to reduce the iron losses resulting from the varying magnetic field in the FMPs. While these losses are lower with the low frequency of wave energy applications, it will be a useful investigation as to the benefits in power transfer over an increase in cost and manufacturing complexity.

Pole Skewing

Cogging torque is a major factor contributing to higher starting torque [122]. Jungmayr et. al analsyed the effect of skewing poles in order to reduce the cogging torque [123] and found that skewing can significantly reduce the cogging torque while the peak torque is largely unaffected. Though pole skewing will increase a gear's construction complexity, it should be considered in improved gear designs.

Improved Bearings

Since bearing friction is the dominant factor in mechanical losses, using low friction bearings would have a significant impact on a MG's efficiency. Alternative systems such as hydrostatic bearings [124], magnetic bearings [125] or a combination [126] have the potential to eliminate the losses associated with friction and facilitate completely contactless operation. While the advantages of such systems are clear there will be potential associated increases in cost, complexity and failure rates [127, 128].

7.2.2 FloWave Testing

As part of the e-Drive project an OWSC test rig has been designed that will be used with the MG prototypes to observe real time energy harvesting in marine conditions. The rig design is shown in Figure: 7.1.

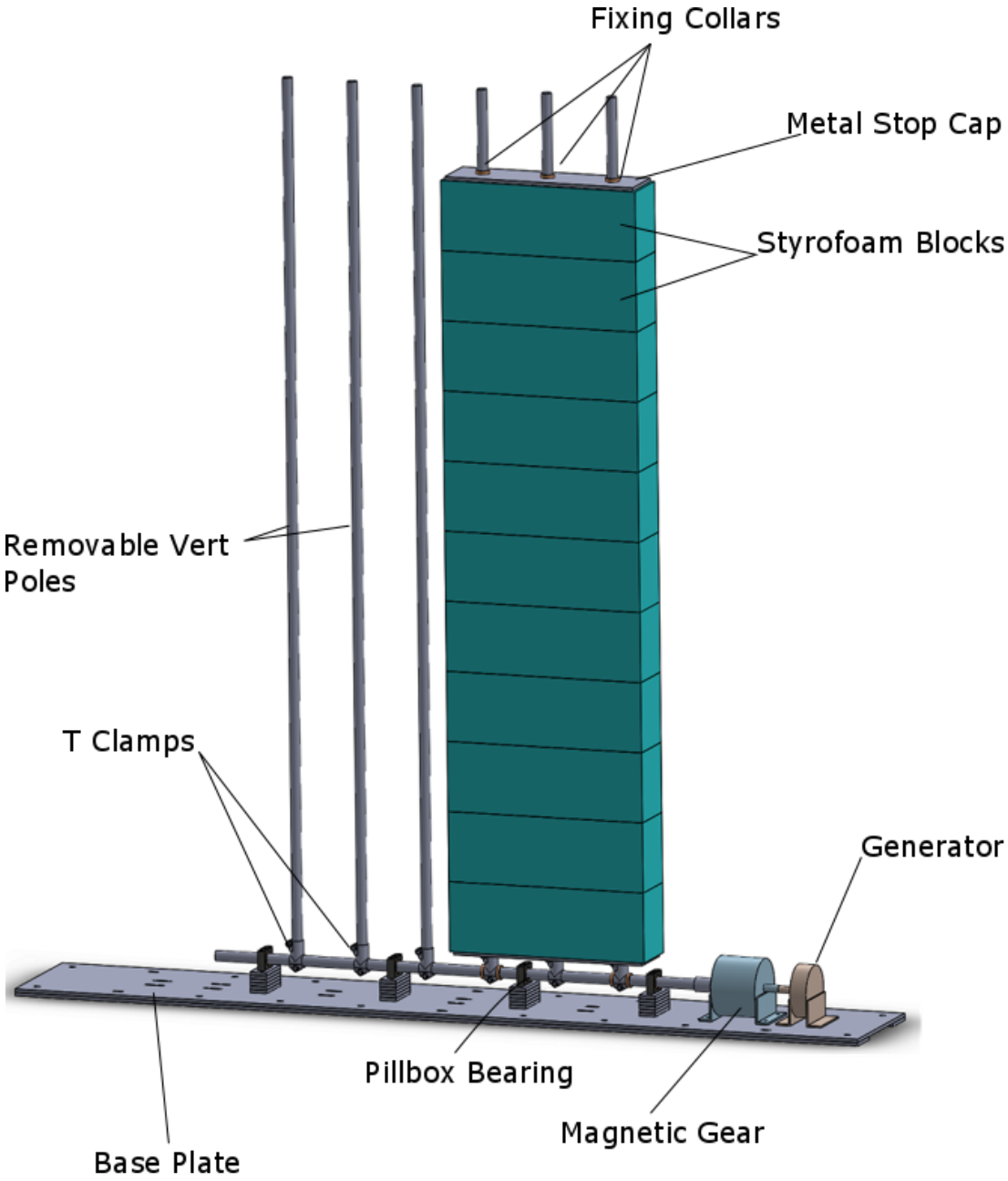

Figure 7.1: FloWave Test Rig

The axial shaft is supported by 4 pillbox bearing support structures and T Clamps are fastened to the shaft supporting the vertical poles. The flap material is made of Styrofoam blocks (600 mm x 20 mm x 16 mm) which can be double stacked making the

flap 1200 mm wide. Metal plates can be added between blocks to add mass. The design is highly modular and can be adapted for a variety of loads. The tall design is to allow for testing in FloWave's 2 meter depth tank. The bearings and clamps are industry standard and selected for high force performance in a marine environment. The rig allows for two magnetically geared generators to be attached as proposed in [42]. A series of tests are planned for a range of sea states and under extreme wave events to observe the effect on the drive train during a slip event.

7.2.3 Novel Geared Generators

The topology of MGs potentially allow for highly compact drive systems. A plan for the near future is to design and build an integrated MG-generator system that can be tested at the UoE. The combined system would incorporate a multi-staged axial C-Gen generator with a multi-staged axial MG as shown in Figure 7.2 which would result in a highly compact, scalable system. Additional options are being investigated such as the use of Halbach array magnetic poles. This would allow for the majority of the iron elements to be removed making for an exceptionally light drive that is high suitable to marine applications.

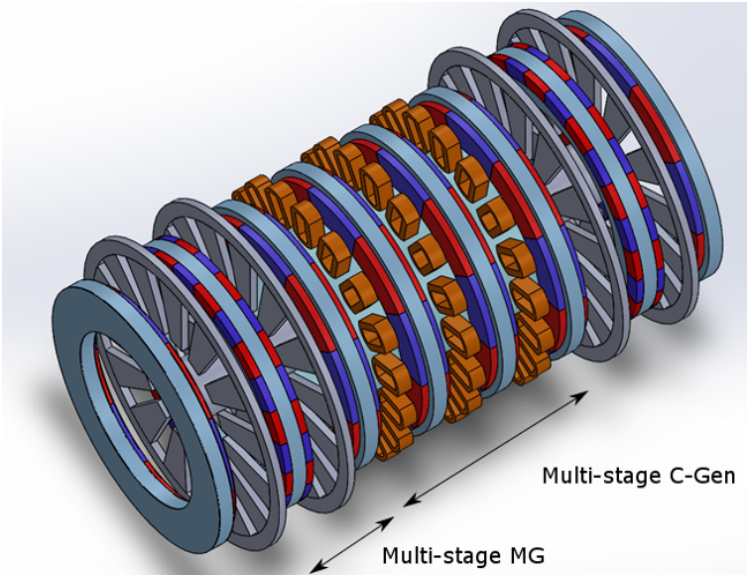

Figure 7.2: Proposed combined magnetic gear drive

7.2.4 Advanced Construction Techniques

The construction of a MG can be challenging due to the large amount of PM material. From the literature review in Chapter 1 it is evident that there are many topologies that

could be potential improvements on the standard concentric design but the difficulties in assembly outweigh the benefits. With the design tools verified, proposed further work is to develop techniques and alternate structures to facilitate easier assembly, installation and maintenance.

7.3 Conclusion

As with most new and potentially disruptive technologies, MGs face challenges to full industry adoption. With MGs reaching a high technology readiness level, future key developments will be efficient design methods and tools, proving the technology's operation at full scale under real world conditions, and demonstrating the technology's advantages. Addressing these points was the primary goal of this work and, with the established tools, design procedures and prototypes, further work can be undertaken to advance the technology in the renewables field.

References

[1] J. P. Kofoed, *The Wave Energy Sector*. Cham: Springer International Publishing, 2017, pp. 17–42, [last accessed: 26/09/19]. [Online]. Available: https://doi.org/10.1007/978-3-319-39889-1_2

[2] European Marine Energy Centre: EMEC. [last accessed: 26/09/19]. [Online]. Available: http://www.emec.org.uk/

[3] C. Cargo, A. Hillis, and A. Plummer, "Strategies for active tuning of wave energy converter hydraulic power take-off mechanisms," *Renewable Energy*, vol. 94, pp. 32 – 47, 2016, [last accessed: 26/09/19]. [Online]. Available: http://www.sciencedirect.com/science/article/pii/S0960148116301914

[4] K. Li and J. Z. Bird, "A review of the volumetric torque density of rotary magnetic gear designs," in *2018 XIII International Conference on Electrical Machines (ICEM)*. IEEE, 2018, pp. 2016–2022.

[5] C.-C. Huang, M.-C. Tsai, D. Dorrell, and B.-J. Lin, "Development of a Magnetic Planetary Gearbox," *IEEE Transactions on Magnetics*, vol. 44, no. 3, pp. 403–412, 2008.

[6] K. Davey, T. Hutson, L. McDonald, C. Ras, R. Weinstein, D. Parks, and R. P. Sawh, "Rotating cylinder planetary gear motor," in *2015 IEEE International Electric Machines Drives Conference (IEMDC)*, May 2015, pp. 503–509.

[7] F. T. Joergensen, T. O. Andersen, and P. O. Rasmussen, "The cycloid permanent magnetic gear," in *Conference Record of the 2006 IEEE Industry Applications Conference Forty-First IAS Annual Meeting*, vol. 1, Oct 2006, pp. 373–378.

[8] J. Rens, K. Atallah, S. D. Calverley, and D. Howe, "A novel magnetic harmonic gear," *IEEE Transactions on Industry Applications*, vol. 46, no. 1, pp. 206–212, 2010.

[9] L. Jian and K. T. Chau, "A coaxial magnetic gear with halbach permanent-magnet arrays," *IEEE Transactions on Energy Conversion*, vol. 25, no. 2, pp. 319–328, June 2010.

[10] P. O. Rasmussen, T. O. Andersen, F. T. Jørgensen, and O. Nielsen, "Development of a high-performance magnetic gear," *IEEE Transactions on Industry Applications*, vol. 41, no. 3, pp. 764–770, 2005.

[11] K. Uppalapati and J. Bird, "A flux focusing ferrite magnetic gear," in *6th IET International Conference on Power Electronics, Machines and Drives (PEMD 2012)*, March 2012, pp. 1–6.

[12] W. N. Fu and L. Li, "Optimal design of magnetic gears with a general pattern of permanent magnet arrangement," *IEEE Transactions on Applied Superconductivity*, vol. 26, no. 7, pp. 1–5, Oct 2016.

[13] V. M. Acharya, M. Calvin, and J. Z. Bird, "A low torque ripple flux focusing axial magnetic gear," in *7th IET International Conference on Power Electronics, Machines and Drives (PEMD 2014)*, April 2014, pp. 1–6.

[14] W. Bomela, J. Z. Bird, and V. M. Acharya, "The performance of a transverse flux magnetic gear," *IEEE Transactions on Magnetics*, vol. 50, no. 1, pp. 1–4, Jan 2014.

[15] D. Zhu, F. Yang, Y. Du, F. Xiao, and Z. Ling, "An axial-field flux-modulated magnetic gear," *IEEE Transactions on Applied Superconductivity*, vol. 26, no. 4, pp. 1–5, June 2016.

[16] W. Li, K. T. Chau, and J. Z. Jiang, "Application of linear magnetic gears for pseudo-direct-drive oceanic wave energy harvesting," *IEEE Transactions on Magnetics*, vol. 47, no. 10, pp. 2624–2627, 2011.

[17] R. C. Holehouse, K. Atallah, and J. Wang, "Design and Realization of a Linear Magnetic Gear," *Magnetics, IEEE Transactions on*, vol. 47, no. 10, pp. 4171–4174, 2011.

[18] M. B. Kouhshahi and J. Z. Bird, "Analysis of A magnetically geared lead screw," *Electrical and Computer Engineering Faculty Publications and Presentations*, no. 421, pp. 1–8, 2017.

[19] L. Jian, S. Member, K. T. Chau, and S. Member, "A Coaxial Magnetic Gear With Halbach Permanent-Magnet Arrays," vol. 25, no. 2, pp. 319–328, 2010.

[20] W. N. Fu and S. L. Ho, "A quantitative comparative analysis of a novel flux-modulated permanent-magnet motor for low-speed drive," *IEEE Transactions on Magnetics*, vol. 46, no. 1, pp. 127–134, Jan 2010.

[21] P. Padmanathan and J. Z. Bird, "Designing a Continuously Variable Magnetic Gear," *Proceedings of the 2013 IEEE International Electric Machines and Drives Conference, IEMDC 2013*, pp. 367–373, 2016.

[22] M. Chen, K. T. Chau, W. Li, C. Liu, and C. Qiu, "Design and analysis of a new magnetic gear with multiple gear ratios," *IEEE Transactions on Applied Superconductivity*, vol. 24, no. 3, pp. 3–6, 2014.

[23] Y. Du, K. T. Chau, M. Cheng, and Y. Wang, "A linear magnetic-geared permanent magnet machine for wave energy generation," in *2010 International Conference on Electrical Machines and Systems*, Oct 2010, pp. 1538–1541.

[24] R. K. Holm, N. I. Berg, M. Walkusch, P. O. Rasmussen, and R. H. Hansen, "Wave energy conversion," *Deep Sea Research Part B. Oceanographic Literature Review*, vol. 30, no. 6, p. 491, 2013.

[25] V. R. Ramanan, "Final technical report - advanced direct-drive generator for improved availability of oscillating wave surge converter (owsc) power generation systems," ABB Inc., Tech. Rep. DE-FOA-0000848, March 2017, [last accessed: 26/09/19]. [Online]. Available: https://www.osti.gov/biblio/1356751

[26] K. Atallah, S. D. Calverley, and D. Howe, "High-performance magnetic gears," *Journal of Magnetism and Magnetic Materials*, vol. 272-276, pp. E1727 – E1729, 2004, proceedings of the International Conference on Magnetism (ICM 2003). [Online]. Available: http://www.sciencedirect.com/science/article/pii/S0304885303022182

[27] K. Nakamura, M. Fukuoka, and O. Ichinokura, "Performance improvement of magnetic gear and efficiency comparison with conventional mechanical gear," *Journal of Applied Physics*, vol. 115, no. 17, p. 17A314, 2014.

[28] O. Keysan, A. McDonald, and M. Mueller, "Aquamarine power oyster - C-GEN rotary machine design," *Aquamarine Final Design Report*, 2009.

[29] Abssac Starflex Catalogue. [last accessed: 26/09/19]. [Online]. Available: https://www.abssac.co.uk

[30] A. A. Almoraya, N. J. Baker, K. Smith, and M. A. H. Raihan, "Development of a double-sided consequent pole linear vernier hybrid permanent-magnet machine for wave energy converters," in *2017 IEEE International Electric Machines and Drives Conference (IEMDC)*, May 2017, pp. 1–7.

[31] I. P. on Climate Change, "Gloabal warming of 1.5 degrees celsius." 2018, [last accessed: 26/09/19]. [Online]. Available: https://www.ipcc.ch/site/assets/uploads/sites/2/2018/07/SR15_SPM_High_Res.pdf

[32] REN21, "Renewables 2018 gloabal status report," 2018, [last accessed: 26/09/19]. [Online]. Available: http://www.ren21.net/wp-content/uploads/2018/06/17-8652_GSR2018_FullReport_web_-1.pdf

[33] M. Fadaeenejad, R. Shamsipour, S. D. Rokni, and C. Gomes, "New approaches in harnessing wave energy: With special attention to small islands," *Renewable and Sustainable Energy Reviews*, vol. 29, pp. 345–354, 2014.

[34] M. A. J. R. Quirapas, H. Lin, M. L. S. Abundo, S. Brahim, and D. Santos, "Ocean renewable energy in southeast asia: A review," *Renewable and Sustainable Energy Reviews*, vol. 41, pp. 799 – 817, 2015, [last accessed: 26/09/19]. [Online]. Available: http://www.sciencedirect.com/science/article/pii/S1364032114006923

[35] M. Mustapa, O. Yaakob, Y. M. Ahmed, C.-K. Rheem, K. Koh, and F. A. Adnan, "Wave energy device and breakwater integration: A review," *Renewable and Sustainable Energy Reviews*, vol. 77, pp. 43 – 58, 2017, [last accessed: 26/09/19]. [Online]. Available: http://www.sciencedirect.com/science/article/pii/S1364032117304409

[36] About:Resolute Marine Energy. [last accessed: 26/09/19]. [Online]. Available: http://www.resolutemarine.com/about

[37] C. Trust, "UK wave energy resource," *Aquamarine Final Design Report*, 2012, [last accessed: 26/09/19]. [Online]. Available: https://www.carbontrust.com/media/202649/ctc816-uk-wave-energy-resource.pdf

[38] D. Krohn, M. Woods, J. Adams, B. Valpy, F. Jones, and P. Gardner, "Wave and tidal energy in the uk: Conquering challenges , generating growth," 2018, [last accessed: 26/09/19]. [Online]. Available: https://hub.globalccsinstitute.com/sites/default/files/publications/115683/wave-tidal-energy-UK-conquering-challenges-generating-growth.pdf

[39] T. Jahns, "Getting rare-earth magnets out of ev traction machines: A review of the many approaches being pursued to minimize or eliminate rare-earth magnets from future ev drivetrains," *IEEE Electrification Magazine*, vol. 5, pp. 6–18, 03 2017.

[40] R. Vertechy, M. Fontana, G. R. Papini, and M. Bergamasco, "Oscillating-water-column wave-energy-converter based on dielectric elastomer generator," in *Electroactive Polymer Actuators and Devices (EAPAD) 2013*, vol. 8687. International Society for Optics and Photonics, 2013, p. 86870I.

[41] I. López, J. Andreu, S. Ceballos, I. Martínez De Alegría, and I. Kortabarria, "Review of wave energy technologies and the necessary power-equipment," *Renewable and Sustainable Energy Reviews*, vol. 27, pp. 413–434, 2013, [last accessed: 26/09/19]. [Online]. Available: http://dx.doi.org/10.1016/j.rser.2013.07.009

[42] B. McGilton, R. Crozier, A. McDonald, and M. Mueller, "Review of magnetic gear technologies and their applications in marine energy," *IET Renewable Power Generation*, vol. 12, no. 2, pp. 174–181, 2018.

[43] J. Ribrant and L. M. Bertling, "Survey of failures in wind power systems with focus on Swedish wind power plants during 1997-2005," *IEEE Transactions on Energy Conversion*, vol. 22, no. 1, pp. 167–173, 2007.

[44] Z. Daneshi-Far, G. a. Capolino, and H. Henao, "Review of failures and condition monitoring in wind turbine generators," *The XIX International Conference on Electrical Machines - ICEM 2010*, pp. 1–6, 2010.

[45] W. Musial, S. Butterfield, and B. McNiff, "Improving Wind Turbine Gearbox Reliability," *European Wind Energy Conference*, pp. 1–13, 2007.

[46] H. Polinder, F. F. a. Van Der Pijl, G. J. De Vilder, and P. J. Tavner, "Comparison of direct-drive and geared generator concepts for wind turbines," *IEEE Transactions on Energy Conversion*, vol. 21, no. 3, pp. 725–733, 2006.

[47] D. McMillan and G. W. Ault, "Techno-economic comparison of operational aspects for direct drive and gearbox-driven wind turbines," *IEEE Transactions on Energy Conversion*, vol. 25, no. 1, pp. 191–198, 2010.

[48] P. J. Tavner, G. J. W. V. Bussel, and F. Spinato, "Machine and Converter Reliabilities in Wind Turbines," *International Conference on Power Electronics, Machines and Drives*, pp. 1–4, 2006.

[49] E. Echavarria, B. Hahn, G. J. W. van Bussel, and T. Tomiyama, "Reliability of Wind Turbine Technology Through Time," *Journal of Solar Energy Engineering*, vol. 130, no. 3, p. 031005, 2008.

[50] G. T. Son, H. J. Lee, T. S. Nam, Y. H. Chung, U. H. Lee, S. T. Baek, K. Hur, and J. W. Park, "Design and control of a modular multilevel HVDC converter with redundant power modules for noninterruptible energy transfer," *IEEE Transactions on Power Delivery*, vol. 27, no. 3, pp. 1611–1619, 2012.

[51] R. Henderson, "Design, simulation, and testing of a novel hydraulic power take-off system for the pelamis wave energy converter," *Renewable Energy*, vol. 31, no. 2, pp. 271 – 283, 2006, marine Energy. [Online]. Available: http://www.sciencedirect.com/science/article/pii/S0960148105002259

[52] G. S. Payne, U. B. Stein, M. Ehsan, N. J. Caldwell, and W. Rampen, "Potential of digital displacement hydraulics for wave energy conversion," in *Proceedings of the sixth European wave and tidal energy conference, Glasgow*, 2005.

[53] D. Zhang, W. Li, Y. Lin, and J. Bao, "An overview of hydraulic systems in wave energy application in china," *Renewable and Sustainable Energy Reviews*, vol. 16,

no. 7, pp. 4522 – 4526, 2012, [last accessed: 26/09/19]. [Online]. Available: http://www.sciencedirect.com/science/article/pii/S1364032112002626

[54] Magnomatics: Technology Application. [last accessed: 26/09/19]. [Online]. Available: http://www.magnomatics.com/pages/applications/uses-for-our-technology.htm

[55] C. Armstrong, "Power-transmitting device," Nov. 26 1901, uS Patent 687,292. [Online]. Available: http://www.google.co.uk/patents/US687292

[56] H. Faus, "Magnet gearing." Aug. 21 1941, uS Patent 353,472. [Online]. Available: https://patents.google.com/patent/US2243555A

[57] S. Kikuchi and K. Tsurumoto, "Design and characteristics of a new magnetic worm gear using permanent magnet," *IEEE Transactions on Magnetics*, vol. 29, no. 6, pp. 2923–2925, 1993.

[58] K. Kikuchi, Shinki Tsurumoto, "Trial construction of a new magnetic skew gear using permanent magnet," *IEEE Transactions on Magnetics*, vol. 30, no. 6, pp. 4767–4769, 1994.

[59] P. Tlali, R.-J. Wang, and S. Gerber, "Magnetic gear technologies: A review," *Electrical Machines (ICEM), 2014 International Conference on*, pp. 544–550, 2014.

[60] X. Li, K.-T. Chau, M. Cheng, and W. Hua, "Comparison of magnetic-geared permanent magnet machines," *Progress In Electromagnetics Research*, vol. 133, no. 2013, pp. 177–198, 2013.

[61] F. T. Jorgensen, T. O. Andersen, and P. O. Rasmussen, "Two dimensional model of a permanent magnet spur gear," in *Fourtieth IAS Annual Meeting. Conference Record of the 2005 Industry Applications Conference, 2005.*, vol. 1, Oct 2005, pp. 261–265 Vol. 1.

[62] T. B. Martin Jr, "Magnetic transmission," Apr. 16 1968, uS Patent 3,378,710. [Online]. Available: http://www.google.co.uk/patents/US3378710

[63] K. Atallah and D. Howe, "A novel high-performance magnetic gear," *IEEE Transactions on Magnetics*, vol. 37, no. 4 I, pp. 2844–2846, 2001.

[64] M. Johnson, M. C. Gardner, and H. A. Toliyat, "Design comparison of ndfeb and ferrite radial flux surface permanent magnet coaxial magnetic gears," *IEEE Transactions on Industry Applications*, vol. 54, no. 2, pp. 1254–1263, March 2018.

[65] E. Schmidt, M. Kaltenbacher, and A. Wolfschluckner, "Eddy current losses in permanent magnets of surface mounted permanent magnet synchronous machines—analytical calculation and high order finite element analyses," *e & i Elektrotechnik und Informationstechnik*, vol. 134, no. 2, pp. 148–155, Apr 2017. [Online]. Available: https://doi.org/10.1007/s00502-017-0498-y

[66] C. Hurst, "4 - China's Rare Earth Elements Industry: What Can the West Learn?" no. March, p. 43, 2010, [last accessed: 26/09/19]. [Online]. Available: http://www.iags.org/rareearth0310hurst.pdf

[67] M. Johnson, M. C. Gardner, and H. A. Toliyat, "Analysis of axial field magnetic gears with halbach arrays," in *2015 IEEE International Electric Machines Drives Conference (IEMDC)*, May 2015, pp. 108–114.

[68] L. Yong, X. Jingwei, P. Kerong, and L. Yongping, "Principle and simulation analysis of a novel structure magnetic gear," in *2008 International Conference on Electrical Machines and Systems*, Oct 2008, pp. 3845–3849.

[69] K. Atallah, J. Wang, S. Mezani, and D. Howe, "A novel high-performance linear magnetic gear," *Ieej Transactions on Industry Applications*, vol. 126, pp. 1352–1356, 01 2006.

[70] J. Hashimoto and Y. Kubo, "A magnetic screw device," Patent US 5,687,614, 1997.

[71] J. Wang, K. Atallah, and J. Barnes, "Analysis and design of a high force density linear electromagnetic actuator," *PCIM Europe Conference Proceedings*, vol. 47, no. 10, pp. 177–185, 2012.

[72] S. Pakdelian, N. W. Frank, and H. A. Toliyat, "Analysis and Design of the Trans-Rotary Magnetic," *Energy Conversion Congress and Exposition (ECCE), 2012 IEEE*, pp. 3340–3347, 2012.

[73] K. Lu and W. Wu, "Electromagnetic Lead Screw for Potential Wave Energy Application," *IEEE Transactions on Magnetics*, vol. 50, no. 11, pp. 2–5, 2014.

[74] J. Wang, K. Atallah, and S. D. Carvley, "A magnetic continuously variable transmission device," *IEEE Transactions on Magnetics*, vol. 47, no. 10, pp. 2815–2818, Oct 2011.

[75] Magnomatics, "Magnomatics - magsplit," 2019, [last accessed: 26/09/19]. [Online]. Available: http://www.magnomatics.com/pages/technology/magsplit.htm

[76] L. L. Wang, J. X. Shen, P. C. K. Luk, W. Z. Fei, C. F. Wang, and H. Hao, "Development of a magnetic-geared permanent-magnet brushless motor," *IEEE Transactions on Magnetics*, vol. 45, pp. 4578–4581, 2009.

[77] E. Spooner and L. Haydock, "Vernier hybrid machines," *IEE Proceedings-Electric Power Applications*, vol. 150, no. 6, pp. 655–662, 2003.

[78] F. Li, K. T. Chau, C. Liu, J. Z. Jiang, and W. Y. Wang, "Design and analysis of magnet proportioning for dual-memory machines," *IEEE Transactions on Applied Superconductivity*, vol. 22, no. 3, pp. 4 905 404–4 905 404, June 2012.

[79] A. J. Vining and A. Muetze, "Linear Generators for Direct-Drive Ocean Wave Energy Conversion," *Electric Machines and Drives Conference, 2003. IEMDC'03. IEEE International*, 2007.

[80] H. Polinder, B. C. Mecrow, A. G. Jack, P. G. Dickinson, and M. A. Mueller, "Conventional and tfpm linear generators for direct-drive wave energy conversion," *IEEE Transactions on Energy Conversion*, vol. 20, no. 2, pp. 260–267, June 2005.

[81] S. Pakdelian, Y. Deshpande, and H. A. Toliyat, "An electric machine integrated with trans-rotary magnetic gear," in *2012 IEEE Energy Conversion Congress and Exposition (ECCE)*, Sep. 2012, pp. 3356–3362.

[82] S. Pakdelian and H. A. Toliyat, "Trans-rotary magnetic gear for wave energy applicaion," in *2012 IEEE Power and Energy Society General Meeting*, July 2012, pp. 1–4.

[83] R. H. Hansen, T. O. Andersen, and H. C. Pedersen, "Model Based Design of Efficient Power Take-Off Systems for Wave Energy Converters," *Proceedings of the 12th Scandinavian International Conference on Fluis Power*, pp. 1–15, 2011.

[84] R. H. Hansen and M. M. Kramer, "Modelling and Control of the Wavestar Prototype," *Proceedings of the 9th European Wave and Tidal Energy Conference*, pp. 1–10, 2011.

[85] K. K. Uppalapati, J. Z. Bird, D. Jia, J. Garner, and A. Zhou, "Performance of a magnetic gear using ferrite magnets for low speed ocean power generation," in *2012 IEEE Energy Conversion Congress and Exposition (ECCE)*, Sep. 2012, pp. 3348–3355.

[86] S. Hazra, S. Bhattacharya, K. K. Uppalapati, and J. Bird, "Ocean energy power take-off using oscillating paddle," in *2012 IEEE Energy Conversion Congress and Exposition (ECCE)*, Sep. 2012, pp. 407–413.

[87] M. Johnson, M. C. Gardner, H. A. Toliyat, S. Englebretson, W. Ouyang, and C. Tschida, "Design, construction, and analysis of a large scale inner stator radial flux magnetically geared generator for wave energy conversion," in *2017 IEEE Energy Conversion Congress and Exposition (ECCE)*, Oct 2017, pp. 5017–5024.

[88] L. Y. L. Yong, X. J. X. Jingwei, P. K. P. Kerong, and L. Y. L. Yongping, "Principle and simulation analysis of a novel structure magnetic gear," *International Conference on Electrical Machines and Systems*, no. 1, pp. 3845–3849, 2008.

[89] N. W. Frank and H. A. Toliyat, "Gearing ratios of a magnetic gear for wind turbines," *2009 IEEE International Electric Machines and Drives Conference, IEMDC '09*, pp. 1224–1230, 2009.

[90] D. J. Evans and Z. Q. Zhu, "Influence of design parameters on magnetic gear's torque capability," *2011 IEEE International Electric Machines and Drives Conference, IEMDC 2011*, pp. 1403–1408, 2011.

[91] D. C. Meeker, *Finite Element Method Magnetics Version 4.2 User's Manual*, 2010.

[92] Mentor MagNet Hompage. [last accessed: 26/09/19]. [Online]. Available: https://www.mentor.com/products/mechanical/magnet/magnet/

[93] A. Penzkofer and K. Atallah, "Scaling of pseudo direct drives for wind turbine application," *IEEE Transactions on Magnetics*, vol. 52, no. 7, pp. 1–5, July 2016.

[94] N. Niguchi and K. Hirata, "Cogging torque analysis of magnetic gear," *IEEE Transactions on Industrial Electronics*, vol. 59, no. 5, pp. 2189–2197, 2012.

[95] Z. Q. Zhu and D. Howe, "Influence of design parameters on cogging torque in permanent magnet machines," *IEEE Transactions on Energy Conversion*, vol. 15, no. 4, pp. 407–412, 2000, [last accessed: 26/09/19]. [Online]. Available: http://ieeexplore.ieee.org/lpdocs/epic03/wrapper.htm?arnumber=900501

[96] T. Lubin, S. Mezani, and A. Rezzoug, "Analytical computation of the magnetic field distribution in a magnetic gear," *IEEE Transactions on Magnetics*, vol. 46, no. 7, pp. 2611–2621, 2010.

[97] L. Jian, G. Xu, C. C. Mi, K. T. Chau, and C. C. Chan, "Analytical method for magnetic field calculation in a low-speed permanent-magnet harmonic machine," *IEEE Transactions on Energy Conversion*, vol. 26, no. 3, pp. 862–870, 2011.

[98] L. Jian and K.-T. Chau, "Analytical Calculation of Magnetic Field Distribution in Coaxial Magnetic Gears," *Progress In Electromagnetics Research*, vol. 92, pp. 1–16, 2009, [last accessed: 26/09/19]. [Online]. Available: http://www.jpier.org/PIER/pier.php?paper=09032301

[99] A. Penzkofer, "Analytical Modelling and Analysis of Magnetic Gears and Pseudo Direct Drives for Large Wind Turbines," no. November, p. 196, 2016.

[100] C. Mi, G. R. Slemon, and R. Bonert, "Modeling of iron losses of permanent-magnet synchronous motors," *IEEE Transactions on Industry applications*, vol. 39, no. 3, pp. 734–742, 2003.

[101] H. Polinder, M. Hoeijmakers, and M. Scuotto, "Eddy-current losses in the solid back-iron of pm machines for different concentrated fractional pitch windings," in *2007 IEEE International Electric Machines & Drives Conference*, vol. 1. IEEE, 2007, pp. 652–657.

[102] Y. Diab, F. Ville, C. Changenet, and P. Velex, "Windage losses in high speed gears: Preliminary experimental and theoretical results," in *ASME 2003 international design engineering technical conferences and computers and information in engineering conference*. American Society of Mechanical Engineers Digital Collection, 2008, pp. 941–947.

[103] T. Judendorfer, J. Fletcher, N. Hassanain, M. Mueller, and M. Muhr, "Challenges to machine windings used in electrical generators in wave and tidal power plants," in *2009 IEEE Conference on Electrical Insulation and Dielectric Phenomena*. IEEE, 2009, pp. 238–241.

[104] R. G. Montague, C. M. Bingham, and K. Atallah, "Magnetic gear dynamics for servo control," in *Melecon 2010 - 2010 15th IEEE Mediterranean Electrotechnical Conference*, April 2010, pp. 1192–1197.

[105] R. Crozier, B. Mcgilton, and M. Mueller, "Dynamic Model Testing of a Combined C-Gen Magnetic Gear System for an Oscillating Wave Surge Converter," *Asian Wave and Tidal Energy Conference - 2018*, 2018.

[106] P. Masarati, M. Morandini, and P. Mantegazza, "An efficient formulation for general-purpose multibody/multiphysics analysis," *Journal of computational and nonlinear dynamics.*, vol. 9, no. 4, 2014.

[107] O. Keysan, M. Mueller, R. Doherty, M. Hamilton, and A. McDonald, "C-GEN, a lightweight direct drive generator for marine energy converters," *5th IET International Conference on Power Electronics, Machines and Drives (PEMD 2010)*, pp. 244–244, 2010.

[108] M. Stålberg, R. Waters, O. Danielsson, and M. Leijon, "Influence of generator damping on peak power and variance of power for a direct drive wave energy converter," *Journal of offshore mechanics and Arctic engineering*, vol. 130, no. 3, p. 031003, 2008.

[109] R. Montague, C. Bingham, and K. Atallah, "Servo control of magnetic gears," *IEEE/ASME Transactions on Mechatronics*, vol. 17, no. 2, pp. 269–278, April 2012.

[110] Y. H. Yu, D. S. Jenne, R. Thresher, A. Copping, S. Geerlofs, and L. A. Hanna, "Reference Model 5 (RM5): Oscillating Surge Wave Energy Converter," 1 2015, [last accessed: 26/09/19]. [Online]. Available: https://www.nrel.gov/docs/fy15osti/62861.pdf

[111] Wec-sim (wave energy converter simulator). National Renewable Energy Laboratory (NREL) and Sandia National Laboratories (Sandia). [last accessed: 26/09/19]. [Online]. Available: https://wec-sim.github.io/WEC-Sim/index.html

[112] R. Crozier and M. Mueller, "Development of a multi-rate wave-to-wire modelling tool," in *Proceedings of the 12th European Wave and Tidal Energy Conference (EWTEC)*, 2017.

[113] RenewNet Foundry. [last accessed: 26/09/19]. [Online]. Available: https://sourceforge.net/projects/rnfoundry/

[114] e-Drive: All Electrical Drive Train for Marine Energy Converters - Homepage. [last accessed: 26/09/19]. [Online]. Available: https://www.edrive.eng.ed.ac.uk/

[115] B. McGilton, R. Crozier, and M. Mueller, "Magnetic Gear Design for an Oscillating Wave Surge Converter," *Proceddings of Europeant Wave and Tidal Energy Conference, 2017*, no. 421, pp. 1–7, 2017.

[116] Fountain Design LTD Hompage. [last accessed: 26/09/19]. [Online]. Available: http://www.fountaindesign.co.uk//

[117] The FloWTurb Project. [last accessed: 26/09/19]. [Online]. Available: https://www.flowturb.eng.ed.ac.uk/

[118] A. Chipperfield, P. Fleming, H. Pohlheim, and C. Fonseca, "Genetic algorithm toolbox user guide," 2007, [last accessed: 26/09/19]. [Online]. Available: http://codem.group.shef.ac.uk/index.php/ga-toolbox

[119] B. McGilton, R. Crozier, and M. Mueller, "Optimisation procedure for designing a magnetic gear," *The Journal of Engineering*, vol. 2017, no. 13, pp. 840–843, 2017.

[120] N. J. Baker, M. A. Mueller, and M. A. H. Raihan, "All electric drive train for wave energy power take off," in *5th IET International Conference on Renewable Power Generation (RPG) 2016*, Sept 2016, pp. 1–6.

[121] M. A. Mueller and N. J. Baker, "Modelling the performance of the vernier hybrid machine," *IEE Proceedings - Electric Power Applications*, vol. 150, no. 6, pp. 647–654, Nov 2003.

[122] L. Jian, K. T. Chau, and J. Z. Jiang, "A magnetic-geared outer-rotor permanent-magnet brushless machine for wind power generation," *IEEE Transactions on Industry Applications*, vol. 45, no. 3, pp. 954–962, 2009.

[123] G. Jungmayr, J. Loeffler, B. Winter, F. Jeske, and W. Amrhein, "Magnetic gear: Radial force, cogging torque, skewing, and optimization," *IEEE Transactions on Industry Applications*, vol. 52, no. 5, pp. 3822–3830, 2016.

[124] M. A. Mueller and N. J. Baker, "Direct drive electrical power take-off for offshore marine energy converters," *Proceedings of the Institution of Mechanical Engineers, Part A: Journal of Power and Energy*, vol. 219, no. 3, pp. 223–234, 2005. [Online]. Available: https://doi.org/10.1243/095765005X7574

[125] J. . Yonnet, "Passive magnetic bearings with permanent magnets," *IEEE Transactions on Magnetics*, vol. 14, no. 5, pp. 803–805, Sep. 1978.

[126] C. G. Anderson, "First assessment of the magnetic-hydrostatic main bearing proposed for the duck wave-energy converter," 1985, PhD Thesis.

[127] J. W. Burchell, "Advancement of direct drive generator systems for offshore renewable energy production," 2018, PhD Thesis.

[128] J. I. Barajas Solano, "Novel active magnetic bearings for direct drive c-gen linear generator," 2017, PhD Thesis.

Appendix A

Simulink Dynamic Model

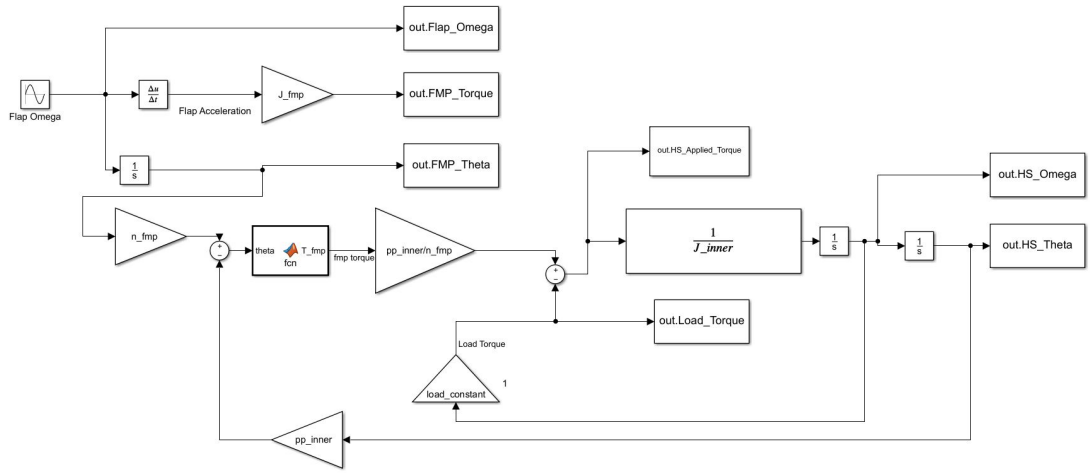

Figure A.1: Simulink Dynamic Model for Simply Driven Gear and Load Model comparison

Appendix B

Geared Speed-Torque Relationship

The power at the generator side, P_{gen}, will be the power on the motor side, P_{mot}, with losses related to efficiency:

$$P_{gen} = P_{mot}\eta \tag{B.1}$$

The mechanical power of the motor and generator is calculated from the measured torque, τ, and speed, ω, of each machine:

$$P_{mot} = \tau_{mot}\omega_{mot} \tag{B.2}$$

$$P_{gen} = \tau_{gen}\omega_{gen} \tag{B.3}$$

Equation A.1 can then be rewritten as:

$$\tau_{mot}\omega_{mot} = \frac{\tau_{gen}\omega_{gen}}{\eta} \tag{B.4}$$

The generator speed will be the motor speed times the gear ratio, GR, while the generator remains a fixed controlled value giving:

$$\tau_{mot}\omega_{mot} = \frac{\tau_{gen}\omega_{mot}GR}{\eta} \tag{B.5}$$

If a change, Δ, is made in the motor's speed $\Delta\omega_{mot}$, the generator speed will increase

by this change times the gear ratio GR giving;

$$\tau_{mot}\Delta\omega_{mot} = \frac{\tau_{gen}(\Delta\omega_{mot}GR)}{\eta} \tag{B.6}$$

Since τ_{gen} is constant in the test setup, for the power to balance as in equation (B.1) there must be a corresponding rise in power on the motor side to account for the geared increase on the generator side and the motor torque must change to make this balance. The change in motor torque, $\Delta\tau_{mot}$, can then be described as:

$$\Delta\tau_{mot} \propto \Delta\omega_{mot}\frac{\tau_{gen}GR}{\eta} \tag{B.7}$$

Appendix C

Gear Load Test Measurements

The results of the geared system tests are shown in the following plots. The results are listed in Figure C.1.

Gear Load Test Results Key

		Load Torque (Nm)																
		0	0.2	0.4	0.6	0.8	1	1.2	1.4	1.6	1.8	2	2.2	2.4	2.6	2.8	3	3.2	3.4
Speed (rpm)	6	A0	A1	A2	A3	A4	A5	A6	A7	A8	A9	A10	A11	A12	A13	A14	A15	A16	A17
	8	B0	B1	B2	B3	B4	B5	B6	B7	B8	B9	B10	B11	B12	B13	B14	B15	B16	
	10	C0	C1	C2	C3	C4	C5	C6	C7	C8	C9	C10	C11	C12	C13	C14	C15		
	12	D0	D1	D2	D3	D4	D5	D6	D7	D8	D9	D10	D11	D12	D13	D14	D15		
	14	E0	E1	E2	E3	E4	E5	E6	E7	E8	E9	E10	E11	E12	E13				
	16	F0	F1	F2	F3	F4	F5	F6	F7	F8	F9	F10	F11	F12					
	18	G0	G1	G2	G3	G4	G5	G6	G7	G8	G9	G10	G11						

Figure C.1: Gear load test results key

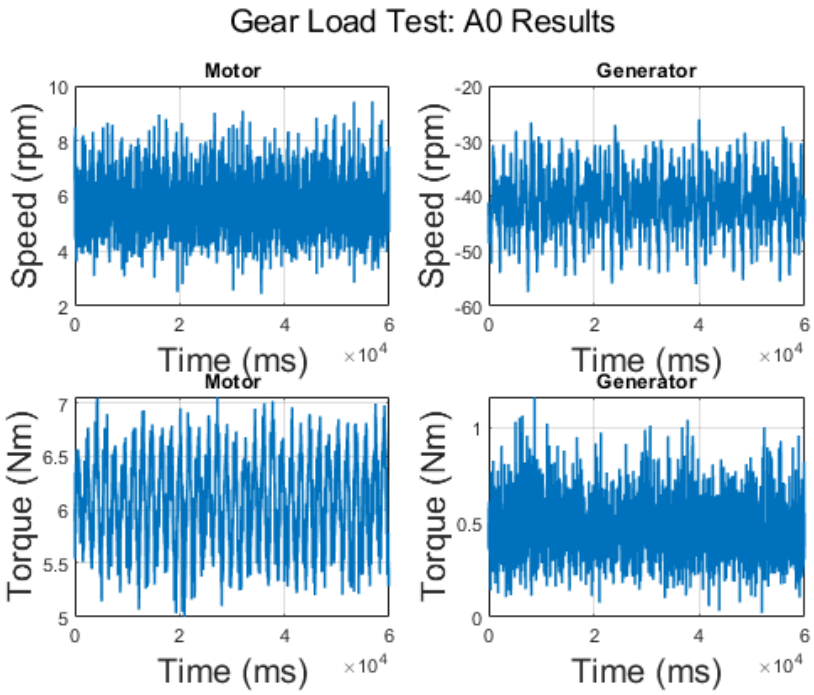

Figure C.2: Gear load test results: A0

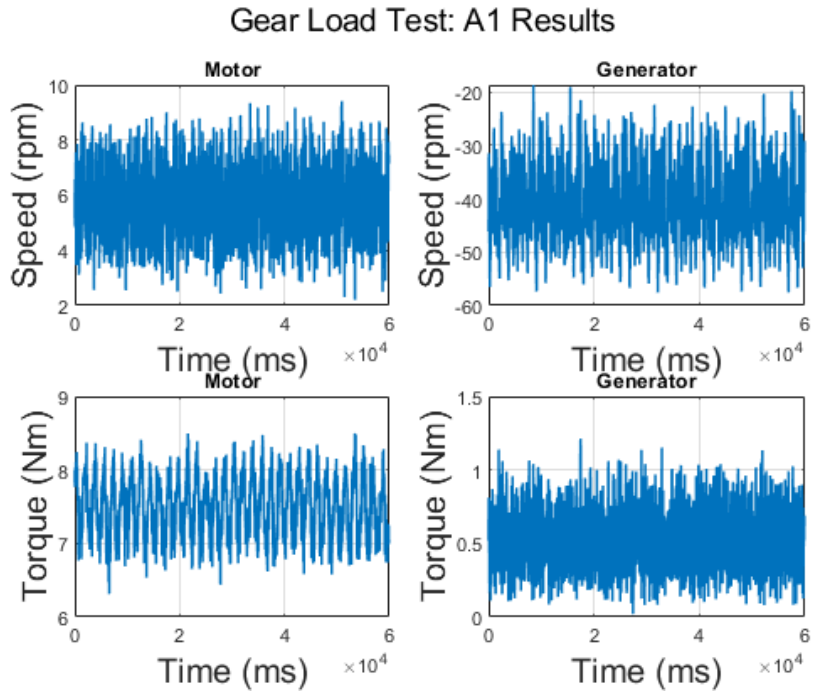

Figure C.3: Gear load test results: A1

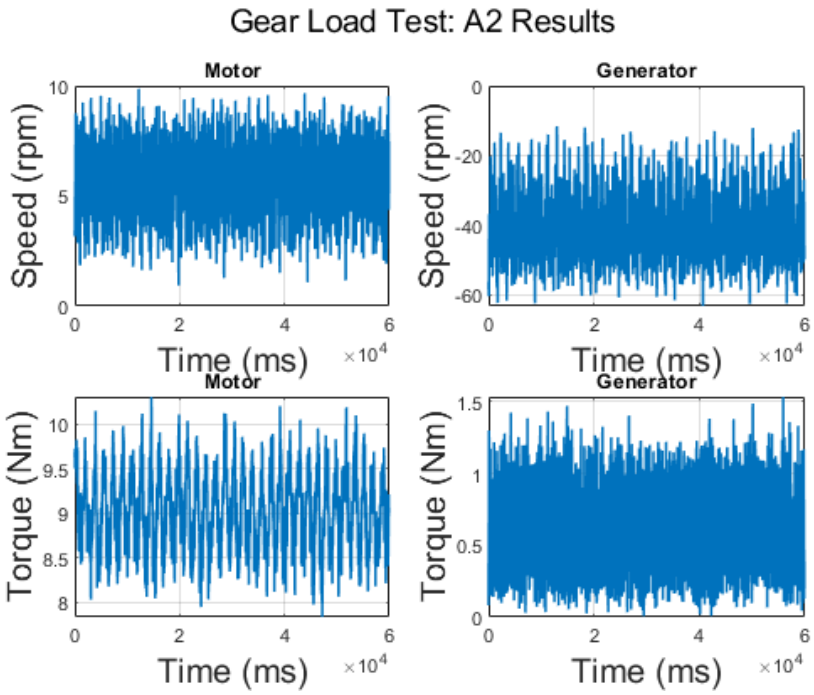

Figure C.4: Gear load test results: A2

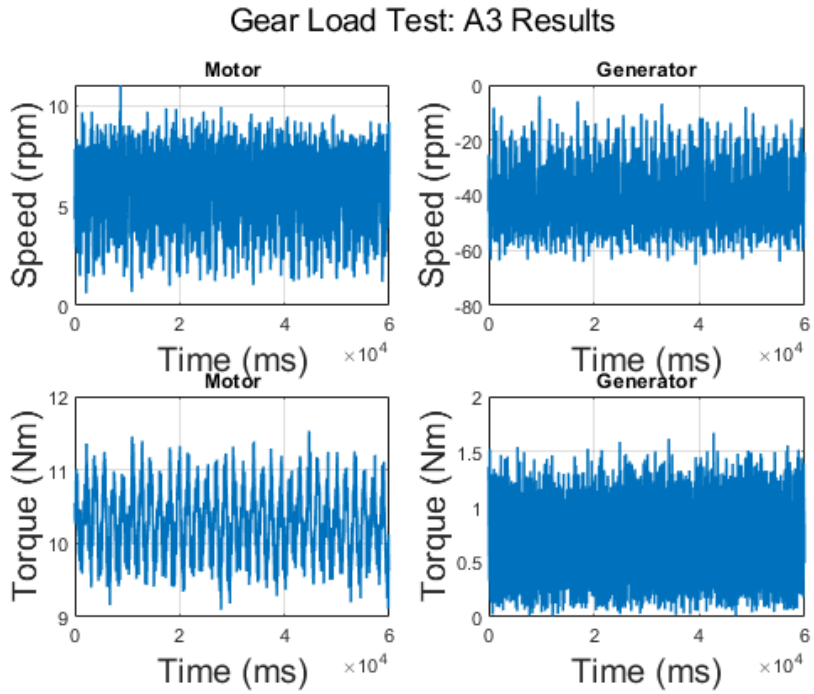

Figure C.5: Gear load test results: A3

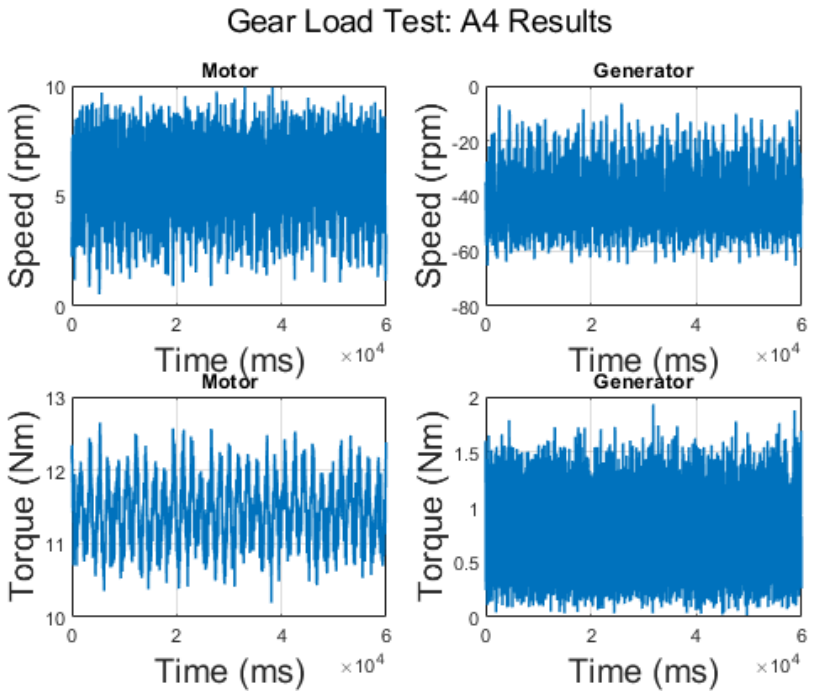

Figure C.6: Gear load test results: A4

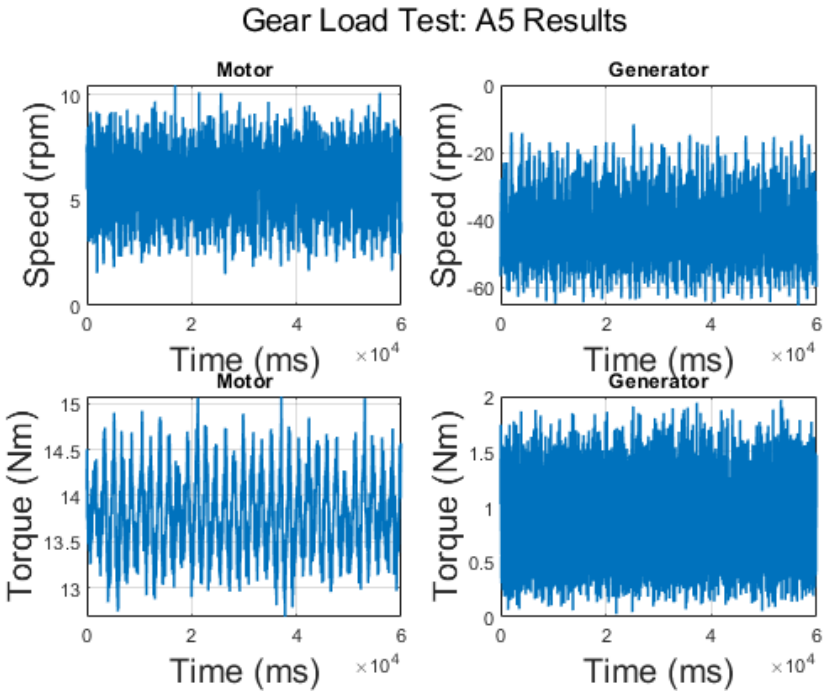

Figure C.7: Gear load test results: A5

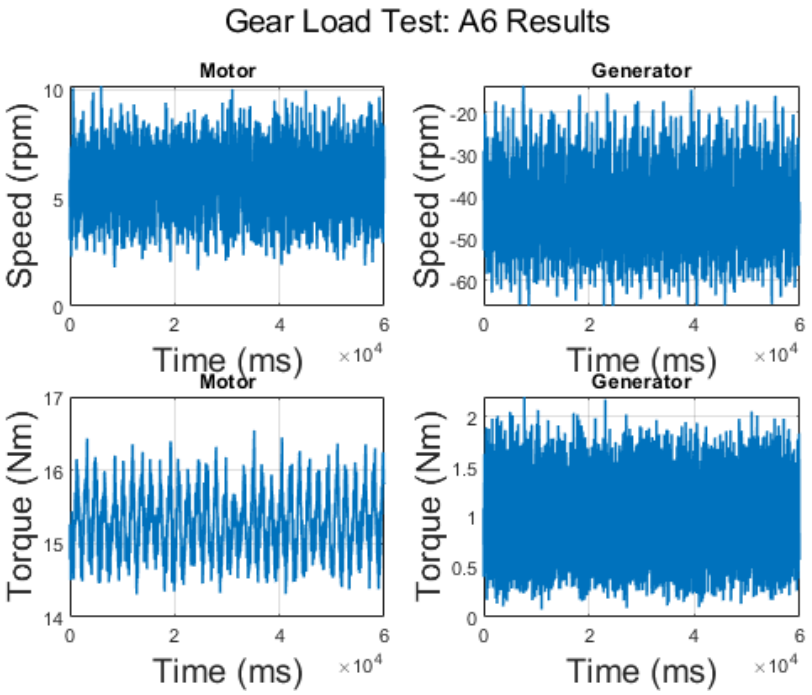

Figure C.8: Gear load test results: A6

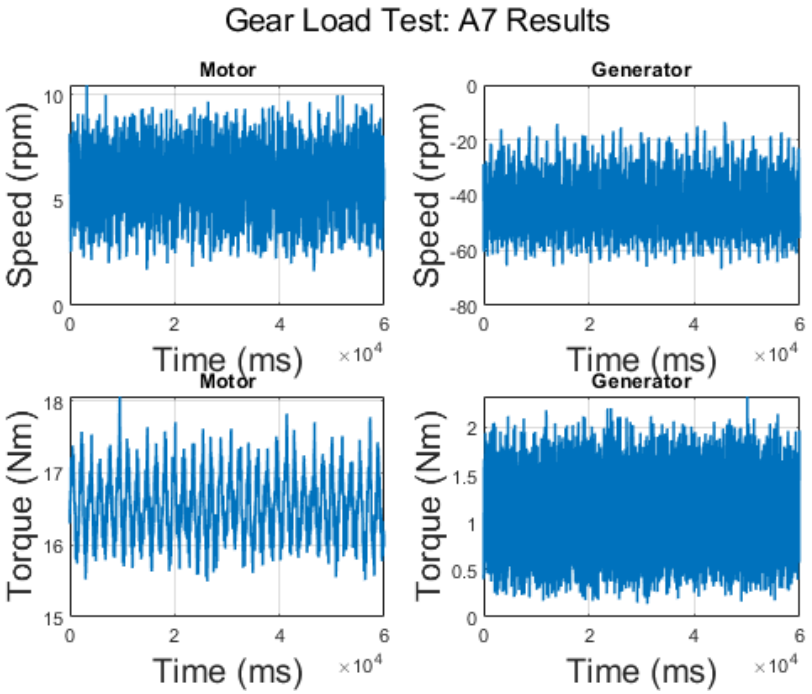

Figure C.9: Gear load test results: A7

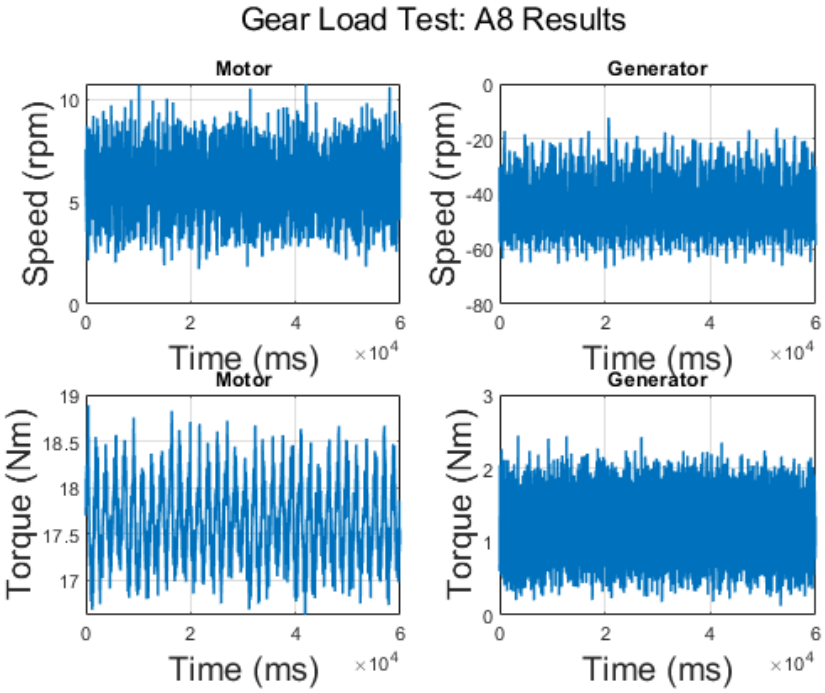

Figure C.10: Gear load test results: A8

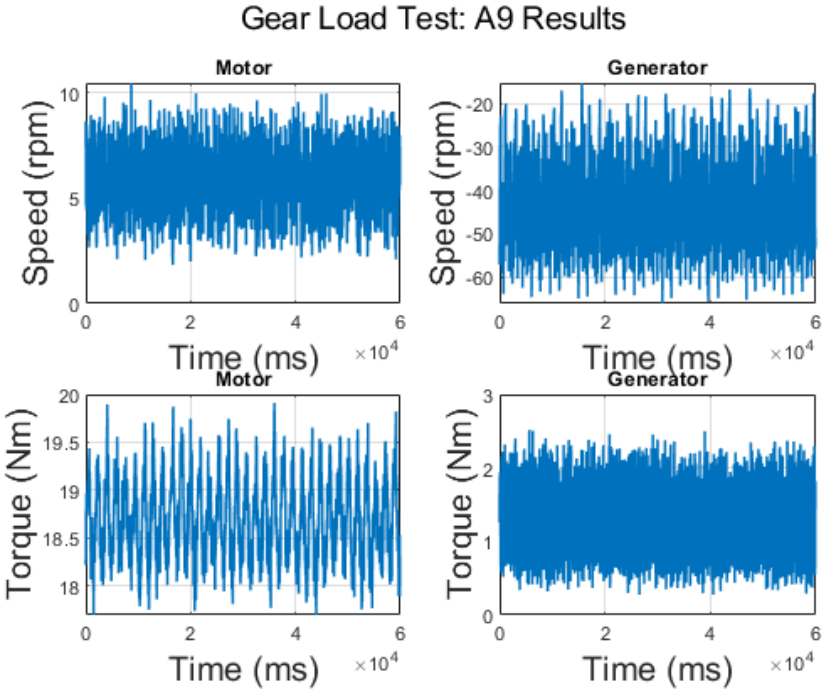

Figure C.11: Gear load test results: A9

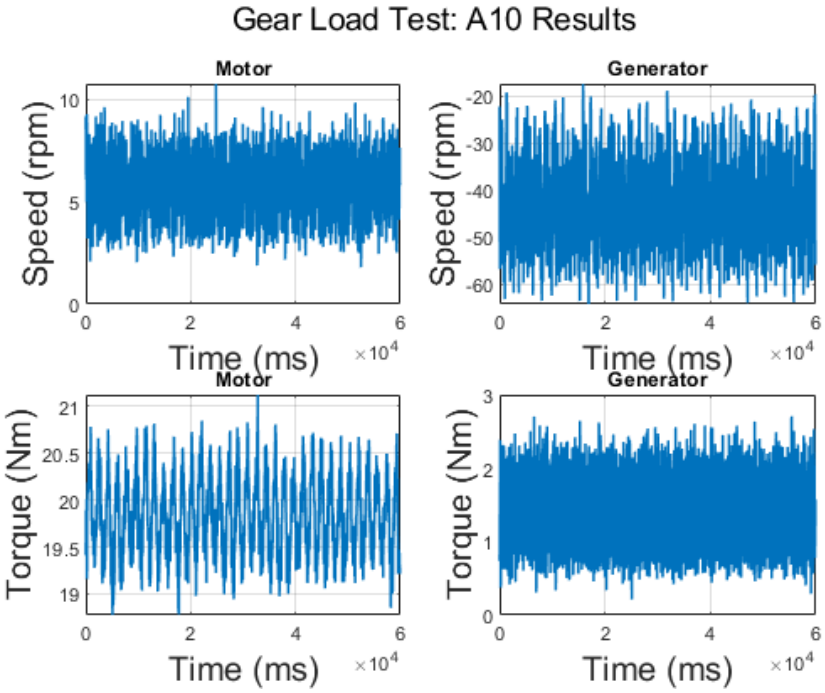

Figure C.12: Gear load test results: A10

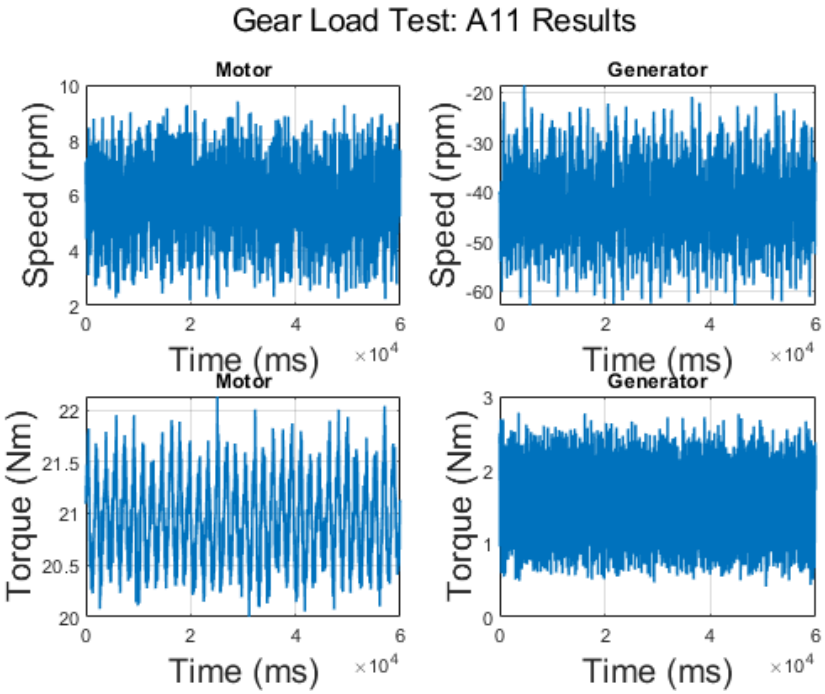

Figure C.13: Gear load test results: A11

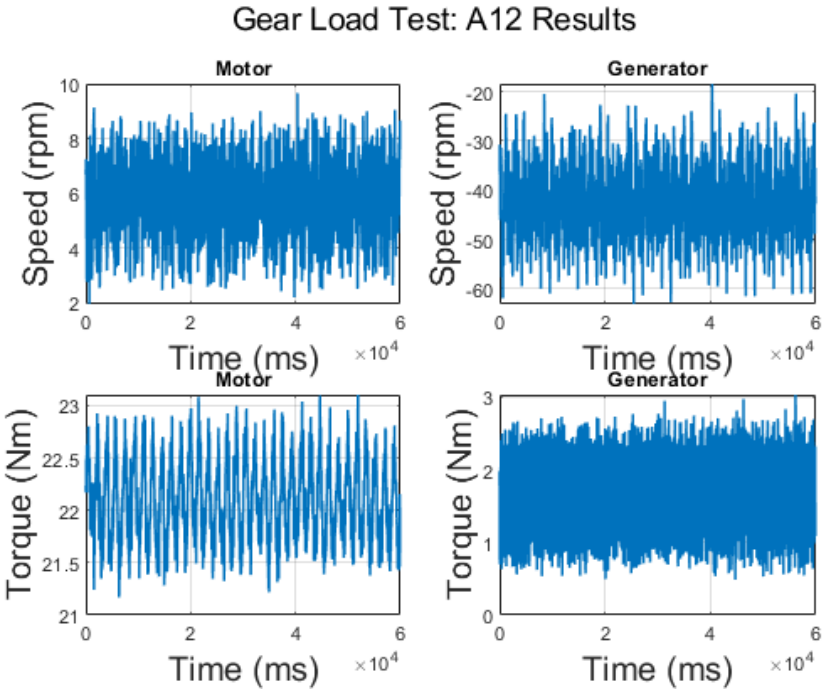

Figure C.14: Gear load test results: A12

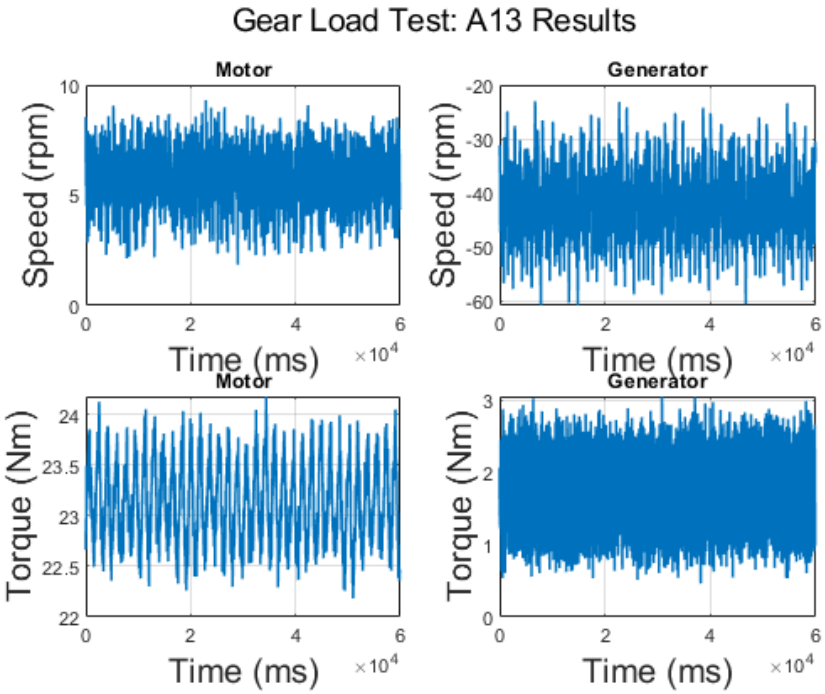

Figure C.15: Gear load test results: A13

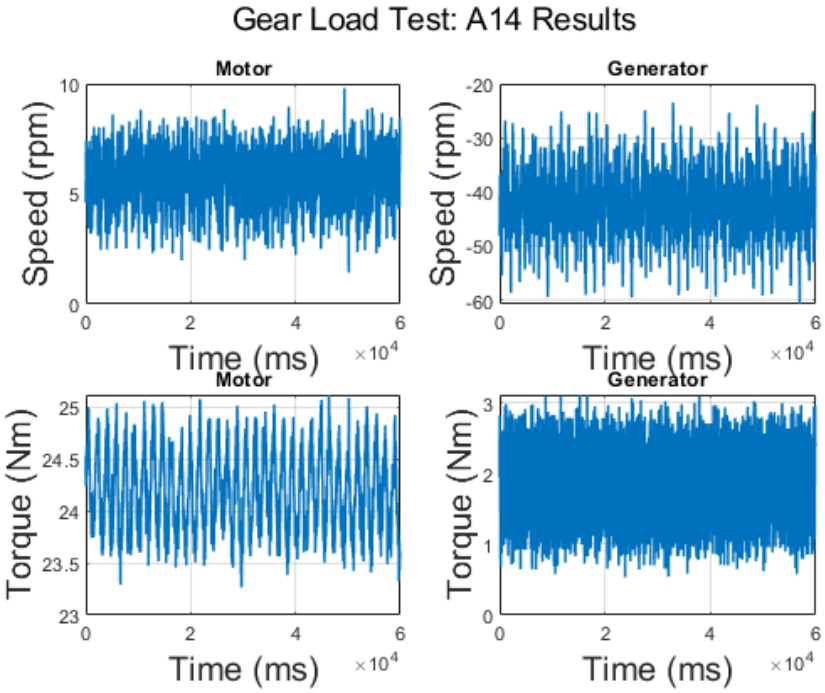

Figure C.16: Gear load test results: A14

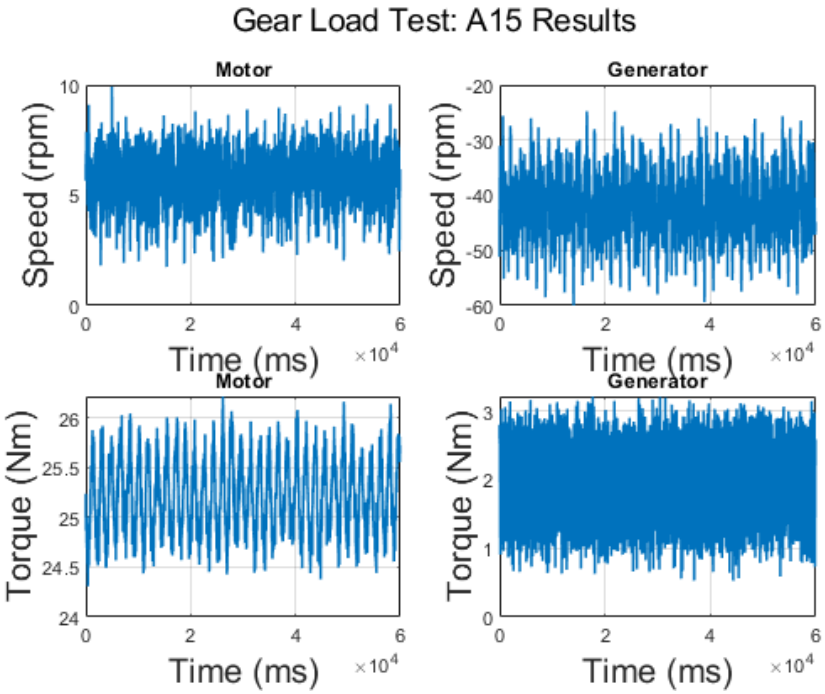

Figure C.17: Gear load test results: A15

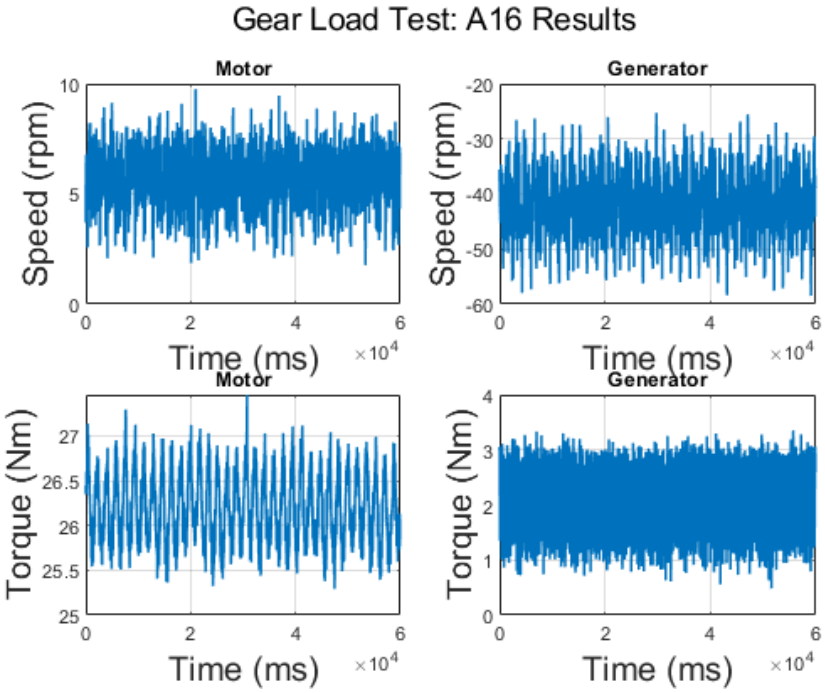

Figure C.18: Gear load test results: A16

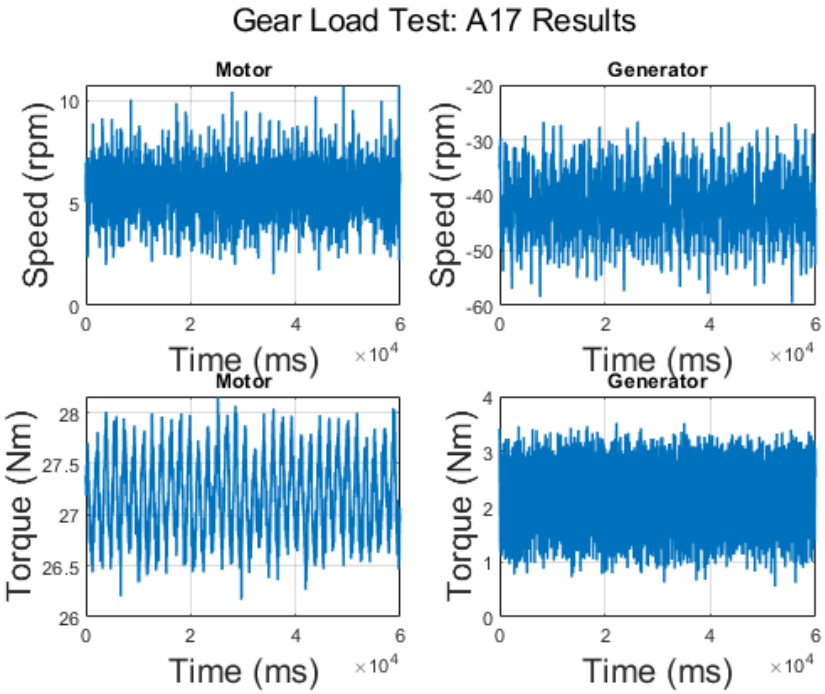

Figure C.19: Gear load test results: A17

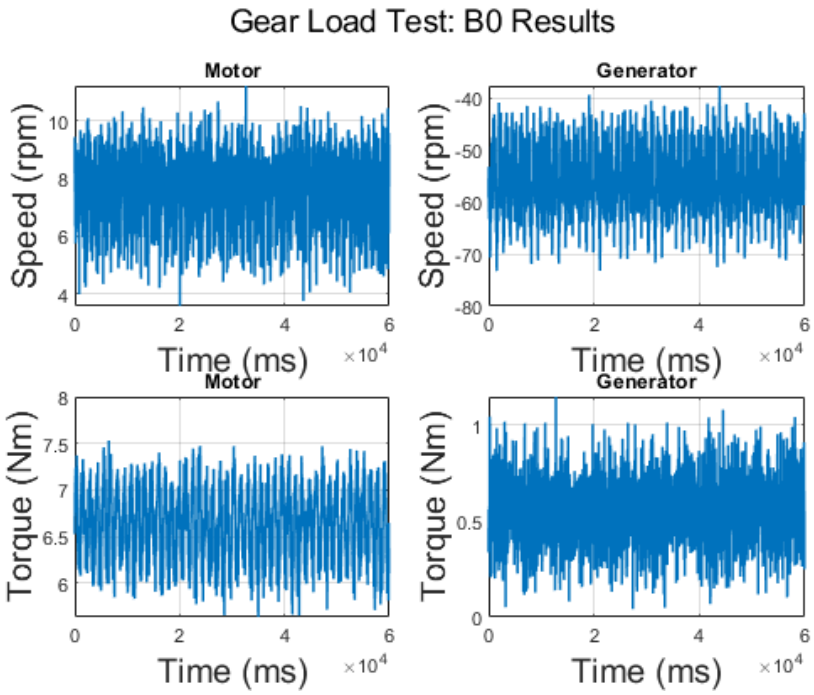

Figure C.20: Gear load test results: B0

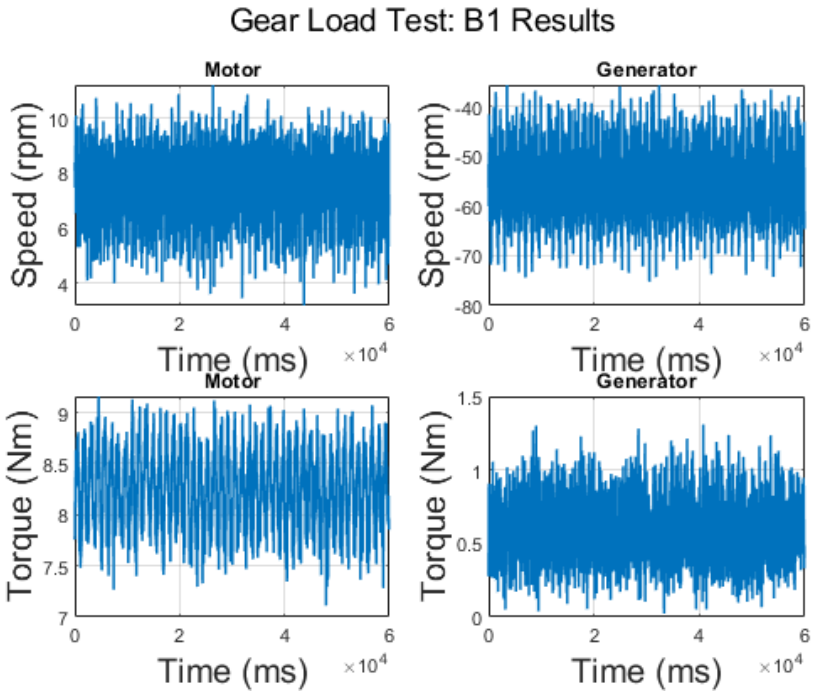

Figure C.21: Gear load test results: B1

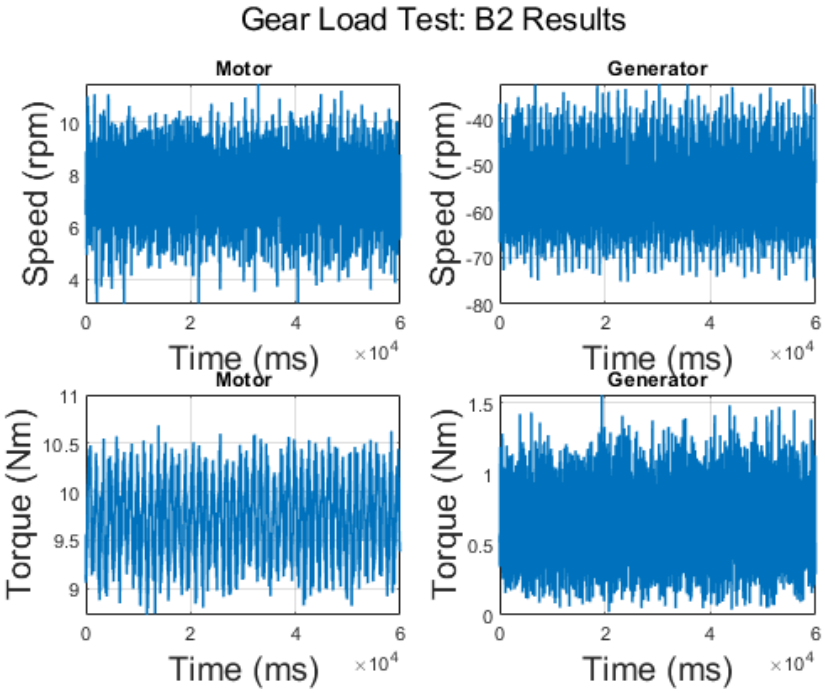

Figure C.22: Gear load test results: B2

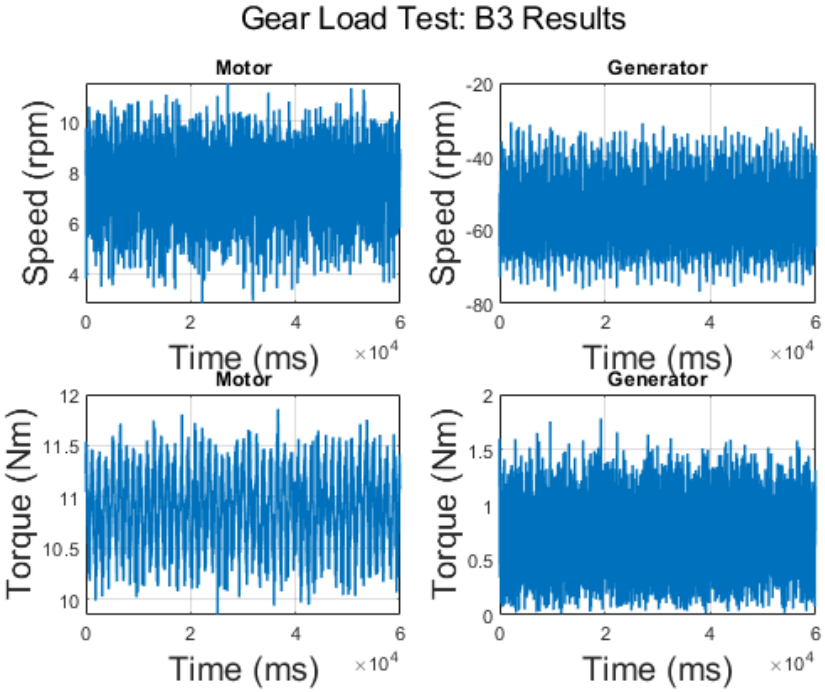

Figure C.23: Gear load test results: B3

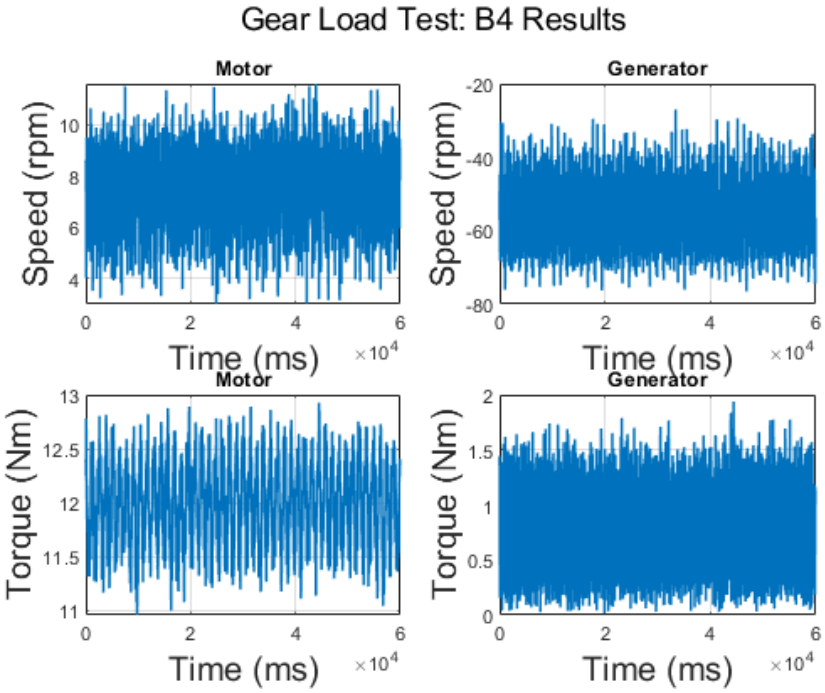

Figure C.24: Gear load test results: B4

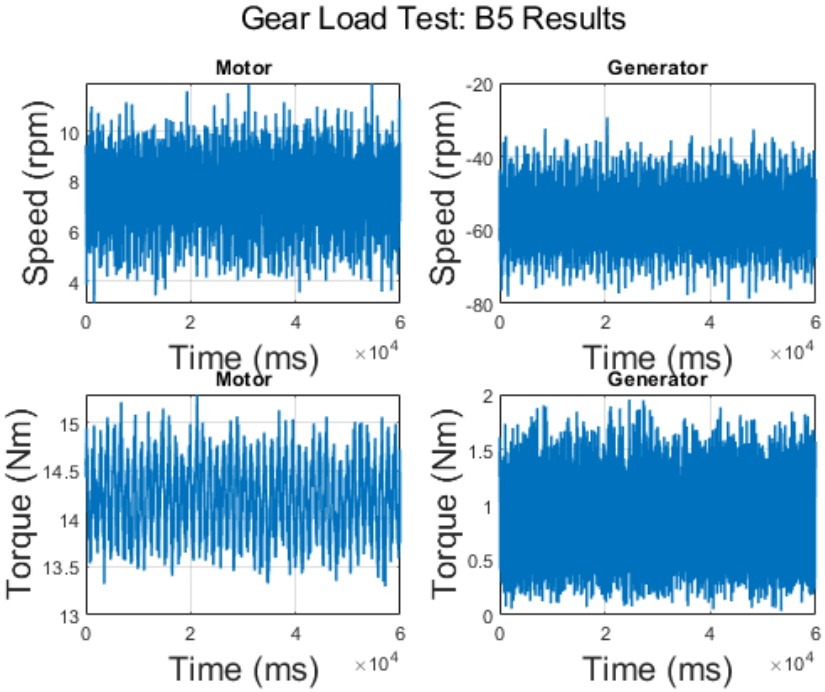

Figure C.25: Gear load test results: B5

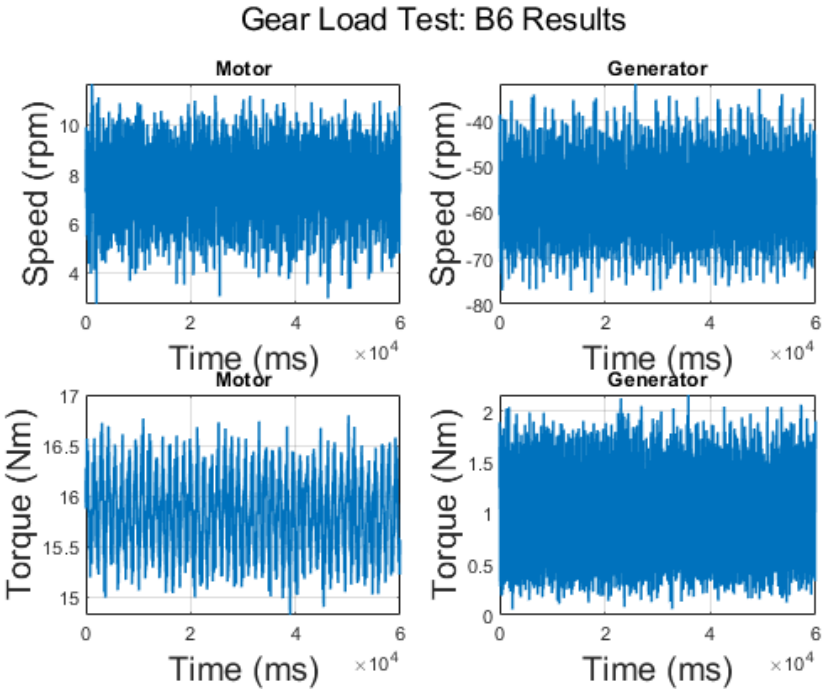

Figure C.26: Gear load test results: B6

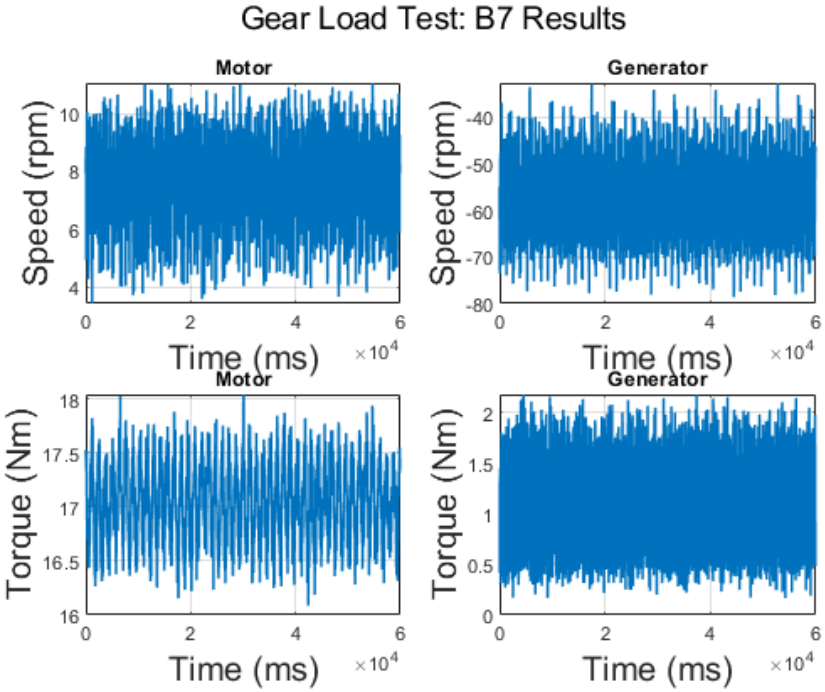

Figure C.27: Gear load test results: B7

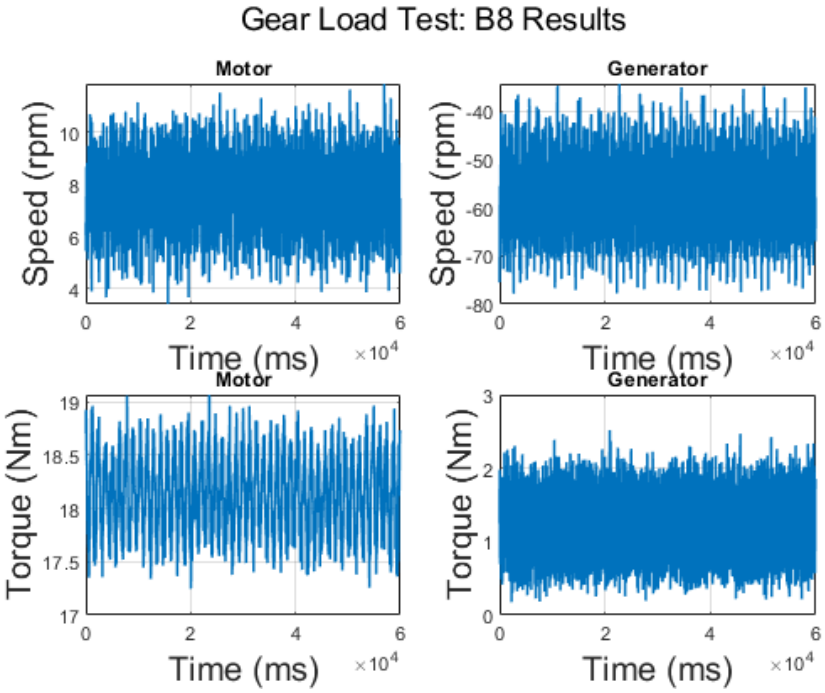

Figure C.28: Gear load test results: B8

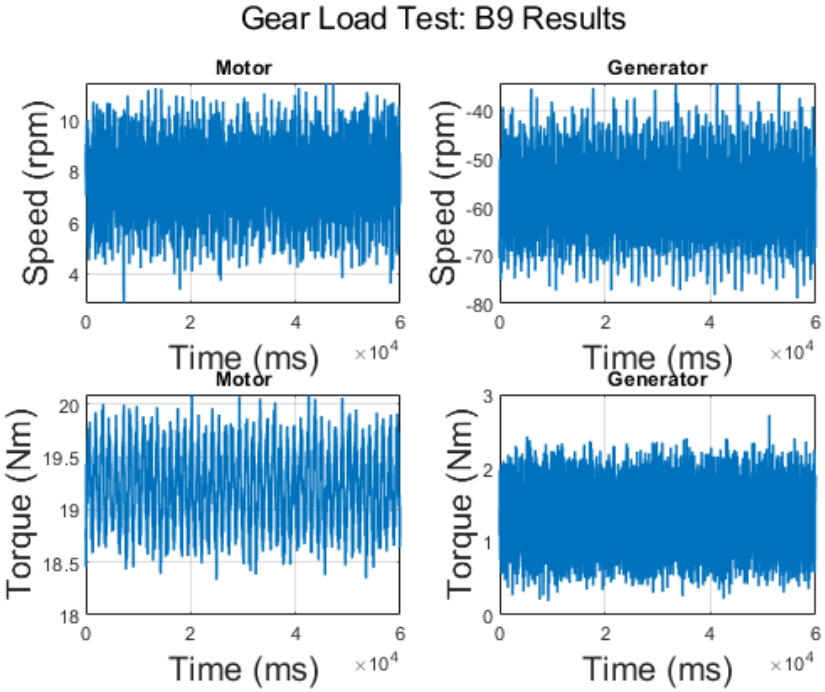

Figure C.29: Gear load test results: B9

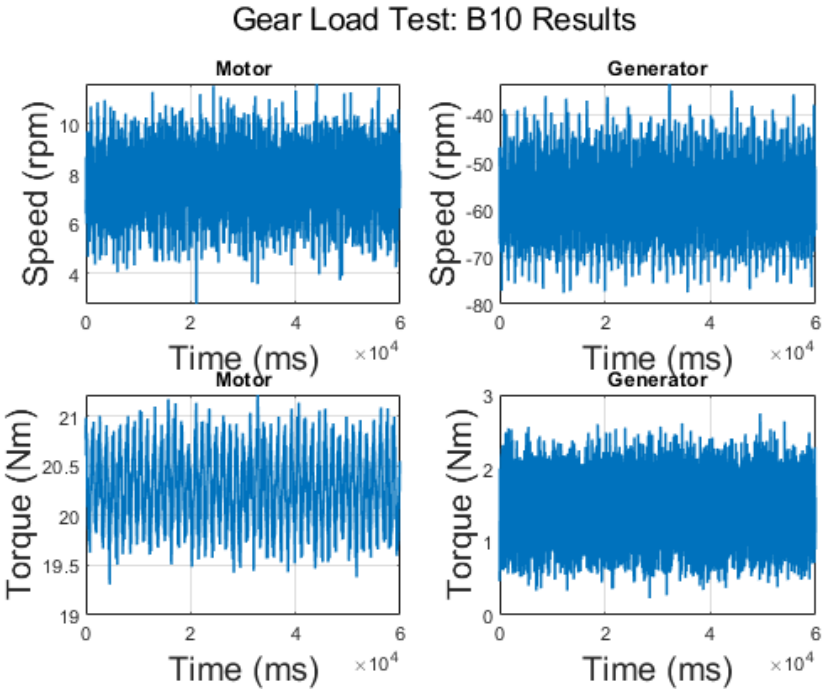

Figure C.30: Gear load test results: B10

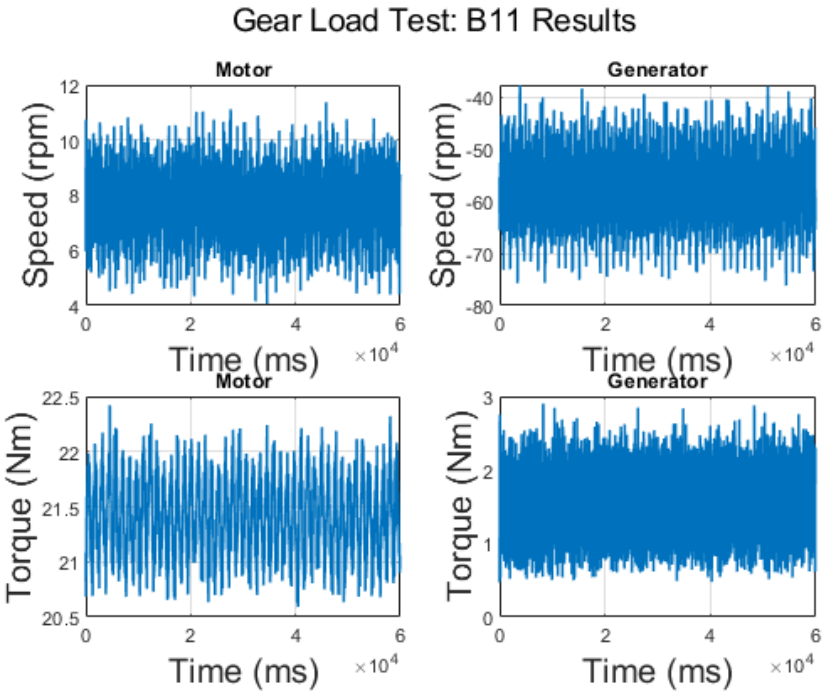

Figure C.31: Gear load test results: B11

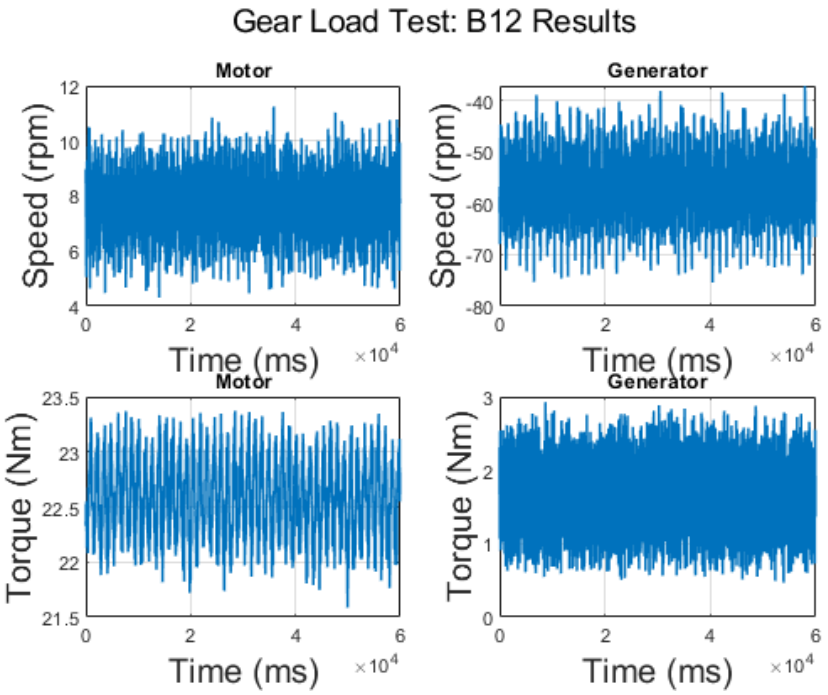

Figure C.32: Gear load test results: B12

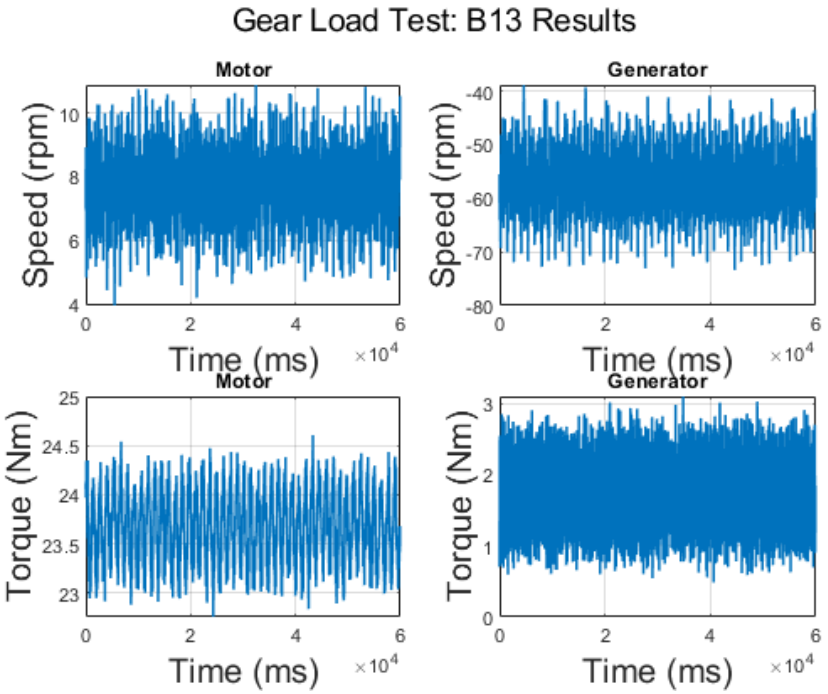

Figure C.33: Gear load test results: B13

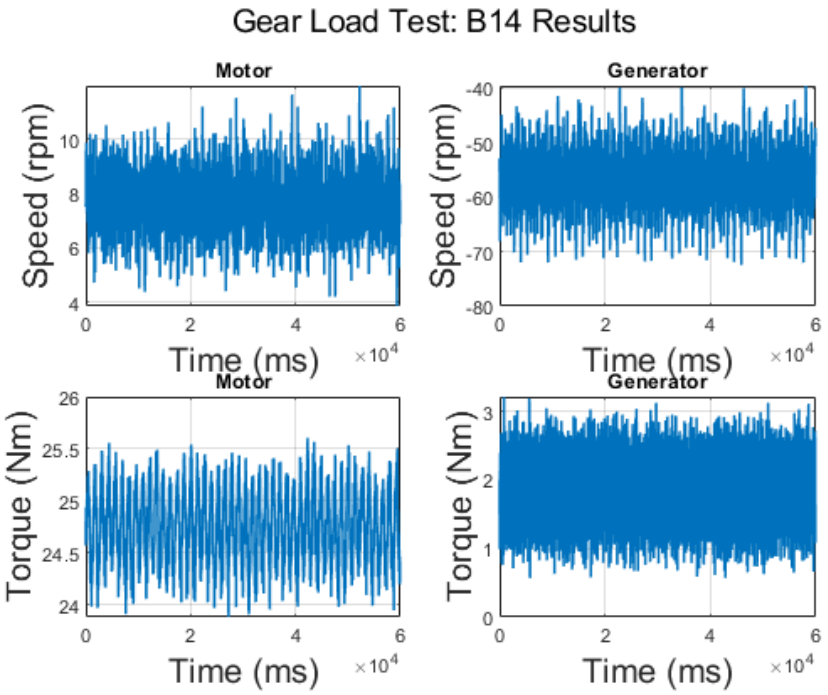

Figure C.34: Gear load test results: B14

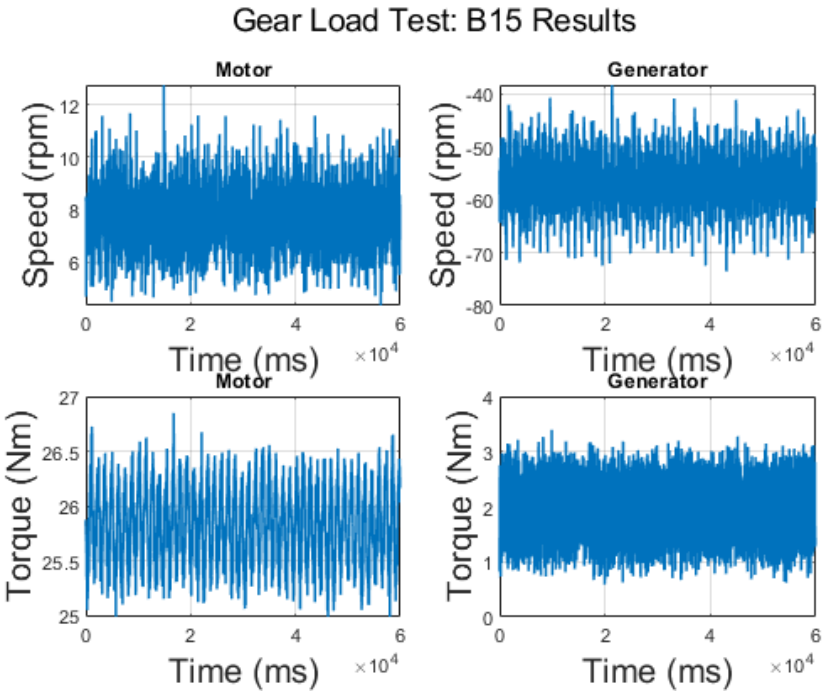

Figure C.35: Gear load test results: B15

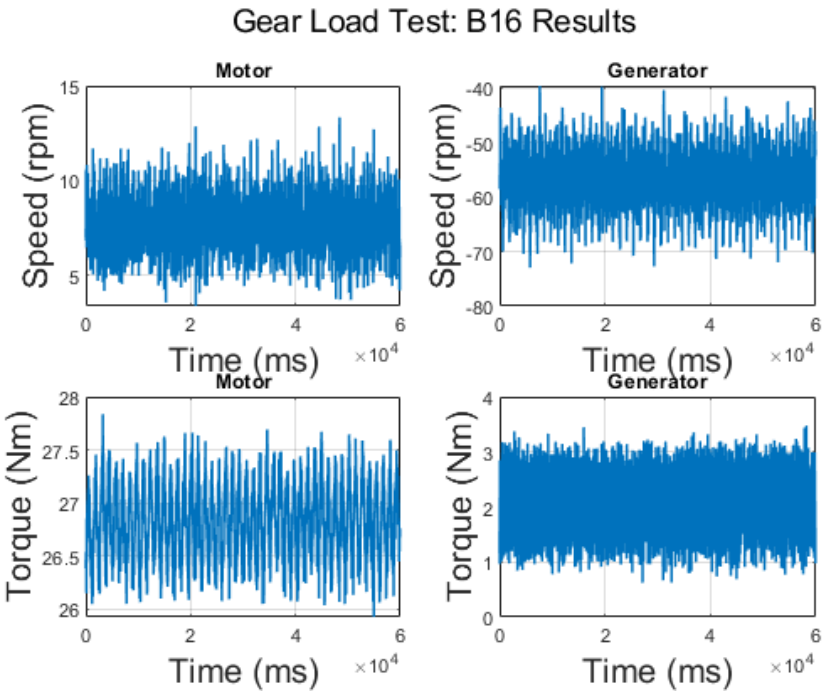

Figure C.36: Gear load test results: B16

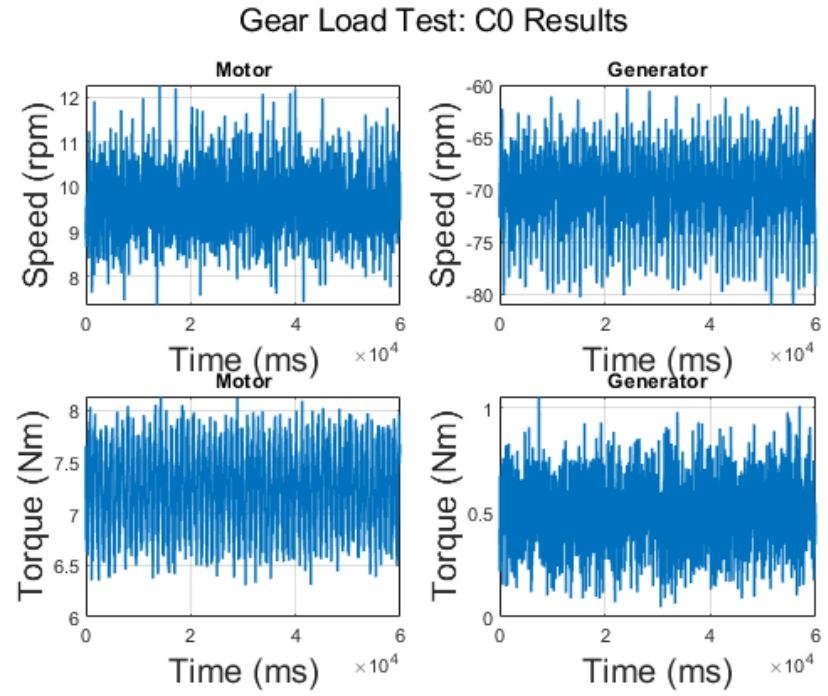

Figure C.37: Gear load test results: C0

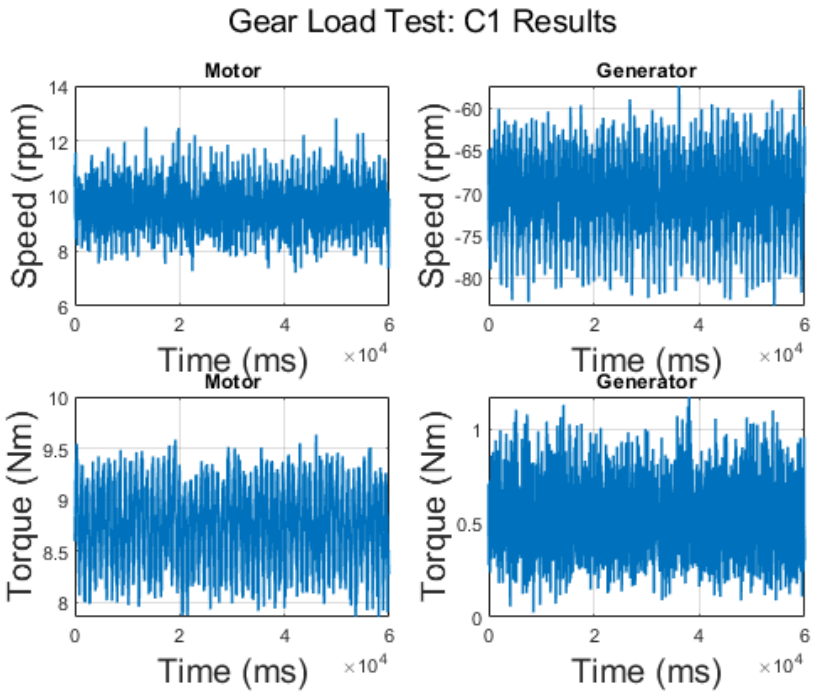

Figure C.38: Gear load test results: C1

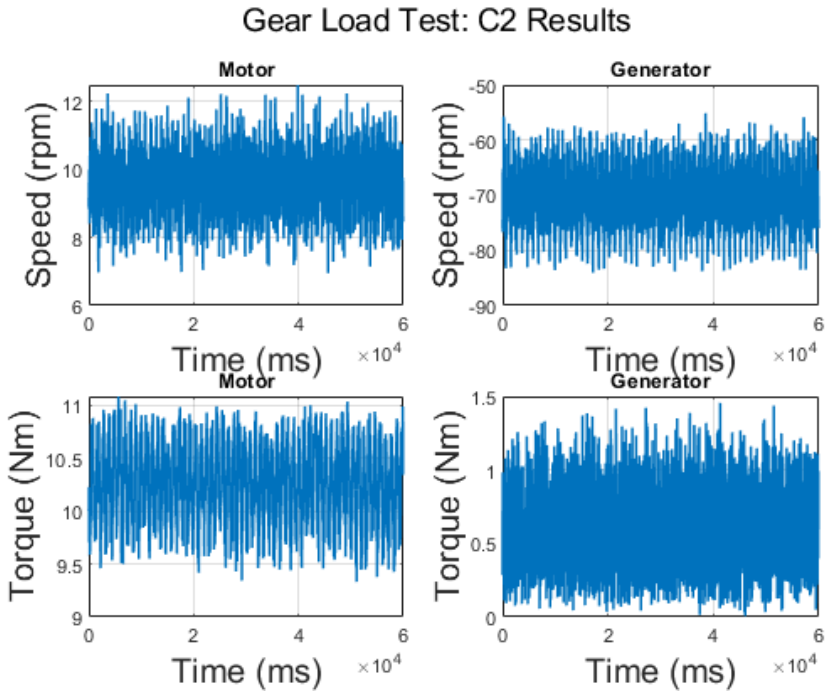

Figure C.39: Gear load test results: C2

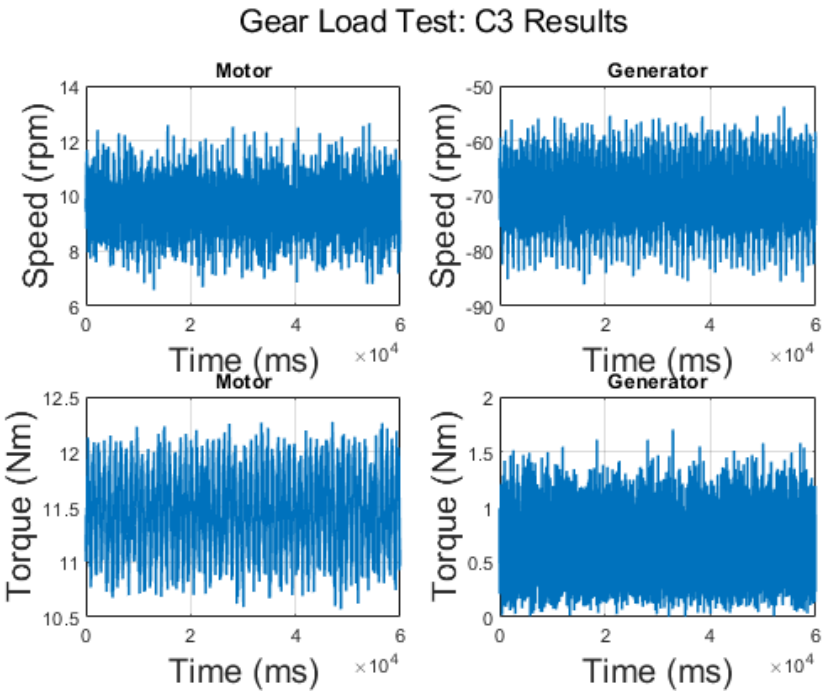

Figure C.40: Gear load test results: C3

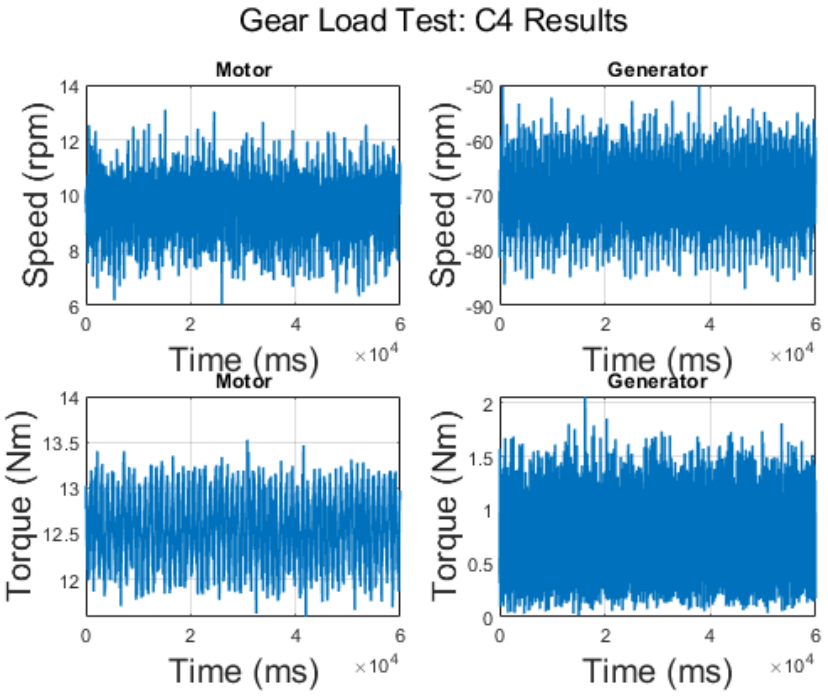

Figure C.41: Gear load test results: C4

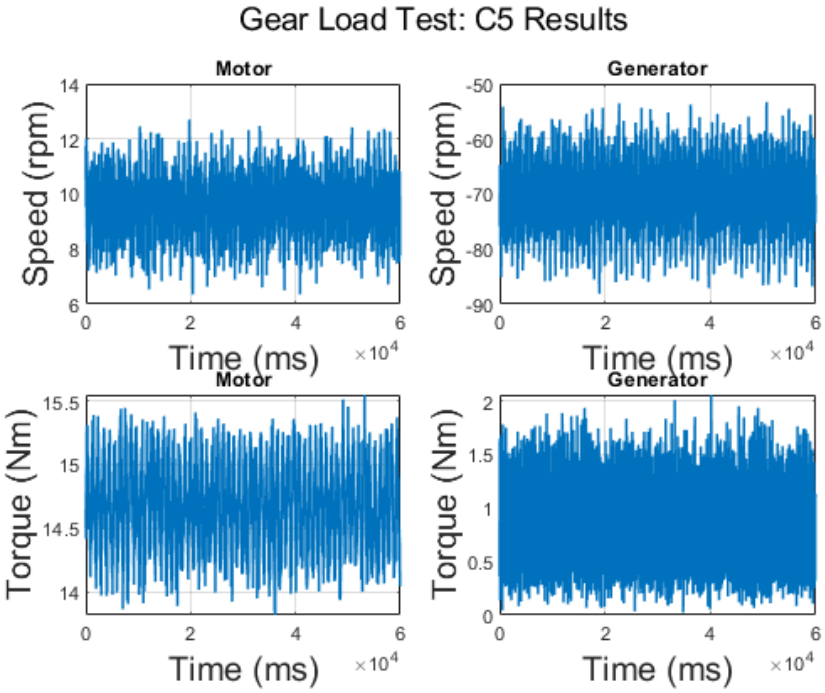

Figure C.42: Gear load test results: C5

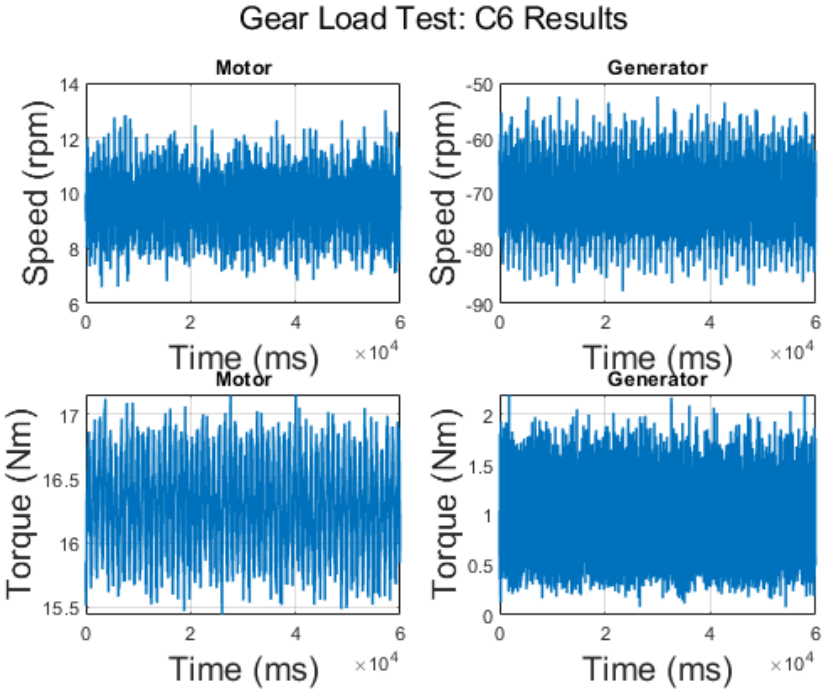

Figure C.43: Gear load test results: C6

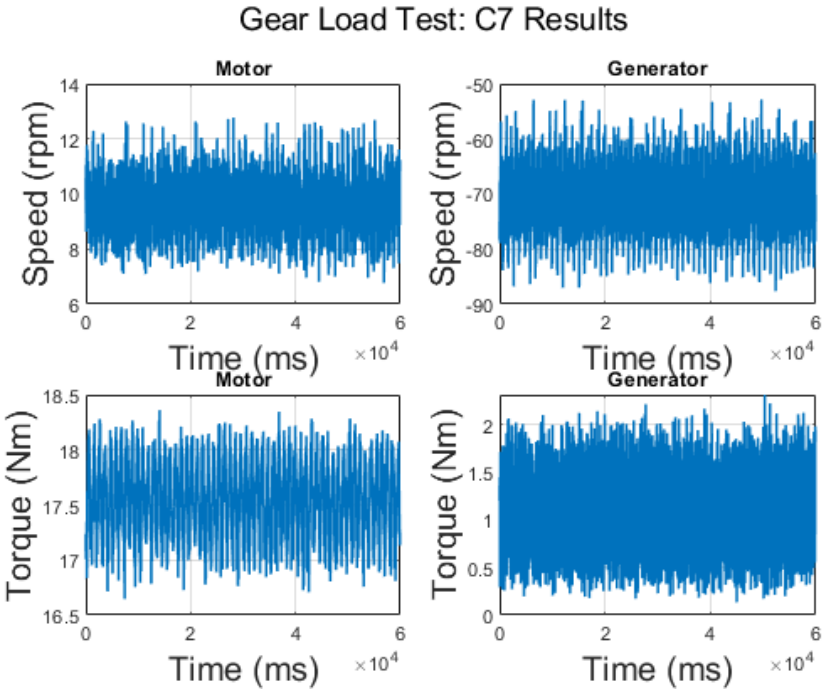

Figure C.44: Gear load test results: C7

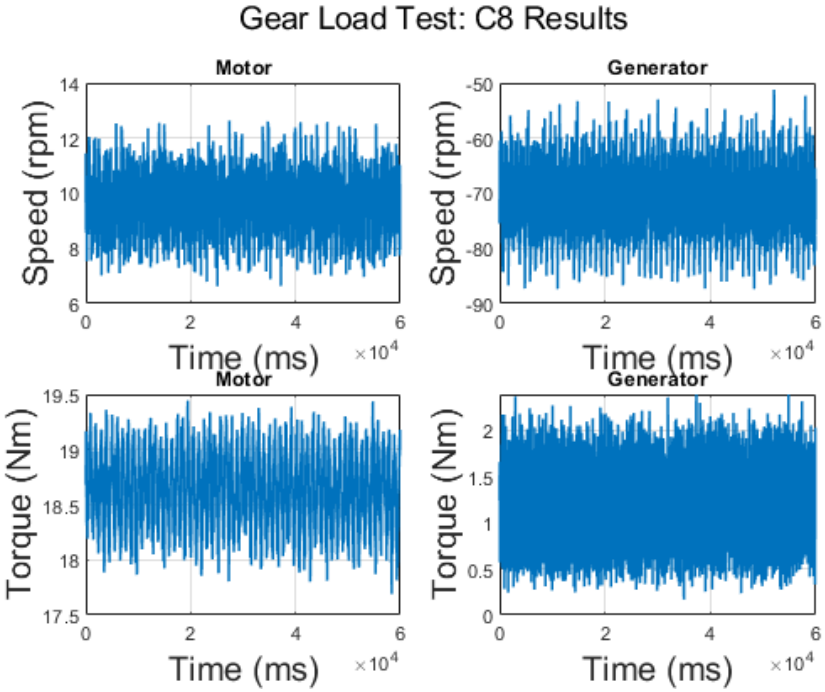

Figure C.45: Gear load test results: C8

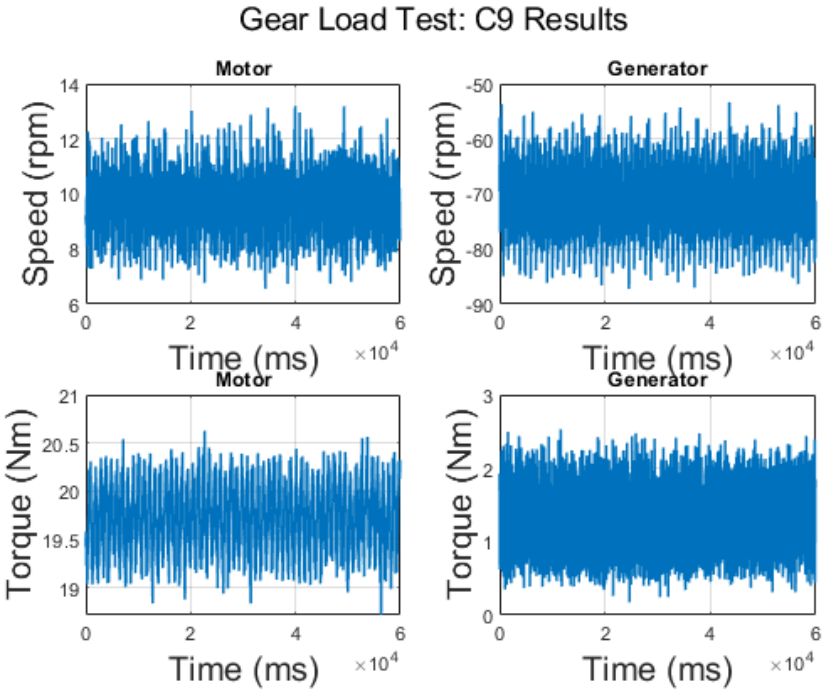

Figure C.46: Gear load test results: C9

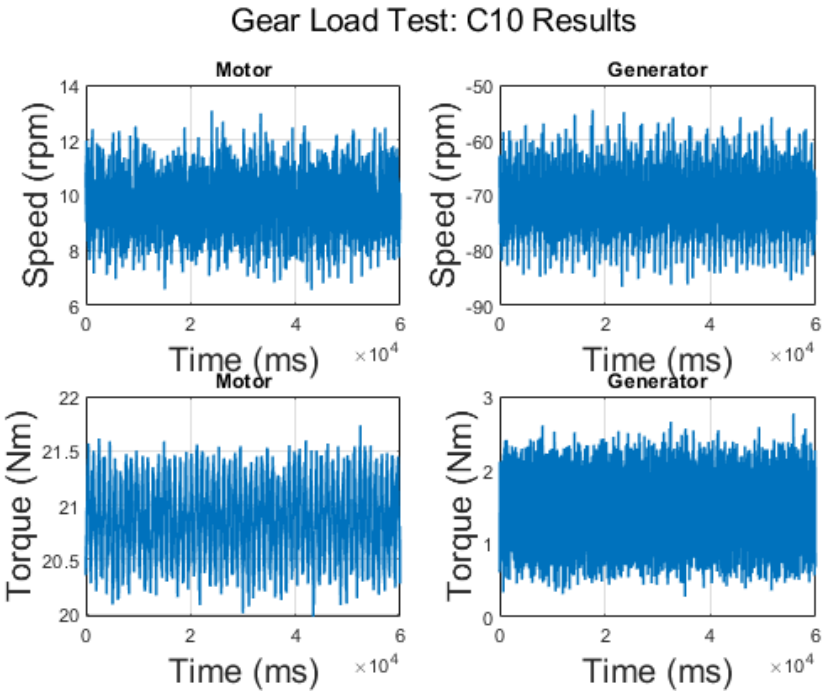

Figure C.47: Gear load test results: C10

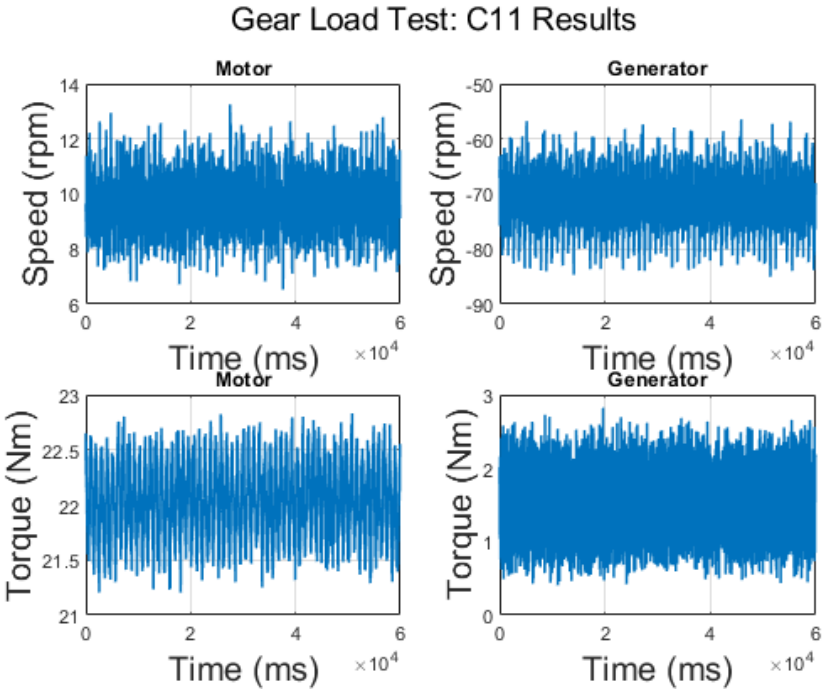

Figure C.48: Gear load test results: C11

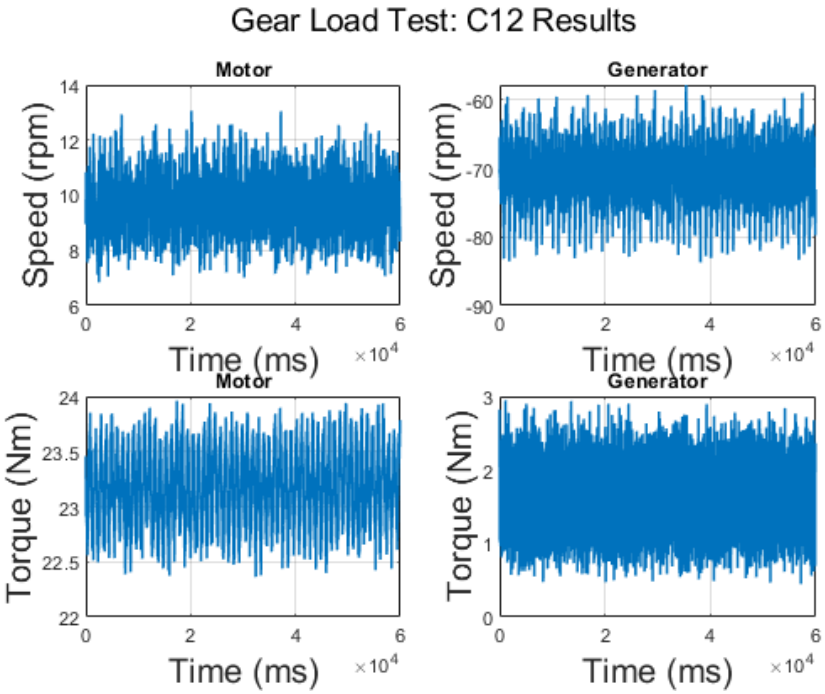

Figure C.49: Gear load test results: C12

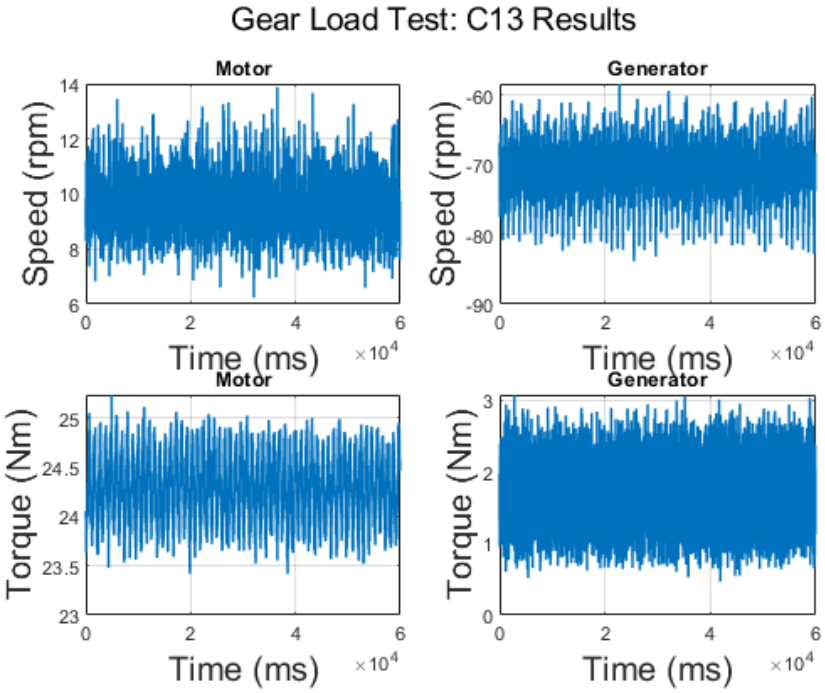

Figure C.50: Gear load test results: C13

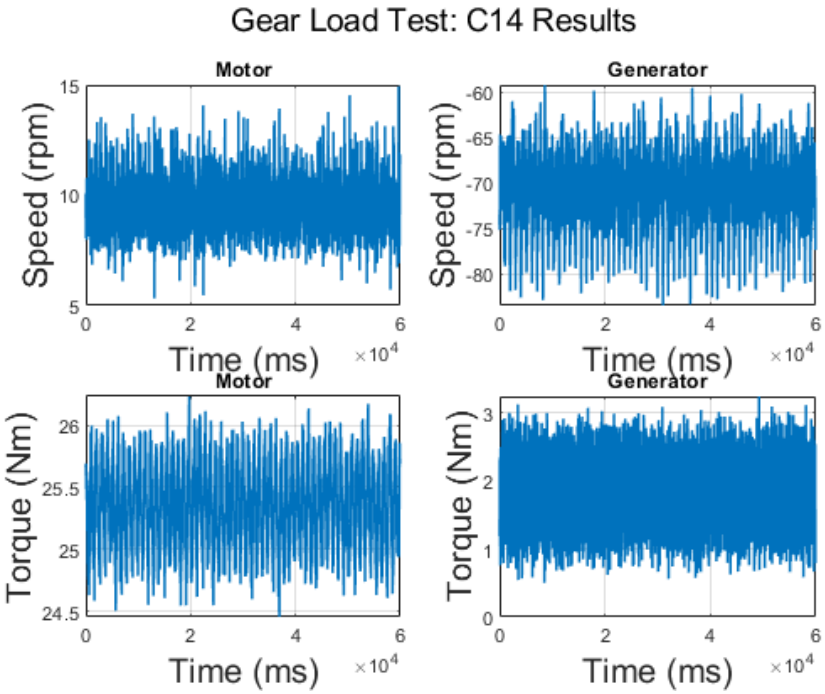

Figure C.51: Gear load test results: C14

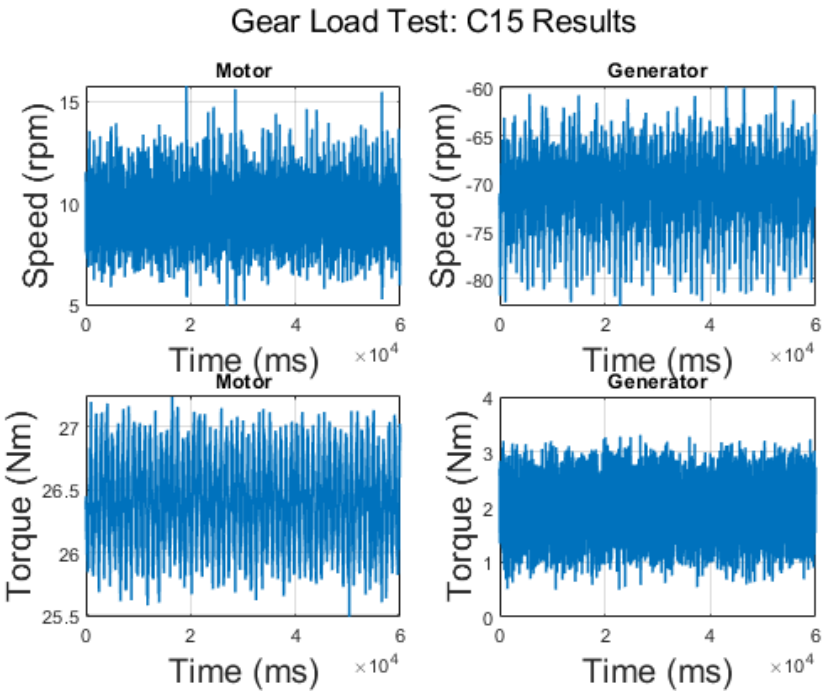

Figure C.52: Gear load test results: C15

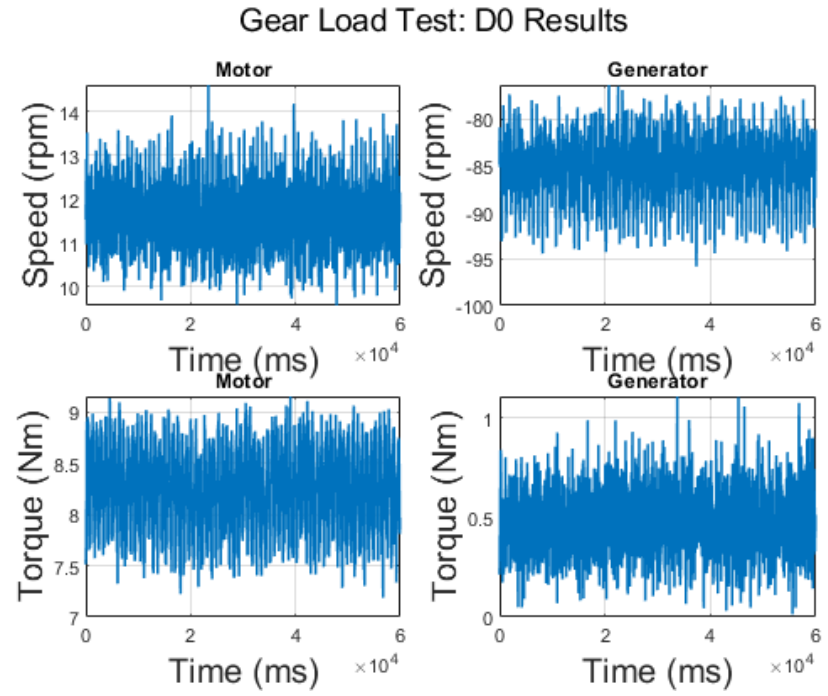

Figure C.53: Gear load test results: D0

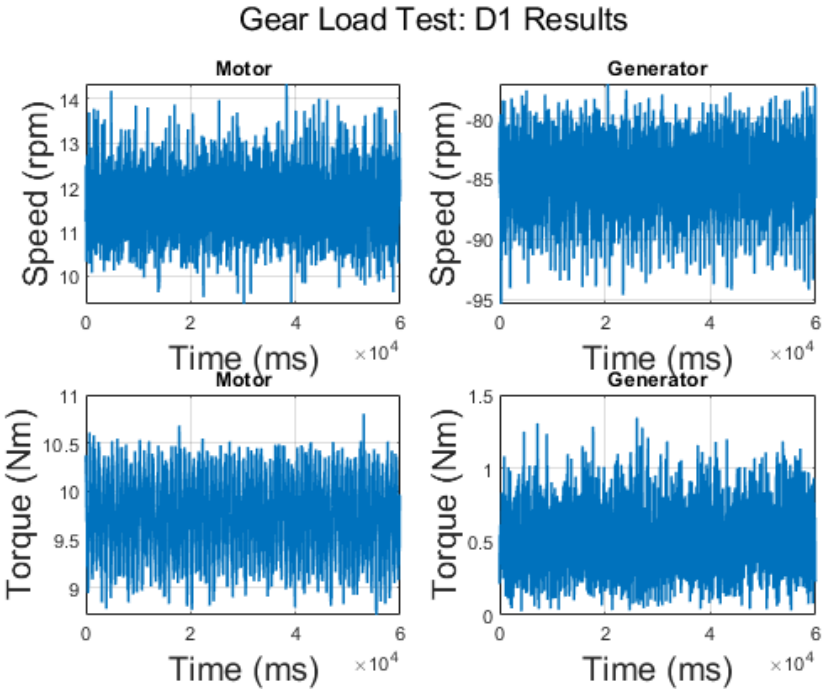

Figure C.54: Gear load test results: D1

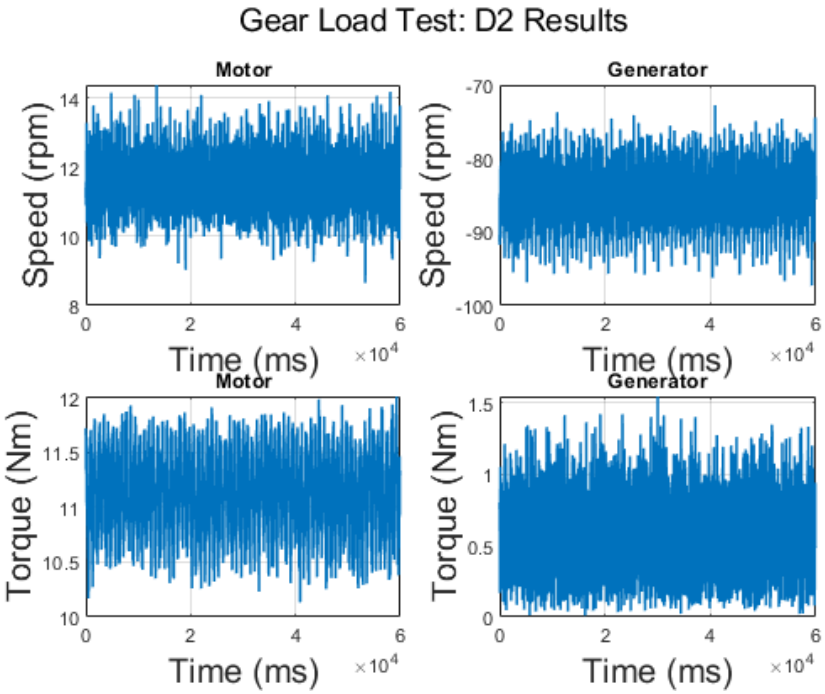

Figure C.55: Gear load test results: D2

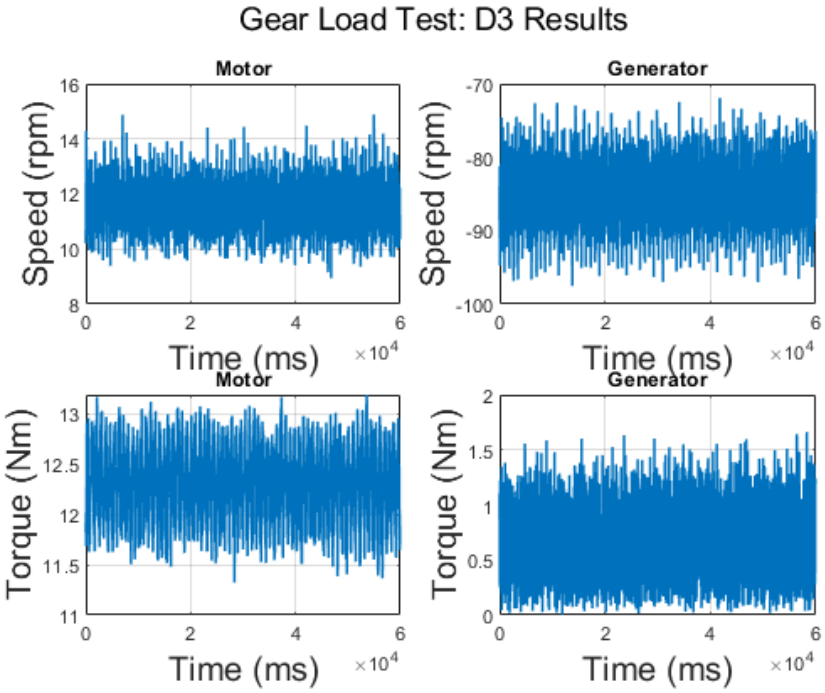

Figure C.56: Gear load test results: D3

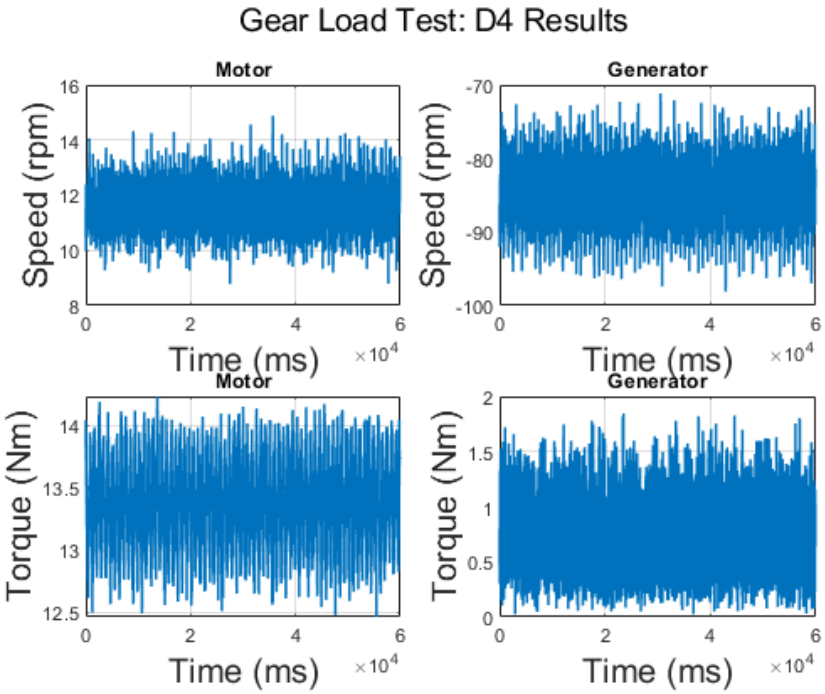

Figure C.57: Gear load test results: D4

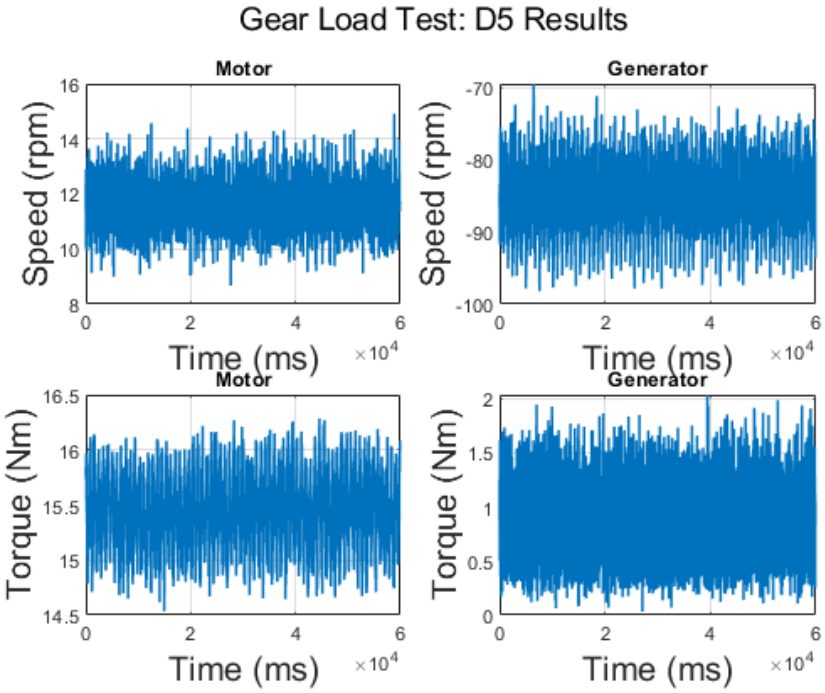

Figure C.58: Gear load test results: D5

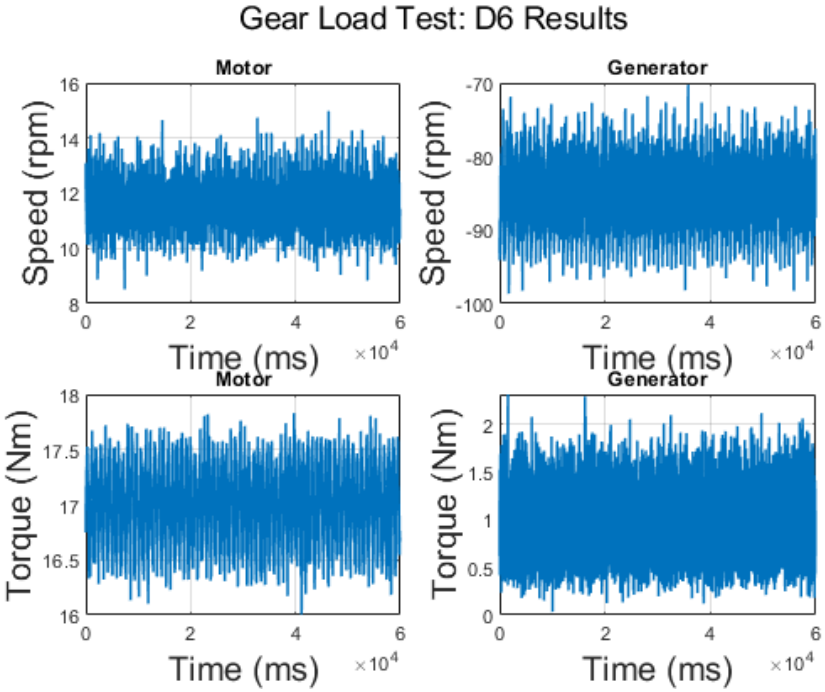

Figure C.59: Gear load test results: D6

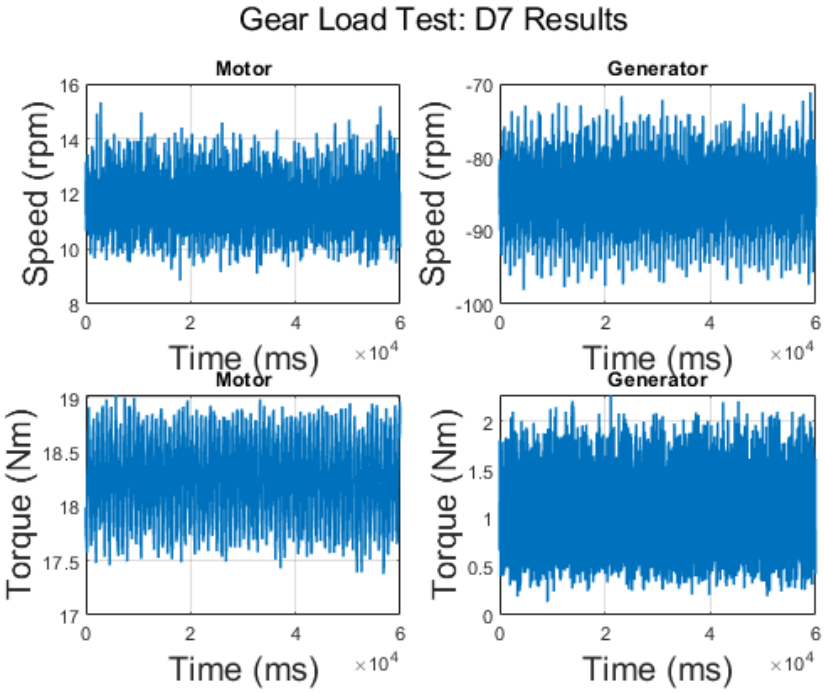

Figure C.60: Gear load test results: D7

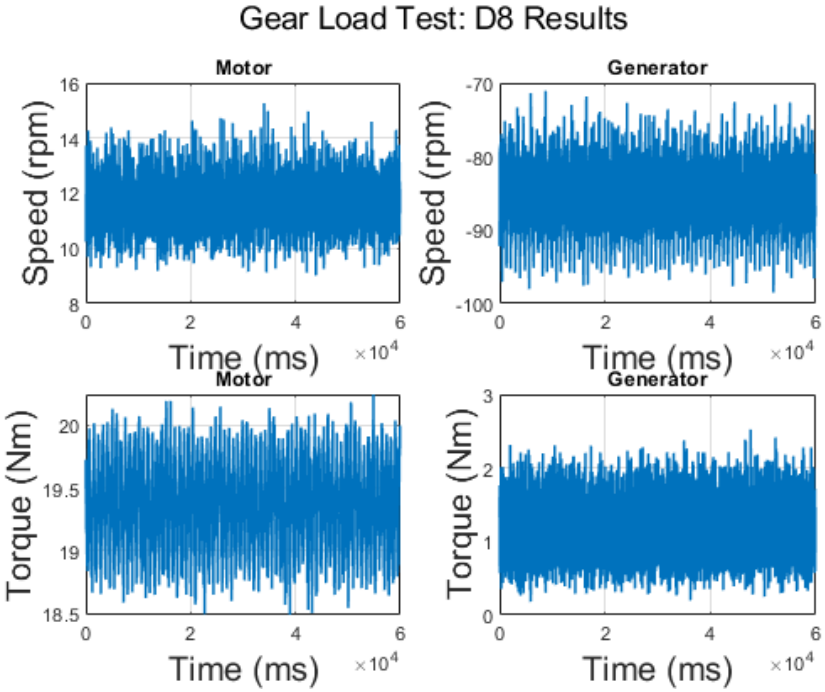

Figure C.61: Gear load test results: D8

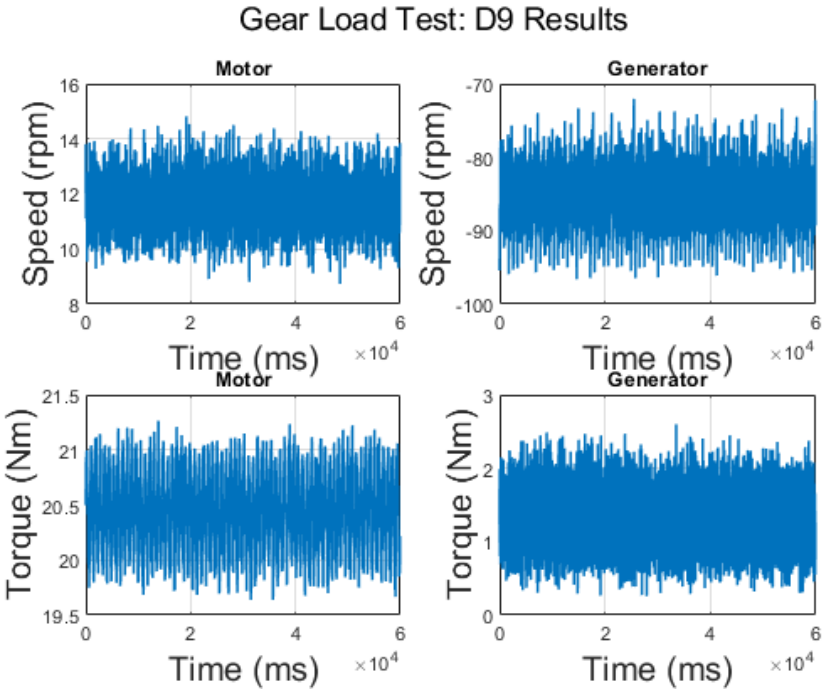

Figure C.62: Gear load test results: D9

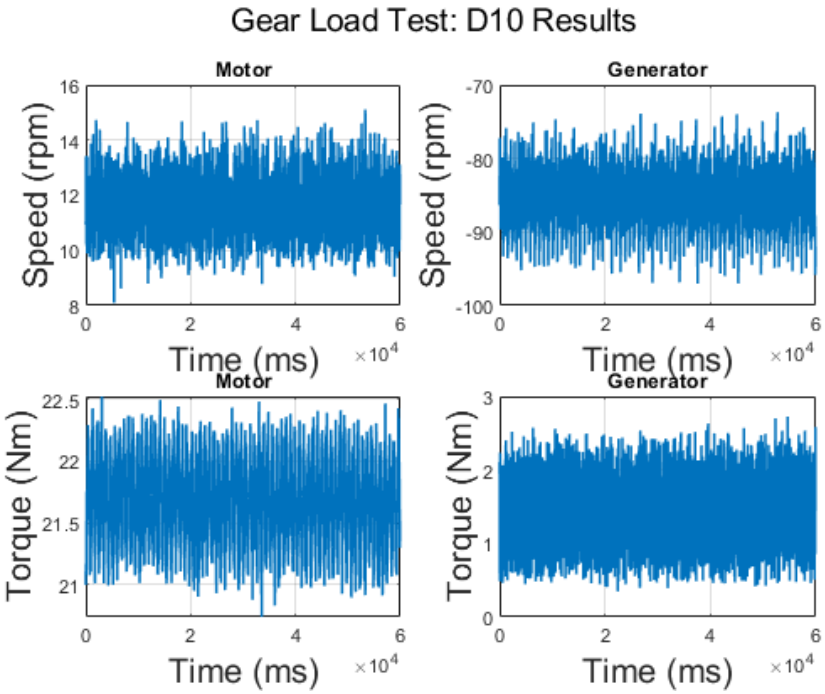

Figure C.63: Gear load test results: D10

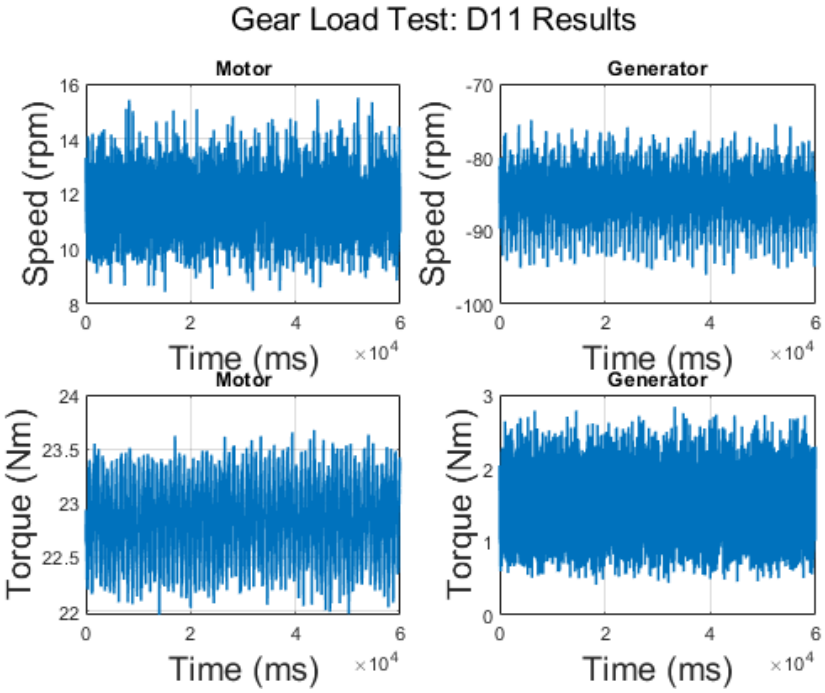

Figure C.64: Gear load test results: D11

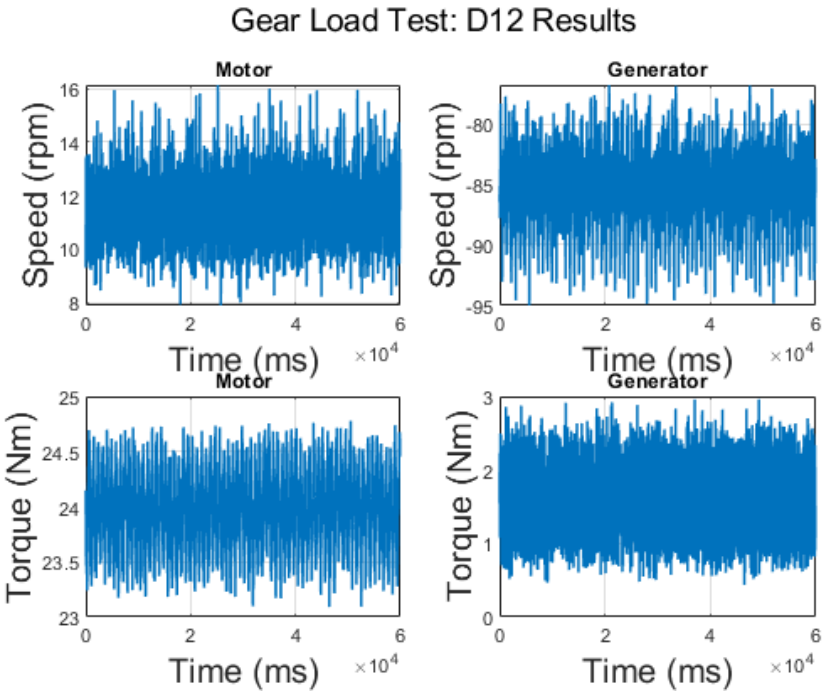

Figure C.65: Gear load test results: D12

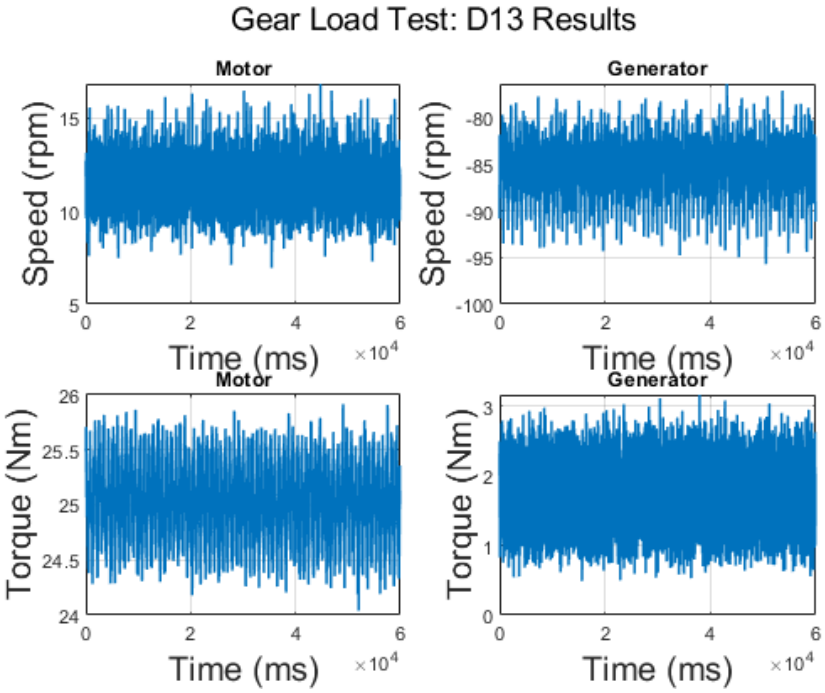

Figure C.66: Gear load test results: D13

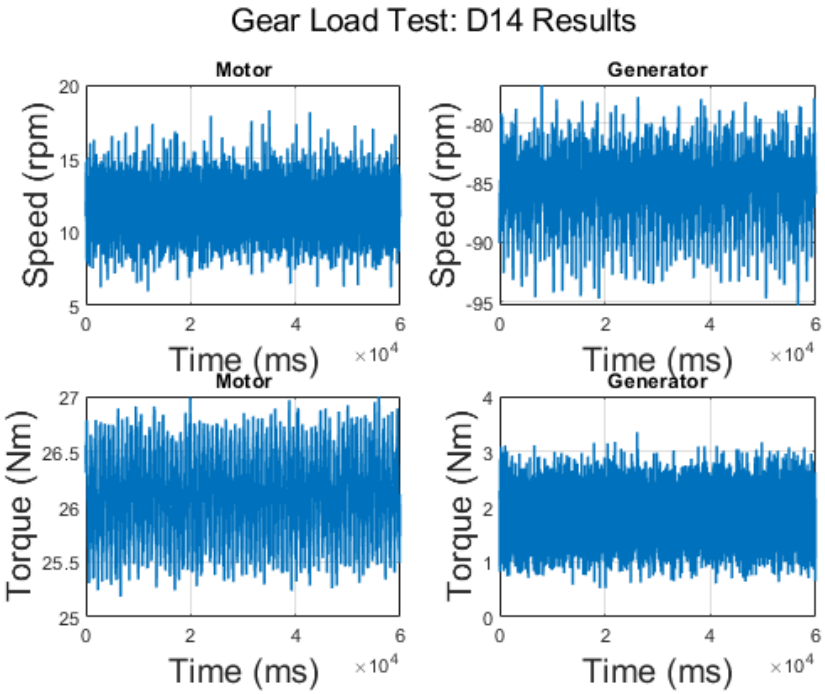

Figure C.67: Gear load test results: D14

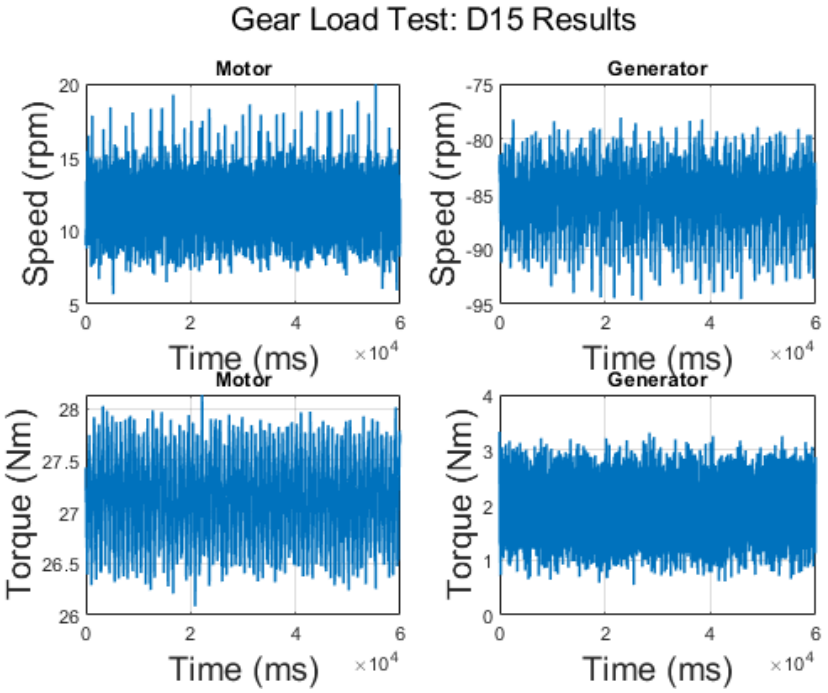

Figure C.68: Gear load test results: D15

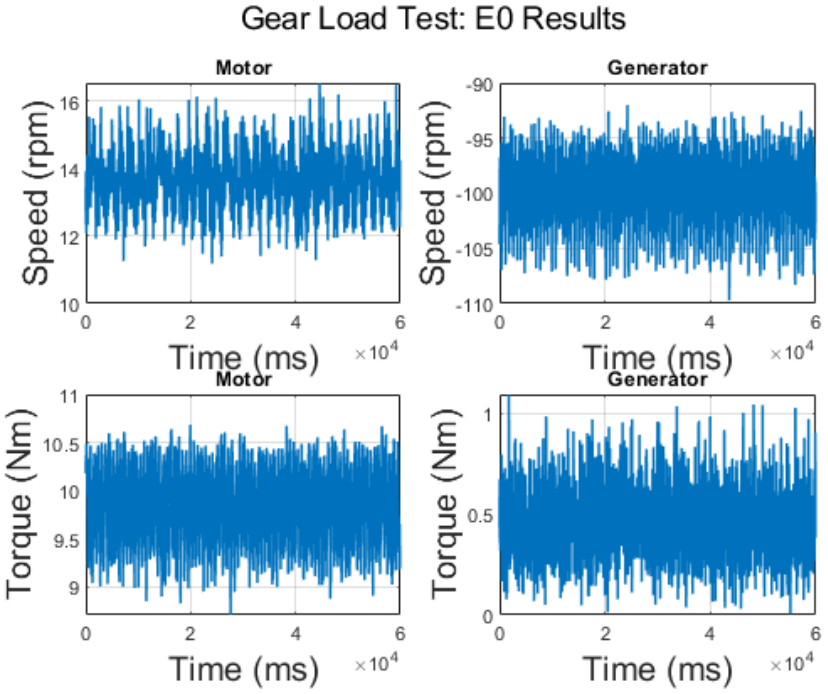

Figure C.69: Gear load test results: E0

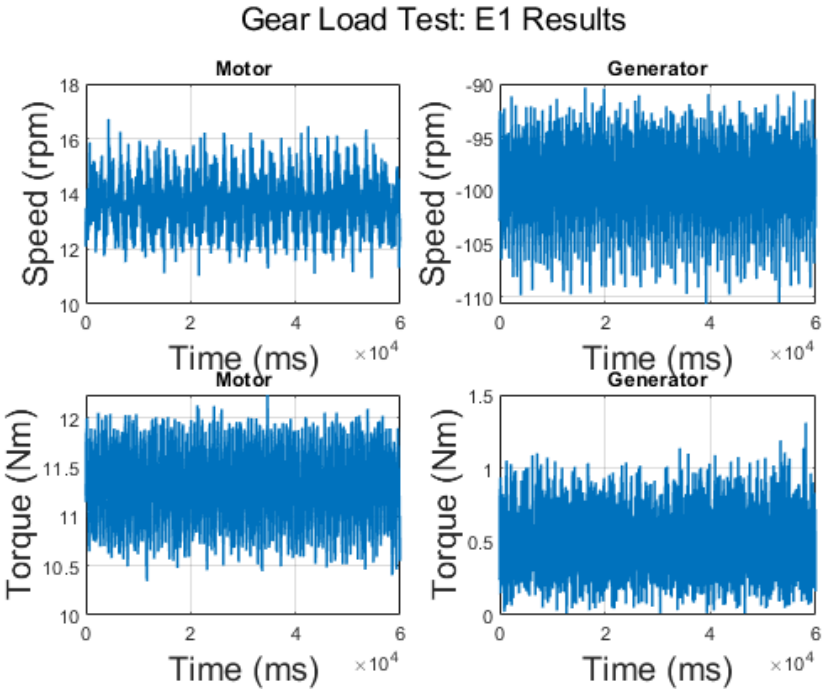

Figure C.70: Gear load test results: E1

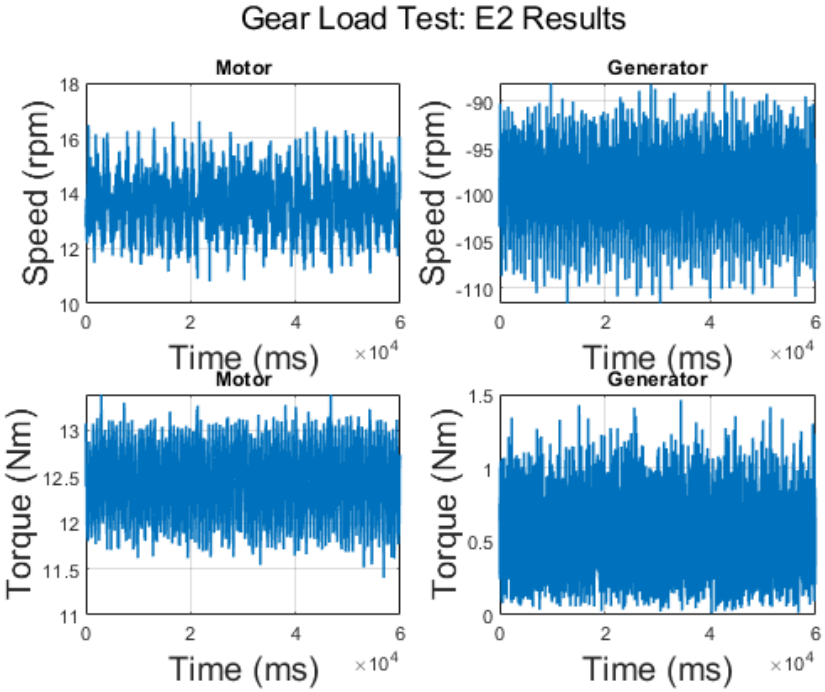

Figure C.71: Gear load test results: E2

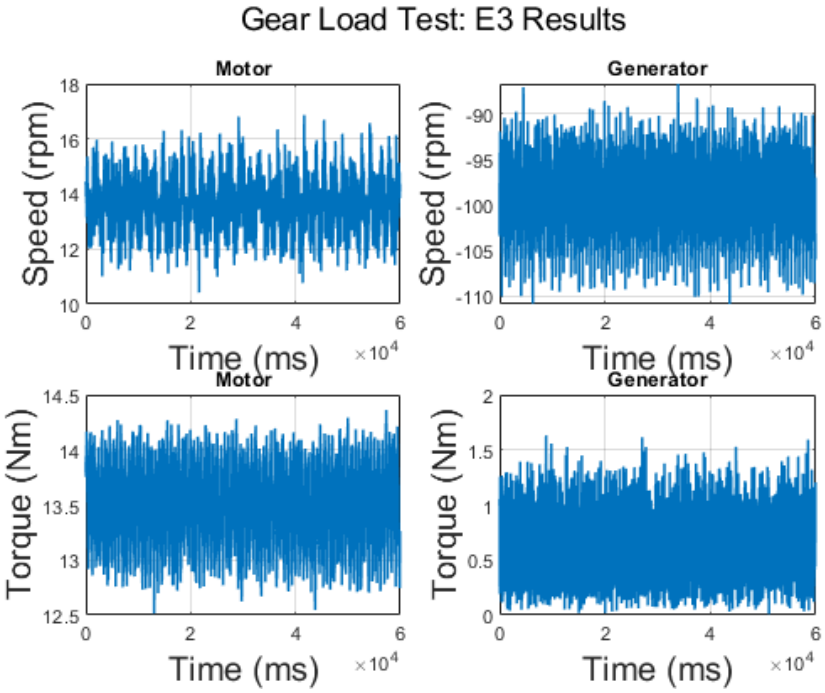

Figure C.72: Gear load test results: E3

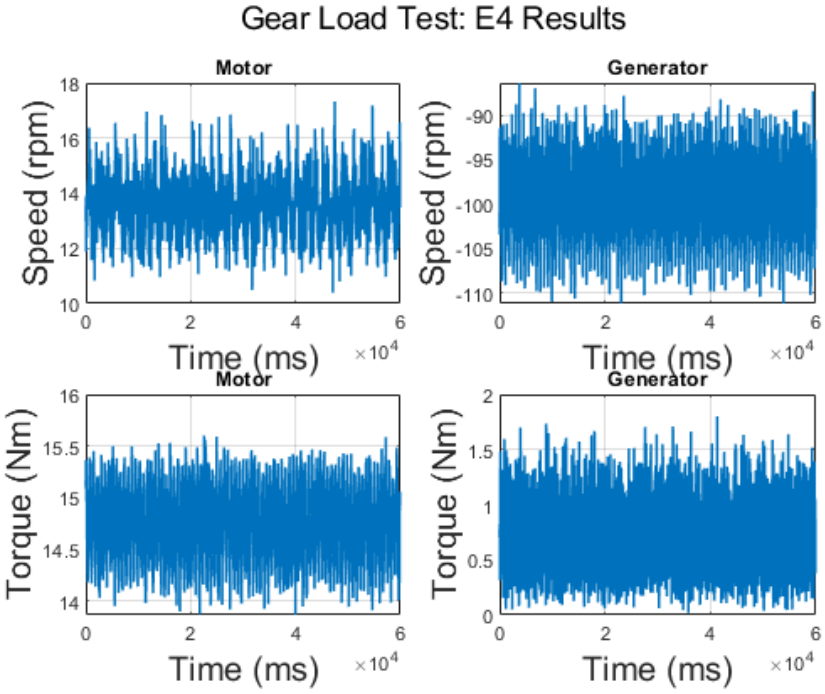

Figure C.73: Gear load test results: E4

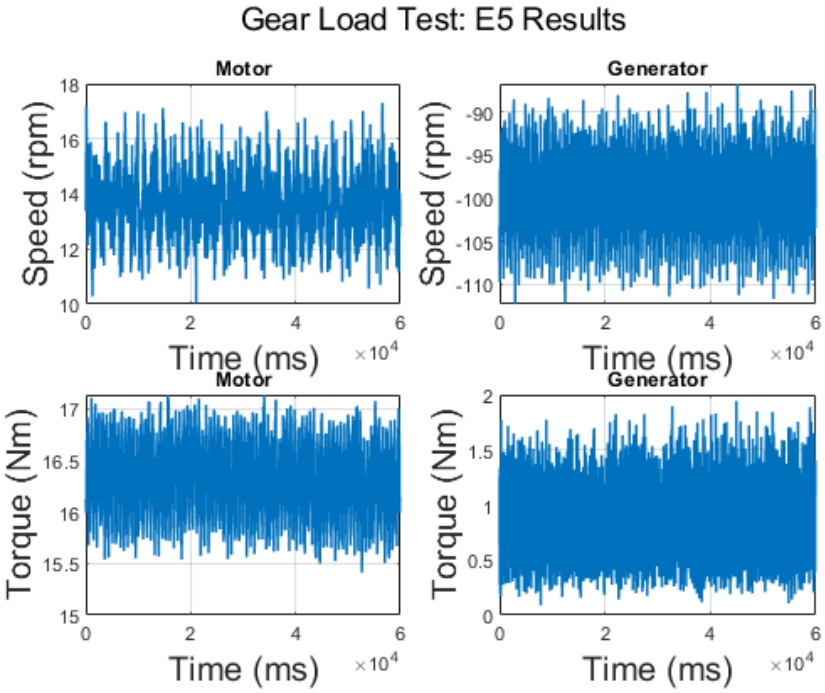

Figure C.74: Gear load test results: E5

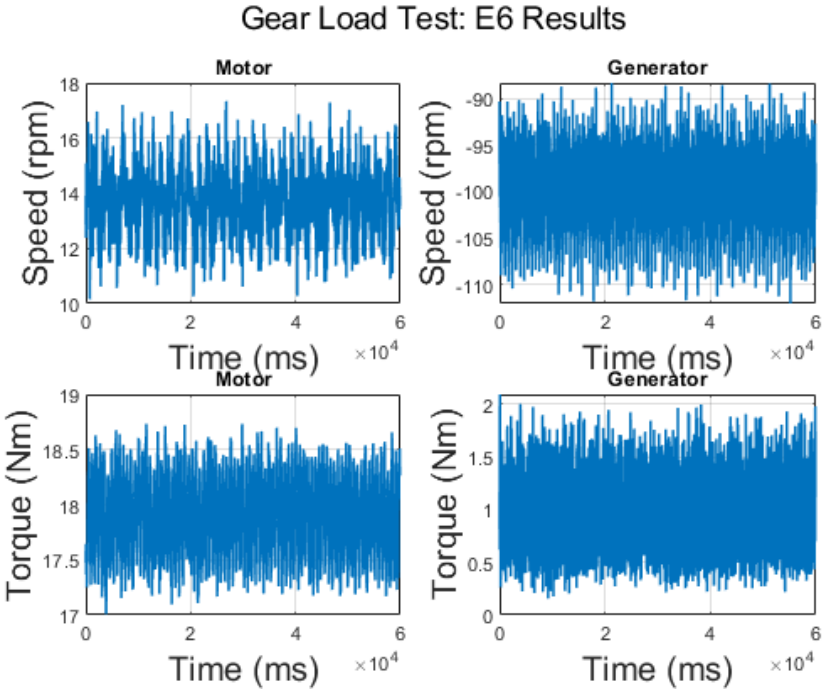

Figure C.75: Gear load test results: E6

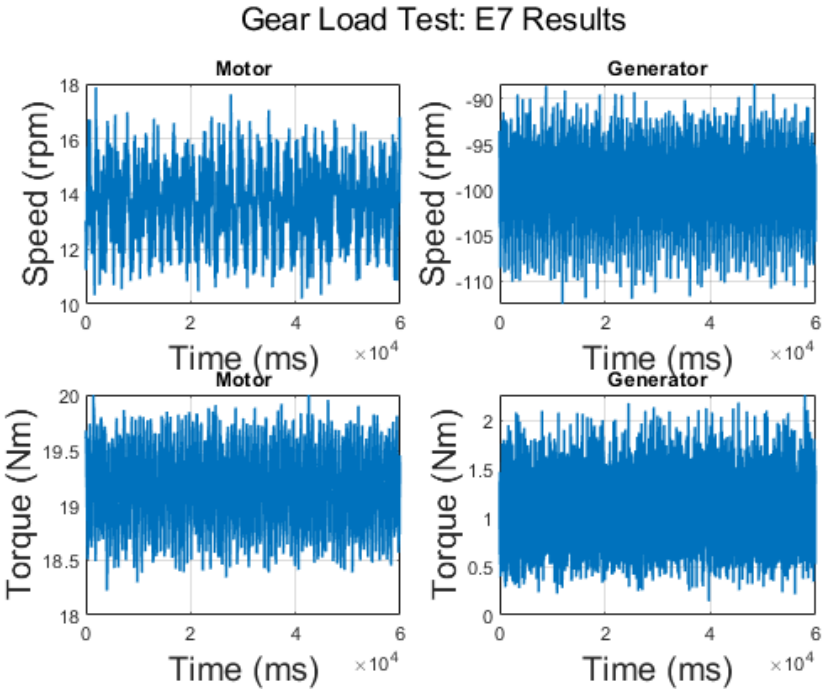

Figure C.76: Gear load test results: E7

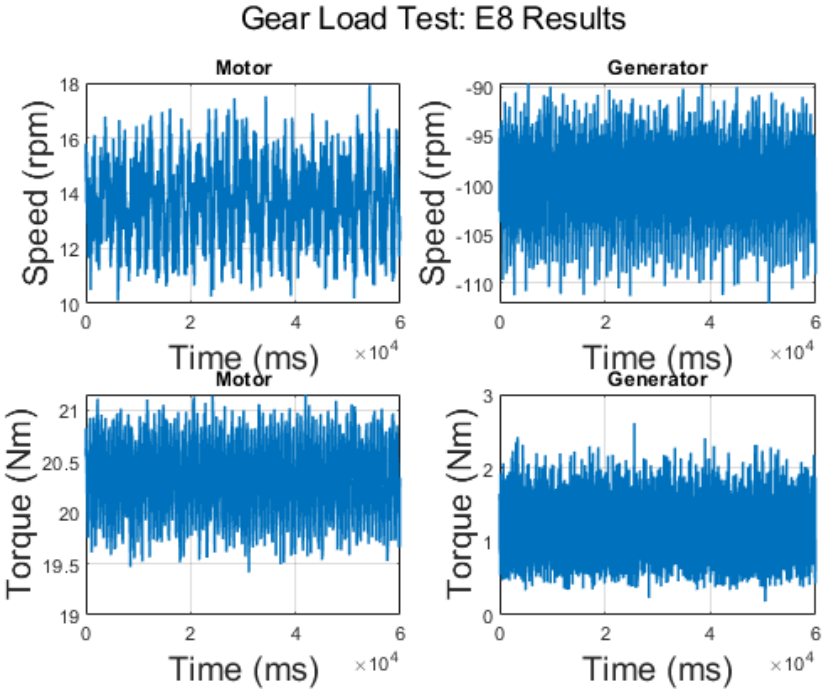

Figure C.77: Gear load test results: E8

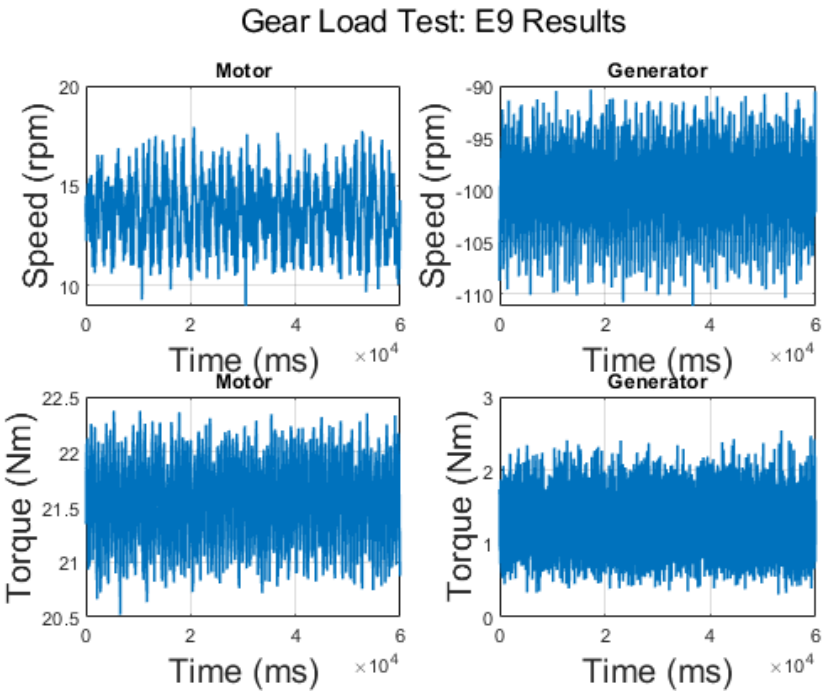

Figure C.78: Gear load test results: E9

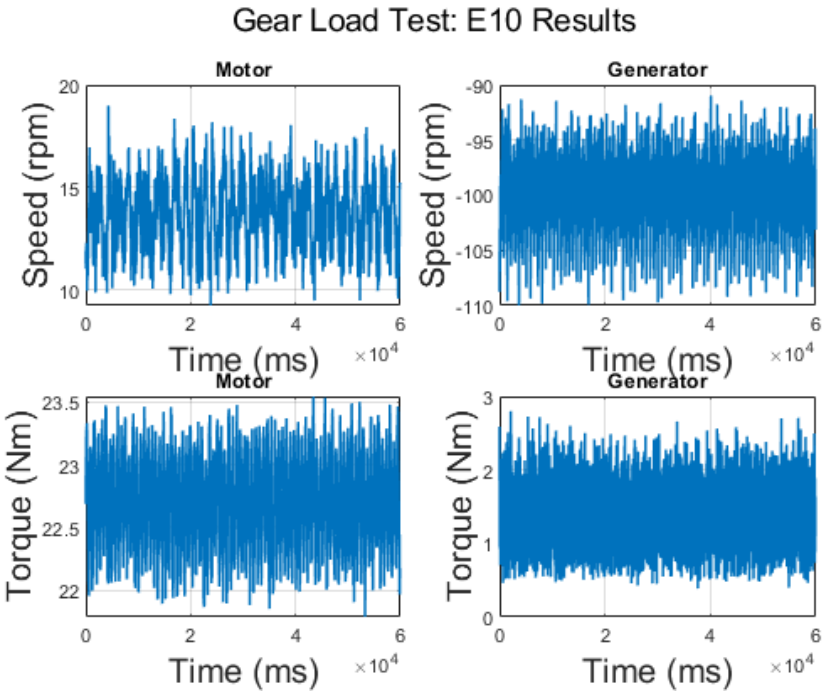

Figure C.79: Gear load test results: E10

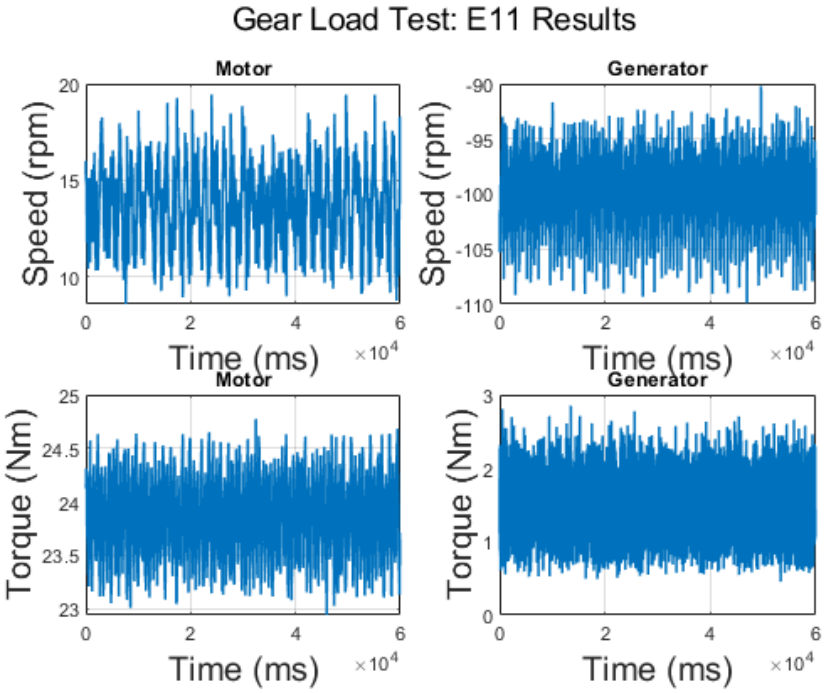

Figure C.80: Gear load test results: E11

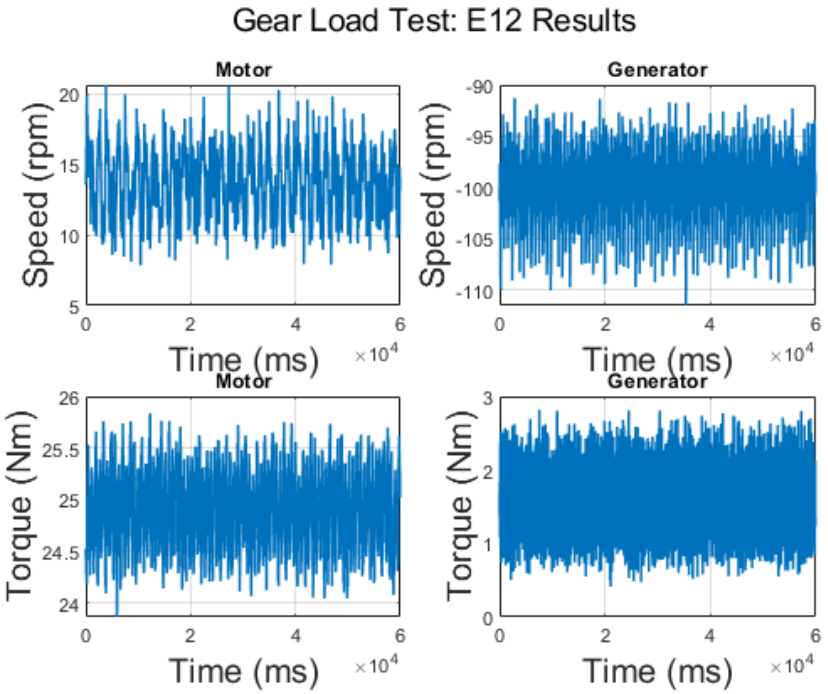

Figure C.81: Gear load test results: E12

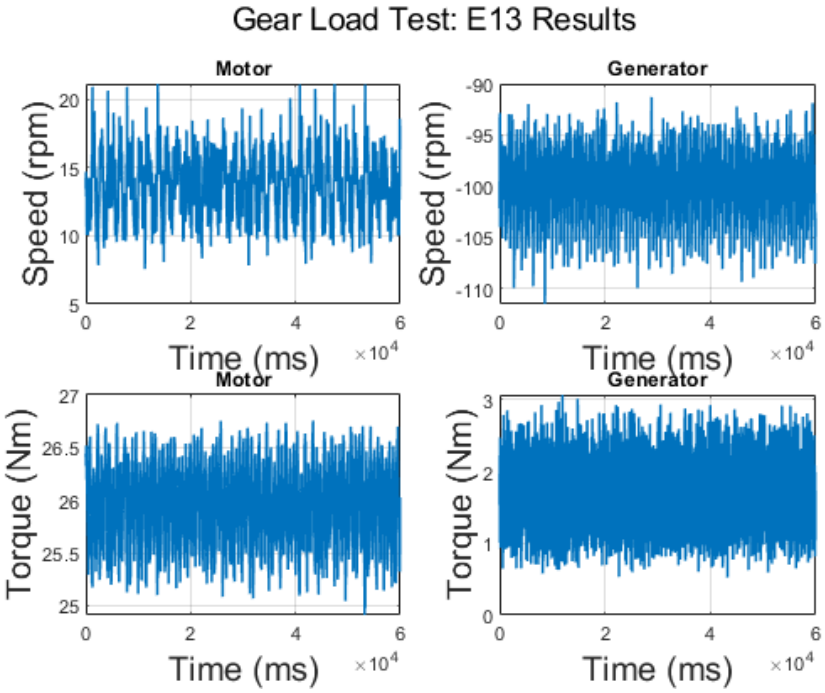

Figure C.82: Gear load test results: E13

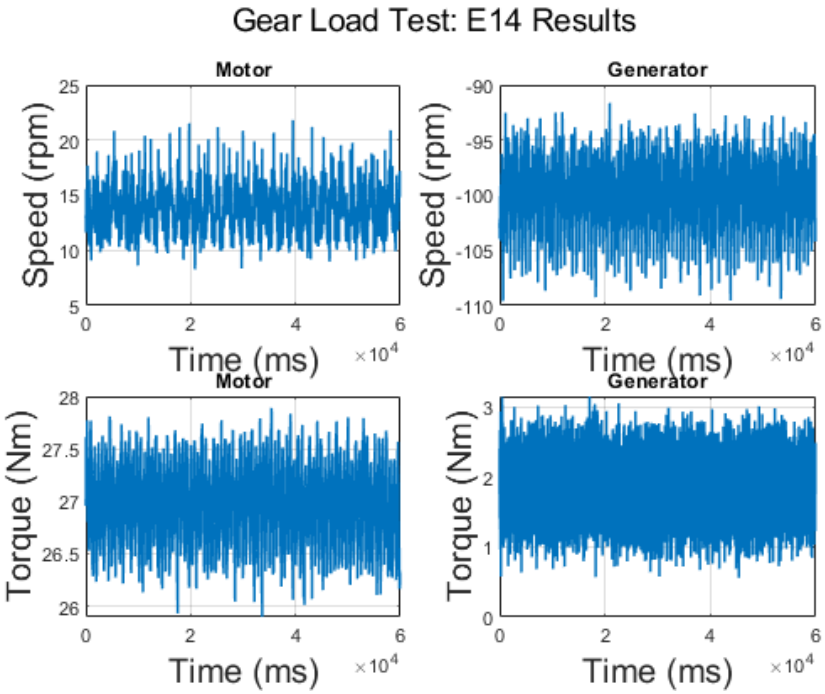

Figure C.83: Gear load test results: E14

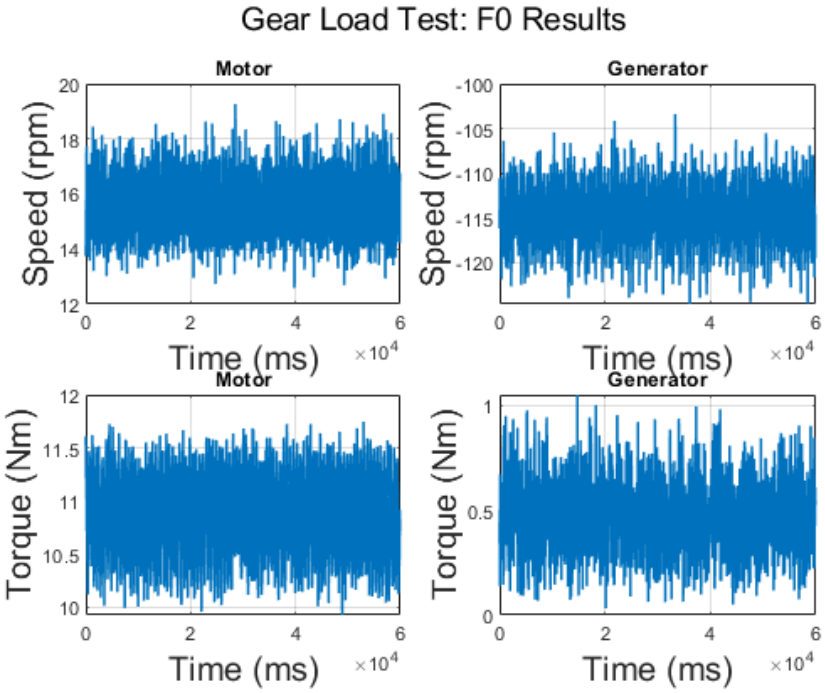

Figure C.84: Gear load test results: F0

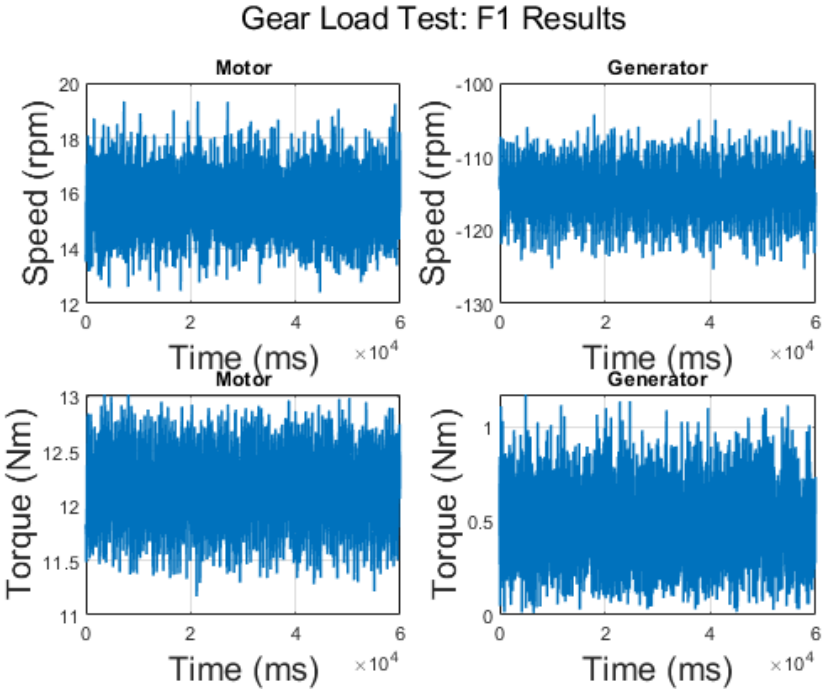

Figure C.85: Gear load test results: F1

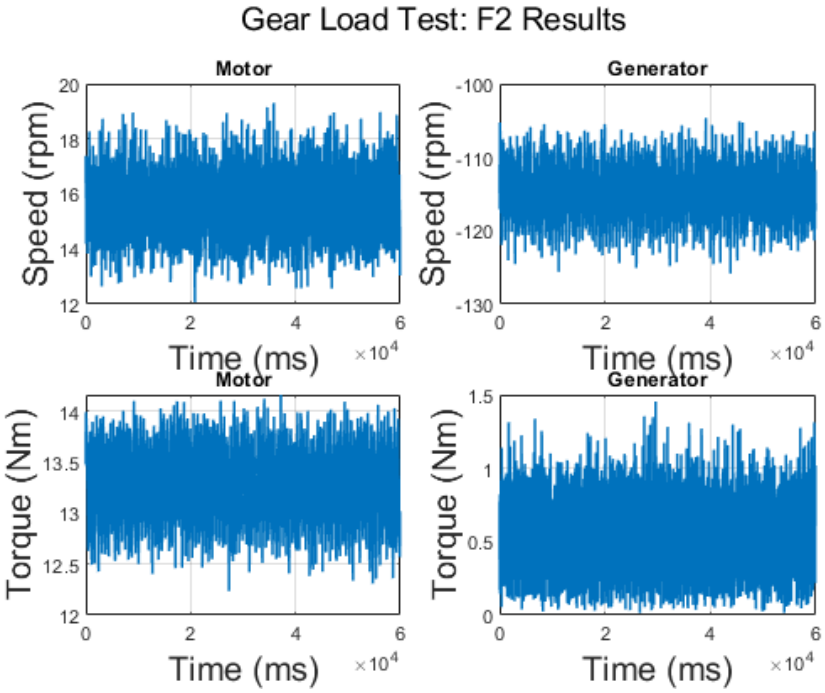

Figure C.86: Gear load test results: F2

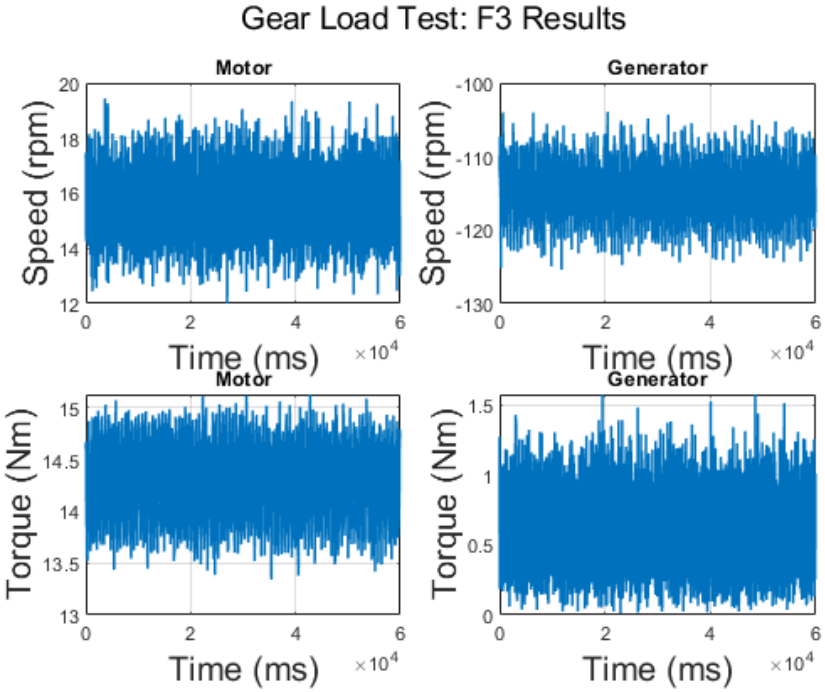

Figure C.87: Gear load test results: F3

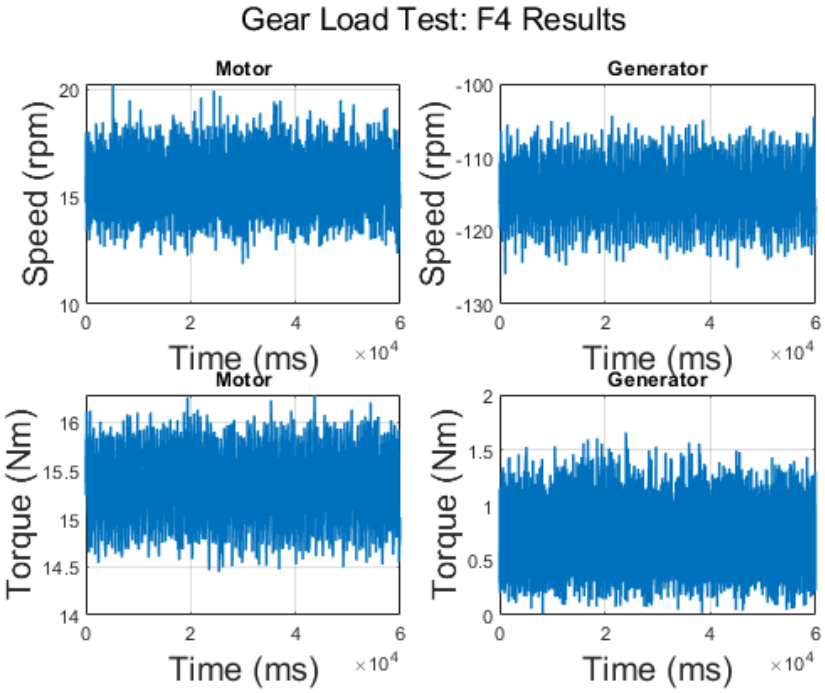

Figure C.88: Gear load test results: F4

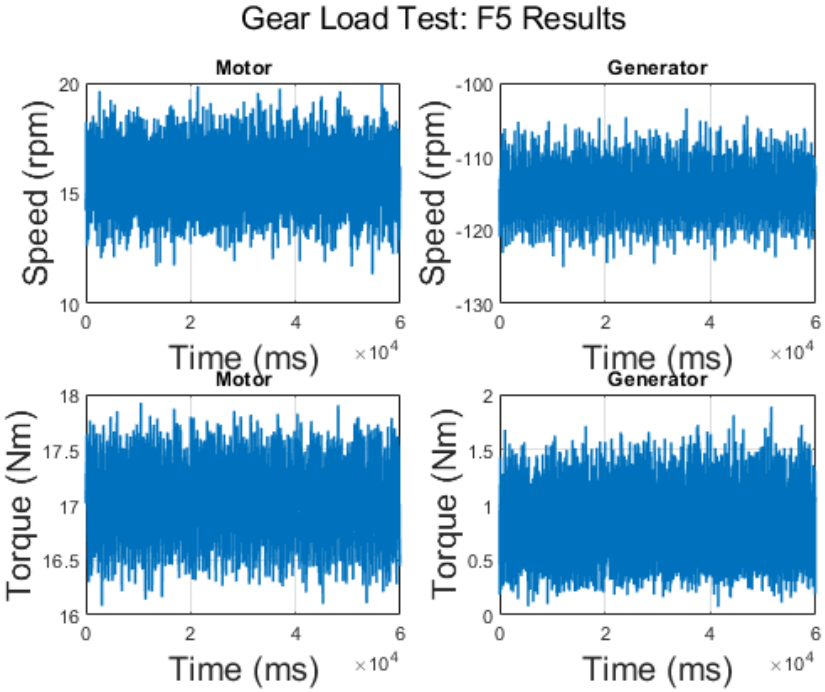

Figure C.89: Gear load test results: F5

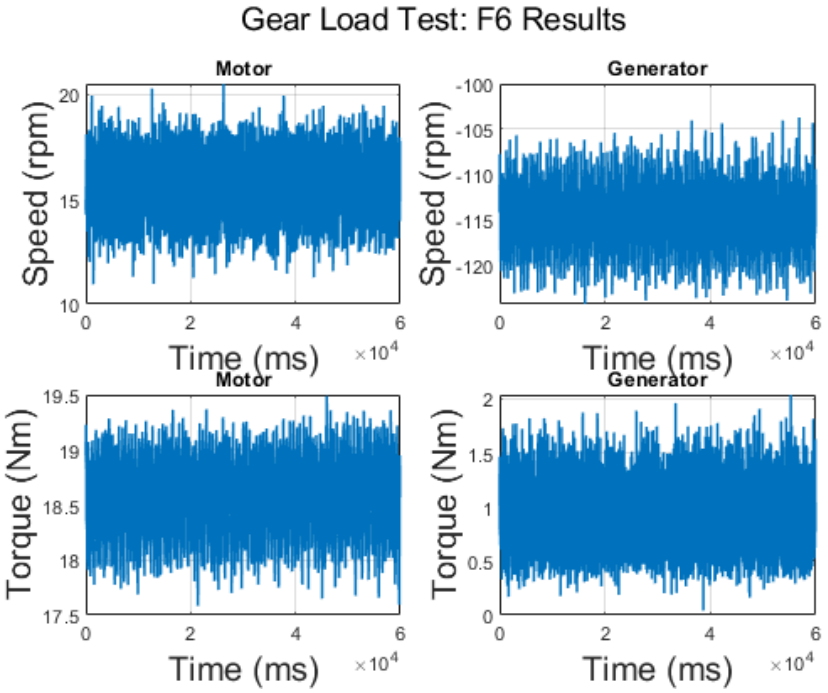

Figure C.90: Gear load test results: F6

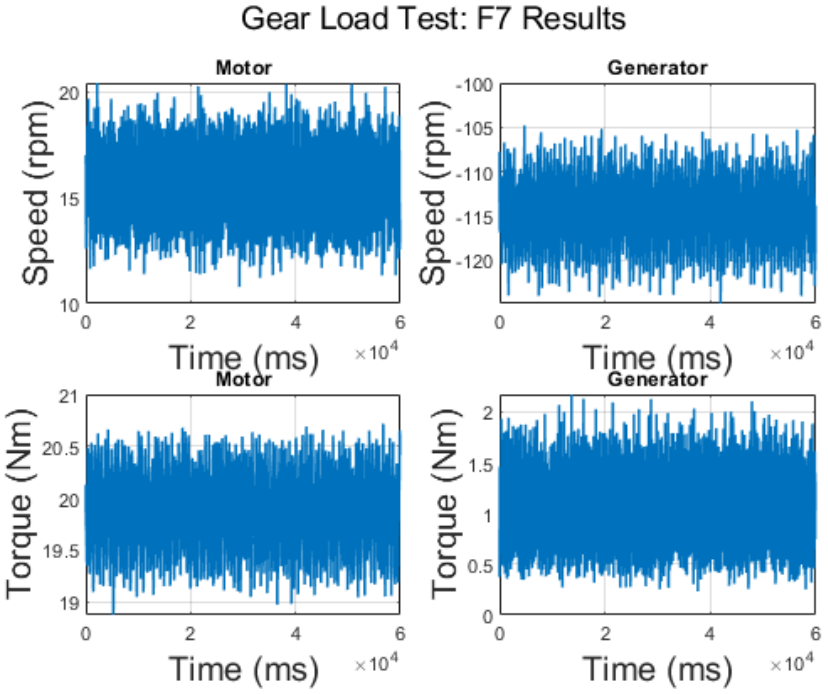

Figure C.91: Gear load test results: F7

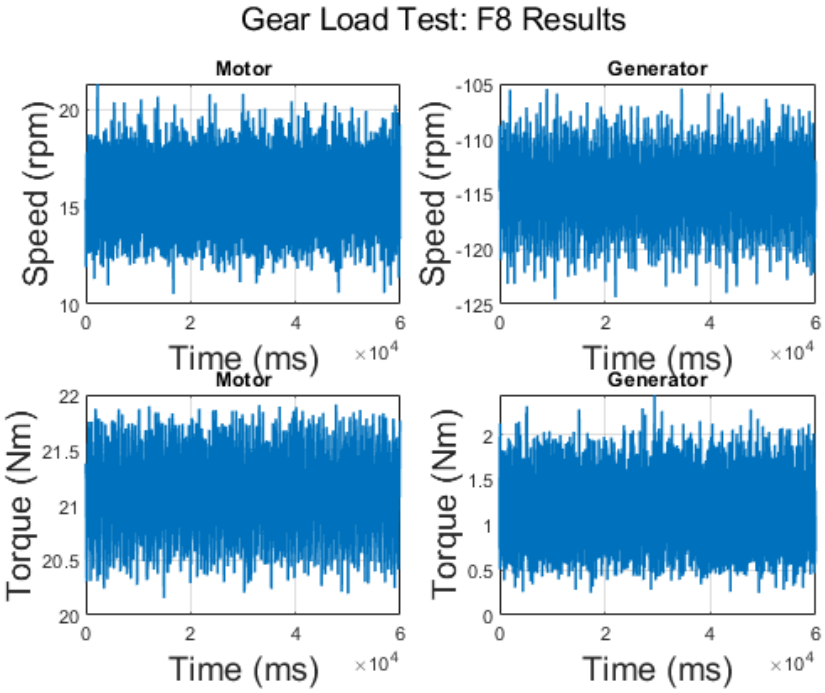

Figure C.92: Gear load test results: F8

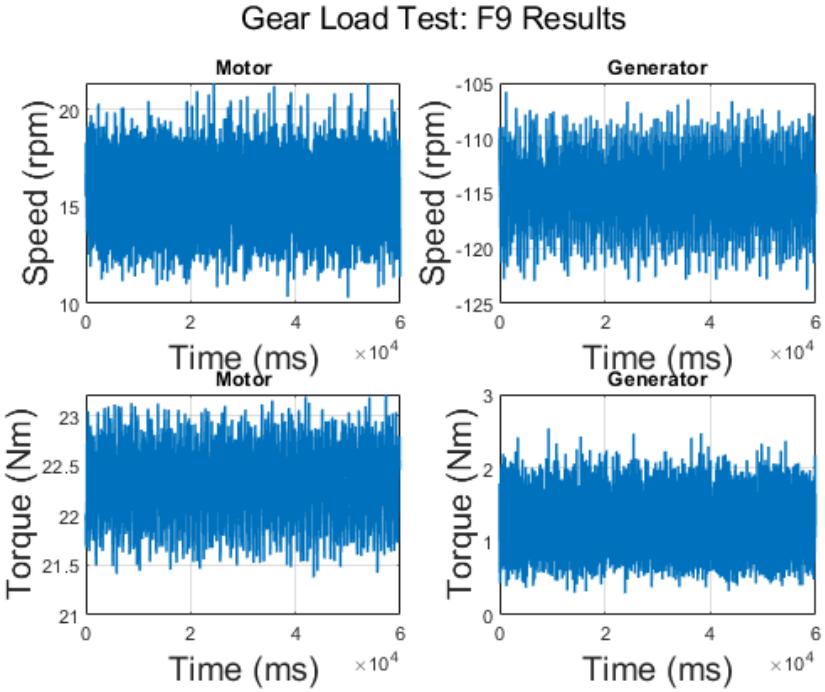

Figure C.93: Gear load test results: F9

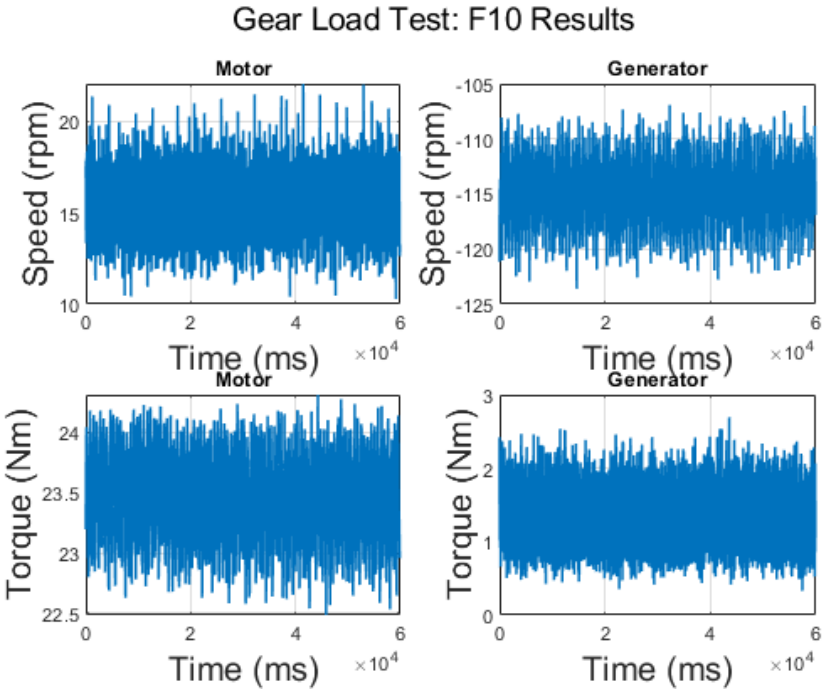

Figure C.94: Gear load test results: F10

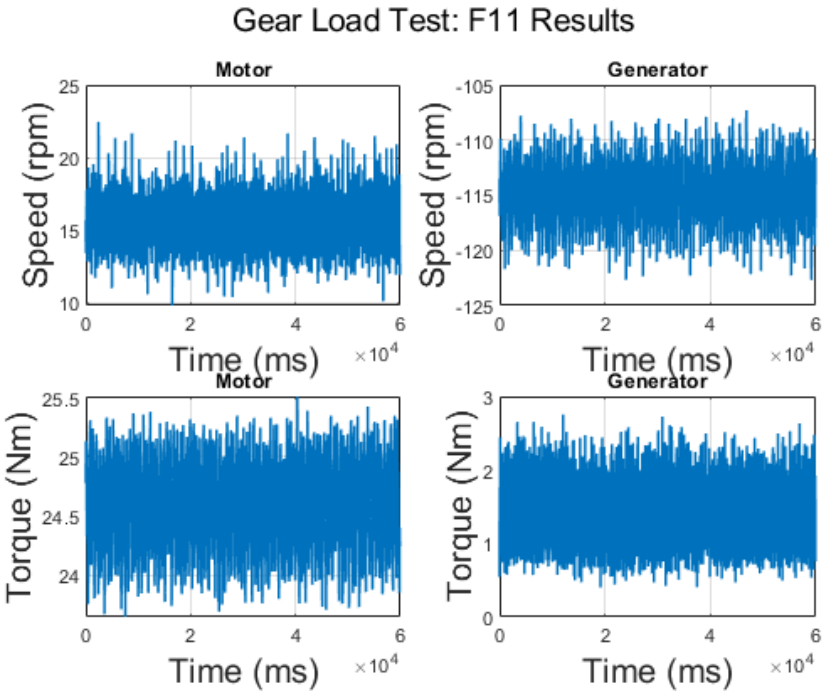

Figure C.95: Gear load test results: F11

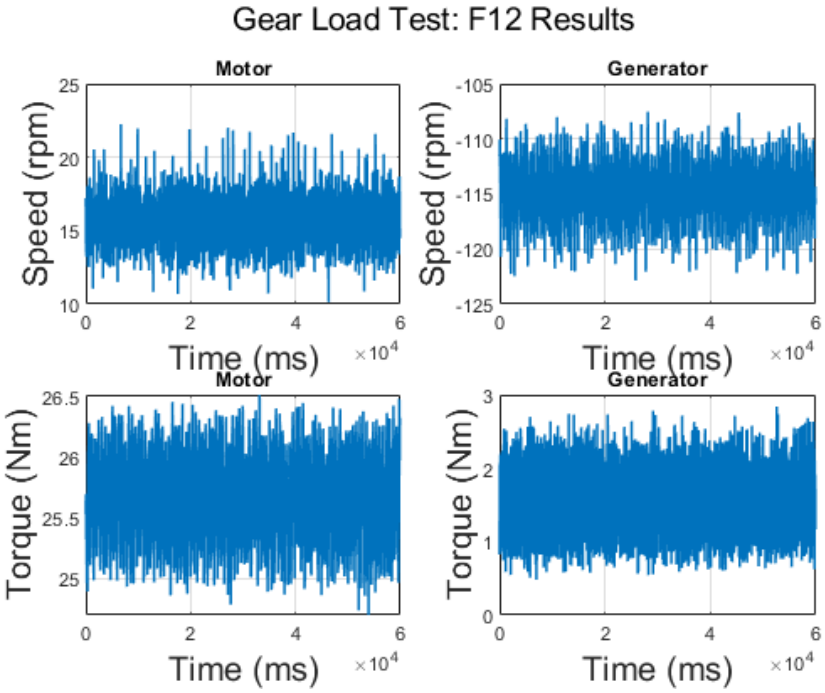

Figure C.96: Gear load test results: F12

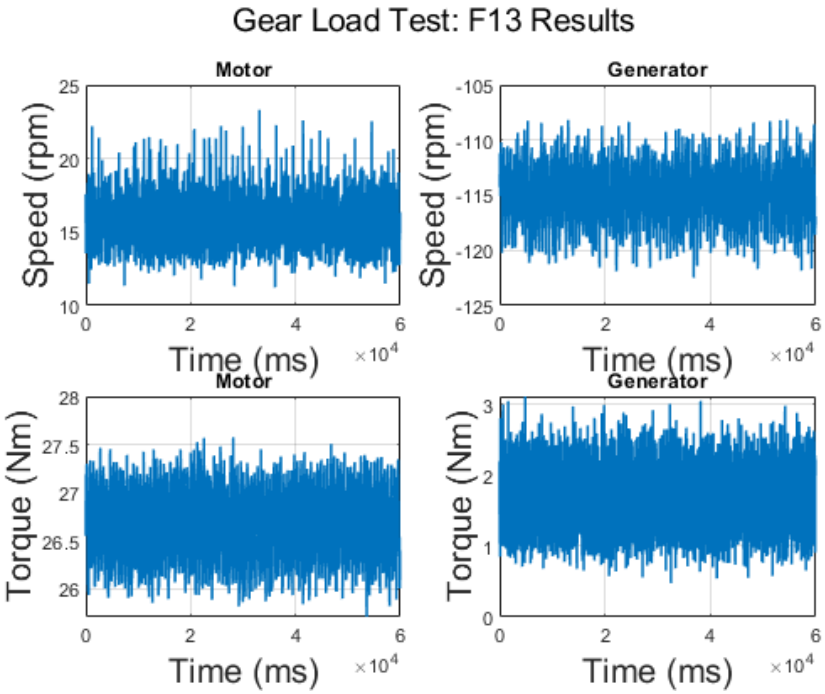

Figure C.97: Gear load test results: F13

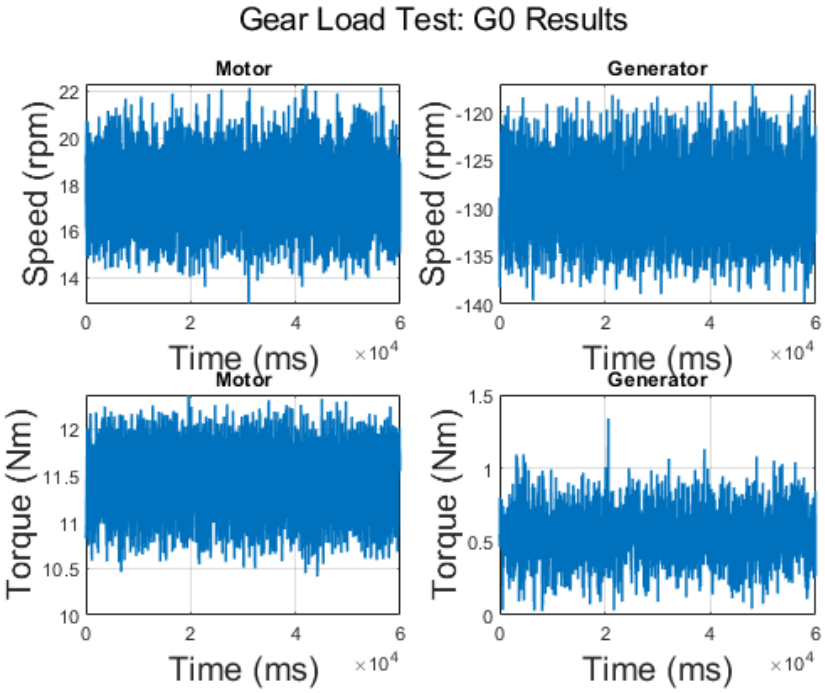

Figure C.98: Gear load test results: G0

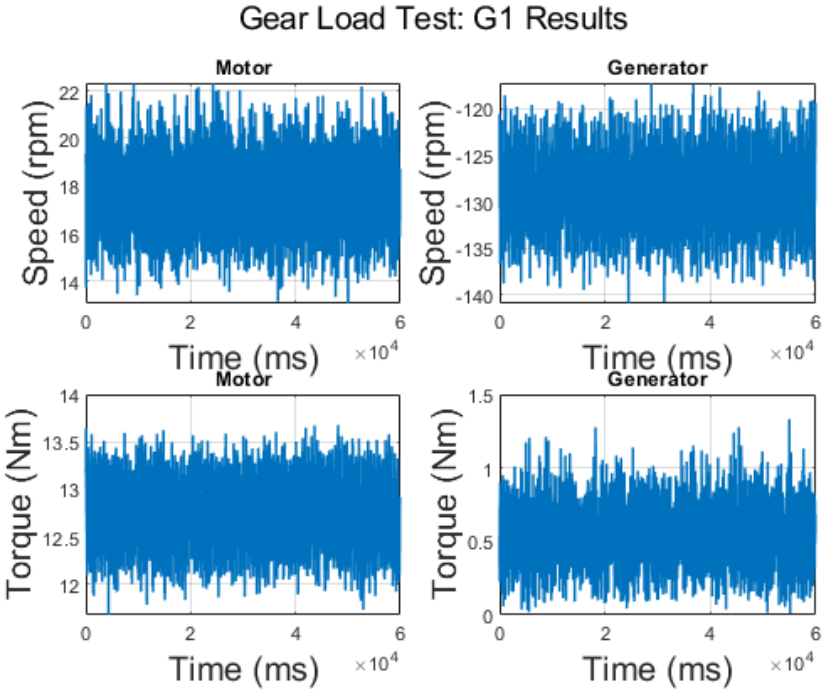

Figure C.99: Gear load test results: G1

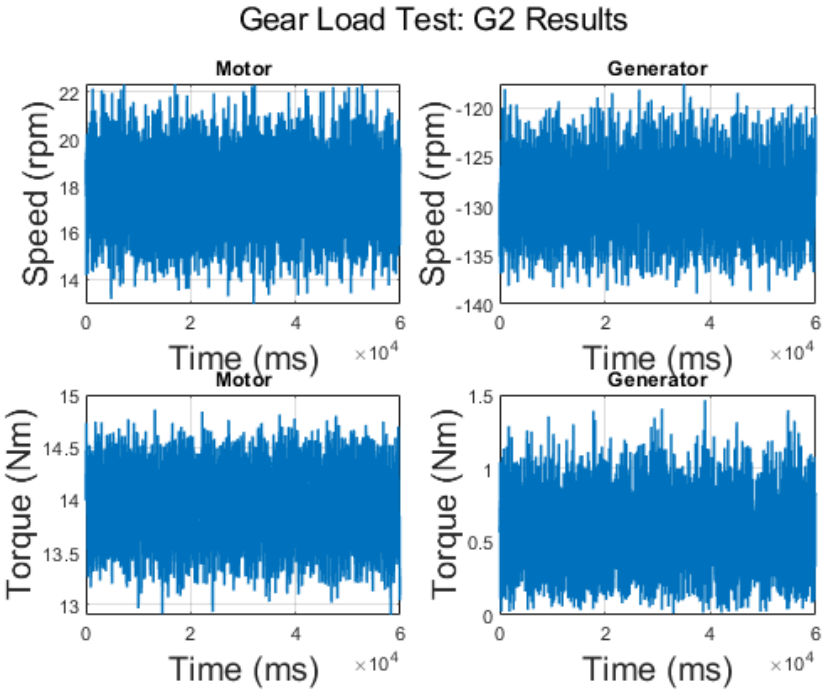

Figure C.100: Gear load test results: G2

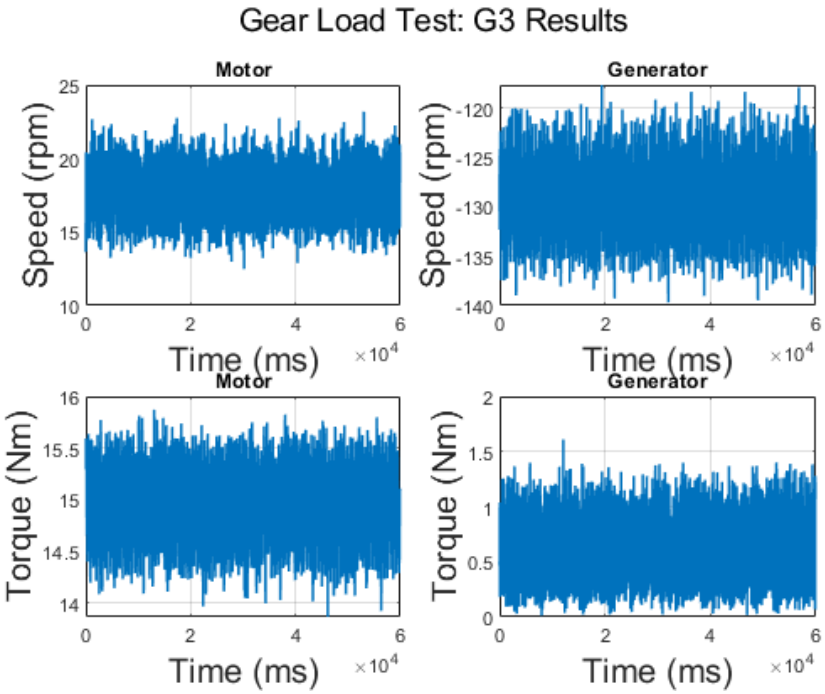

Figure C.101: Gear load test results: G3

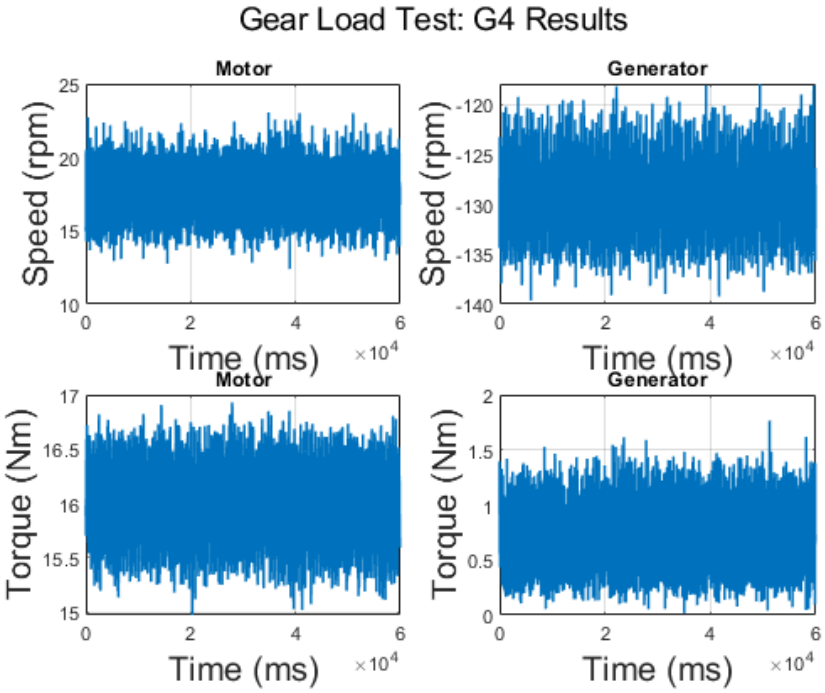

Figure C.102: Gear load test results: G4

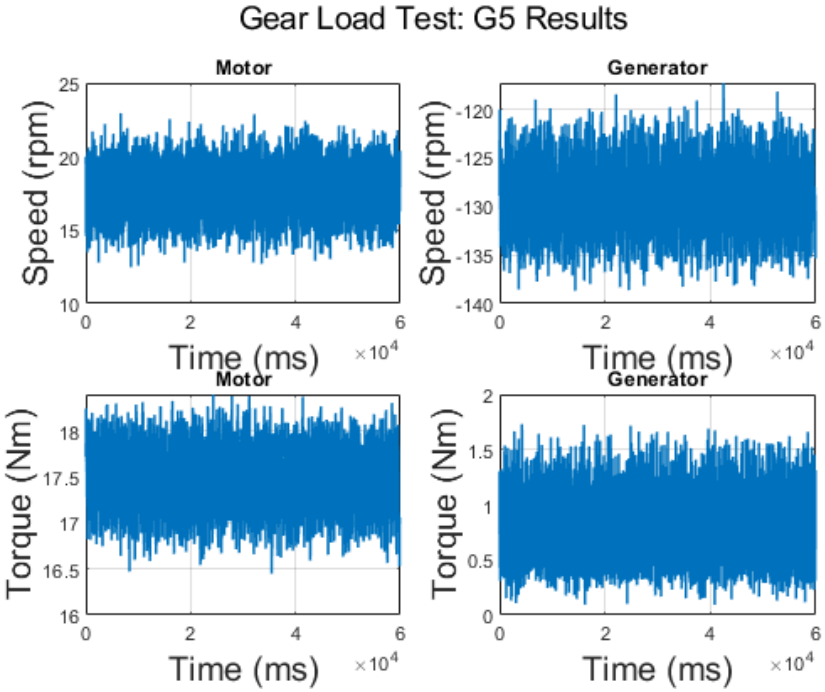

Figure C.103: Gear load test results: G5

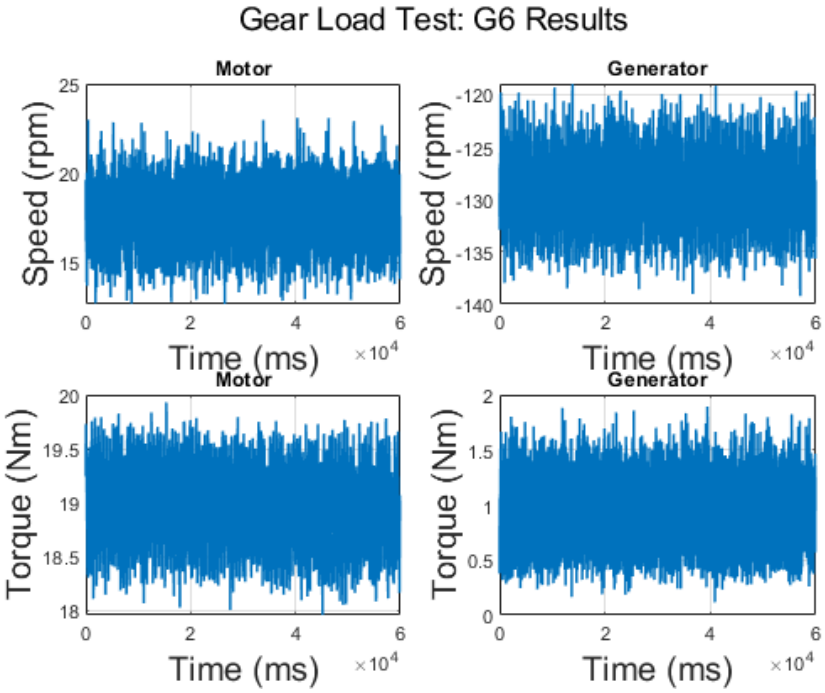

Figure C.104: Gear load test results: G6

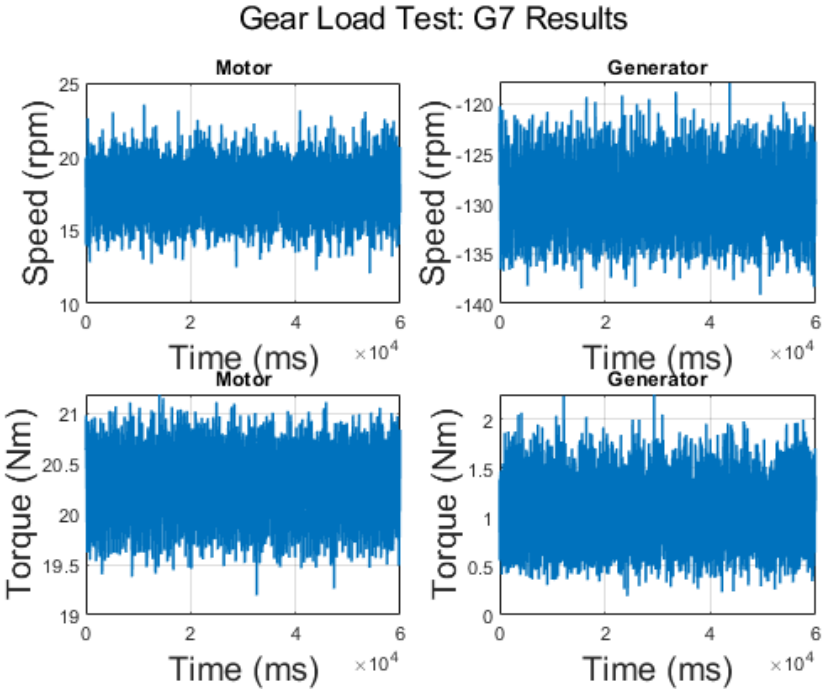

Figure C.105: Gear load test results: G7

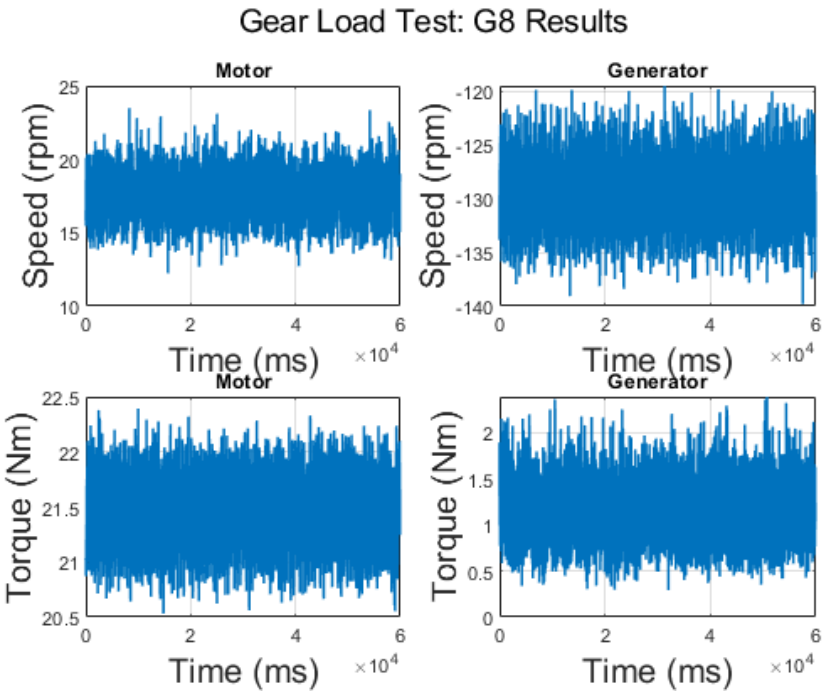

Figure C.106: Gear load test results: G8

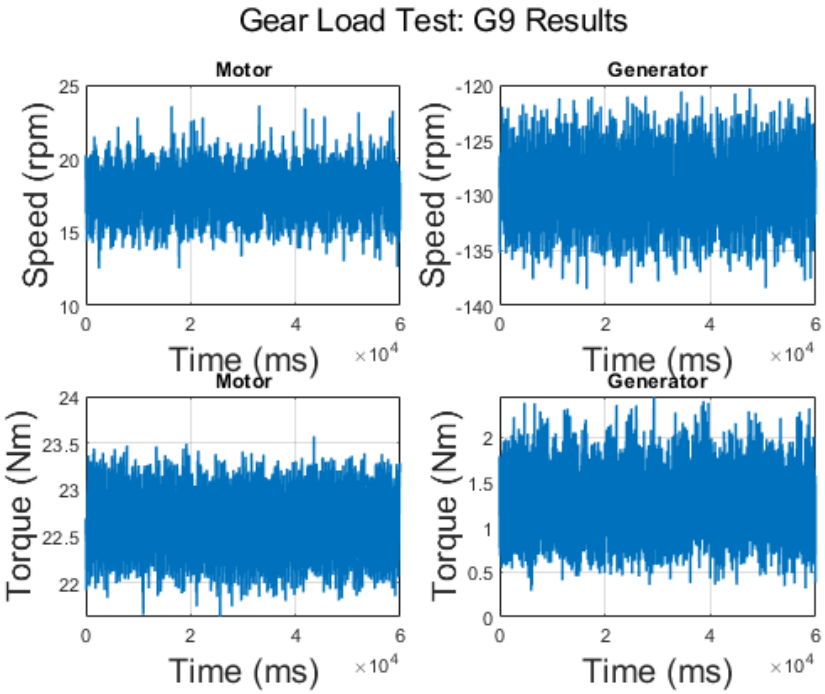

Figure C.107: Gear load test results: G9

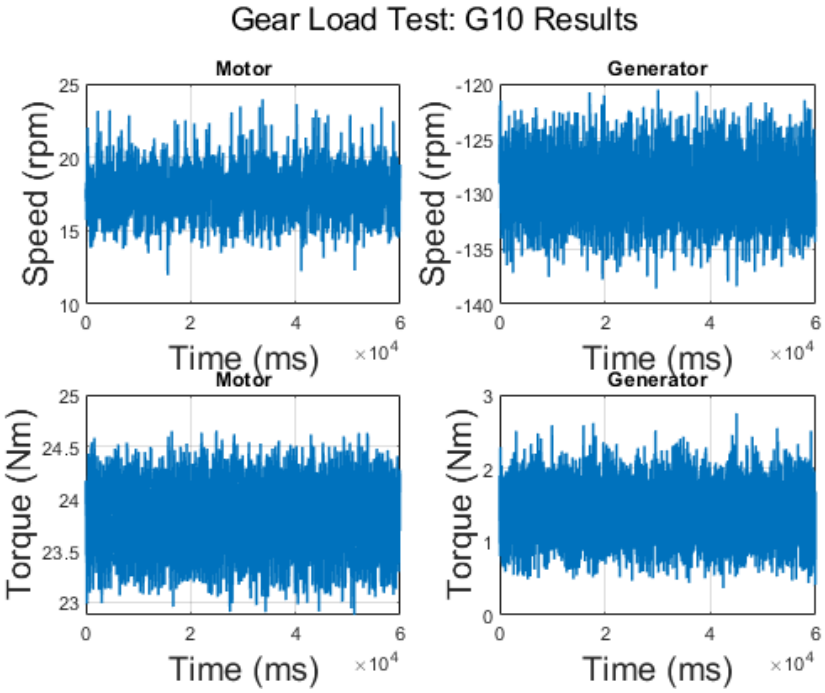

Figure C.108: Gear load test results: G10

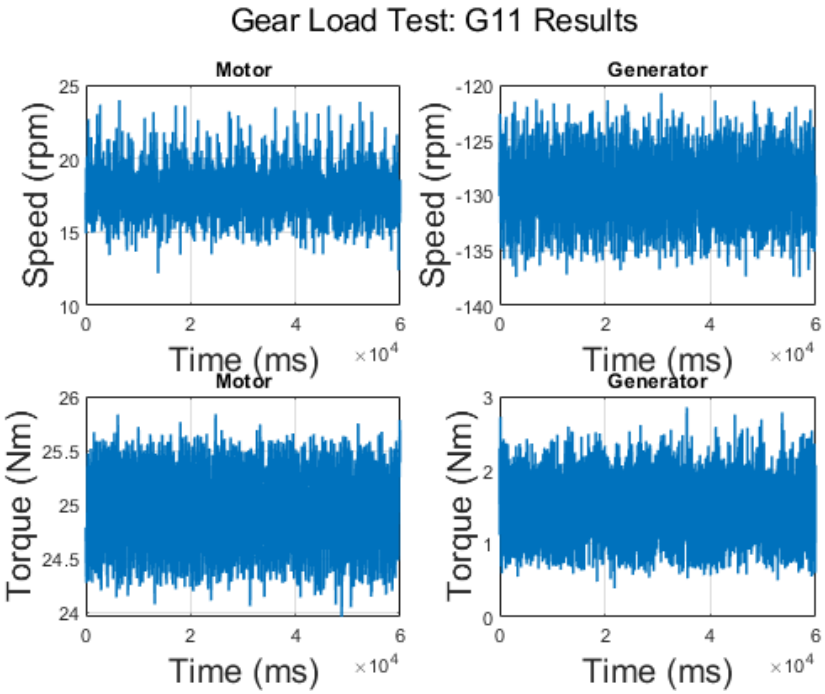

Figure C.109: Gear load test results: G11

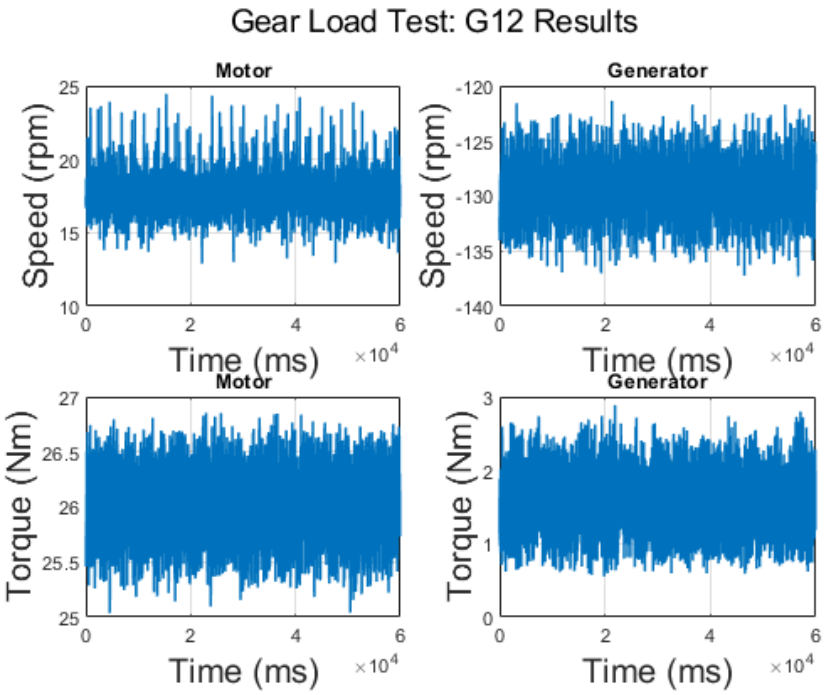

Figure C.110: Gear load test results: G12